

https://dspace.org/

Investigation into the identification and modelling of time-dependent behaviour of deep level excavations in hard rock

Malan, Daniel Francois

2013-06-12
http://hdl.handle.net/10539/12780

Downloaded from a DSpace repository. https://dspace.org/

The copyright of the above-mentioned described thesis rests with the author or the University to which it was submitted. No portion of the text derived from it may be published without the prior written consent of the author or University (as may be appropriate). *Short quotations may be included in the text of a thesis* or dissertation for purposes of illustration, comment or criticism, provided full acknowledgement is made of the source, author and University.

An investigation into the identification and modelling of time-dependent behaviour of deep level excavations in hard rock

Daniël Francois Malan

A thesis submitted to the Faculty of Engineering, University of the Witwatersrand, in fulfilment of the requirements for the degree Doctor of Philosophy

Johannesburg, 1998

I declare that this thesis is my own, unaided work. It is being submitted for the Degree of Doctor of Philosophy in the University of the Witwatersrand, Johannesburg. It has not been submitted before for any degree or examination in any other University.



D.F. Malan

17 March 1998

Date

The objective of this study was to understand the mechanisms leading to the time-dependent deformation of deep excavations in hard rock and to develop appropriate numerical techniques to simulate it. Although hard rock is not usually associated with large creep deformation, data collected from the excavations of the deep South African gold mines illustrates significant time-dependent behaviour. The initial part of this study focused on the uniaxial creep testing of quartzite and lava specimens, indicating that the creep rates of these rock specimens are low. These laboratory measurements were compared with closure data collected in underground stopes. The continuous closure data illustrates significant time-dependent behaviour and contains much information that is lost if only daily measurements are taken. This closure behaviour is the result of the rheology of the fracture zone and the time-dependent extension of this zone following a mining increment. An important finding of this study is that continuous closure data provides useful diagnostic information about the stress conditions in the fracture zone ahead of the stope. This may possibly be used to identify hazardous conditions such as areas prone to face bursting. As no previous attempt has been made to simulate the continuous time-dependent closure behaviour of tabular stopes in hard rock, various approaches were investigated. The author developed a viscoelastic convergence solution for the incremental mining of a stope. Both an analytical approach and implementation in a displacement discontinuity program were considered. Although this model gave a good fit to the observed closure behaviour, some problems are associated with this approach as it is unable to simulate the fracture zone. To simulate the time-dependent development of this zone, a continuum viscoplastic approach was developed and implemented in a finite difference code. This proved successful in modelling the time-dependent closure of stopes and squeezing conditions in weaker quartzites. As the shear creep of discontinuities may be an important time-dependent mechanism, a laboratory testing programme was conducted. Results indicated that discontinuities with gouge infilling undergo noticeable shear creep while the creep rate for mining induced extension fractures is negligible. To simulate this behaviour, a viscoplastic displacement discontinuity technique was developed. This, combined with a tessellation approach, enabled the successful modelling of typical stope closure behaviour and the time-dependent formation of fractures.

The author conducted this research while working for the Deep Gold Mine Fracture Zone Behaviour project of the Rock Engineering programme, CSIR Division of Mining Technology, South Africa. It was funded by the Safety in Mines Research Advisory Committee (SIMRAC), whose support is gratefully acknowledged. I would also like to thank the following individuals and institutions who made this study possible:

Dr. John Napier for acting as co-promoter. He has been my mentor for many years and his deep understanding of science will always be an inspiration to me. I would like to thank him for many valuable discussions and his endless encouragement throughout this study.

Prof. Ugur Özbay for his role as promoter and ensuring that a quality thesis emerged from the research.

Dr. Güner Gurtunca, Director of Miningtek, who created opportunities for post graduate studies.

Mr. Apie Janse van Rensburg for his assistance with the underground measurements. Without his intimate knowledge of the people and operations of the South African mining industry, the time-dependent closure measurements would not have been possible.

Mr. Uli Vogler whose ingenuity and meticulous attention to detail made the shear creep experiments possible.

Mr. Karsten Drescher for his assistance in the creep experiments and willingness to make adjustments to these experiments over weekends.

Dr. Ewan Sellers for participating in many useful discussions. His knowledge of plasticity theory and numerical modelling guided me past many pitfalls.

Mr. Koos Bosman and the other personnel from the Rock Mechanics Department at Hartebeestfontein Mine for their assistance and support of this study. They recognised the importance of studying the time-dependent behaviour of hard rock when others were still doubtful.

The rock mechanics and production personnel at Western Deep Levels Mine, South Shaft, for their assistance in providing panels for the experimental closure measurements.

And finally my wife, Marlie, for her support and for constantly reminding me that there is more to life than just science and engineering.

Page

Declaration ii
Abstract iii
Acknowledgments iv
Contents v
List of figures viii
List of tables xiv

1. Introduction

1.1 Introduction 1
1.2 Need for research into time-dependent behaviour of hard rock surrounding deep excavations 4
1.3 Tabular excavations of the deep South African gold mines 9
1.4 Thesis outline 13

2. Laboratory creep of intact hard rock specimens

2.1 Introduction 15
2.2 Laboratory testing methodology 23
2.3 Results for laboratory specimens 26
2.4 Effect of stress level on the secondary creep phase 33
2.5 Rheological parameters for the laboratory creep data 36
2.6 Summary 41

3. Development of a viscoelastic convergence model for tabular excavations

3.1 Introduction 43
3.2 Deriving a viscoelastic convergence solution for a single parallel-sided panel 44
3.3 Properties of the Burgers convergence model 52
3.4 Dealing with incremental face advance 58
3.5 Parameter calibration from incremental stope closure data 61
3.6 Numerical modelling of incremental viscoelastic stope problems using the displacement discontinuity approach 62

4. Time-dependent closure measurements

4.1 Introduction and previous work 76

4.2 Experimental equipment and methodology 80
4.3 Experimental results - Ventersdorp Contact Reef 84
4.4 Experimental results - Vaal Reef 96
4.5 Comparison between typical closure profiles of the Ventersdorp Contact Reef and Vaal Reef 99
4.6 Continuous closure data versus long period measurements 100
4.7 Calibration and applicability of the developed viscoelastic stope closure model 104

5. The applicability of a continuum viscoplastic model

5.1 Introduction 109
5.2 Model formulation 112
5.3 Simulation of time-dependent fracture zone behaviour 119
5.4 Simulating time-dependent closure of tabular excavations 122
5.5 Analysis of pump chamber deformation at Hartebeestfontein Mine 129
5.6 Effect of support in the squeezing conditions at Hartebeestfontein Mine 137

6. Laboratory investigation of discontinuity creep

6.1 Previous work 141
6.2 Development of testing equipment and methodology 148
6.3 Creep of discontinuities with gouge infilling 153
6.4 Creep of fractures with no gouge infilling 171
6.5 Summary: Shear creep of discontinuities 173

7. A proposed discontinuum viscoplastic model for the time-dependent behaviour of hard rock

7.1 Introduction 175
7.2. Seismicity and time-dependent deformation 176
7.3 Viscoplastic displacement discontinuity model for unfilled dicontinuities 177
7.4 Solution scheme 181
7.5 Incremental mining of a tabular stope: Numerical results 182
7.6 Simulating the creep of gouge-filled discontinuities 186

8. Conclusions and recommendations

8.1 Conclusions 199
8.2 Recommendations for further work 205

List of references 208

Appendix A

A1: Calculating the time-dependent strain of a cylindrical specimen of Burgers material under uniaxial compression 217

Appendix B

B1: Viscoelastic convergence solution for a parallel-sided tabular excavation in a Kelvin material 220

B2: Viscoelastic convergence solution for a parallel-sided tabular excavation in a 3-parameter solid material 224

Appendix C

C1: Calculating the inverse Laplace transformation for the Burgers convergence model 227

Appendix D

D1: Listing of the displacement discontinuity program developed to solve incremental problems in viscoelasticity 230

D2: Input file for solving the incremental enlargement of a tabular stope 247

Appendix E

E1: Correction procedure for the clockwork closure meter data 252

E2: Pascal program to implement the correction procedure 256

Appendix F

F1: Implementation of the elasto-viscoplastic model as a constitutive model in FLAC 258

LIST OF FIGURES

Figure **Page**

1.1 Adverse haulage conditions at Hartebeestfontein Gold Mine in South Africa caused by slow time-dependent deformation processes in the rock 6
1.2 Hypothetical potential for squeezing conditions in ultra deep mining excavations in hard rock 8
1.3 Typical fracture patterns surrounding the tabular excavations in the South African gold mining industry (after Adams et al., 1981) 11
1.4 Typical values of displacement measured at an experimental site at Doornfontein Gold Mine in response to a 1 m face advance (after Legge, 1984) 13

2.1 Typical creep behaviour of rock 16
2.2 Commonly used viscoelastic models and their respective strain-time behaviour for a suddenly applied constant stress 20
2.3 Creep curve for quartzite at room temperature (after Roux and Denkhaus, 1954) 21
2.4 Creep curves obtained for quartzite from Hartebeestfontein Gold Mine (after CSIR, 1963) 22
2.5 Deadweight creep tester 25
2.6 Complete strain-time record of a quartzite sample from Lorraine Mine 27
2.7 Incremental creep curves of the last four stages for the test in Figure 2.6 27
2.8 Complete strain-time record for a lava sample from Western Deep Levels Mine. 28
2.9 Incremental creep curves of the last four stages for the test in Figure 2.8 28
2.10 Complete strain-time record of a quartzite sample from Western Deep Level Mine 30
2.11 Incremental creep curves of the last three stages for the test in Figure 2.10 30
2.12 Complete creep curve for the last loading increment of a quartzite sample from Western Deep Levels Mine 31
2.13 Complete strain-time record of a quartzite sample from Hartebeestfontein Mine.. 32
2.14 Incremental creep curves of the last three stages for the test in Figure 2.13 32
2.15 Effect of stress on the steady-state creep rate of different hard rocks in the South African gold mining industry 33
2.16 The steady-state creep rate of hard rock as a function of the σ/UCS ratio 34
2.17 Log (strain rate) versus log (stress) for the lava sample 35
2.18 Burgers viscoelastic model fitted to the creep of the lava sample from Western Deep Levels Mine 38
2.19 Burgers viscoelastic model fitted to the creep of the quartzite sample from Lorraine Mine 38
2.20 Burgers viscoelastic model fitted to the creep of the quartzite sample from Western Deep Levels Mine 39
2.21 Burgers viscoelastic model fitted to the creep of the quartzite sample from Hartebeestfontein Mine 39
2.22 Dependence of the viscosity coefficient η_M on the applied stress magnitude for lava 41

3.1 Schematic diagram of a typical tabular ore body dipping at α° (after Salamon et al., 1964) ... 45
3.2 Single parallel-sided panel ... 45
3.3 The Burgers model representing the rock behaviour in distortion ... 49
3.4 The effect of the value of G_2 on the closure behaviour of a tabular opening ... 53
3.5 The effect of the value of G_1 on the closure behaviour of a tabular opening ... 54
3.6 The effect of the value of η_2 on the closure behaviour of a tabular opening ... 54
3.7 The effect of the value of η_1 on the closure behaviour of a tabular opening ... 55
3.8 Effect of stope span on the convergence at the centre of an imaginary panel which is mined in one step ... 56
3.9 Comparison of convergence behaviour at different positions of an imaginary panel which is mined in one step ... 56
3.10 Rate of steady-state convergence along a panel of span 100 m ... 58
3.11 Instantaneous incremental convergence as a function of position ... 60
3.12 The equivalent stope principle ... 62
3.13 A flow chart for the calculation of the displacement discontinuity components for incremental viscoelastic problems ... 68
3.14 Thick-walled tube ... 69
3.15 Radial displacement for a pressurised thick-walled tube at point (a+b)/2 ... 70
3.16 Incremental enlargement of a two-dimensional stope ... 71
3.17 Numerical and analytical solution of the convergence at a distance of 0.125 m from the centre of the stope for the problem illustrated in Figure 3.16 ... 73
3.18 Vertical stress 6 m ahead of original stope face ... 74
3.19 Displacements in the material above the stope ... 74

4.1 Typical closure curves obtained from long period measurements (after Wiggill, 1965) ... 77
4.2 Typical time-dependent closure profiles measured at East Rand Proprietary Mines (after Leeman, 1958) ... 78
4.3 Mechanism of the clockwork closure meter used to collect time-dependent closure data ... 80
4.4 An example of continuous closure data recorded using the clockwork closure meter ... 82
4.5 The corrected closure data for the measurements depicted in Figure 4.4 ... 82
4.6 Installation of the clockwork closure meter in a stope ... 83
4.7 Installation of the clockwork closure meter normal to the plane of the excavation ... 83
4.8 Plan view of the mining geometry in the area where the closure data was collected at Western Deep Levels Mine ... 85
4.9 Enlarged plan view of the W3 up-dip panel in the 87-49 longwall with the positions of the meters indicated ... 86
4.10 Numbering convention used for the clockwork closure meters in the up-dip panel ... 87
4.11 Typical time-dependent stope closure for the Ventersdorp Contact Reef at Western Deep Levels Mine ... 88
4.12 Closure as a function of time for different positions in the panel following the blast on 15/4/97 ... 89
4.13 Closure as a function of time for different positions parallel to the face following the blast on 15/4/97 ... 89
4.14 Closure as a function of time for different positions from the face following a seismic event of magnitude 1.2 on 16/4/97 ... 90

4.15 Closure as a function of time for different positions parallel to the face following a seismic event of magnitude 1.2 on 16/4/97 91
4.16 Closure measured when there was no mining activity for a period of 4 days from 25/4/97 to 29/4/97 92
4.17 Closure behaviour, including the typical overshoot recorded for some seismic events 93
4.18 Installation of the closure meters in the breast panel 94
4.19 Closure as a function of time for closure station no. 3. The last mining activity in the panel was on 13/6/97 95
4.20 Closure as a function of time for closure station no. 1 95
4.21 Plan view of the mining geometry of the No. 6 shaft pillar area, Hartebeestfontein Mine where the closure data was collected 96
4.22 Location of the clockwork closure instrument in the 78N23 longwall 97
4.23 Closure measured at Hartebeestfontein Mine 98
4.24 Closure measurements at Hartebeestfontein Mine for a larger distance to face compared to Figure 4.23 98
4.25 Comparison of typical closure profiles of the Ventersdorp Contact Reef and Vaal Reef 100
4.26 Continuous closure measured in the up-dip panel at Western Deep Levels Mine.. 102
4.27 This is the resulting closure curve for the same data set as above, but with a sampling period of 24 hours 102
4.28 Comparison between continuous and daily closure measurements where the measurements are taken further from the face than in Figures 4.26 and 4.27 103
4.29 Postulated relationship between continuous and daily closure measurements 100
4.30 Position of the closure station in the 25-15E longwall at Deelkraal Gold Mine.... 105
4.31 Time-dependent closure measured in the 25-15E longwall at Deelkraal Gold Mine 106
4.32 The Burgers viscoleastic convergence solution fitted to the experimental closure measured at Deelkraal 106
4.33 Proposed addition of a third elastic component to the Burgers model to simulate the gradual reduction in steady state closure rate in the absence of mining activity 107

5.1 Conceptualization of the fracture zone surrounding tabular excavations and time-dependent extension of this zone following a mining increment 110
5.2 The Bingham rheological model 111
5.3 Representation of the developed elasto-viscoplastic model 113
5.4 The evolution of the yield surface for intact rock to the eventual residual surface for failed rock 114
5.5 Simulated time-dependent fracture zone formation surrounding a tunnel in elasto-viscoplastic rock subjected to constant field stresses 121
5.6 Simulated tunnel closure (sidewall - sidewall) as a function of time caused by the time-dependent fracture zone formation described above 121
5.7 Effect of different rates of cohesion weakening on the closure behaviour of the tunnel 122
5.8 Geometry and boundary conditions used for simulating tabular excavations 123
5.9 Simulated time-dependent closure 124
5.10 Comparison of the major principal stress as a function of distance ahead of the face 126
5.11 Comparison of the closure behaviour as a function of time after the blast 126
5.12 Simulated time-dependent movement of the major principal stress peak ahead of the face after blasting 127

5.13 Experimental and simulated stope closure after blasting 128
5.14 View of the excavations surrounding the pump chamber 130
5.15 Increase in vertical stress measured at the pump chamber 130
5.16 Footwall deformation of the pump chamber measured with rod extensometers anchored at different depths 131
5.17 Hangingwall deformation of the pump chamber measured with rod extensometers anchored at different depths 132
5.18 Sidewall deformation on the south side of the pump chamber measured with rod extensometers anchored at different depths 132
5.19 Sidewall deformation on the north side of the pump chamber measured with rod extensometers anchored at different depths 133
5.20 Major principal stress contours (MPa) surrounding the pump chamber on a plane normal to the long axis of the excavation 133
5.21 Major principal stress contours (MPa) before failure using the developed two-dimensional elasto-viscoplastic code 134
5.22 Pattern of cable anchor support simulated in the model 135
5.23 Comparison between the numerical simulation and experimental data for the 2 m extensometer on the south side of the pump chamber 136
5.24 Comparison between the numerical simulation and experimental data for the 2 m extensometer on the north side of the pump chamber 136
5.25 Numerical results for the surface deformation of the footwall and hangingwall 137
5.26 Haulage conditions experienced in the squeezing rock at Hartebeestfontein Mine 138
5.27 Cable anchor support used in the simulation 139
5.28 Typical effect of cable anchor installation on the closure rate in the tunnel 140

6.1 Axial strain versus time for a cylindrical water-saturated Westerly granite sample with an inclined discontinuity 143
6.2 Time-dependent deformation of cylindrical Westerly granite samples with inclined discontinuities at different values of deviatoric stress 144
6.3 Shear creep of shale discontinuities for low shear stress/shear strength ratios (after Bowden and Curran, 1984) 146
6.4 Shear creep of shale discontinuities for high shear stress/shear strength ratios (after Bowden and Curran (1984)) 146
6.5 Attachment of the LVDT's to the discontinuity sample 149
6.6 Shear box developed for the testing of discontinuity creep 150
6.7 Shear box developed to investigate the creep of discontinuities in hard rock 151
6.8 Details of the LVDTs and attachments glued to the surface of the rock 151
6.9 The lower half of a natural discontinuity obtained from a drill core and cast in a resin mixture 152
6.10 Particle size distribution (% weight) of the artificially prepared gouge material 154
6.11 Grains of the artificially prepared gouge material 154
6.12 Shear behaviour of the unfilled sawcut discontinuity in quartzite 156
6.13 Typical shear creep behaviour of the discontinuity with gouge infilling and periodic increases of shear stress 157
6.14 Normal displacement for the specimen in Figure 6.13 157
6.15 Typical shear creep behaviour of a discontinuity with gouge infilling 158
6.16 Normal creep behaviour for the specimen in Figure 6.15 159
6.17 Shear displacement for a specimen with gouge thickness of 2 mm. The shear load was removed 4 hours after application 160
6.18 Shear displacement for a specimen with gouge thickness of 2 mm. The shear load was removed 48 hours after application 160
6.19 The effect of shear stress magnitude on the creep behaviour 161

6.20 The effect of shear stress magnitude on the cumulative instantaneous shear displacement 162
6.21 The effect of shear stress magnitude on the creep rate of the secondary phase..... 162
6.22 The effect of shear stress magnitude on the creep rate of the secondary phase..... 163
6.23 The effect of shear stress magnitude on the creep behaviour 164
6.24 The effect of shear stress magnitude on the creep rate of the secondary phase..... 164
6.25 Shear creep rate of the secondary phase as a function of gouge thickness..... 165
6.26 Effect of water on the creep rate of the discontinuity..... 166
6.27 Log (shear displacement rate) versus log (shear stress/shear strength) for the data in Figure 6.21 167
6.28 Size distribution of the particles (% weight) in the gouge collected from the bedding plane layers at Hartebeestfontein Mine..... 168
6.29 Microscope photograph of the natural gouge material collected..... 169
6.30 Shear creep behaviour of the discontinuity with gouge infilling from Hartebeestfontein Mine..... 169
6.31 Normal displacement for the specimen in Figure 6.30..... 170
6.32 The effect of shear stress magnitude on the creep rate of the secondary phase for the Hartebeestfontein gouge tested at 100 % humidity..... 170
6.33 Shear creep behaviour of the extension fracture in Ventersdorp lava for a periodic increase of shear stress..... 172
6.34 The dilation of the sample that accompanied the shear creep of Figure 6.33..... 172

7.1 Evolution of the yield surface for intact discontinuities to the eventual residual surface..... 180
7.2 Time-stepping solution scheme..... 181
7.3 Initial random distribution of potential fracture planes surrounding the reef..... 182
7.4 Development of the fracture zone 24 hours after the 9th mining increment..... 183
7.5 Increase in cumulative fracture length after the 9th increment..... 184
7.6 Numerical stope closure as a function of time. Blasting took place at 0, 24, 48, 72 and 96 hours..... 185
7.7 Numerical and experimental rate of closure as a function of time..... 186
7.8 Rheological model to approximate the shear creep of discontinuities with infilling..... 187
7.9 Simulating the experimental shear creep using the rheological model given in equation [7.17]..... 189
7.10 Experimental and simulated compaction accompanying the shear results in Figure 7.9..... 190
7.11 Relationship between the Maxwell stiffness, K_{ds1}, and the (τ/τ_s) ratio..... 191
7.12 $\text{Log}(K_{ds1})$ versus $\log(\tau/\tau_s)$ plot..... 191
7.13 Relationship between the Maxwell viscosity, η_{ds1}, and the (τ/τ_s) ratio..... 192
7.14 $\text{Log}(\eta_{ds1})$ versus $\log(\tau/\tau_s)$ plot..... 193
7.15 Relationship between the Kelvin stiffness, K_{ds2}, and (τ/τ_s) ratio..... 194
7.16 $\text{Log}(K_{ds2})$ versus $\log(\tau/\tau_s)$ plot..... 194
7.17 Incremental mining towards a fault with gouge infilling..... 197
7.18 Simulated fault creep measured during the last three mining increments..... 198

A1 Burgers model..... 217
B1 The Kelvin model representing the rock behaviour in distortion..... 220

B2 The effect of the viscosity parameter (η) on the behaviour of the Kelvin convergence model 223
B3 The effect of Young's modulus (E) on the behaviour of the Kelvin convergence model 223
B4 The 3-parameter solid representing the rock behaviour in distortion 224
D1 Fixed format used for the input files of VISCODD 248
E1 Recording mechanism of the clockwork closure meter 252
E2 Sample of the calibration curves of the clockwork closure meters 253
E3 Calculation of the radius r from the calibration curves 253
E4 Illustration of the error in x-value as the curve deviates from the central horizontal line 254

LIST OF TABLES

Table **Page**

2.1 Average values of elastic and strength properties of the rocks analysed in this study 23

2.2 Calibrated values for the power law given in equation [2.6] 36

2.3 Calibrated Burgers viscoelastic parameters for the different rock types 40

4.1 Differences between continuous closure measurements and long period measurements 101

5.1 Model parameters used to simulate time-dependent fracture formation surrounding a tunnel 120

5.2 Properties used for the incremental mining of the tabular stope to obtain the results in Figure 5.9 124

5.3 Properties used to obtain the results in Figure 5.10 and 5.11 125

5.4 Parameters used to simulate the pump chamber deformation 135

6.1 Summary of discontinuity creep tests described in the literature 147

6.2 Petrographic analysis of the quartzite before crushing 155

6.3 Calibrated values for the power law in equation [6.1] 167

Chapter 1

Introduction

1.1 Introduction

Changes in the local stress state due to mining activity perturb the stability of the rock mass surrounding excavations. The subsequent readjustment of the rock towards a new equilibrium does not occur instantaneously but as a gradual process over time. This process can include two types of inelastic deformation namely aseismic (creep-like) movements and violent failures or rockbursts. Depending on the rock type and stress, excavations can show a propensity towards either of these two phenomena. In relation to mine safety, it is preferable that all deformation occurs in a non-violent fashion. It is therefore important to determine the conditions associated with the transition from stable deformation to rockbursts. Excessive aseismic rock movements are also undesirable as they may significantly affect the long term stability of underground openings. The rock may deform continuously leading to an eventual collapse. Any engineering design must therefore include the time-dependent properties of the rock. To accomplish these objectives, time-dependent constitutive laws for rock, including hard brittle material, must be established.

The terms *creep* and *time-dependency* are loosely defined by many authors and unfortunately are often used interchangeably to describe the various creep-like phenomena. As a further complication, some mining engineers tend to associate the term *creep* only with the gradual deformation in salt mines and not with other rock types. To avoid this confusion, the following definitions are introduced and will be used throughout this thesis.
a) *Creep* is continued deformation due to a constant applied stress and will be used exclusively in relation to laboratory-sized specimens containing no large scale discontinuities. Note that the mechanism of creep may differ in various rock types, ranging

from dislocation processes in salt to microfracture initiation and growth in hard rocks (Dusseault and Fordham, 1993). Regardless of the mechanism involved, the gradual deformation of all intact rock specimens in the laboratory will be referred to as *creep*.

b) *Time-dependency* will be used as a more general term encompassing concepts like the creep of intact rock, creep of large scale discontinuities, delayed failure and long term strength. As the rheological behaviour of the rock mass underground is a complex interrelation of these factors, it will therefore be referred to as time-dependent. When used in relation to underground measurements, time-dependency is also understood to refer to deformations not related to geometric changes in the dimensions of an excavation. It occurs on a time scale of days to years and is therefore not related to elastodynamic behaviour.

Creep of rocks has been studied since the early part of this century (Griggs, 1939) resulting in the availability of a large amount of data. Most of the studies, however, have focused on the softer saltrocks because they show significant creep under stress and temperature conditions easily applied in the laboratory. (See Lama and Vutukuri, 1978 and Dusseault and Fordham, 1993 for a detailed summary of creep studies.) For engineering applications, the importance of time-dependent behaviour in the form of rapid convergence of tunnels in salt or weak rock is well known. *Squeezing* conditions are said to exist if an excavation is subjected to very large time-dependent deformation. A review of the squeezing potential of rock around tunnels can be found in Aydan et al. (1996). The definition of squeezing as proposed by the ISRM commission on the squeezing of rock in tunnels is as follows (Barla, 1995).

"Squeezing of rock is the time-dependent large deformation which occurs around the excavation, and is essentially associated with creep caused by exceeding a limiting shear stress. Deformation may terminate during construction or continue over a long period."

When a tunnel is driven into soft squeezing rock (such as soft clays or mudstone), the ground advances slowly into the opening without visible fracturing or loss of continuity (Gioda and Cividini, 1996). A large research effort is devoted to obtaining suitable time-dependent constitutive laws for these rocks (e.g. Gioda, 1982; Gioda and Cividini, 1996; Aydan et al., 1996) and designing effective support for excavations in these conditions (Matsushita et al., 1995; Panet, 1996; Schubert, 1996; Steiner, 1996; Blümel, 1996).

In comparison, creep strain in crystalline rock is of limited importance in most engineering projects due to the very low creep rate. The creep of hard rock has nevertheless been extensively studied in relation to earthquake research and crustal deformation (Carter and Kirby, 1978; Tan and Wu, 1989; Paterson and Luan, 1990). Near the earth's surface the behaviour of these crystalline rocks is elastic brittle. However at moderate depths at elevated temperature and pressure, the behaviour is semi-brittle with thermally activated processes contributing to the creep strain. Therefore, many laboratory experiments have been performed with the specimens subjected to elevated temperatures and pressures. Some examples of creep at high temperature and pressure can be found in Carter et al. (1981), Koch et al. (1989) and Post et al. (1996). Even though these results illustrate appreciable creep strains, the pressures and temperatures are far in excess of what can be expected in typical mining engineering applications. Even in the deep gold mines in South Africa, the rock temperatures rarely exceed 70° C (Dusseault and Fordham, 1993). For hard rocks it is known that heating from room temperature to 100° C does not affect the creep rate significantly (Pusch, 1993; Dusseault and Fordham, 1993).

An engineering application where the time-dependent behaviour of hard rock recently became more important is the study of long term stability of chambers used for nuclear waste repositories (Blacic, 1981; Pusch, 1993). An important aspect of the problem is that the excavations must be maintained for a minimum time of 100 years to allow retrieval of waste and monitoring of repository performance. Although, intuitively, damage to excavations in hard rock from time-dependent deformation seems unlikely, Blacic (1981) showed that time-dependent microcracking and water-induced stress corrosion can lead to significant reductions in strength in the near field region of a repository. The issue of roof stability of these repositories has also become important. Although these roofs may remain stable for hundreds of years, depending on the rock type, excavation dimensions and stress conditions, problems may appear soon after development as noted in the deep mines in South Africa. Pusch (1993) estimated the rock disintegration of the roof of the Swedish repository at Forsmark where the excavation is intersected by a fracture zone. By generalising the structure to be one of regular layers of blocks and applying a log-time creep law, he estimated that the roof would disintegrate to a depth of 3 m over a period of a thousand years.

1.2 Need for research into time-dependent behaviour of hard rock surrounding deep excavations

Researchers in the South African mining industry (Roux and Denkhaus, 1954; Denkhaus et al., 1958) recognised as long as four decades ago that the time-dependent behaviour of hard rock is important as it may cast light on why rockbursts do not always occur at blasting time, but also when there is no external influence that could account for changes in stress distribution. The importance of including the time factor in analyses of instabilities in mines was recently emphasised by Linkov (1995, 1996, 1997). Intuitively one would not expect significant time-dependent rock behaviour in the South African mines as the creep rate of the intact hard rock is low. Contrary to this belief, appreciable time-dependent movements have been observed underground (See Chapter 4). This thesis is an attempt to increase the understanding of the mechanisms controlling the time-dependent behaviour in hard rock and to simulate them numerically.

Significant time-dependent deformation is important as it may cause a gradual non-violent reduction of abutment stress and hence diminish the danger of rockbursts. Dusseault and Fordham (1993) noted that for the mining engineer, ongoing time-dependent deformation is an indication of the efficient redistribution of stress, preventing the build-up of large stress concentrations. Although not directly related to hard rock, Pomeroy (1956) carried out creep experiments on a number of coal specimens. Anthracite samples did not creep (within the limits of sensitivity of the equipment used) and always failed explosively. He related this to the frequent occurrence of violent bursts in anthracite mines. These bursts are much less common in mines for which significant creep is observed in the coal. Similarly, Denkhaus et al. (1958) noted that in South African mines the susceptibility to bursts was much more prevalent in stopes in the Central Rand, where the reef lies between hard brittle quartzite bands, than on the Far East Rand where the reef lies on ductile shale. Unfortunately a systematic study of the creep of hard rock throughout the South African industry has never been conducted, probably owing to the long duration of individual tests and the lack of suitable testing equipment. Historically, the sixties and the early seventies have been regarded as the golden era of rock mechanics in the South African mining industry. Significant advances were made in the application of elastic theory to mining problems (Ryder and Officer, 1964; Salamon et al., 1964; Cook et al., 1966; Salamon, 1974). With the arrival of computers, much research effort was then directed towards the development of numerical codes based on elastic theory to simulate mine layouts

(Plewman et al., 1969; Deist et al., 1972; Deiring, 1980; Napier and Stephanson, 1987). As this work presented big technical challenges in its own right, the study of inelastic rock behaviour and especially time-dependency was somewhat neglected. The situation was further aggravated by a school of thought which associated creep phenomena exclusively with soft rocks like halite and potash. The need for the time-dependent testing of hard rock, whether for intact samples, discontinuities or *in situ,* has not always been recognised.

One strategy that may be useful in controlling the stability of the fracture zone in hard rock is the rate of stope face advance. Cook et al. (1966) found from a statistical analysis of rockburst data in the South African mines that there is an increase in rockbursts for a face advance rate of more than 4 m a month, for small abutments, to 8 m a month, for large abutments. Similarly, Linkov (1996) noted that in the Kizel coal mines, doubling the rate of coal cutting on a face from 0.27 m/min to 0.54 m/min resulted in a drastic increase in the incidence of rockbursts. A time-dependent constitutive law appropriate to rock on a mine-wide scale could therefore lead to some generalisations regarding safe rates of extraction and better control of the fracture zone. Unfortunately no complete understanding of the time-dependent behaviour of excavations in hard brittle rock has, as yet, been achieved.

Time-dependent rock behaviour plays a further important role in determining the long term stability of service excavations where delayed fracture may lead to eventual failure. Potts and Hedly (1964) pointed out that:

"One of the most important features of a material which exhibits 'creep' characteristics is the incidence of delayed fracture. In mining this would imply that a room and pillar area, which is stable immediately after extraction deteriorates in time and ultimately goes to failure."

Because of the great depth of the South African mines, some mines in areas with weaker argillaceous quartzites (uniaxial compressive strength of 130 MPa) also experience rock movements reminiscent of squeezing conditions in weak rock. The combination of weak quartzites and high stress at Hartebeestfontein Mine leads to appreciable time-dependent movement of the rock (Malan and Bosman, 1997). This is most notable in service excavations located in highly stressed ground where the rock becomes progressively more fractured with time. Movements of up to 6 cm per shift can be observed, leading to severe

support difficulties. Figure 1.1 illustrates typical conditions in excavations experiencing significant time-dependent deformation. This necessitates frequent rehabilitation of the tunnels. If the time-dependent fracture processes could be better understood, optimum strategies could be developed to reduce the cost of continually installing new support. As an illustration of the costs involved, in a particular section of this mine, mining is impossible without constant rehabilitation of the access ways leading to the reef. Besides the development cost and the cost of initial support work, the rehabilitation of excavations is estimated to cost R2.4 million (US $540 000) per annum in 1997 terms. Although the loss of revenue due to production losses is difficult to quantify, this is conservatively estimated at R11 million per annum. Nevertheless, the benefit of this squeezing behaviour is that strain bursting is virtually absent in this area. It should however be noted that these severe squeezing conditions are not encountered often at the current depths of the South African industry.



Figure 1.1. Adverse haulage conditions at Hartebeestfontein Gold Mine in South Africa caused by slow time-dependent deformation processes in the rock. Note that this is not rockburst damage (courtesy W.D. Ortlepp).

Unfortunately the depletion of shallow ore reserves is forcing the South African industry to exploit reefs at ever increasing depths (see also Section 1.3). Of significance are recent discussions of possible ultra-deep mining operations at depths between 3500 m and 5000 m (Diering, 1997). As the estimated overburden stress at these depths will vary between 95 MPa and 135 MPa (assuming a rock density of 2700 kg/m^3), there is no doubt that the challenges facing the industry are immense. As these excavations will be the first attempt ever to mine at these depths, there is no guarantee that the current rock mechanics knowledge and associated empirical rules will ensure viable ore extraction. Apart from the expected increase in the rockburst problem, there might also be an increased potential for squeezing conditions in ultra-deep mining. This will put additional strain on the profitability of these mines and it is therefore imperative that the conditions leading to squeezing conditions in hard rock are better understood.

For tunneling in soft rock, an empirical rule frequently used to identify squeezing conditions is the competency factor c. This is defined as the ratio of the uniaxial compressive strength of the rock to the overburden stress (Muirwood, 1972; Nakano, 1979; Barla, 1995; Aydan et al., 1996).

$$c = \frac{\sigma_c}{\rho g H} \qquad [1.1]$$

where σ_c is the uniaxial compressive strength of intact laboratory specimens, ρ is the density of the rock, g is gravitational acceleration and H is the depth below surface. In general, squeezing conditions are found for $c < 2$. This was recently confirmed by Aydan et al. (1996) who did an extensive survey of squeezing tunnels in Japan. The depth of tunnels in this study was less than 400 m and the host rock comprised typical soft types like mudstone, tuff, shale and siltstone. It is therefore unclear if this simple rule can be extended to ultra-deep mining in hard rock. The squeezing behaviour at Hartebeestfontein Mine occurs at a depth of 2500 m. As the uniaxial compressive strength of the quartzite in which the excavations are developed can be as low as 130 MPa, the competency factor can be calculated from equation [1.1] as $c = 1.9$ (assuming a rock density of 2700 kg/m^3). It should be noted that the value of $c = 1.9$ is only a conservative estimate as the vertical stress in this area is higher than the overburden stress owing to the extensive mining in the surrounding area. Therefore c is in effect less than 1.9. It should also be noted that the

uniaxial compressive strength of the quartzite varies from area to area (Malan and Bosman, 1997) and therefore c will vary correspondingly.

In Figure 1.2, a competency factor of c = 2 (ρ = 2700 kg/m^3, g = 9.81 m/s^2) is plotted on a graph of uniaxial compressive strength versus depth. The validity of the initial portion of the line (< 400 m) is confirmed by the many investigations of squeezing behaviour in soft rock. To illustrate the increased potential for squeezing conditions in ultra-deep mines, this line is extended to 5000 m. In Figure 1.2 any combination of depth and rock strength below the c = 2 squeezing line will lead to squeezing conditions. Of particular concern is the average strength of the Witwatersrand quartzites of only 200 MPa (see Section 1.3). Figure 1.2 suggests that ultra-deep tunnels developed in these rocks would be subject to squeezing conditions. It should, however, be emphasised that there is currently little evidence of squeezing in hard rock at great depths apart from the conditions at Hartebeestfontein Mine. The relationship in equation [1.1] may only be valid for squeezing in soft rock. Note that σ_c in this equation refers to the strength of intact laboratory specimens and not the strength of the rock mass that can be weakened by bedding planes and joints. Equation [1.1] should probably be rewritten for deep hard rock mines to include a rock mass rating and use the actual value of stress rather than an estimated overburden stress.

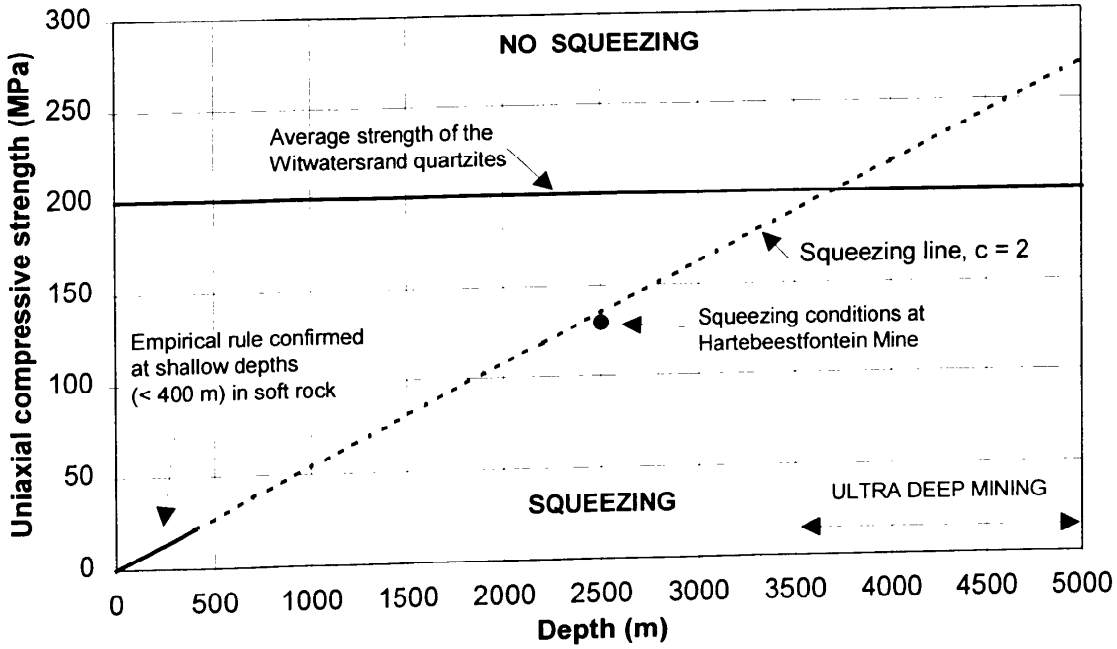

Figure 1.2. Hypothetical potential for squeezing conditions in ultra-deep mining excavations in hard rock.

1.3 Tabular excavations of the deep South African gold mines

As this study was originally motivated by the lack of understanding of time-dependent rock behaviour in the tabular excavations of the South African gold mines, the work presented here will naturally be biased towards the rock and excavation types found in this industry. A general discussion of tabular excavations and the rock types typically encountered is therefore appropriate at this stage.

The gold-bearing conglomerates of the Witwatersrand system are essentially plane tabular in nature implying a negligible height compared to the lateral extent of the orebody (see Figure 3.1 in Chapter 3). Although the reef is frequently dislocated by faults and dykes, the plane tabular nature of the orebody can persist for many square kilometres in some areas. Although the reef can be nearly horizontal in certain locations, it is generally inclined between 25° and 45° (*dip angle*). The reef thickness can vary from a few centimetres to more than a metre. In order to maintain economical viability, the reefs are mined with as small a working height or *stoping width* as possible. In 1980 the average stoping width throughout the industry was estimated to be 1.33 m (Gay and Jager, 1980). Reef extraction may extend over several square kilometres resulting in large stope spans and eventual contact between the roof (hangingwall) and floor (footwall) of the excavations in the areas far away from the working faces. The relative movement of the hangingwall and footwall normal to the plane of the reef is called *closure*. *Convergence* refers to the elastic component of closure. Closure is therefore the sum of elastic convergence and inelastic deformation. The average rock breaking depth is approximately 2000 m, although workings deeper than 3500 m can be found (Schweizer and Johnson, 1997). It is forecast that by the year 2010 some 30% of South African gold production will come from depths greater than 3000 m (Johnson and Schweizer, 1996). Typical stresses encountered at a depth of 2500 m are 66 MPa in the vertical direction and 33 MPa in the horizontal direction.

A description of the most important gold-bearing reefs currently exploited can be found in Lurie (1977) and Schweizer and Johnson (1997). The *Carbon Leader* is a carbon-rich streak or seam in quartzite. It varies in thickness from a few millimetres up to 8 cm in width. The footwall of excavations exploiting this reef is generally characterised by competent quartzites. Bedded siliceous quartzite (0-3 m in thickness) and the shaly Green

Bar (1-5 m in thickness) form the hangingwall. The *Ventersdorp Contact Reef* (VCR) is an intermittent conglomerate at the base of the Ventersdorp Supergroup with pebble sizes varying from a few millimetres up to 40 cm. The footwall of these excavations in different areas consists of a great variety of quartzites ranging from siliceous to argillaceous. The hangingwall of the VCR is formed by volcanic rocks that can be divided into Westonaria Formation lavas (termed soft lava) and Alberton Porphyry Formation lavas (termed hard lava). The *Vaal Reef* is a conglomerate consisting of small pebbles closely packed in a pyritic matrix. It varies in width from a carbon parting to over 1.2 m. The footwall and hangingwall of the excavations in these areas consist of argillaceous quartzites.

The main rock types exposed by these tabular excavations are therefore hard brittle quartzites and lavas. The strength of these rock types varies greatly from area to area. The uniaxial (unconfined) compressive strength (UCS) of an average Witwatersrand quartzite is 200 MPa (Gay and Jager, 1980), although it can be as low as 130 MPa (Malan and Bosman, 1997). Some of the Ventersdorp lavas are very rigid and can have UCS values of more than 400 MPa (see Table 2.1 in Chapter 2).

As a result of the great depth and the tabular nature of the excavations, large stresses are experienced ahead of the working faces. These normally exceed the strength of the rock, resulting in the formation of an extensive fracture zone. Under high stress conditions, this zone can extend to more than 5 m ahead of the face (Adams et al., 1981). Figure 1.3 illustrates typical discontinuity types surrounding the face area of a tabular excavation.

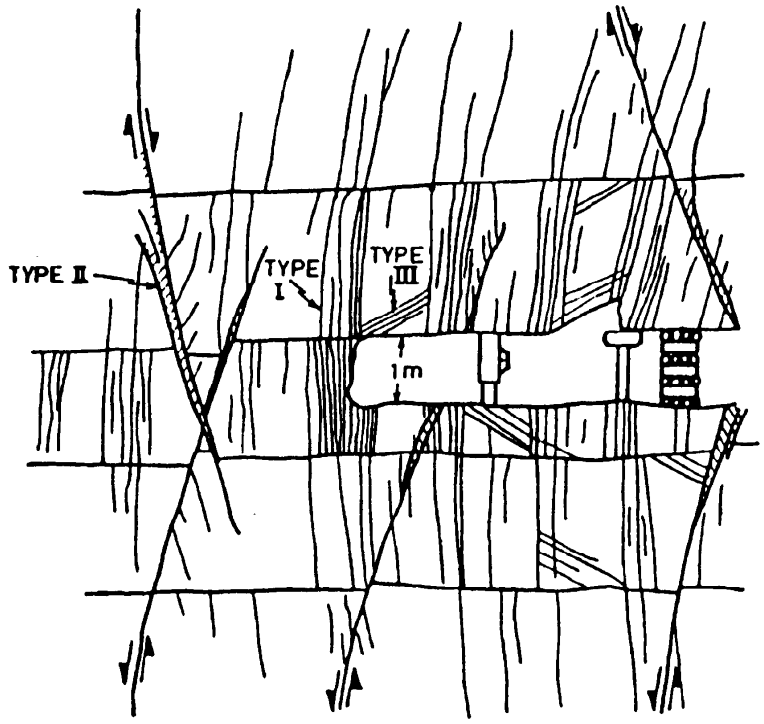

Figure 1.3. Typical fracture patterns surrounding the tabular excavations in the South African gold mining industry (after Adams et al., 1981). Type I fractures are steep fractures parallel to the stope face. These fractures are extensile in nature and form some distance ahead of the face. Some of these fractures show evidence of subsequent shearing as the face approaches. Type II fractures are mining-induced shear fractures which dip away from the stope and often occur as conjugate pairs. Large displacements have been observed on these fractures. Type III are low angle fractures which form close to the face. Other discontinuities playing a prominent role in the rock behaviour are the bedding planes parallel to plane of the reef.

After blasting, the fracture zone needs to adapt to the changing stress conditions. Little is known about the time-dependent nature of this process. Adams and Jager (1980) investigated the extent of the fracture zone and the pattern of rock failure that occurs ahead of advancing stope faces. These studies mostly concentrated on the Chamber of Mines' mechanized rock breaking site at Doornfontein Gold Mine, although some blasted stopes were also investigated. They found the formation of fractures to be associated with the face advance with the majority of new fractures forming within a relatively short period after blasting. The amount of new fracturing taking place then diminished with time. Their observations indicated that if the face was not mined for a period of two weeks, no new fractures formed. Turner (1984) also observed time-dependent fracture development at the mechanized rock breaking site. He investigated the occurrence of hard patches in the face.

Fracturing was absent in these patches which were therefore difficult to mine using mechanical equipment. It was noted that some of these patches became mineable after a few days as the rock became more fractured. This time-dependent fracturing of the hard patches occurred even when no mining had taken place for several days. Joughin and Jager (1983) monitored seismic activity and fracture zone development at the mechanized rock breaking site. Again it was found that most fractures develop in direct response to the mining of the stope face. As the face is advanced, the fracture zone migrates forward ahead of the face. The new fractures form within a short time after advancing the face and little fracturing takes place more than three hours after the blast. It was noted that most of the seismic activity was confined to a small part of the stope where the face was intersected by a group of minor faults. The only difference in the behaviour of the fracture zone in this active part of the stope was that the fractures did not form regularly when the face was advanced. Legge (1984) made a series of measurements of displacements associated with the development and behaviour of fractures. Extensometer data indicated that new fractures initiated as narrow dilating zones some distance ahead of the face in response to advances of 0.5 m or more. Continuous recordings of extensometer data indicated that these movements occurred in a time-dependent fashion that typically lasted up to nine hours after blasting. If stopes were not mined for extended periods, only the portion of the fracture zone close to the face ($\leq$ 1 m) showed significant further time-dependent dilation. During one period at the mechanized rock breaking site at Doornfontein Gold Mine, the panel was not mined for a month. The rock within 1.5 m of the face nevertheless experienced a further dilation of 10 mm in this period. From his extensive set of measurements, Legge (1984) was able to deduce a conceptual picture of the deformation patterns surrounding a typical face. These values (Figure 1.4) are superimposed on an idealised picture of the typical fractures found in this area. There is significant shear on some of the larger discontinuities, but it is not clear how these displacements evolve over a period of time.

Fracturing was absent in these patches which were therefore difficult to mine using mechanical equipment. It was noted that some of these patches became mineable after a few days as the rock became more fractured. This time-dependent fracturing of the hard patches occurred even when no mining had taken place for several days. Joughin and Jager (1983) monitored seismic activity and fracture zone development at the mechanized rock breaking site. Again it was found that most fractures develop in direct response to the mining of the stope face. As the face is advanced, the fracture zone migrates forward ahead of the face. The new fractures form within a short time after advancing the face and little fracturing takes place more than three hours after the blast. It was noted that most of the seismic activity was confined to a small part of the stope where the face was intersected by a group of minor faults. The only difference in the behaviour of the fracture zone in this active part of the stope was that the fractures did not form regularly when the face was advanced. Legge (1984) made a series of measurements of displacements associated with the development and behaviour of fractures. Extensometer data indicated that new fractures initiated as narrow dilating zones some distance ahead of the face in response to advances of 0.5 m or more. Continuous recordings of extensometer data indicated that these movements occurred in a time-dependent fashion that typically lasted up to nine hours after blasting. If stopes were not mined for extended periods, only the portion of the fracture zone close to the face ($\leq$ 1 m) showed significant further time-dependent dilation. During one period at the mechanized rock breaking site at Doornfontein Gold Mine, the panel was not mined for a month. The rock within 1.5 m of the face nevertheless experienced a further dilation of 10 mm in this period. From his extensive set of measurements, Legge (1984) was able to deduce a conceptual picture of the deformation patterns surrounding a typical face. These values (Figure 1.4) are superimposed on an idealised picture of the typical fractures found in this area. There is significant shear on some of the larger discontinuities, but it is not clear how these displacements evolve over a period of time.

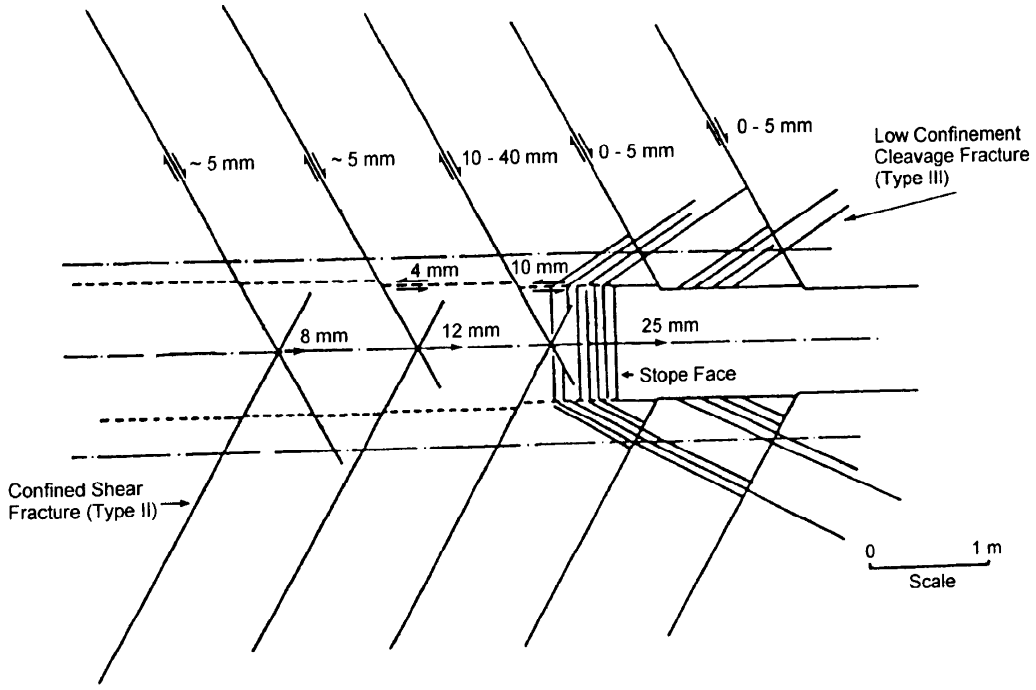

Figure 1.4. Typical values of displacement measured at an experimental site at Doornfontein Gold Mine in response to a 1 m face advance (after Legge, 1984).

1.4 Thesis outline

The objective of this thesis is to quantify and model the time-dependent behaviour of deep excavations in hard brittle rock. The creep of intact hard rock is not expected to make a significant contribution to the time-dependent closure observed underground. The creep of rocks in the South African industry has, however, never been properly quantified and virtually no data is available in the literature. Therefore, Chapter 2 is devoted to the investigation of laboratory creep of intact rock. Some existing data is analysed while additional experiments were performed for this study. This data is important for comparison with the more significant time-dependent behaviour observed underground. To investigate the feasibility of using viscoelastic theory to analyse underground data, a viscoelastic convergence model for tabular stopes was derived by the author. As this analytical solution cannot be found in the literature, Chapter 3 is devoted to this solution and the method used to derive it. A novel displacement discontinuity approach to solve incremental problems in viscoelasticity is also developed in this chapter. Underground closure measurements are presented in Chapter 4. As the existing data was very limited, the author established several underground sites to collect additional data. This is

presented in Chapter 4 together with a discussion of the applicability of the viscoelastic model developed in Chapter 3. In order to address several drawbacks of the viscoelastic model, a continuum viscoplastic model is developed in Chapter 5. This model is used to simulate the behaviour of service excavations at Hartebeestfontein Mine. Although this model proved successful in simulating the time-dependent fracture zone formation and stress transfer processes observed underground, it is incapable of modelling the time-dependent behaviour of prominent discontinuities. Although the time-dependent behaviour of discontinuities is expected to play a prominent role in the underground behaviour, almost no experimental data is available in the literature regarding this phenomenon. Therefore, a laboratory testing programme to investigate the shear creep of discontinuities was undertaken for this study. The testing methodology and experimental results are presented in Chapter 6. To incorporate the time-dependent behaviour of discontinuities in numerical analyses, a discontinuum viscoplastic model for use in boundary element codes is proposed in Chapter 7. Finally the important conclusions and recommendations for further research are summarised in Chapter 8.

Chapter 2

Laboratory creep of intact hard rock specimens

2.1 Introduction

Low porosity hard rock usually does not display significant steady-state creep under engineering conditions (Dusseault and Fordham, 1993). This is also expected for the hard rock surrounding the deep excavations in the South African mines. As almost no published data is available on the creep of South African hard rocks, the objective of this chapter is to illustrate typical laboratory creep rates of these rocks. This data serves as an important introduction to this study and emphasizes the apparent contradiction caused by the high closure rates measured underground (Chapter 4). This chapter is not intended to be an exhaustive study of the creep behaviour of all the different rock types found in South African gold mines, but to quantify the typical strain rates when subjecting some of these rocks to constant applied stresses. Some of the experimental data presented in this chapter was collected (but not analysed) by other workers (Vogler, 1990; Vogler and Drescher, 1996). This data, together with some from new experiments performed for this study, will be analysed.

Creep of hard rock

A vast amount of data on the laboratory creep of intact rock has been collected over the years. A complete review of all this data is beyond the scope of this work where the focus is on low temperature (< 100° C) creep of hard rock. This introduction will only briefly review concepts and earlier work relevant to this study. Figure 2.1 illustrates a typical creep curve for rock with the primary (transient), secondary (steady-state) and tertiary

creep phases visible (Lama and Vutukuri, 1978). This behaviour is also observed for the creep of brittle crystalline rock. After application of the load, there is an instantaneous elastic strain followed by the primary creep phase. This strain is recoverable on unloading, although recovery of the primary creep is a delayed process. Following the primary creep is the secondary phase in which permanent deformation occurs. After a period of time, depending on the stress level, this can lead to accelerating creep of the tertiary phase and failure. Dusseault and Fordham (1993) suggested that hard rocks such as granite, gneiss and dolomite which exhibit tertiary creep leading to rupture, probably do not experience true steady-state creep. The apparent steady-state phase should be seen as a transition between primary and tertiary creep. Unlike salt and ice, no mechanisms for true steady-state creep exist in these materials. Although the rate of creep in general is influenced by temperature, humidity and chemical environments, as noted in Chapter 1 a temperature variation from 20° C to 100° C does not affect the creep of hard rock significantly (Pusch, 1993; Dusseault and Fordham, 1993). Of significance is that the creep process can lead to delayed failure even though the stresses are below the short term laboratory strength.

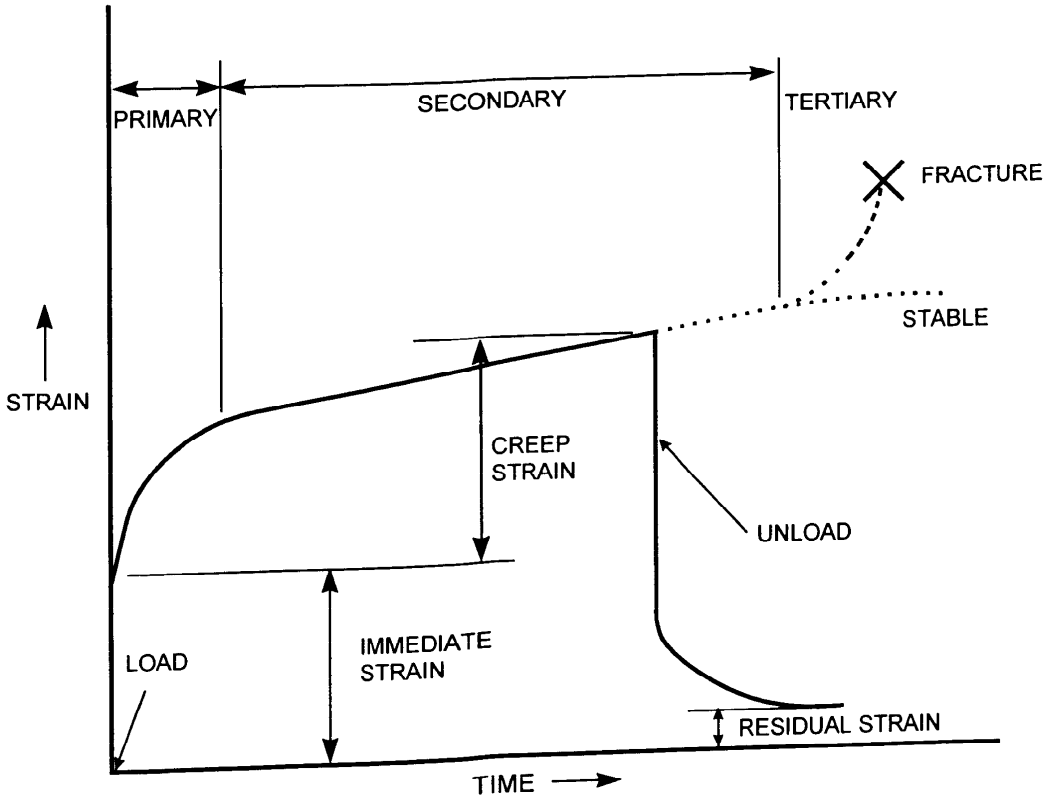

Figure 2.1. Typical creep behaviour of rock.

Creep laws

A general equation for creep is (Robertson, 1964)

$$\varepsilon = \varepsilon_e + \varepsilon(t) + Ct + \varepsilon_T(t) \qquad [2.1]$$

where ε is the total strain, t is time, ε_e is the instantaneous elastic strain, $\varepsilon(t)$ is a function expressing the decelerating creep of the primary phase, Ct is the steady-state creep component and $\varepsilon_T(t)$ is a function expressing the accelerating creep of the tertiary phase.

Various empirical laws have been used to represent the transient (primary) creep behaviour. Most can be expressed in the form (Pusch, 1993)

$$\dot{\varepsilon}(t) = Bt^{-m} \qquad (0 \le m \le 1) \qquad [2.2]$$

where B is a constant. For m = 1, equation [2.2] is the logarithmic creep law (Robertson, 1964) which in metals applies to creep at low temperatures. For m = 1/3, equation [2.2] is the well-known power law of Andrade which apparently fits creep of metals better at higher temperatures (Robertson, 1964). Although some success can be achieved with this power law in fitting data from rock, there is unfortunately no established link between the field and laboratory primary creep response. It appears that the primary response of the rock in the laboratory is dependent on the level of microscopic damage during specimen collection and preparation.

The most widely used law for the steady-state creep of rock is (Dusseault and Fordham, 1993)

$$\dot{\varepsilon}_{ss} = A(\sigma_1 - \sigma_3)^n e^{-\frac{Q}{RT}} \qquad [2.3]$$

where $\dot{\varepsilon}_{ss}$ is the steady-state creep rate, A is a constant, σ_1 and σ_3 are the major and minor principal stresses respectively, R is the universal gas constant, T is the temperature in degrees Kelvin and Q is the creep activation energy. Q is different for the various creep mechanisms and should be calculated from creep tests at different temperatures. For

dislocation creep, Q is the energy required by dislocations to overcome obstacles in their path.

Tertiary creep of rock has not been investigated in the same detail as the other two phases and there is currently no acceptable fundamental equation to describe this phase. Most empirical equations are based on power or exponential laws and most predictions are based on site-specific measurements (Dusseault and Fordham, 1993). Although Carter and Kirby (1978) made a detailed study of transient creep of crystalline rocks, this focused mostly on high temperature (200° C to 600° C) creep and is not directly relevant to mining excavations in these rocks.

The dominant mechanism of creep in crystalline rock has been shown to be the development and growth of microfractures (Kranz, 1979). The concept of stress-corrosion has been used to explain this phenomenon (Lama and Vutukuri, 1978; Atkinson, 1987). The tertiary creep stage is generally attributed to increased microfracture formation and coalescence leading to macroscopic failure. Kranz and Scholtz (1977) emphasized that a critical dilatant volume increase may be necessary to produce a tertiary creep stage by coalescence of microcracks at an associated critical crack density.

Rheological models

In linear viscoelastic theory, complex strain-time behaviour can be described by various combinations of two principal states of deformation namely elastic behaviour (represented by a spring) and viscous behaviour (represented by a dashpot). There is some doubt about the usefulness of this theory in representing rock behaviour, as explained by Robertson (1964), owing to the functional dependence of the viscosity values on stress, temperature and chemical environments. It might be argued that this does not detract from its usefulness as a concept in creep analysis as long as its limitations are clearly understood. Similarly the parameters of linear elasticity theory, when applied to rock, are not constant over a wide range of strain rates and temperatures, but it is nevertheless an important approximation used frequently in rock mechanics. In regard to viscoelasticity, even recent publications can be found were it has been used to simulate time-dependent behaviour of rock (Pan and Dong, 1991(a)). In this current study however (Chapters 3 and 4), it was discovered that there are some subtle problems associated with the use of viscoelasticity theory to simulate time-dependent closure of tabular excavations. These problems arise as

a result of the special tabular geometry of the excavations and are not apparent when applying the theory to circular tunnels (Pan and Dong, 1991(a)). This is a symptom of the fundamental problem of linear viscoelasticity in relation to rock mechanics, namely the inability to simulate failure. This is where the concept of viscoplasticity is useful as discussed in Chapters 5 and 7.

As no attempt is made to review viscoelastic theory in this text, the reader is referred to Függe (1975) for a good introduction to the subject. Figure 2.2 lists the commonly used models and the time-dependent strain profile of each when subjected to a stepwise application of constant stress. The spring represents elastic behaviour and therefore gives an instantaneous response which remains constant with time. The dashpot represents idealised viscous behaviour and, after application of the load, gives a linearly increasing strain with time. The slope of this curve is dependent on the viscosity coefficient and the applied stress. The Maxwell model is a combination of these two elements in series and gives an instantaneous response followed by a linearly increasing strain with time. For the Kelvin model the strain is zero at the time of stress application and then increases approaching an asymptotic value. The 3-parameter solid behaves similarly to the Kelvin model but differs in the fact that it displays an instantaneous response. Finally, the Burgers model is a combination of the Kelvin and Maxwell models in series with the strain-time response illustrated in Figure 2.2. For this model the strain does not approach an asymptotic value but continues to increase linearly. From Figures 2.1 and 2.2 it appears that the Burgers model can be used successfully to simulate the primary and secondary creep phases of rock. The historical use of different viscoelastic models to simulate the creep of rocks is given in Lama and Vutukuri (1978).

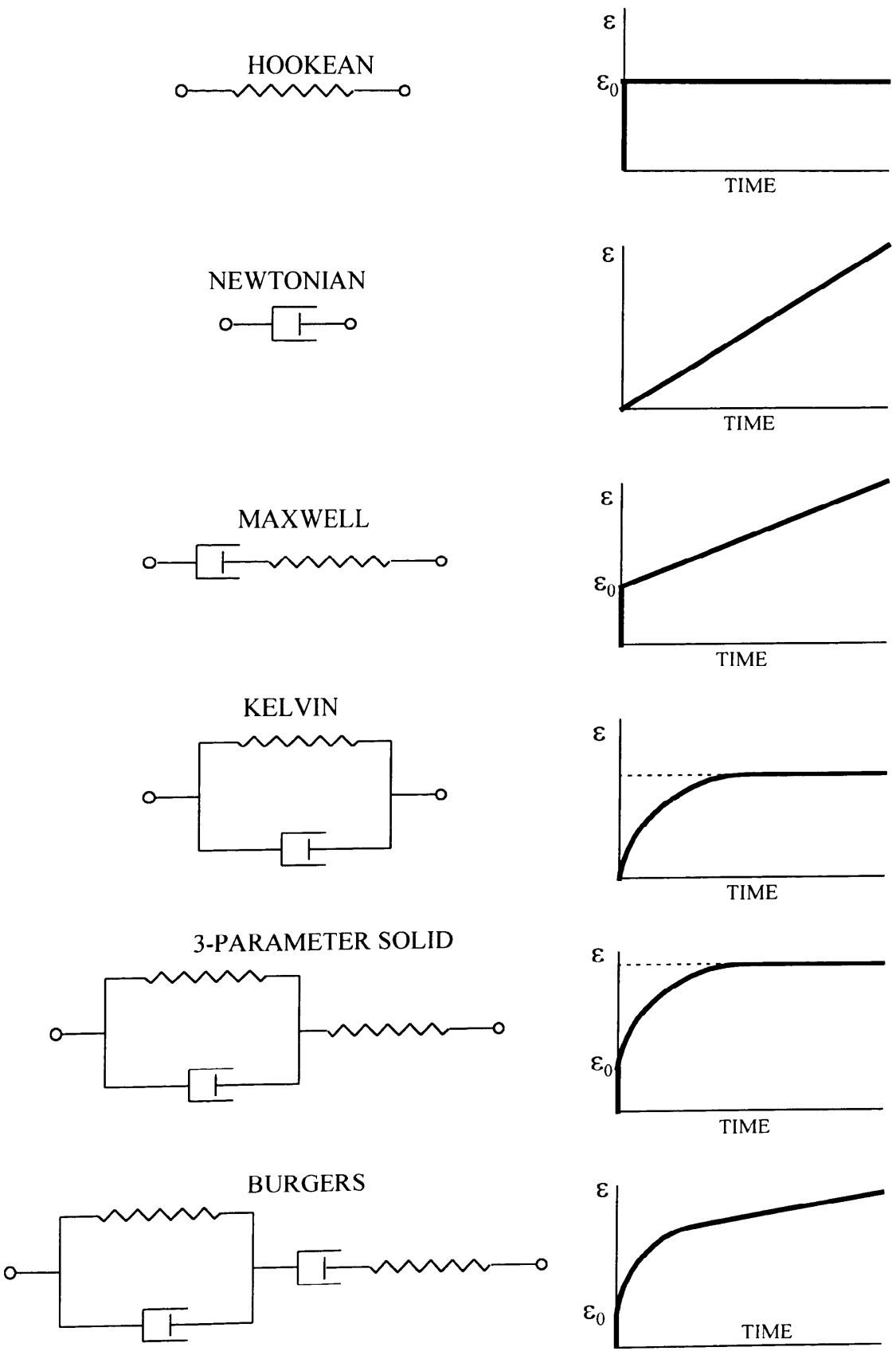

Figure 2.2. Commonly used viscoelastic models and their respective strain-time behaviour for a stepwise application of constant stress.

Laboratory testing of creep in hard rock from the South African gold mining industry

In an attempt to quantify these effects in the South African industry, some initial studies on the time-dependent behaviour of hard rock were conducted by the Rock Mechanics Division of the CSIR's National Mechanical Engineering Research Institute. These studies investigated the creep of intact specimens but concentrated mostly on long term strength measurements. The following is a description of these studies.

Roux and Denkhaus (1954) published results for the creep of quartzite at room temperature as shown in Figure 2.3. Unfortunately no information on the type of quartzite or test methodology is available. What is significant is that measurable creep was observed within a reasonable period of time. Typical primary and secondary creep phases can be distinguished from Figure 2.3 with the primary phase lasting approximately 2 days. The creep strain rate in the secondary phase for the applied stress of 32.9 MPa was calculated as 2.6×10^{-11} s^{-1} .

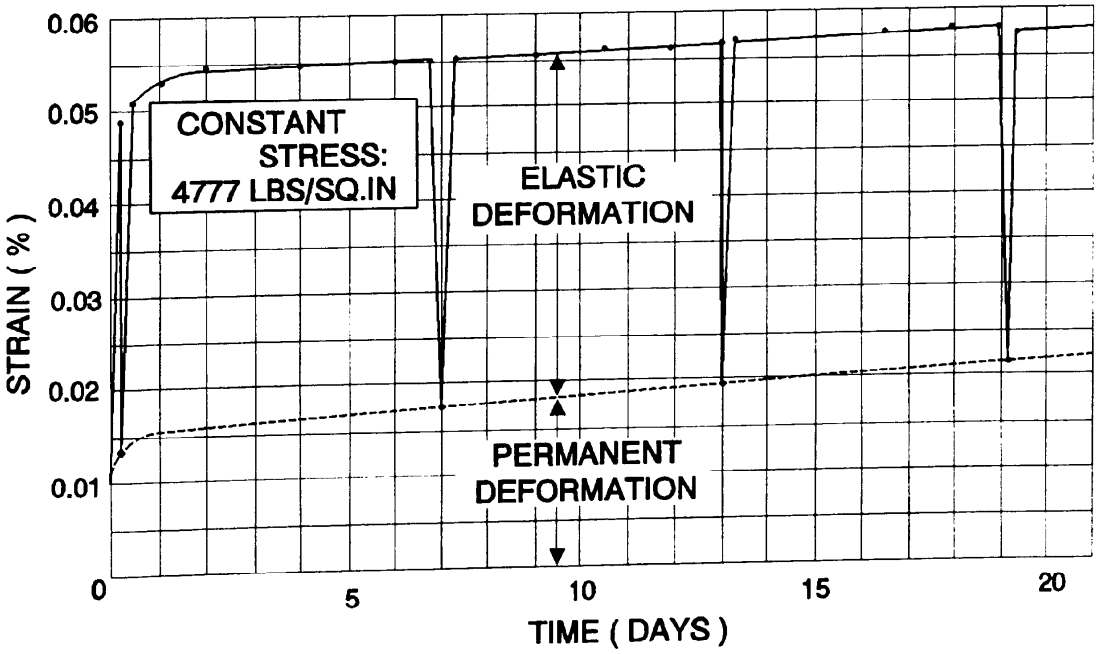

Figure 2.3. Creep curve for quartzite at room temperature (after Roux and Denkhaus, 1954). The applied stress was 32.9 MPa in metric units.

The CSIR (1963) conducted further experiments on quartzites from the Hartebeestfontein Mine. The quartzite specimens were medium grained argillaceous samples obtained from a single borehole. The rock properties varied considerably along the length of the borehole owing to alternating argillaceous and siliceous bands in some sections. The uniaxial

compressive strength for the different samples varied between 117 MPa and 248 MPa with an average of 192 MPa. Specimens were subjected to a constant uniaxial compressive stress of 138 MPa in a deadweight testing machine. Examples of the strain-time curves obtained are displayed in Figure 2.4. It is evident that the creep behaviour showed appreciable differences between different samples. Unfortunately no attempt was made to analyse this behaviour quantitatively or to link it to the mineralogy of individual specimens. The creep rate in the secondary phase (calculated from Figure 2.4) varied between 1.6×10^{-8} s^{-1} and 1×10^{-9} s^{-1}. These values should however be considered as approximate only, as it is difficult to determine the onset of the secondary creep phase. Note that the primary phase appears to last for less than an hour while for the sample in Figure 2.3 it persisted for two days. The reason for this is not known.

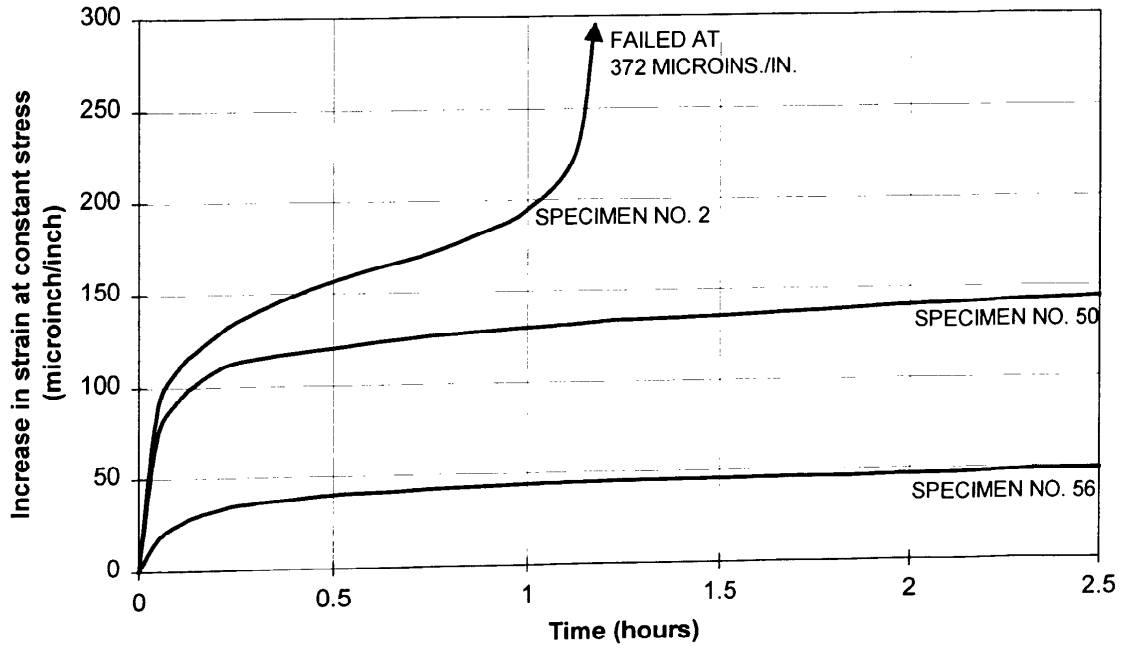

Figure 2.4. Creep curves obtained for quartzite from Hartebeestfontein Mine (after CSIR, 1963). The applied stress was 138 MPa.

Further studies concentrated mainly on the long term strength of rock. Bieniawski (1967) showed that the long term strength of rock under uniaxial loading can be determined from the plot of axial stress versus volumetric strain. The onset of unstable fracture propagation (the point on the plot where the slope changes from negative to positive) indicates the long term strength. Tests on norite samples showed that the long term strength can be as low as 73 % of the uniaxial compressive strength. Bieniawski's hypothesis was confirmed by experiments conducted by Wiid (1966) on dolerite and sandstone. Again, the long term strength could be as low as 70 % of the uniaxial compressive strength. Kovács (1971)

investigated the relationship between time to failure (t_F) and applied load (σ_t) for samples of quartzite with $\sigma_L < \sigma_t < \sigma_C$ where σ_L is the long term strength and σ_C the uniaxial compressive strength. The following empirical relationship was used to represent this relationship.

$$t_F = a\left(\frac{1}{i} - 1\right)^b \qquad [2.4]$$

where

$$i = \frac{\sigma_t - \sigma_L}{\sigma_C - \sigma_L} \qquad [2.5]$$

For argillaceous quartzite, the calculated values of a and b were 24.75 and 1.95 respectively (for t_F calibrated in hours).

2.2 Laboratory testing methodology

In this study the creep data for lava and different types of quartzite will be analysed. These rocks together with their strength and elastic properties are given in Table 2.1. Note that these are average values and the individual samples used for the creep tests in Section 2.3 may have slightly different strengths and elastic properties.

Table 2.1. Average values of elastic and strength properties of the rocks analysed in this study. The number of samples indicates the number of tests conducted to calculated these average values and not the number of creep tests. The abbreviations are: UCS - Uniaxial compressive strength, E - Young's modulus, ν - Poisson's ratio.

Rock Type	*Location*	*UCS (MPa)*	*E (GPa)*	*ν*	*Number tested*
A: Argillaceous quartzite	Lorraine Mine	100	63	0.18	2
B: Ventersdorp lava	Western Deep Levels Mine	436	88	0.26	5
C: Quartzite	Western Deep Levels Mine	237	79	0.13	10
D: Argillaceous quartzite	Hartebeestfontein Mine	142	72	0.26	1

The creep tests of specimens A and B were performed as part of other investigations. Details of the tests were reported by Vogler (1990) and Vogler and Drescher (1996) but unfortunately the data was not analysed. Specimens C and D were additional tests carried out for this study. In all the experiments the specimens were loaded under uniaxial conditions.

Testing equipment

All the creep experiments, except for those on rock A, were conducted using the CSIR creep testing machine (Figure 2.5). This machine is the actual one used by Bieniawski (1967) to conduct his experiments on the long term strength of rock. It uses deadweights and cantilevers to maintain a desired constant load on the specimen. For tests where the load was incrementally increased in steps, the next stress level was attained by adding further weights. This machine is housed in a climate controlled laboratory with the temperature maintained at 22° C and the humidity at 50 %

For the tests on specimen A, Vogler (1990) used a servo-controlled Amsler compression testing machine. The control system of the equipment maintained the constant load. Minor fluctuations in load (below 0.1 MPa) took place as the machine continuously made the necessary adjustments. Loading to each successive stress level was achieved by adjusting the settings of the load control. This machine was housed in an open laboratory, subject to ambient temperature variations. This was in turn influenced by the heat generated by the machine. Therefore the temperature of the test specimen was monitored throughout the experiment. The experiment lasted 24 days and the minimum and maximum temperatures recorded were 20.6° C and 28.0° C respectively.

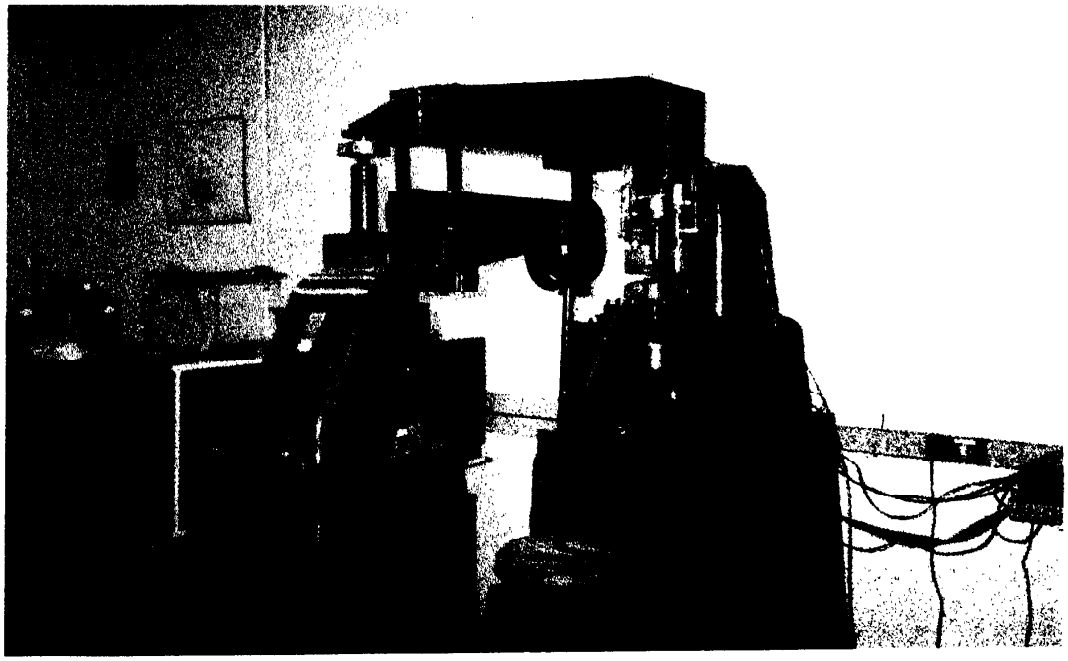

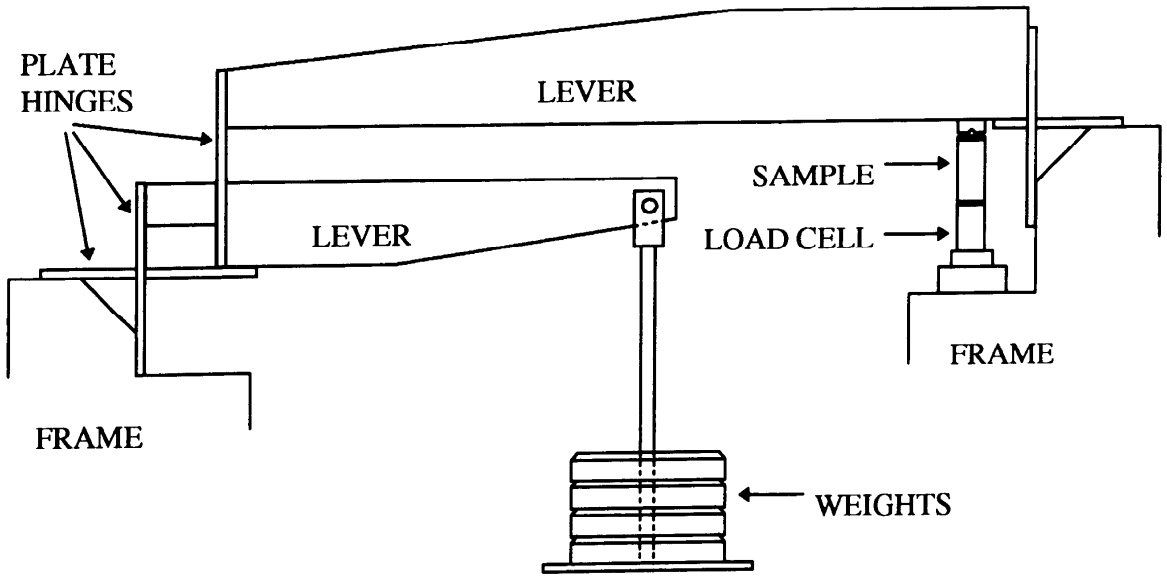

Figure 2.5. Deadweight creep tester.

Load application principles

Two methods of conducting laboratory creep experiments are available namely:

a) Specimens are loaded to a pre-determined, constant stress level. This stress level may, for instance, be the stress level expected around a mining excavation. The creep strain and the time to failure may be monitored. If, however, the aim of the testing programme is to fully characterize the creep behaviour of the material or its time-dependent strength

characteristics, many tests have to be performed at different stress levels. If the material properties vary considerably, it may be difficult to determine the time to failure for the material when loaded to a particular stress or the long term strength (the stress below which failure will not occur). It may happen that a specimen loaded to a certain stress level fails after a few days while another loaded to the same stress level does not fail after a period of months. This could be the result of a stress level having been chosen just above or below the specimen's long term strength.

b) The same specimen is loaded to different stress levels by starting at a low value and increasing the stress in steps, allowing a certain time interval for creep. The obvious advantage of this approach is that the creep strain may be monitored for an "identical" material at different stress levels and that each specimen will be tested to failure within a reasonable time. The total test duration is determined by the choice of the stress level of the first creep stage, the duration of each creep stage and the magnitude of subsequent stress level increases. This methodology was used for all the tests reported in the next section.

Strain measurements

Strain measurements were obtained using strain gauges and inductive transducers. The inductive transducer measurements were used to monitor any possible creep in the strain gauges. No noticeable creep was observed in these gauges and the strain gauge measurements, giving higher resolution, were used for subsequent evaluations.

2.3 Results for laboratory specimens

Rock A: Argillaceous quartzite (Lorraine Gold Mine)

Figure 2.6 illustrates the complete strain-time record for this specimen. The total number of loading stages was 24. The duration of each stage was 24 hours. Only the last four stages showed significant creep. The incremental creep curves for these four stages are plotted in Figure 2.7 using a common origin for the time axis of each. Note that this figure excludes the instantaneous elastic response of each stage. The primary and secondary creep phases are clearly visible.

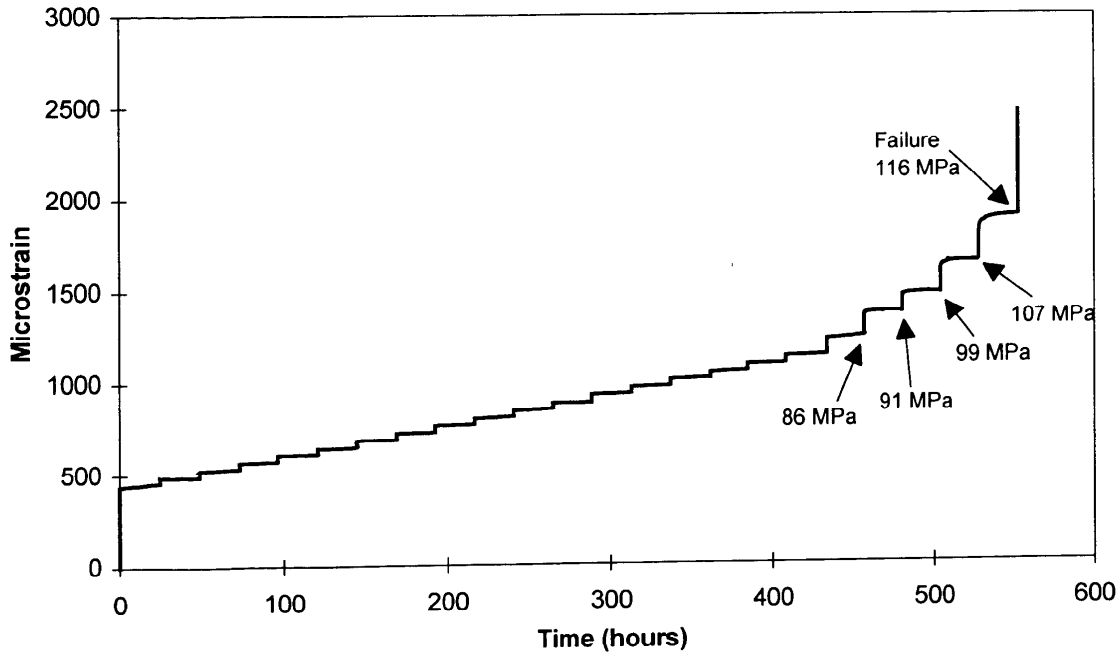

Figure 2.6. Complete strain-time record of a quartzite sample from Lorraine Mine.

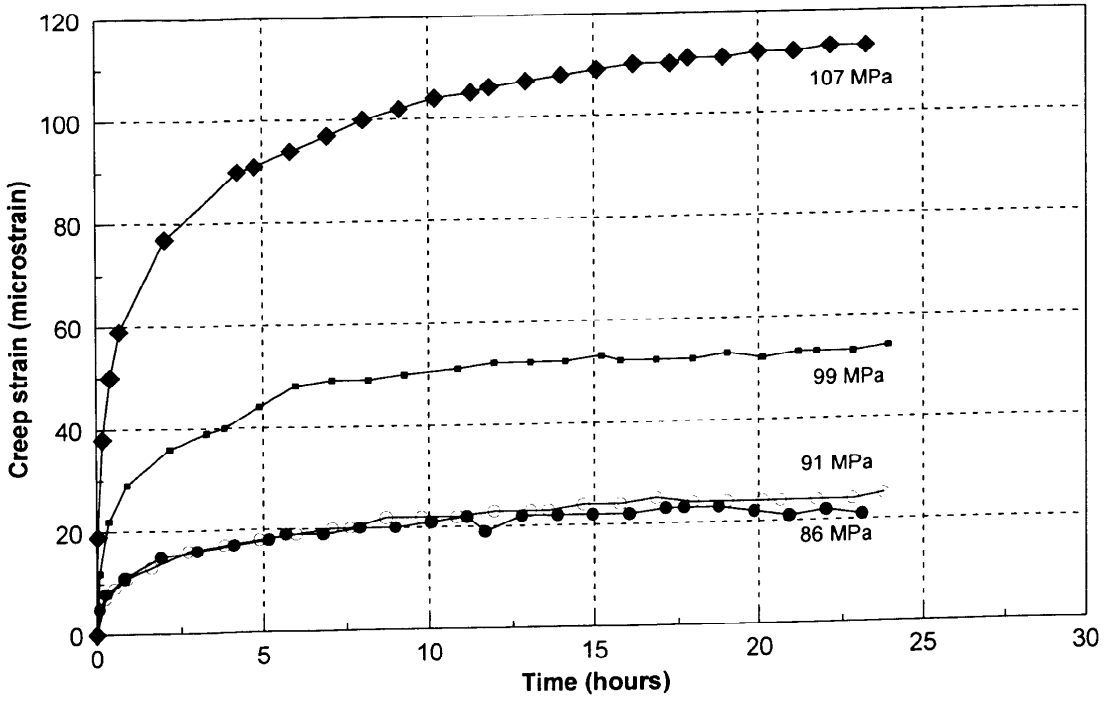

Figure 2.7. Incremental creep curves of the last four stages for the test in Figure 2.6.

Rock B: Ventersdorp lava (Western Deep Levels Mine)

The complete strain-time record for a representative sample is given in Figure 2.8. Note that each loading step was preceded by a partial unloading. This was done by placing a mechanical jack below the weights and elevating the load to the load setting of the previous step. After the additional weight was added, the jack was slowly released to apply the new load in a gradual fashion. As the weights are manually loaded, the objective of this procedure was to prevent any dynamic loading of the specimen when adding the extra weights. This procedure also allowed for the monitoring of any changes in the deformation modulus after the specimen had been subjected to a creep phase. A study of the effect of creep on the deformation modulus is however beyond the scope of this work and is not explored in this study. The incremental creep strain for each creep stage is given in Figure 2.9. Similar to the quartzite specimen, primary and secondary creep phases are observed. Note however that much higher stresses were applied.

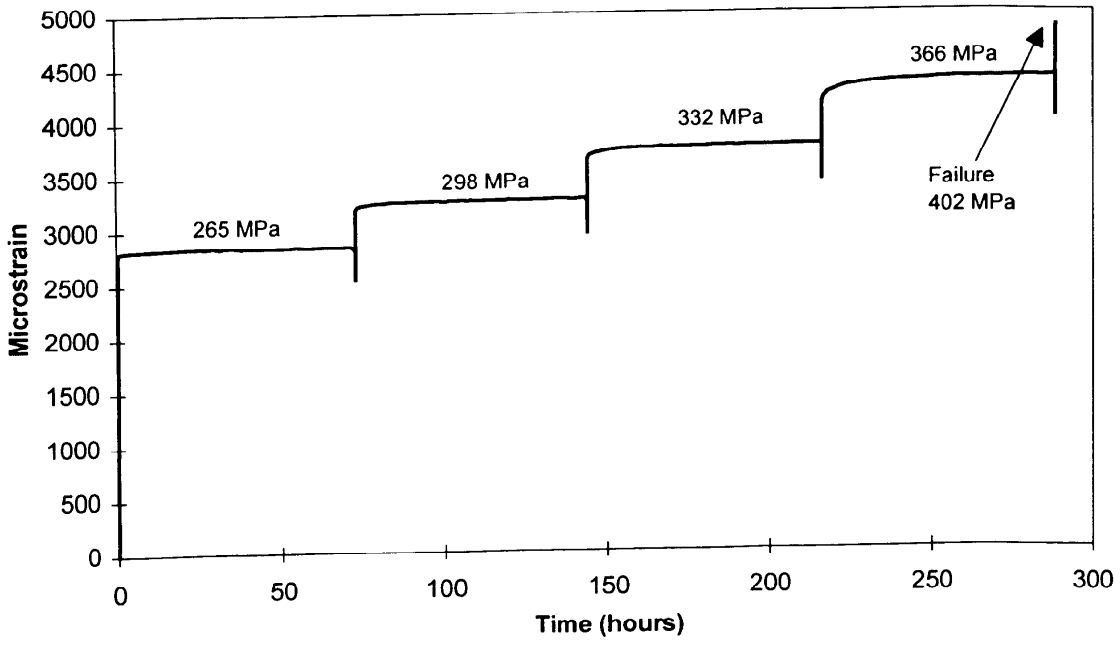

Figure 2.8. Complete strain-time record of a lava sample from Western Deep Levels Mine.

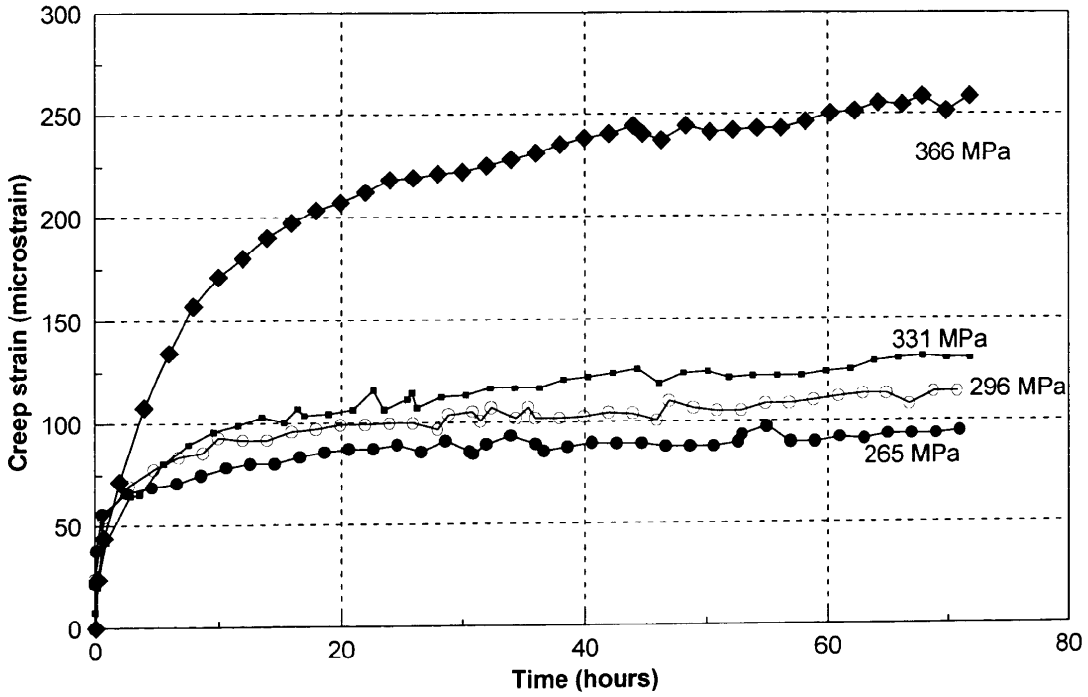

Figure 2.9. Incremental creep curves of the last four stages for the test in Figure 2.8.

Rock C: Quartzite (Western Deep Levels Mine)

The complete strain-time record and incremental creep curves for the last three loading stages are illustrated in Figures 2.10 and 2.11 respectively. For one of the tests a complete creep curve, including the final tertiary phase, was observed. This is illustrated in Figure 2.12. This is a rare data set as most samples failed during, or very soon after, the load adjustment phase of the test.

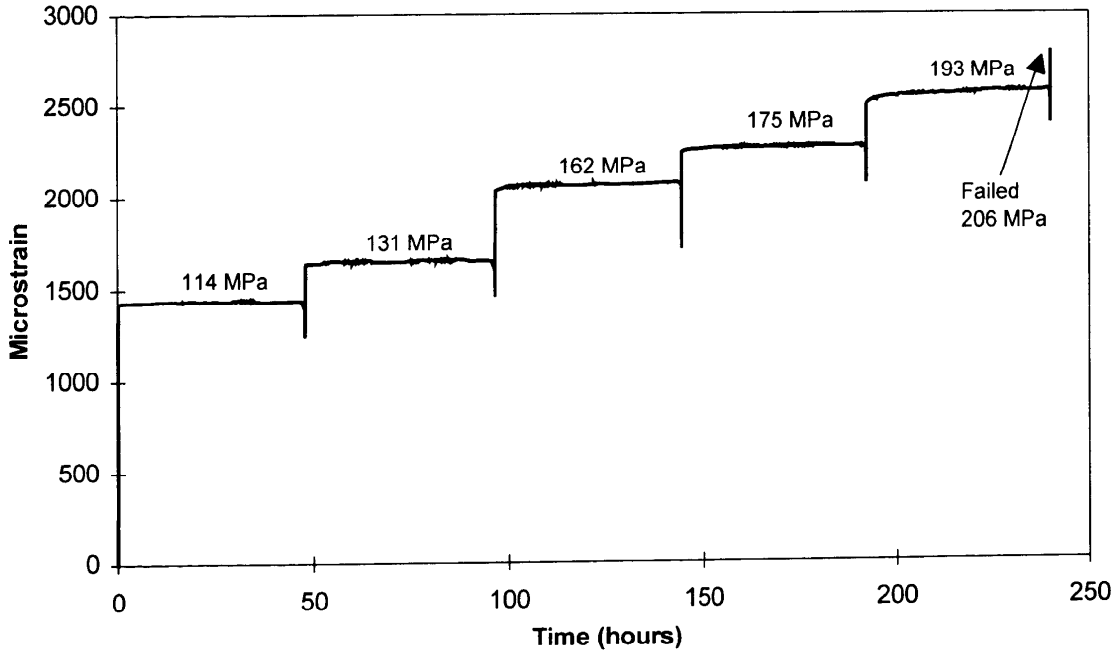

Figure 2.10. Complete strain-time record of a quartzite sample from Western Deep Levels Mine.

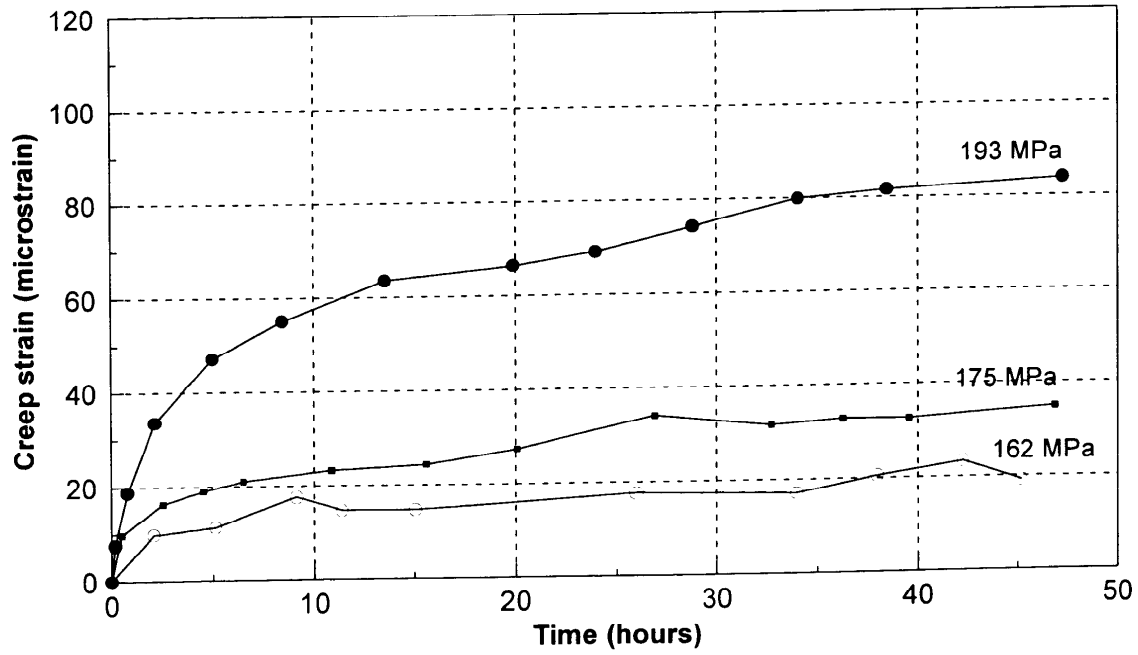

Figure 2.11. Incremental creep curves of the last three stages for the test in Figure 2.10. The noise in Figure 2.10 was reduced by only plotting every 10th data point in Figure 2.11.

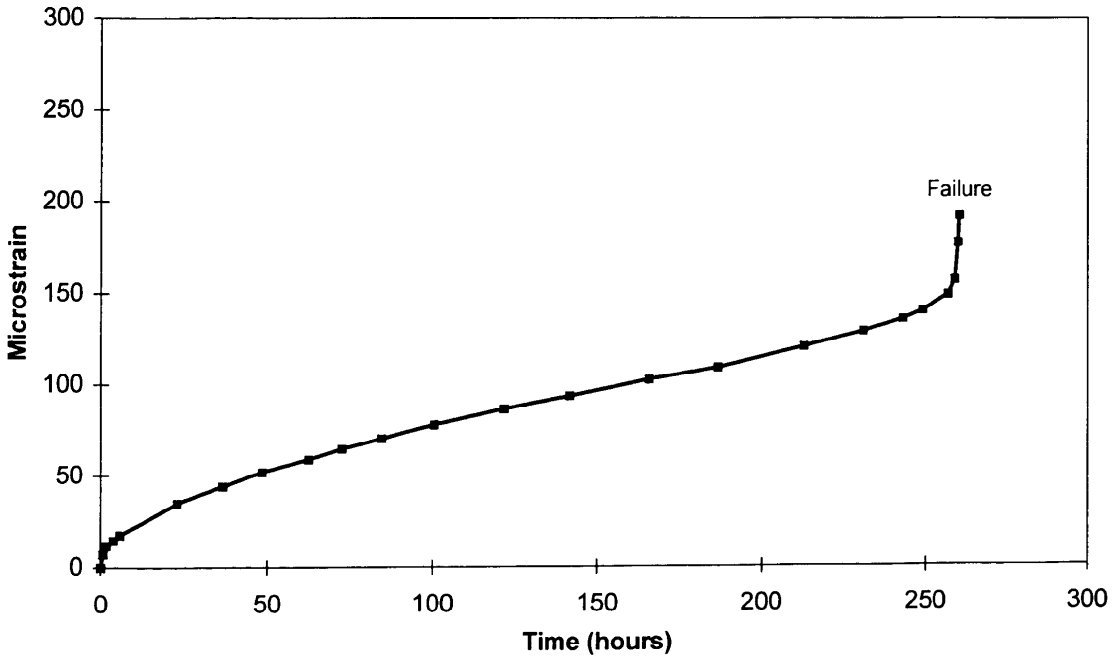

Figure 2.12. Complete creep curve for the last loading increment of a quartzite sample from Western Deep Levels Mine. The creep rate in the secondary phase between 100 and 200 hours is 9.88×10^{-11} s^{-1}. The applied load was 190 MPa.

Rock D: Argillaceous quartzite (Hartebeestfontein Mine)

The complete strain-time record and incremental creep curves for the last three loading stages of this rock type are illustrated in Figures 2.13 and 2.14 respectively.

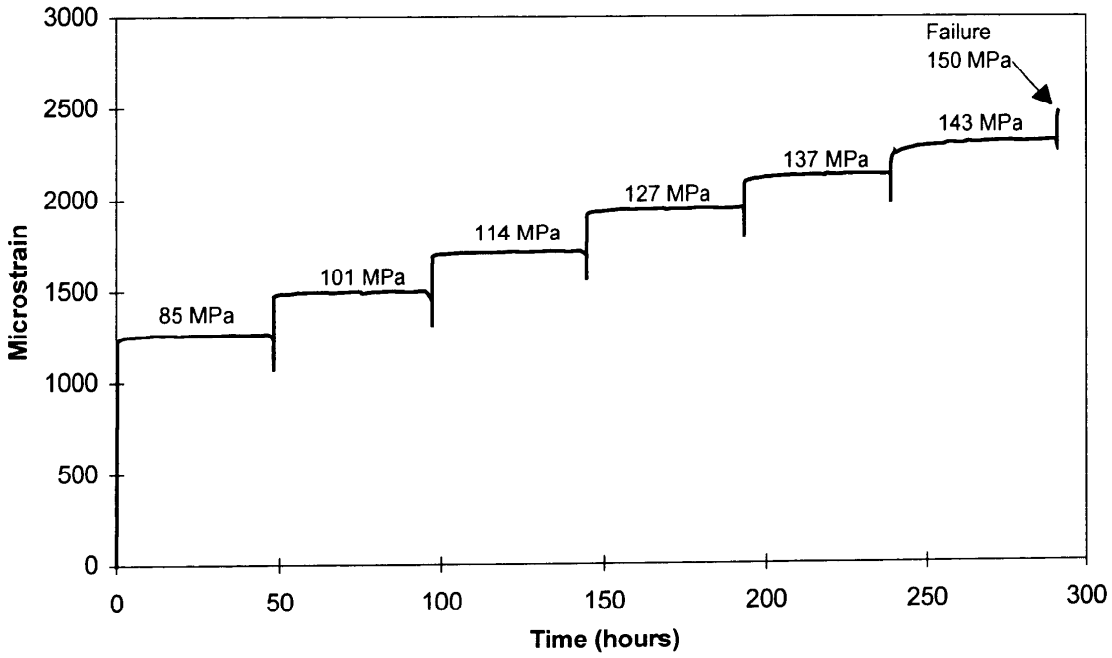

Figure 2.13. Complete strain-time record of a quartzite sample from Hartebeestfontein Mine.

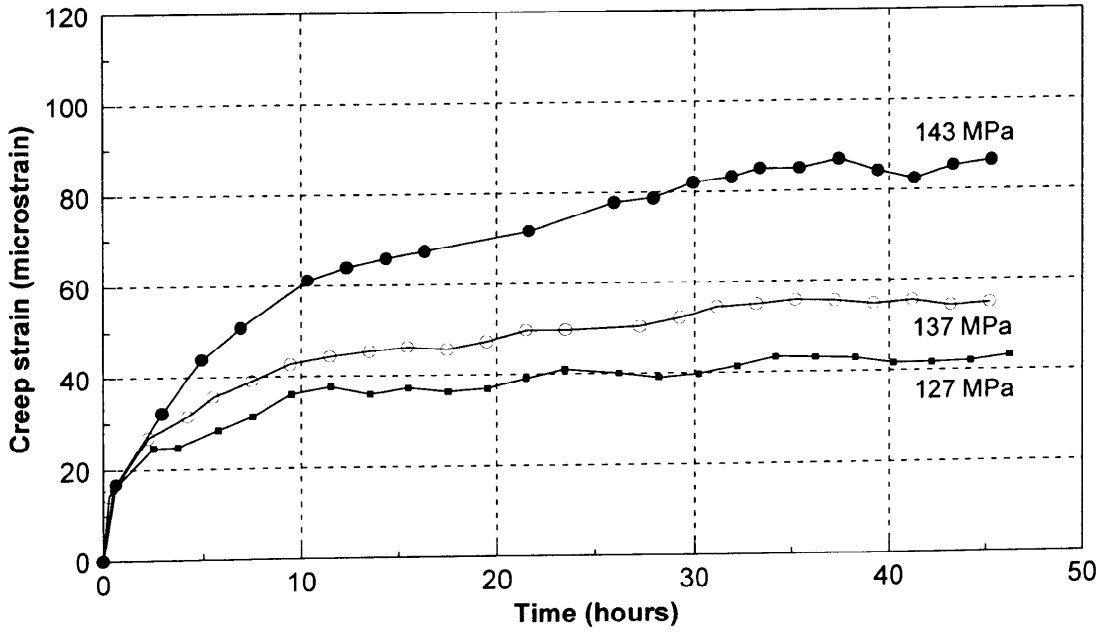

Figure 2.14. Incremental creep curves of the last three stages for the test in Figure 2.13.

2.4 Effect of stress level on the secondary creep phase

It is well known that for soft rocks the steady-state creep rate depends on the stress level (Lama and Vutukuri, 1978). From the previous results this also appears to be true for the creep of lava and quartzite specimens. Figure 2.15 illustrates the steady-state creep rates for the different rock types at various stress levels. For all specimens, higher stresses lead to higher creep rates. As it is difficult to determine the onset of the secondary creep phase, it is not clear how to choose the interval for calculating the steady-state creep rate. Unfortunately the duration of the load increments was not similar for the different rock types as some of the data was collected by other workers (see Section 2.2). Therefore different intervals had to be used to calculate the secondary creep rates in Figure 2.15. For the quartzites from Hartebeestfontein Mine and Western Deep Levels Mine, the rates were calculated for the period from 20 hours to 48 hours after the load increases. For the lava, this period was from 32 hours to 72 hours after the load increases while for the quartzite from Lorraine Mine, the period was from 10 hours to 24 hours after the load increases. For the quartzite from Lorraine, the strain rate for this assumed secondary phase could still be artificially high due to the influence of primary creep.

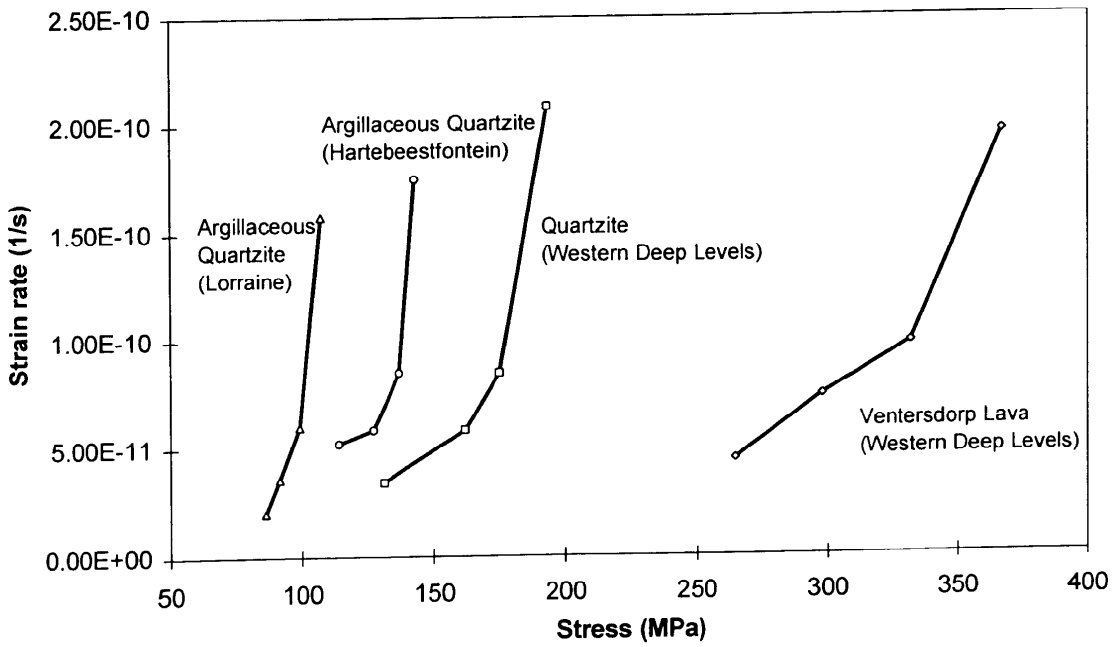

Figure 2.15. Effect of stress on the steady-state creep rate of different hard rocks in the South African gold mining industry.

When normalising the data from Figure 2.15 with respect to the uniaxial compressive strength (UCS) of the particular sample, it appears that the actual strain rate is determined

by the ratio of the applied stress σ to UCS and independent of material type or absolute stress values. At the current depths of the South African mining industry the quartzites with the lower uniaxial compressive strengths will have a higher σ/UCS ratio than the lava. From Figure 2.16 the creep rate of the quartzite will therefore be higher. High creep rates will lead to creep failure in a shorter period. It is therefore postulated that mining in quartzite host rock as opposed to lava at a particular depth may lead to a more stable fracture zone extending further away from the stope. At the boundary between fractured and unfractured rock, the intact rock will undergo secondary creep leading to the time-dependent formation of new fractures. This creep process zone may extend further into the rock for quartzite. As stable fracturing dissipates stored energy, this behaviour may be advantageous in reducing violent rockbursts. Mining of the Ventersdorp Contact Reef (lava hangingwall, quartzite footwall) in areas where the lava is particularly hard can be difficult owing to the rolling nature of the reef. In areas where the reef rolls into the footwall, the mining is sometimes slow to follow, resulting in mining taking place entirely in the lava. The stable formation of the fracture zone might be disrupted leading to face bursting. This phenomenon has been observed at mines in the Carletonville area (Handley, 1996). Other factors such as the increased stoping width may however also play a role and should be investigated further.

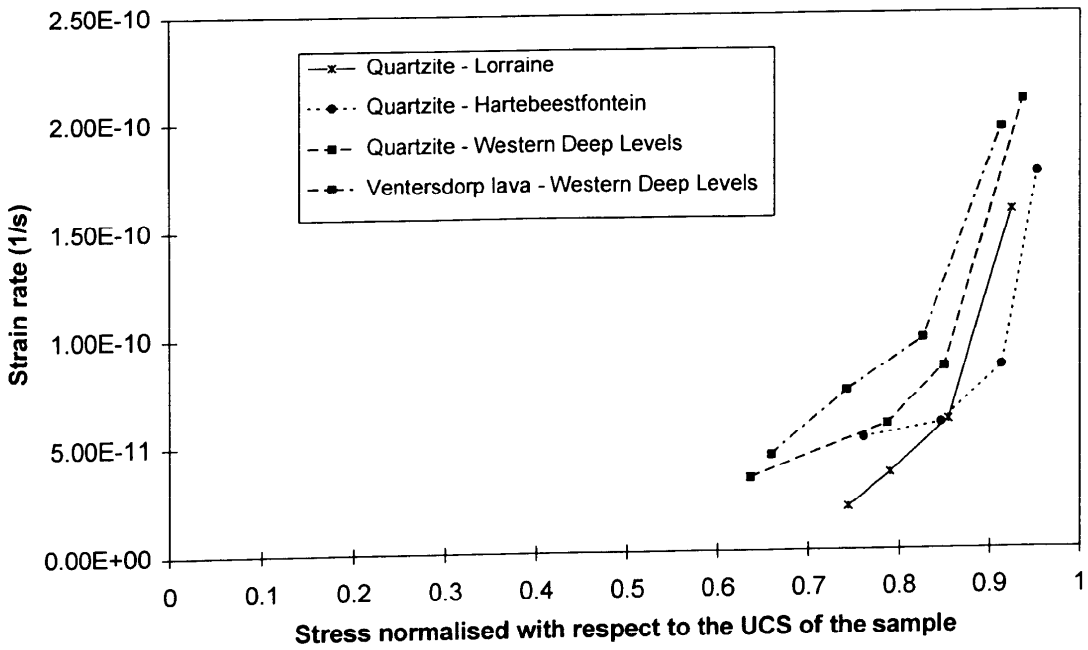

Figure 2.16. The steady-state creep rate of hard rock as a function of the σ/UCS ratio.

Modelling the stress dependence of the steady-state creep rate

A widely used steady-state creep law to simulate the stress dependence of the steady-state creep rate has been given in equation [2.3]. The experiments above were conducted at a constant temperature under uniaxial conditions. Equation [2.3] can therefore be reduced to

$$\dot{\varepsilon}_{ss} = A'\sigma^n \qquad [2.6]$$

where $A' = Ae^{-\frac{Q}{RT}}$ with units $Pa^{-n}s^{-1}$ and $\sigma = \sigma_1$ is the applied axial stress. The coefficient n can be determined from the slope of the curve of a $\log(\dot{\varepsilon}_{ss})$ versus $\log(\sigma)$ plot. Figure 2.17 shows this graph for the Ventersdorp lava. The linear nature of the curve illustrates the applicability of equation [2.6]. The values of n for the different rocks are given in Table 2.2.

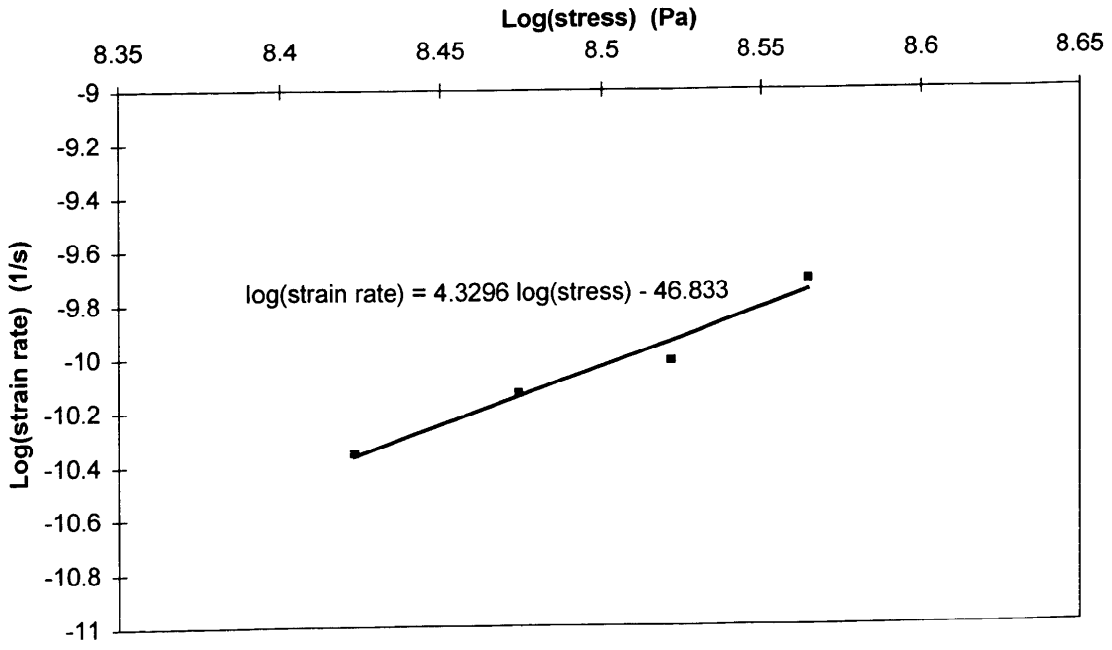

Figure 2.17. Log (strain rate) versus log (stress) for the lava sample. The straight line was fitted using linear regression. The slope of the line is n and the intercept is log(A').

A value for n of approximately 4 was obtained and this is of the same order as that obtained for the granite and shale (Table 2.2). The value of n = 9.1 for the quartzite from

Lorraine is much larger and needs to be confirmed by further experiments. It is possible that this value is too high as the time duration of individual loading steps for the quartzite was only 24 hours. As explained above, the strain rate of the assumed secondary phase could still be artificially high due to the influence of the primary creep phase.

Table 2.2. Calibrated values for the power law given in equation [2.6]. (* See comment in text above.)

Rock	**Maximum strain x 10^{-3}**	**Maximum Stress MPa**	**Exponent n**	**Coefficient log(A')**
Ventersdorp Lava (Western Deep Levels Mine)	4.7	366	4.3	-46.8
Quartzite (Western Deep Levels Mine)	2.6	193	4.4	-19.8
Argillaceous Quartzite (Hartebeestfontein Mine)	2.3	143	4.8	-20.2
Argillaceous Quartzite (Lorraine Mine)	1.9	107	9.1*	-83.2
Granite (Lama and Vutukuri, 1978)	1.0	345	3.3	Unknown
Shale (Lama and Vutukuri, 1978)	3.0	9.7	2.7	Unknown

2.5 Rheological parameters for the laboratory creep data

In an attempt to compare the laboratory creep rates with the underground measurements in Chapter 4, viscoelastic theory (as explained in Section 2.1) was considered. This comparison might be useful to determine the contribution of intact rock creep to the time-dependent closure in the underground stopes. As described in Section 2.1, however, care should be taken with the application of viscoelastic theory to rock as the model parameters are not fundamental constants but functions of parameters such as stress, temperature and humidity. The Burgers viscoelastic model (Figure 2.2) has been used frequently to model laboratory creep results as both the primary and secondary phase can be simulated. When it

is assumed that the rock sample under uniaxial load behaves as a Burgers viscoelastic material, the time-dependent strain can be derived as (Appendix A1)

$$\varepsilon_t = \frac{\sigma}{E_M} + \frac{\sigma t}{2(1+\nu)\eta_M} + \frac{\sigma}{E_K}\left(1 - e^{-\frac{E_K t}{2(1+\nu)\eta_K}}\right) \qquad [2.7]$$

where E_M and E_K are the Young's moduli for the Maxwell and Kelvin units, η_K and η_M are the viscosity coefficients for the Kelvin and Maxwell units, ν is Poisson's ratio and t is time. This model was fitted to the data of the last creep stage for the quartzite and lava specimens as illustrated in Figures 2.18, 2.19, 2.20 and 2.21.

The calibrated parameters for the different rock types are given in Table 2.3. Note that the calibrated values in Table 2.3 are only applicable to these particular laboratory specimens at the indicated stress magnitudes and a temperature of 22° C and a humidity of 50 %. In the model, the strain rate of the secondary phase is determined by the viscosity coefficient η_M. The quartzite samples have lower values of η_M at lower stresses and will therefore be prone to higher creep rates than the lava samples at a particular stress magnitude. Note that the Young's modulus of the Maxwell component (E_M) controls the instantaneous elastic response of the model and the calibrated values of this parameter in Table 2.3 should therefore be approximately similar to the Young's moduli given in Table 2.1. The slight differences are the result of the values in Table 2.1 being average values while those in Table 2.3 are for individual samples.

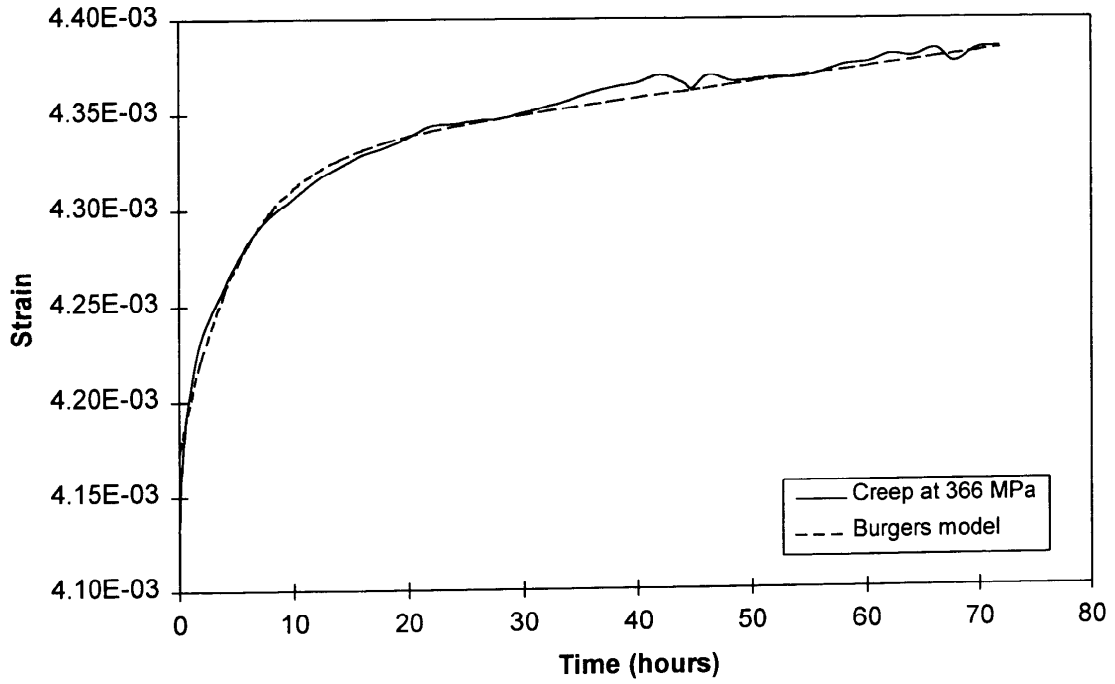

Figure 2.18. Burgers viscoelastic model fitted to the creep of the lava sample from Western Deep Levels Mine.

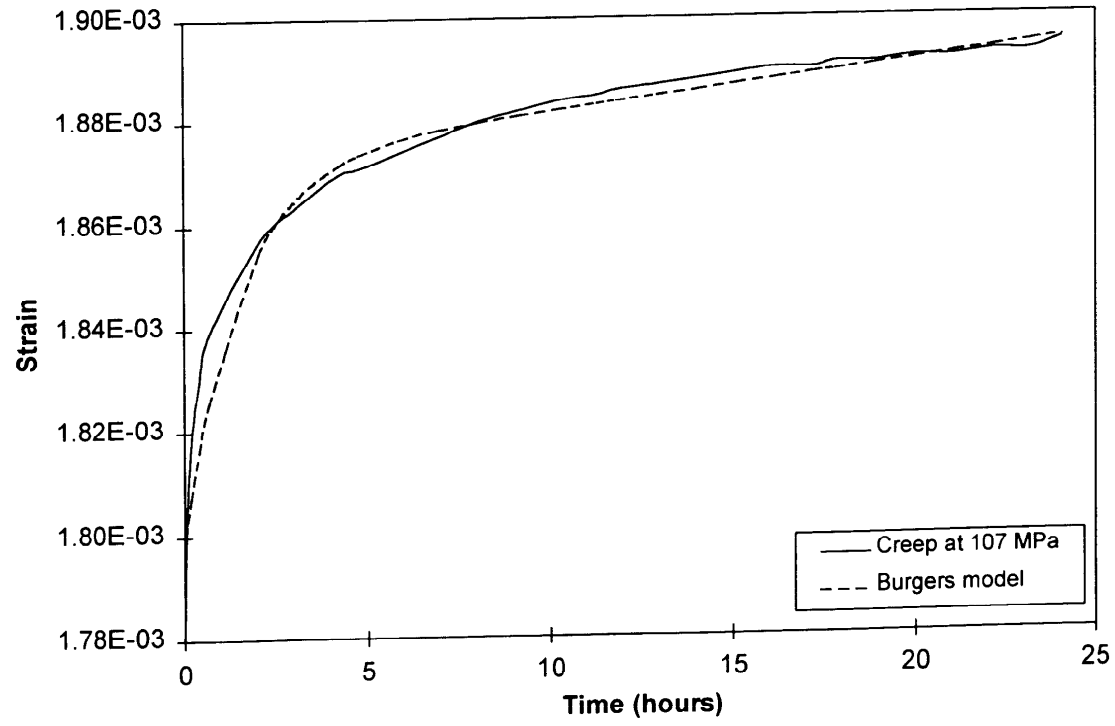

Figure 2.19. Burgers viscoelastic model fitted to the creep of the quartzite sample from Lorraine Mine.

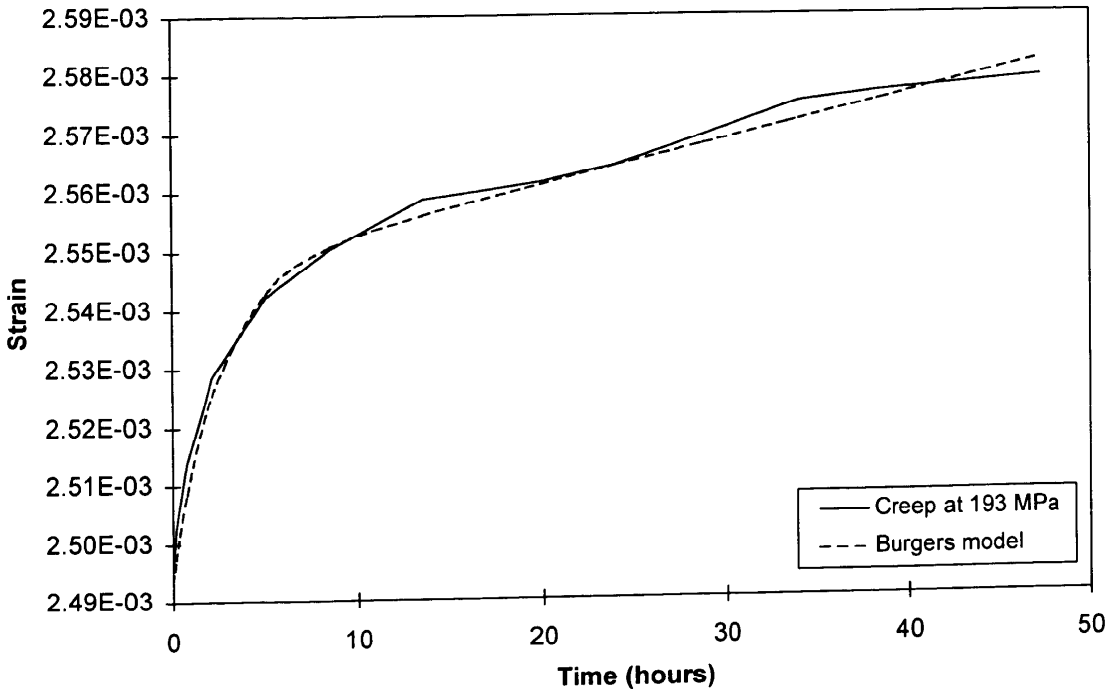

Figure 2.20. Burgers viscoelastic model fitted to the creep of the quartzite sample from Western Deep Levels Mine.

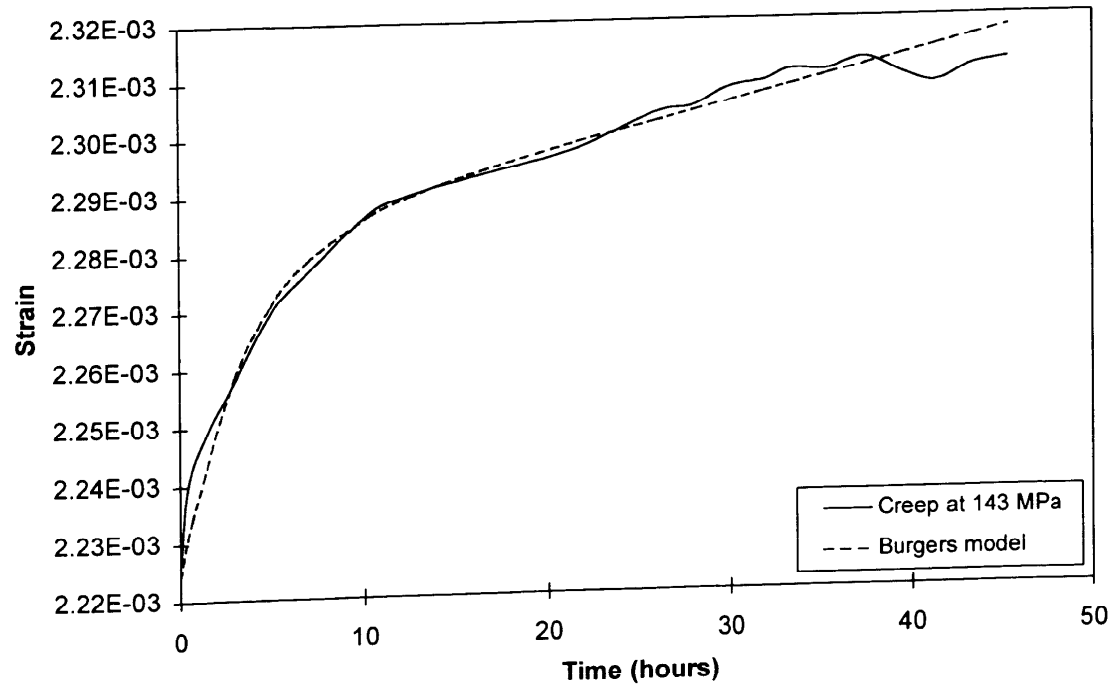

Figure 2.21. Burgers viscoelastic model fitted to the creep of the quartzite sample from Hartebeestfontein Mine.

Table 2.3. Calibrated Burgers viscoelastic parameters for the different rock types. Note that the failure stresses given are for the individual samples and are therefore not identical to the average values of uniaxial compressive stress given in Table 2.1. The abbreviation WDL is used for Western Deep Levels.

Rock Type	**E_M (GPa)**	**E_k (GPa)**	**η_M (Pa.h)**	**η_k (Pa.h)**	**Applied Stress (MPa)**	**Failure Stress (MPa)**
Lava (WDL)	87.7	2400	1.8×10^{14}	5×10^{12}	366	402
Quartzite (Lorraine)	59.6	1450	4.5×10^{13}	9×10^{11}	107	116
Quartzite (WDL)	77.4	4000	9×10^{13}	3×10^{12}	193	206
Quartzite (Hartebeest -fontein)	64.3	2500	7×10^{13}	3.5×10^{12}	143	150

From the discussion in Section 2.1 and the results in Section 2.3 it appears that η_M is not a fundamental material constant but a function of stress. To describe this dependence, the following model was derived in this study. It utilises the empirical creep law described in Section 2.4. For the Burgers model, the steady-state strain is determined by the Maxwell dashpot (see Appendix A1) and is given by

$$\dot{\varepsilon} = \frac{\sigma}{2(1+\nu)\eta_M} \qquad [2.8]$$

Inserting equation [2.6] and rearranging gives

$$\eta_M = \frac{\sigma^{1-n}}{2(1+\nu)A'} \qquad [2.9]$$

This equation is plotted in Figure 2.22 using calibrated values of n and A' (Table 2.2) together with the values of η_M obtained directly by fitting equation [2.7] to the creep of the lava specimen at the different stress levels. The results illustrate the clear stress dependence of the viscosity coefficient. Equation [2.8] appears to be successful in describing this stress dependency.

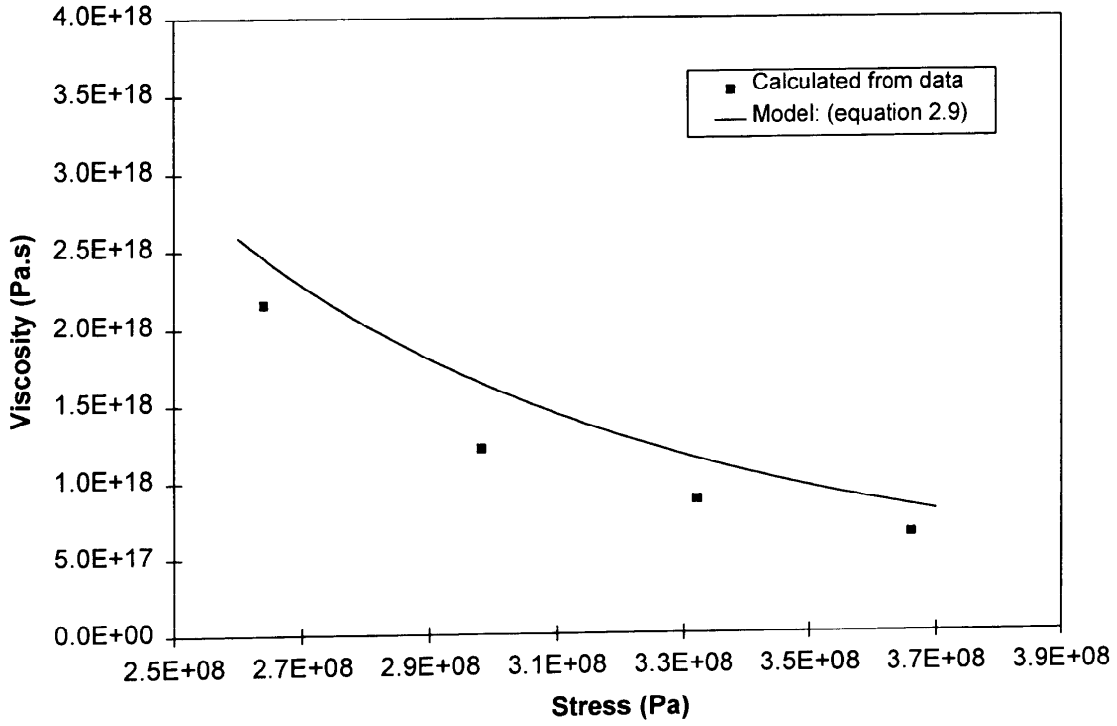

Figure 2.22. Dependence of the viscosity coefficient η_M on the applied stress magnitude for lava.

2.6 Summary

It was found that the hard rocks of the South African gold mines undergo measurable room temperature creep under uniaxial loading conditions with primary, secondary and tertiary creep phases visible. When loading samples uniaxially to above 90% of their failure strength (Figure 2.16), steady-state creep rates of typically 7.5×10^{-11} s^{-1} to 2×10^{-10} s^{-1} are observed. These values were measured for different quartzites and lava specimens. It should however be noted that the uniaxial compressive strength of the lava is significantly higher than that of the quartzites, requiring a much higher applied stress to obtain a load above 90% of the failure strength. The strain rate in the steady-state creep phase is strongly dependent on stress magnitude for both quartzite and lava and increases with increasing stress. This can be successfully modelled with a stress power law. As a viscoelastic model

proved successful in simulating the creep data, the feasibility of using such a model to describe the time-dependent closure measured underground is investigated in Chapters 3 and 4. As no analytical viscoelastic solution for tabular excavations is available in the literature, such a solution is derived by the author in Chapter 3.

Chapter 3

Development of a viscoelastic convergence model for tabular excavations

3.1 Introduction

The theory of viscoelasticity provides a theoretical basis for analysing time-dependent rock movement and for extrapolation beyond the range of an experimental data set. In particular, analysis of time-dependent behaviour of deep level excavations requires such a basis and, in this study, viscoelasticity was investigated as a method to simulate the closure behaviour of tabular stopes. As no analytical solution for the convergence of tabular openings in a viscoelastic medium is available in the literature, a solution for a parallel-sided stope is derived in this chapter.

The use of viscoelastic theory to analyse the time-dependent strain of laboratory creep samples has been discussed in Chapter 2. Various applications of this theory to the rheology of underground excavations can also be found. Gnirk and Johnson (1964) calculated the stress and displacement fields resulting from the excavation of a circular mine shaft in salt under hydrostatic stress. Of practical interest is that the viscoelastic analysis enabled the authors to investigate the time-dependent behaviour of a shaft lined with an elastic material. It was found that the Burgers model provided the best representation of the overall deformational behaviour of the rock. The analysis showed that the stresses in the shaft lining become progressively greater with time and may eventually exceed the failure strength of the concrete. Chin and Rogers (1987) excavated vertical shafts in carbonate shale, weathered limestone and tuff to measure rheological parameters of rock on an engineering scale. Changes in the shaft diameter under a constant applied radial pressure were recorded. Viscoelastic analysis of the data showed that the Burgers model gives a better fit to the data than the 3-parameter solid (these models are

illustrated in Figure 2.2). The viscosities determined in situ were found to be much lower than those calculated from experiments on small intact specimens, by up to several orders of magnitude. Pan and Dong (1991a) investigated time-dependent tunnel convergence and the effect of advance rate and tunnel-support interaction. Viscoelastic solutions for a circular opening in the rock mass were derived for two models namely a Kelvin model and a 3-parameter solid. The Kelvin model provided a good fit with measured tunnel convergence (Pan and Dong, 1991b).

3.2 Deriving a viscoelastic convergence solution for a single parallel-sided panel.

The approach followed in this section is to use a known elastic solution for tabular stopes, choose an appropriate viscoelastic model and apply the correspondence principle to obtain the desired viscoelastic solution. The correspondence principle (Flügge, 1975) states that if the solution to an elastic problem is known, the Laplace transform of the solution to the corresponding viscoelastic problem may be found by replacing the elastic constants and the loads with their corresponding Laplace transforms. These corresponding Laplace transforms of the elastic constants will depend on the chosen viscoelastic model. The solution in the time domain can then be found by taking the inverse Laplace transform. Instances where the principle breaks down are if the type of boundary condition varies with time and if the boundaries of the body are changing in time, such as for a melting body.

Figure 3.1 illustrates a typical tabular excavation showing areas of contact between the hangingwall and footwall. If the geometry of the excavation does not change for a long distance when moving along the y-axis, the stope can be idealised as a two-dimensional problem (Figure 3.2). For convenience this analysis will be restricted to a single parallel-sided panel with no contact between the hangingwall and footwall. The elastic solution of this problem (Salamon, 1968) is already known and this will be used as the first building block to derive the viscoelastic solution.

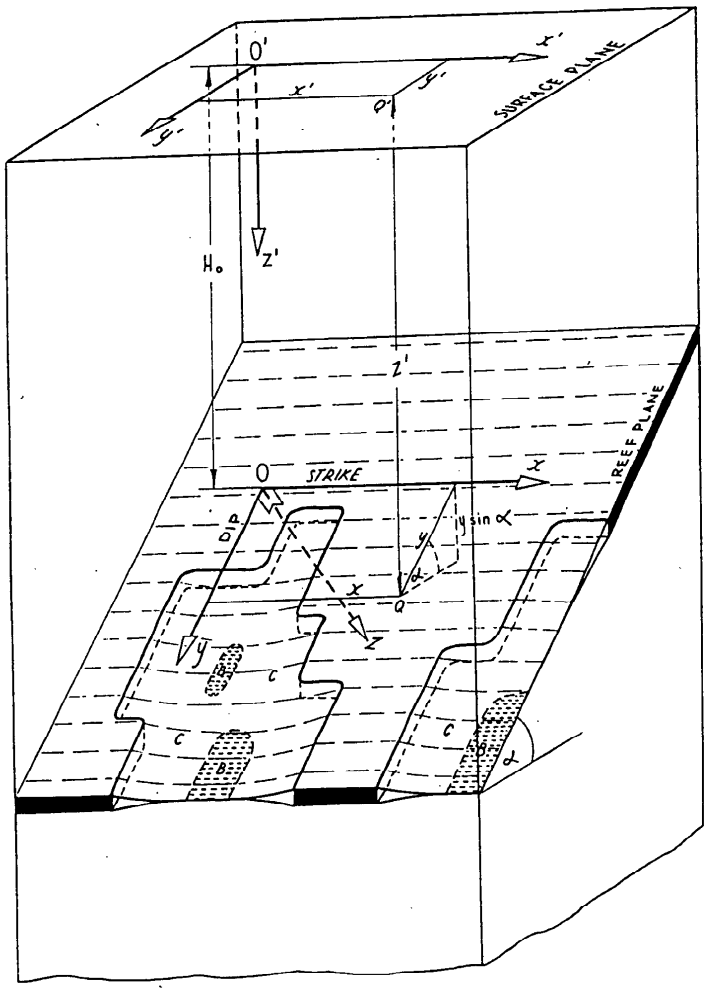

Figure 3.1. Schematic diagram of a typical tabular ore body dipping at $\alpha°$. (after Salamon et al., 1964). The co-ordinate system used here will also be adopted when deriving the viscoelastic solution in this chapter. Visible are mined regions (C) and areas of contact between the hangingwall and footwall (B).

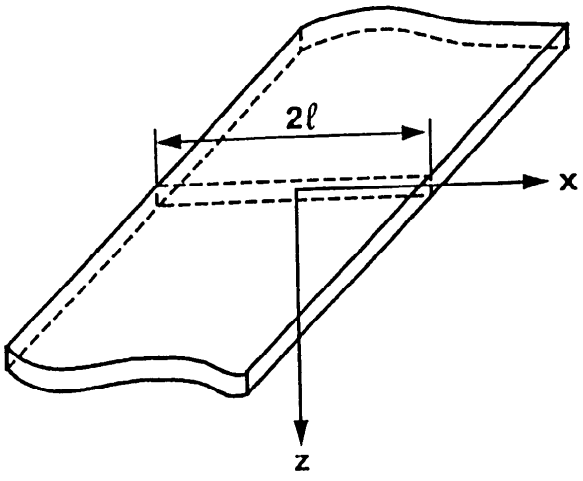

Figure 3.2. Single parallel-sided panel.

Salamon (1968) calculated the elastic convergence (S_z) of a parallel-sided panel in isotropic ground without contact between the hangingwall and footwall as

$$S_z(x) = \frac{-4(1-\nu^2)W_z}{E}\sqrt{\ell^2 - x^2}\ (1+\frac{dx}{2}) \qquad [3.1]$$

where

$$W_z = \frac{-\rho g H}{2}\left[(1+k)+(1-k)\cos 2\alpha\right] \qquad [3.2]$$

and

$$d = \frac{\sin\alpha\cos\beta}{H} \qquad [3.3]$$

2ℓ = span of the stope

ρ = density of the rock

g = gravitational acceleration

H = depth below surface

k = ratio of horizontal to vertical stress

α = dip of the reef

β = angle between x-axis and the dip

ν = Poisson's ratio

E = Young's modulus

Any viscoelastic model can be described by a differential equation of the form (Flügge, 1975)

$$\sigma + p_1\dot{\sigma} + p_2\ddot{\sigma} + \ldots = q_0\varepsilon + q_1\dot{\varepsilon} + q_2\ddot{\varepsilon} + \ldots \qquad [3.4]$$

or

$$P\sigma = Q\varepsilon \qquad [3.5]$$

where

$$P = \sum_{k=0}^{m} p_k \frac{d^k}{dt^k} \qquad Q = \sum_{k=0}^{n} q_k \frac{d^k}{dt^k} \qquad [3.6]$$

with σ the stress tensor, ε the strain tensor and $p_0 = 1$. Subjecting equation [3.5] to the Laplace transformation gives

$$\tilde{P}(s)\tilde{\sigma}(s) = \tilde{Q}(s)\tilde{\varepsilon}(s) \qquad [3.7]$$

where

$$\tilde{P}(s) = \sum_{k=0}^{m} p_k s^k \qquad \tilde{Q}(s) = \sum_{k=0}^{n} q_k s^k \qquad [3.8]$$

When doing an analysis of strain in a viscoelastic material, the stress and strain tensors can be divided in two representing dilatation and distortion (see Flügge, 1975). Equation [3.5] then becomes

$$P'\sigma_m = Q'\varepsilon_m \qquad [3.9]$$

$$P''\sigma_d = Q''\varepsilon_d \qquad [3.10]$$

with equation [3.9] representing dilatation (hydrostatic compression) and equation [3.10] distortion. In these equations, σ_m and ε_m are the dilational stress and strain and σ_d and ε_d the distortional stress and strain. In the limiting case of an elastic solid, Hooke's law for an isotropic medium may be written as (Jaeger and Cook, 1979)

$$\sigma_m = 3K\varepsilon_m \qquad [3.11]$$

$$\sigma_d = 2G\varepsilon_d \qquad [3.12]$$

where K and G are the bulk and shear modulus respectively. In the Laplace domain, equations [3.9], [3.10], [3.11] and [3.12] become

$$\tilde{P}'(s)\tilde{\sigma}_m(s) = \tilde{Q}'(s)\tilde{\varepsilon}_m(s) \qquad [3.13]$$

$$\tilde{P}''(s)\tilde{\sigma}_d(s) = \tilde{Q}''(s)\tilde{\varepsilon}_d(s) \qquad [3.14]$$

$$\tilde{\sigma}_m(s) = 3K\tilde{\varepsilon}_m(s) \qquad [3.15]$$

$$\tilde{\sigma}_d(s) = 2G\tilde{\varepsilon}_d(s) \qquad [3.16]$$

Therefore for an elastic material when choosing $\tilde{P}'(s) = 1$ and $\tilde{P}''(s) = 1$, it follows that

$$\tilde{Q}'(s) = 3K \qquad \tilde{Q}''(s) = 2G \qquad [3.17]$$

Dividing [3.13] by [3.15] and [3.14] by [3.16] gives

$$K = \frac{\tilde{Q}'(s)}{3\tilde{P}'(s)} \qquad [3.18]$$

$$G = \frac{\tilde{Q}''(s)}{2\tilde{P}''(s)} \qquad [3.19]$$

Writing equations [3.18] and [3.19] in terms of Young's Modulus (E) and Poisson's Ratio (ν) gives

$$\tilde{E} = \frac{3\tilde{Q}''\tilde{Q}'}{2\tilde{P}''\tilde{Q}' + \tilde{Q}''\tilde{P}'} \qquad [3.20]$$

$$\tilde{\nu} = \frac{\tilde{P}''\tilde{Q}' - \tilde{Q}''\tilde{P}'}{2\tilde{P}''\tilde{Q}' + \tilde{Q}''\tilde{P}'} \qquad [3.21]$$

Subjecting equation [3.1] to the correspondence principle gives

$$\tilde{S}_z = \frac{-4(1-\tilde{\nu}^2)\tilde{W}_z}{\tilde{E}}\sqrt{\ell^2 - x^2}\,(1+\frac{dx}{2}) \qquad [3.22]$$

Assuming that W_z does not change with time gives

$$\tilde{W}_z(s) = \frac{W_z}{s} \qquad [3.23]$$

Substituting the equations [3.20], [3.21] and [3.23] in equation [3.22] and transforming back to the time domain gives

$$S_z(x,t) = -4W_zF(t)\sqrt{\ell^2 - x^2}\,(1+\frac{dx}{2}) \qquad [3.24]$$

where

$$F(t) = L^{-1}\left[\frac{\tilde{P}''^2\tilde{Q}' + 2\tilde{P}''\tilde{P}'\tilde{Q}''}{s\tilde{Q}''\left(2\tilde{P}''\tilde{Q}' + \tilde{P}'\tilde{Q}''\right)}\right] \qquad [3.25]$$

The symbol L^{-1} is used to signify the inverse Laplace transformation. To obtain the final solution, the inverse Laplace transformation in equation [3.25] must be determined for the appropriate viscoelastic model. The fundamental question remaining is which viscoelastic model is appropriate to describe the time-dependent behaviour of hard rock in general and in particular in the deep South African gold mines. Following the success of Gnirk and Johnson (1964) and Chin and Rogers (1987) in using a Burgers model, the tabular solution will be derived using this model in the next section. The choice of this model will also be further justified in Chapter 4. Solutions for a Kelvin and 3-parameter model were also derived and are given in Appendix B.

Viscoelastic convergence solution for a Burgers model

The Burgers model can be constructed by combining a Maxwell and Kelvin model (Figure 3.3). If it is assumed that the rock behaves like an elastic solid in dilatation and like a Burgers model in distortion, the following differential equation can be derived for the distortional part. Although the general equation of the Burgers model is known in the form of equation [3.4] (Flügge, 1975), the following analysis for the distortional component is necessary to determine the coefficients p_1, p_2, q_1 and q_2 in terms of the viscosity coefficients η_1 and η_2 and shear moduli G_1 and G_2.

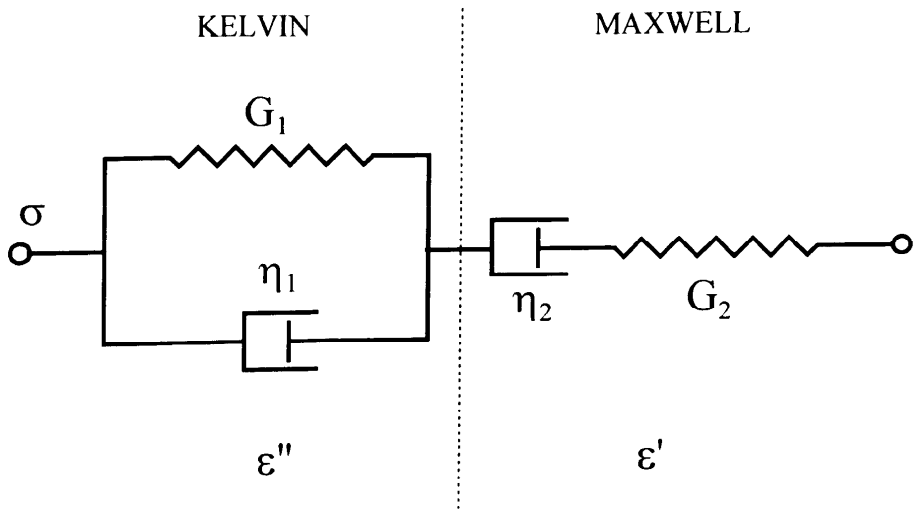

Figure 3.3. The Burgers model representing the rock behaviour in distortion.

For the Maxwell component it can be shown that

$$\sigma_d + p_1'\dot{\sigma}_d = q_1'\dot{\varepsilon}_d' \qquad [3.26]$$

where

$$p_1' = \frac{\eta_2}{2G_2} \qquad q_1' = \eta_2 \qquad [3.27]$$

For the Kelvin component it follows that (Appendix B1)

$$\sigma_d = q_0''\varepsilon_d'' + q_1''\dot{\varepsilon}_d'' \qquad [3.28]$$

where

$$q_0'' = 2G_1 \qquad q_1'' = \eta_1 \qquad [3.29]$$

Taking the Laplace transformation of equations [3.26] and [3.28] gives

$$(1 + p_1's)\tilde{\sigma}_d = q_1's\tilde{\varepsilon}_d' \qquad [3.30]$$

$$\tilde{\sigma}_d = (q_0'' + q_1''s)\tilde{\varepsilon}_d'' \qquad [3.31]$$

Multiplying each equation with a suitable constant and adding gives

$$(1 + p_1's)(q_0'' + q_1''s)\tilde{\sigma}_d + q_1's\tilde{\sigma}_d = q_1's(q_0'' + q_1''s)\tilde{\varepsilon}_d \qquad [3.32]$$

where

$$\tilde{\varepsilon}_d = \tilde{\varepsilon}_d' + \tilde{\varepsilon}_d'' \qquad [3.33]$$

Taking the inverse Laplace transformation and inserting equations [3.27] and [3.29] gives

$$\sigma_d + p_1\dot{\sigma}_d + p_2\ddot{\sigma}_d = q_1\dot{\varepsilon}_d + q_2\ddot{\varepsilon}_d \qquad [3.34]$$

where

$$p_1 = \frac{q_1'' + p_1'q_0'' + q_1'}{q_0''} = \frac{\eta_1G_2 + \eta_2G_1 + \eta_2G_2}{2G_1G_2} \qquad [3.35]$$

$$p_2 = \frac{p_1'q_1''}{q_0''} = \frac{\eta_1\eta_2}{4G_1G_2} \qquad [3.36]$$

$$q_1 = q_1' = \eta_2 \qquad [3.37]$$

$$q_2 = \frac{q_1' q_1''}{q_0''} = \frac{\eta_1 \eta_2}{2G_1} \qquad [3.38]$$

When subjecting equation [3.34] to the Laplace transformation gives

$$\left(1 + p_1 s + p_2 s^2\right)\tilde{\sigma}_d = \left(q_1 s + q_2 s^2\right)\tilde{\varepsilon}_d \qquad [3.39]$$

If the rock behaves elastically in dilatation and according to a Burgers model in distortion it therefore follows from equations [3.13], [3.14], [3.15] and [3.39] that

$$\tilde{P}' = 1 \quad \tilde{P}'' = 1 + p_1 s + p_2 s^2 \quad \tilde{Q}' = 3K \quad \tilde{Q}'' = q_1 s + q_2 s^2 \qquad [3.40]$$

When equation [3.40] is substituted into [3.25]

$$F(t) = L^{-1}\left[\frac{3K\left(1 + p_1 s + p_2 s^2\right)^2 + 2\left(1 + p_1 s + p_2 s^2\right)\left(q_1 s + q_2 s^2\right)}{s\left(q_1 s + q_2 s^2\right)\left[6K\left(1 + p_1 s + p_2 s^2\right) + \left(q_1 s + q_2 s^2\right)\right]}\right] \qquad [3.41]$$

Finding the inverse Laplace transformation by partial fraction expansion gives (Appendix C1)

$$F(t) = g_1\left[1 + c_5 t + c_6 e^{-ft} + \left(c_7 \sinh bt + c_8 \cosh bt\right)e^{\frac{-ht}{2}}\right] \qquad [3.42]$$

where

$$b = \sqrt{\frac{\left(6Kp_1 + q_1\right)^2 - 24K\left(6Kp_2 + q_2\right)}{4\left(6Kp_2 + q_2\right)^2}} \qquad [3.43]$$

$$g_1 = \frac{2Kp_1 q_1 + {q_1}^2 - 2Kq_2}{4K{q_1}^2} \qquad [3.44]$$

$$c_5 = \frac{2Kq_1}{2Kp_1 q_1 + {q_1}^2 - 2Kq_2} \qquad [3.45]$$

$$c_6 = \frac{2K\left(p_2 q_1^2 - p_1 q_1 q_2 + q_2^2\right)}{q_2\left(2Kp_1 q_1 + q_1^2 - 2Kq_2\right)} \qquad [3.46]$$

$$c_7 = \frac{q_1^2\left(-12Kp_2 q_1 + 6Kp_1 q_2 - q_1 q_2\right)}{2b\left(6Kp_2 + q_2\right)^2\left(2Kp_1 q_1 + q_1^2 - 2Kq_2\right)} \qquad [3.47]$$

$$c_8 = \frac{q_1^2 q_2}{\left(6Kp_2 + q_2\right)\left(-2Kp_1 q_1 - q_1^2 + 2Kq_2\right)} \qquad [3.48]$$

$$f = \frac{q_1}{q_2} \qquad [3.49]$$

$$h = \frac{6Kp_1 + q_1}{6Kp_2 + q_2} \qquad [3.50]$$

The parameters p_1, p_2, q_1 and q_2 are given in equations [3.35] to [3.38] in terms of the viscosity coefficients η_1 and η_2 and shear moduli G_1 and G_2. The complete convergence solution for the Burgers model is obtained by inserting equation [3.42] in [3.24].

3.3 Properties of the Burgers convergence model

This convergence model displays typical primary and secondary behaviour. To aid the fit of experimental data, the effect of the different Burgers parameters on the convergence behaviour was examined using a horizontal stope with a span of 100 m at a depth of 2000 m. The total span was mined in one step. The consequences of incremental mining steps will be explored in the next section. The instantaneous response of the model is determined by the shear modulus of the Maxwell component (Figure 3.4) while the convergence rates at any time $t > 0$ remain unaffected by this parameter. For $t = 0$, equation [3.42] is reduced to

$$F(t = 0) = g_1\left[1 + c_6 + c_8\right] \qquad [3.51]$$

Inserting equations [3.35] to [3.38] into equations [3.44], [3.46] and [3.48] and then into equation [3.51] gives

$$F(t=0)=\frac{3K+4G_2}{4G_2(3K+G_2)} \qquad [3.52]$$

showing correctly that the instantaneous response is unaffected by the value of G_1, η_1 or η_2 . The role of G_1 is to control the magnitude of primary creep response as indicated in Figure 3.5. From Figure 3.6 it is clear that the Maxwell viscosity(η_2)controls the rate of convergence in the secondary phase. The Kelvin viscosity(η_1)controls the rate of convergence in the primary phase and therefore how soon the secondary phase is approached (Figure 3.7).

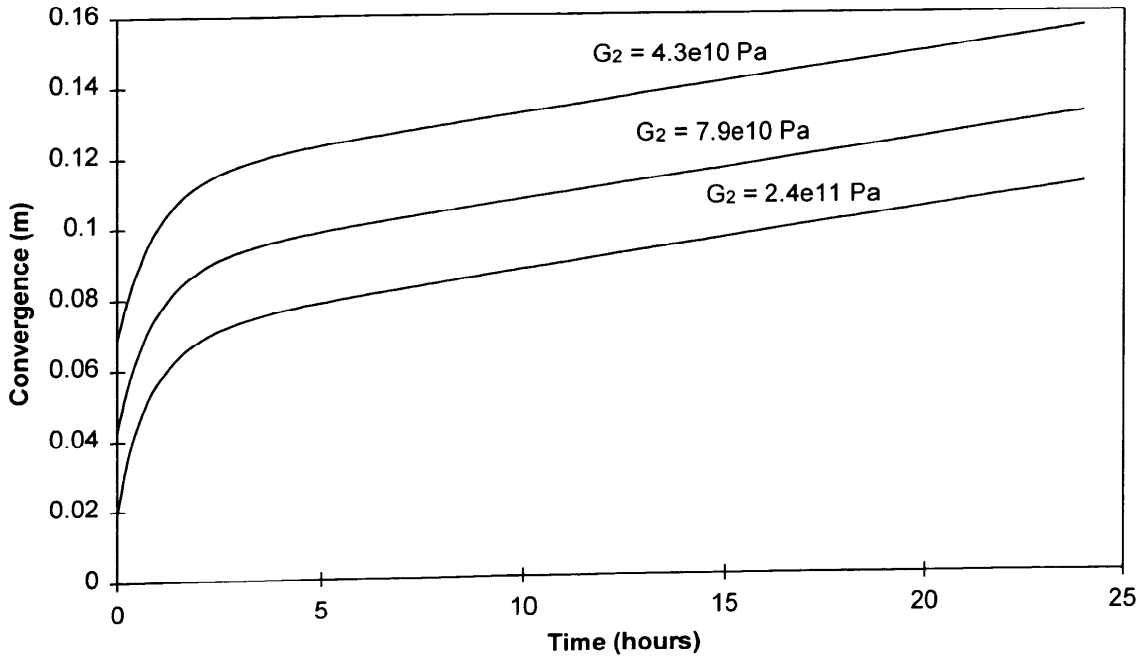

Figure 3.4. The effect of the value of G_2 on the convergence behaviour of a tabular opening. Other values used in this simulation are $\eta_1 = 8\times10^{10}$ Pa.h, $\eta_2 = 2\times10^{12}$ Pa.h, $G_1 = 3.9\times10^{10}$ Pa, L = 50 m, x = 40 m, H = 2000 m, $\alpha = 0°$, k = 0.5, g = 9.81 m/s^2 and $\rho = 2700$ kg/m^3.

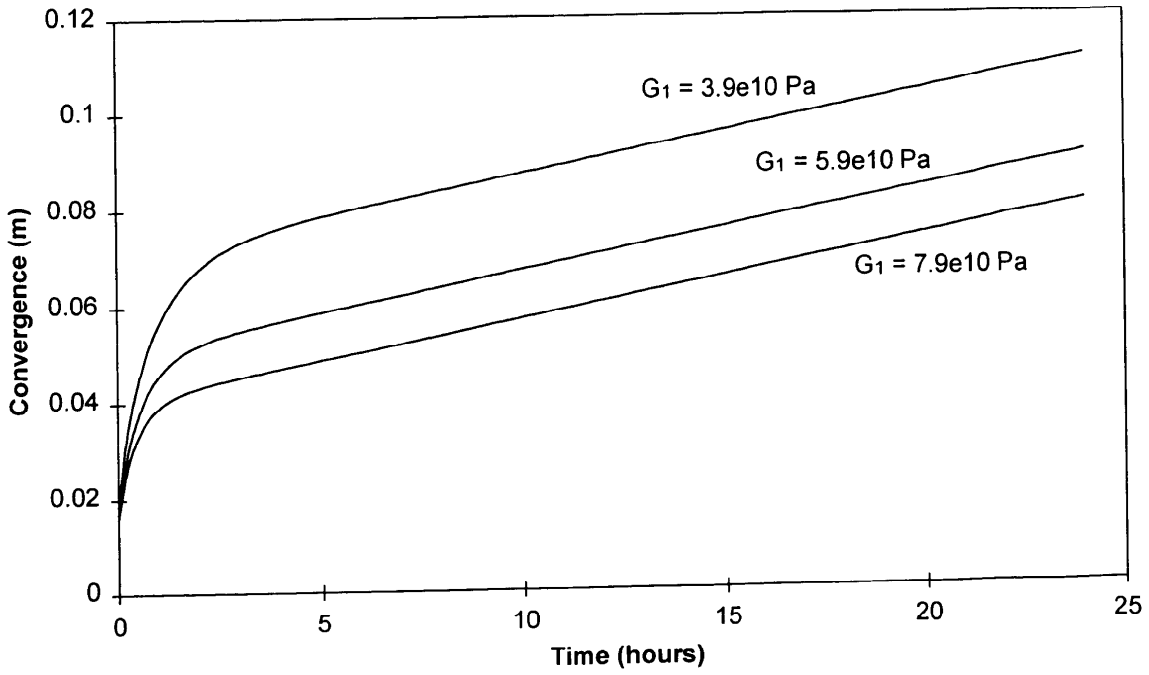

Figure 3.5. The effect of the value of G_1 on the convergence behaviour of a tabular opening. Other values used in this simulation are $\eta_1 = 8\times10^{10}$ Pa.h, $\eta_2 = 2\times10^{12}$ Pa.h, $G_2 = 2.4\times10^{11}$ Pa, L = 50 m, x = 40 m, H = 2000 m, $\alpha = 0°$, k = 0.5, g = 9.81 m/s^2 and $\rho = 2700$ kg/m^3.

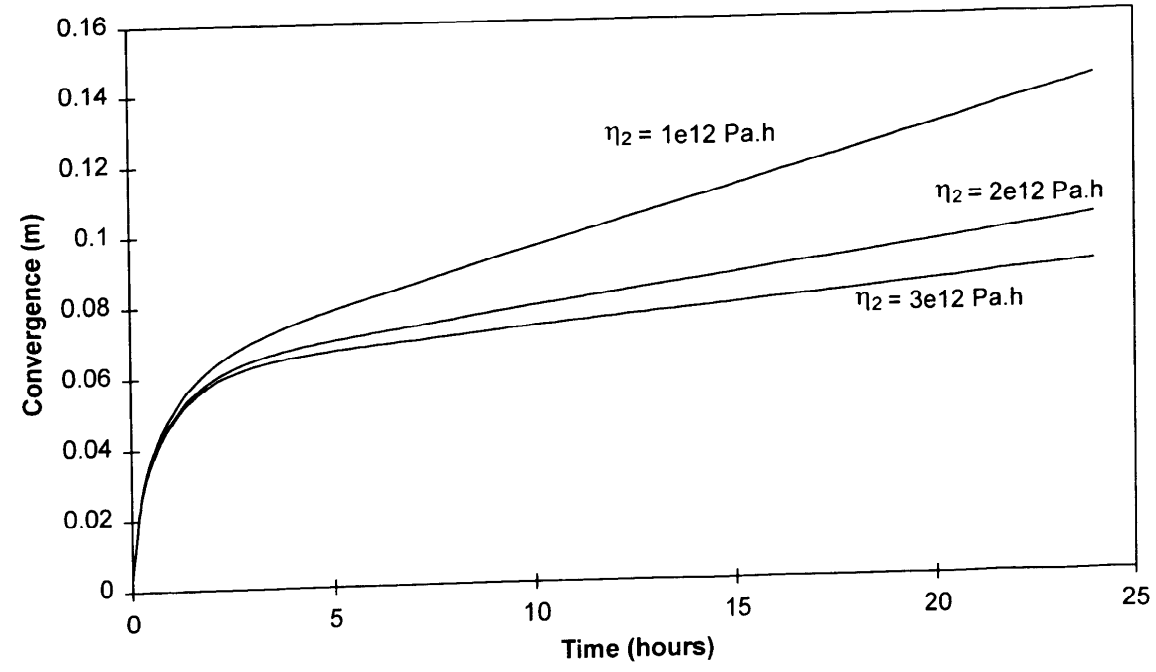

Figure 3.6. The effect of the value of η_2 on the convergence behaviour of a tabular opening. Other values used in this simulation are $\eta_1 = 8\times10^{10}$ Pa.h, $G_1 = 3.9\times10^{10}$ Pa, $G_2 = 2\times10^{12}$ Pa, L = 50 m, x = 40 m, H = 2000 m, $\alpha = 0°$, k = 0.5, g = 9.81 m/s^2 and $\rho = 2700$ kg/m^3.

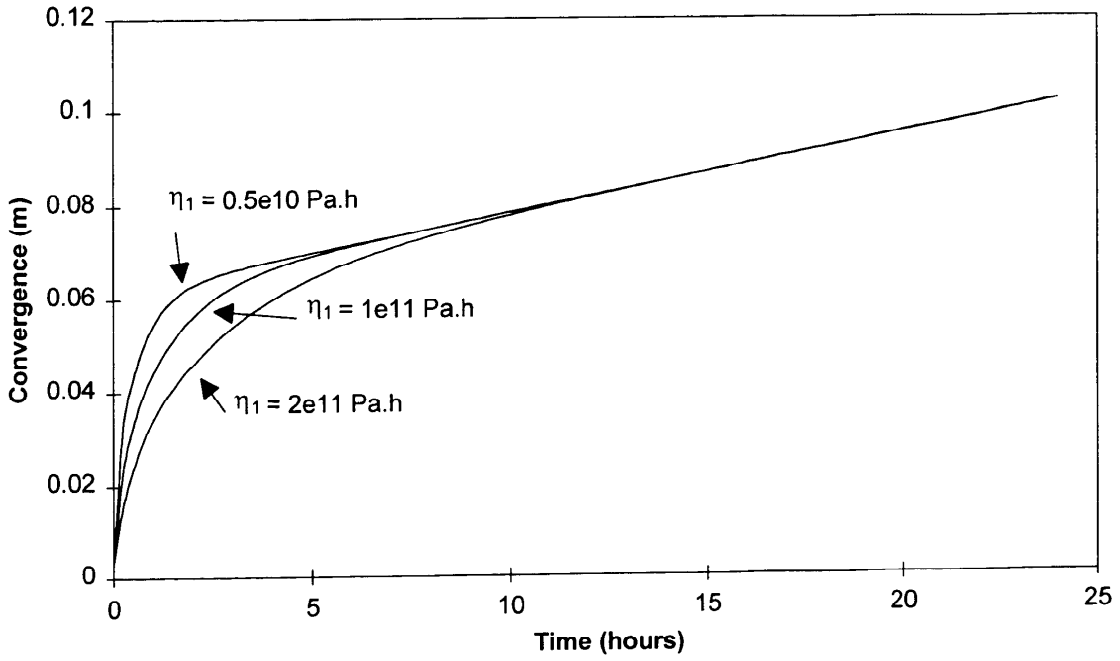

Figure 3.7. The effect of the value of η_1 on the convergence behaviour of a tabular opening. Other values used in this simulation are $\eta_2 = 2\times10^{12}$ Pa.h, $G_1 = 3.9\times10^{10}$ Pa, $G_2 = 2\times10^{12}$ Pa, L = 50 m, x = 40 m, H = 2000 m, $\alpha = 0°$, k = 0.5, g = 9.81 m/s^2 and $\rho = 2700$ kg/m^3.

For an increase in stope span, the magnitude of primary convergence increases correspondingly (Figure 3.8) while the convergence rate in the secondary phase is also affected. Similar behaviour is noted for an increase in stress (depth). Of further significance is that for any particular span, the highest convergence rate in the secondary phase is experienced at the centre of the panel with this rate decreasing towards the face (Figure 3.9). It should be emphasised that these results are for a panel where the total span is excavated in one step. In the next section it will be shown that for the incremental enlargement of a panel, the instantaneous response after each increment is largest at the face and decreases towards the centre of the panel. The convergence rate of the secondary phase will however still have a maximum value in the centre of the panel.

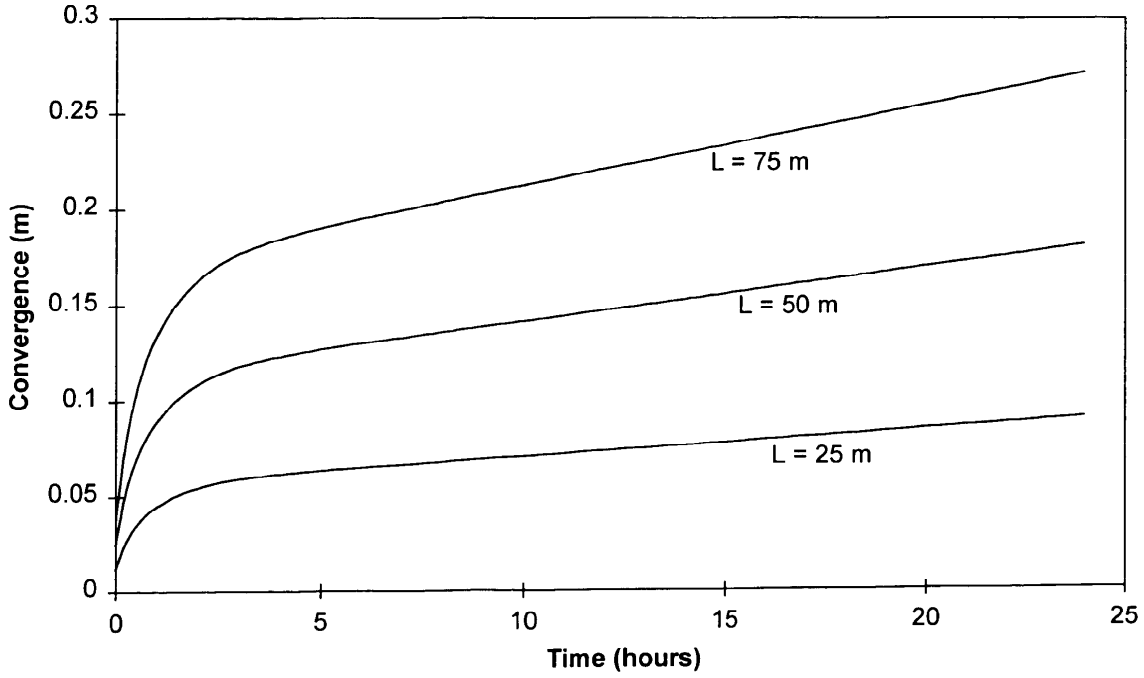

Figure 3.8. Effect of stope span on the convergence at the centre of an imaginary panel which is mined in one step. Other values used in this simulation are $\eta_1 = 8\times10^{10}$ Pa.h, $\eta_2 = 2\times10^{12}$ Pa.h, $G_1 = 3.9\times10^{10}$ Pa, $G_2 = 3.1\times10^{11}$ Pa, x = 40 m, H = 2000 m, $\alpha = 0°$, k = 0.5, g = 9.81 m/s^2 and $\rho = 2700$ kg/m^3.

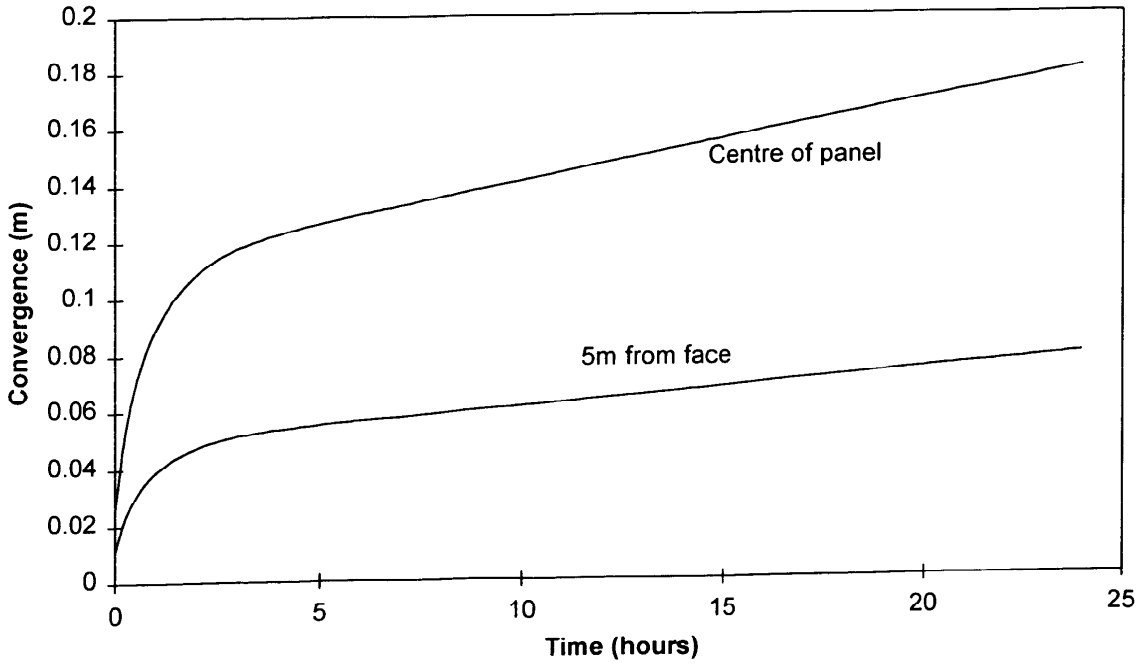

Figure 3.9. Comparison of convergence behaviour at different positions of an imaginary panel which is mined in one step. Other values used in this simulation are $\eta_1 = 8\times10^{10}$ Pa.h, $\eta_2 = 2\times10^{12}$ Pa.h, $G_1 = 3.9\times10^{10}$ Pa, $G_2 = 3.1\times10^{11}$ Pa, L = 50 m, x = 40 m, H = 2000 m, $\alpha = 0°$, k = 0.5, g = 9.81 m/s^2 and $\rho = 2700$ kg/m^3.

The rate of convergence of the model can be calculated from the time derivative of equation [3.24]

$$\frac{dS_z}{dt} = -4W_z\sqrt{\ell^2 - x^2}\left(1+\frac{dx}{2}\right)g_1\frac{d}{dt}\left[1 + c_5 t + c_6 e^{-ft} + \left(c_7 \sinh bt + c_8 \cosh bt\right)e^{\frac{-ht}{2}}\right] \qquad [3.53]$$

which can be written as

$$\frac{dS_z}{dt} = -4W_z\sqrt{\ell^2 - x^2}\left(1+\frac{dx}{2}\right)\times$$
$$g_1\left[c_5 - c_6 f e^{-ft} + \left(c_7 b - \frac{c_8 h}{2}\right)\cosh bt\, e^{\frac{-ht}{2}} + \left(c_8 b - \frac{c_7 h}{2}\right)\sinh bt\, e^{\frac{-ht}{2}}\right] \qquad [3.54]$$

As $t \to \infty$, this reduces to

$$\left.\frac{dS_z}{dt}\right|_{t\to\infty} = -4W_z\sqrt{\ell^2 - x^2}\left(1+\frac{dx}{2}\right)g_1 c_5 \qquad [3.55]$$

After inserting [3.44], [3.45] and [3.37] this can be written as

$$\left.\frac{dS_z}{dt}\right|_{t\to\infty} = \frac{-2W_z\sqrt{\ell^2 - x^2}\left(1+\frac{dx}{2}\right)}{\eta_2} \qquad [3.56]$$

As $t \to \infty$, the convergence rate in the secondary phase is therefore only a function of geometric parameters, stress magnitude and the viscoelastic parameter η_2. This is intuitively expected from Figure 3.3. Also if $\eta_2 = \infty$ (thereby reducing the Burgers model to the 3-parameter solid, see Figure 2.2), equation [3.56] predicts correctly that at $t \to \infty$, the convergence rate becomes zero.

The steady-state convergence rate (equation [3.56]) as a function of position x was plotted in Figure 3.10. The highest rate of convergence is in the centre of the stope which reduces to a value of zero at the stope face.

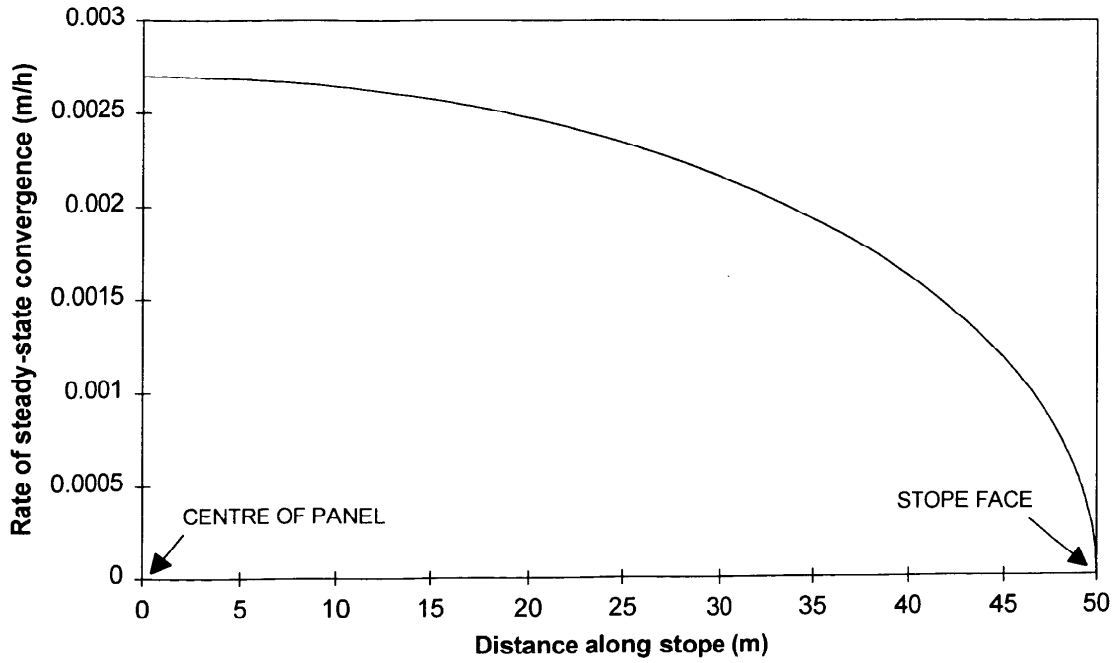

Figure 3.10. The rate of steady-state convergence along a panel of 100 m span at $t \rightarrow \infty$. Values used in this simulation are $\eta_2 = 2x10^{12}$ Pa.h, H = 2000 m, $\alpha = 0°$, k = 0.5, g = 9.81 m/s^2 and $\rho = 2700$ kg/m^3.

3.4 Dealing with incremental face advance

Equation [3.24] is applicable to situations where the total length of the tabular excavation is mined instantaneously. This is not the case in practice where the face is incrementally advanced. Assume that the first mining increment is created at time τ_1 giving a stope of half span L. Equation [3.24] will give the viscoelastic convergence for this step as $S_z(\ell = L, x, t - \tau_1)$. At time τ_2 the face is advanced on both sides of the stope by $\Delta\ell$ giving a half span of $(L + \Delta\ell)$. Using equation [3.24] with a half span of $(L + \Delta\ell)$ at time τ_2 results in the total span being created in one step which is clearly wrong. At time $\tau_2 + \Delta t$ the total viscoelastic convergence is the sum of the viscoelastic convergence caused by a half span of L (excavated at time τ_1) plus an incremental viscoelastic convergence caused by the incremental length $\Delta\ell$, excavated at time τ_2. The incremental viscoelastic convergence is the difference between the viscoelastic convergence of a stope with half span $L + \Delta\ell$ created at time τ_2 and the viscoelastic convergence of a stope with half span L also created at time τ_2 . Therefore at time $\tau_2 + \Delta t$ the viscoelastic convergence is given as

$$S_z = S_z(\ell = L, x, t - \tau_1) + S_z(\ell = L + \Delta\ell, x, t - \tau_2) - S_z(\ell = L, x, t - \tau_2) \qquad [3.57]$$

Salamon (1974) used arguments of negative and positive superposition to give a general expression for an arbitrarily shaped excavation created in n increments as

$$u = \left\{\sum_{i=1}^{n-1}\left[F_i(l_i, t - \tau_i)\right] - \left[F_i\left(l_i, t - \tau_{i+1}\right)\right]\right\} + F_n\left[l_n, t - \tau_n\right] \qquad [3.58a]$$

which is valid for $\tau_n \leq t < \tau_{n+1}$ where

u = displacement component at some point in the rock.
F_i = some function dependent on the shape of the excavation
l_i = a critical linear dimension of the excavation

If the shape of the excavation stays constant ($F_1 = F_2 = F$) and n = 2, then equation [3.58a] is reduced to equation [3.57] with $F = S_Z$. When writing [3.58a] in the notation used for the tabular excavations

$$S_z = \left\{\sum_{i=1}^{n-1}\left[S_z\left(\ell_i, t - \tau_i\right)\right] - \left[S_z\left(\ell_i, t - \tau_{i+1}\right)\right]\right\} + S_z\left[\ell_n, t - \tau_n\right] \qquad [3.58b]$$

which is also valid for $\tau_n \leq t < \tau_{n+1}$. To examine the instantaneous response of the model after the mining of an increment, assume the first increment of a stope was mined at time $t = \tau_1$ followed by another increment at $t = \tau_2$. The incremental instantaneous response of the Burgers convergence model at time $t = \tau_2$ can be obtained from equation [3.57] by subtracting $S_z(\ell = L, x, t - \tau_1)$ and inserting $t = \tau_2$ to give

$$\Delta S_z = S_z(\ell = L + \Delta\ell, x, t = 0) - S_z(\ell = L, x, t = 0) \qquad [3.59]$$

Note that this equation is only valid for $t = \tau_2$ and not $t > \tau_2$. Inserting equations [3.24] and [3.51] in equation [3.59] gives

$$\Delta S_z(x,t) = -4W_z\,(1+\frac{dx}{2})g_1\left(1+c_6+c_8\right)\left[\sqrt{(L+\Delta\ell)^2-x^2}-\sqrt{L^2-x^2}\right] \qquad [3.60]$$

for $x \leq L$. This equation is plotted in Figure 3.11 for a panel with a span of 100 m at depth of 2000 m. The incremental convergence decreases rapidly away from the face. This is in agreement with Leeman's (1958) observation that the effect of blasting upon closure becomes progressively less, the further the point of measurement from the working face. Ideally the measurement station should therefore be installed close to the face to obtain large incremental closure for more accurate parameter calibration.

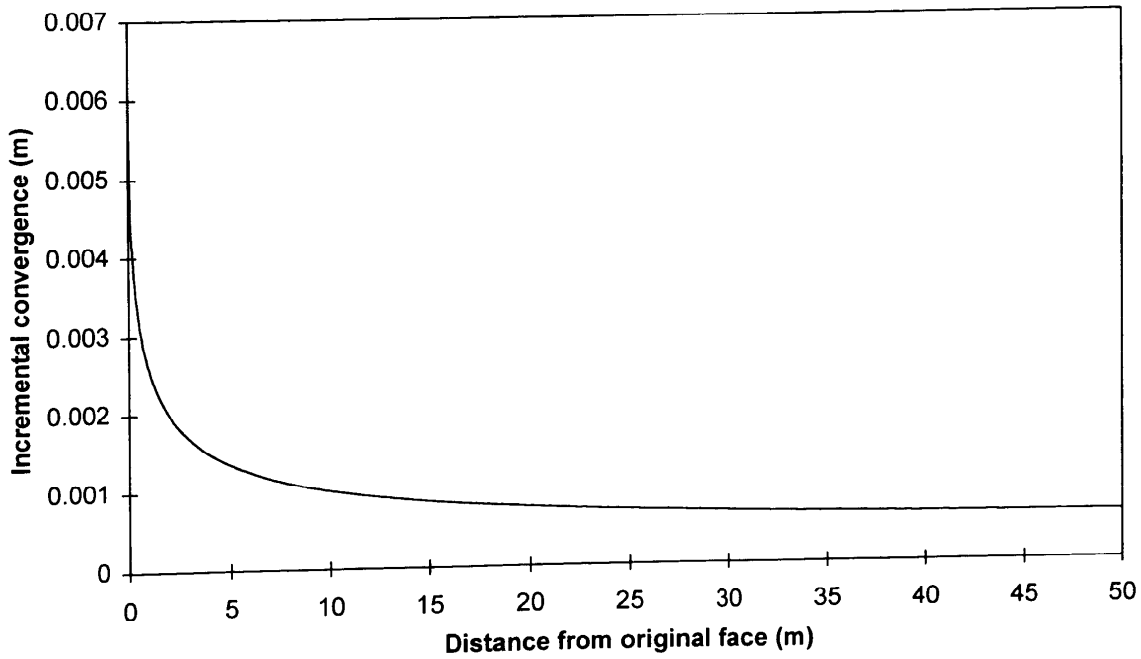

Figure 3.11. Instantaneous incremental convergence as a function of position. Parameters used in this simulation are $\eta_1 = 8\times10^{10}$ Pa.h, $\eta_2 = 2\times10^{12}$ Pa.h, $G_1 = 3.9\times10^{10}$ Pa, $G_2 = 2.4\times10^{11}$ Pa, L = 50 m, $\Delta\ell$ = 1 m, H = 2000 m, $\alpha = 0°$, k = 0.5, g = 9.81 m/s^2 and $\rho = 2700$ kg/m^3.

3.5 Parameter calibration from incremental stope closure data

Instruments to measure closure are usually installed in stopes where the span has already reached a significant length. Although an appreciable amount of closure will have taken place up to the time of installation, the amount is unknown and therefore the closure is taken to be zero at this point as a reference level. Unless the blasting time and face advance of every single increment in the entire history of the panel is known, it is not possible to calibrate equation [3.58b]. Therefore to obtain an appropriate calibration, all the preceding steps will be modelled as one excavation step, followed by the increments after the installation of the closure instrument. This method will be successful as the only value which is essentially required from the initial excavation is the slope of the secondary closure phase. As a result of the linear Burgers viscoelastic assumption, this slope is not dependent on the history of the panel but only on the span.

To illustrate this calibration technique, assume that for a panel consisting of n increments on both sides, a closure instrument was installed after increment (n-1) but before increment n. The half span was L after the $(n-1)^{th}$ increment. The increase in half span after the nth increment was $\Delta\ell$. Assume that the (n-1) increments were mined as one large increment at time $t = \tau_1$. This is followed by the nth increment at time $t = \tau_2$. Therefore inserting equation [3.24] in [3.57] gives

$$S_z = -4W_z\left[\left\{F(t-\tau_1) - F(t-\tau_2)\right\}\sqrt{L^2 - x^2} + \left\{F(t-\tau_2)\right\}\sqrt{(L+\Delta\ell)^2 - x^2}\right]\left(1+\frac{dx}{2}\right) \qquad [3.61]$$

which is valid for $x \le L$ and $t \ge \tau_2$.

When assuming that the material behaves as a Kelvin model or 3-parameter solid, calibration is further simplified as the convergence for the first step approaches an asymptotic value which can be assumed to be zero for convenience. The first term in equation [3.57] therefore disappears.

Equation [3.61a] assumes that both sides of the stope are blasted simultaneously, giving an advance of $\Delta\ell$ at both faces. This is however seldom the case in underground workings where often only one side of the panel is blasted. This problem is solved by introducing an equivalent stope principle. Equation [3.61] is based on both linear elasticity theory and linear viscoelasticity theory and therefore an advance of $\Delta\ell$ on one side only (Figure

3.12(a)), can be represented by an equivalent stope with a simultaneous advance of $\Delta\ell/2$ on both sides, provided that the measuring point is shifted by a distance $\Delta\ell/2$ away from the blasted face to keep the original distance to the new face (length a) the same (Figure 3.12(b)). For a stope with a face advance $\Delta\ell$ at one side only, equation [3.61] can be written as

$$S_z = -4W_z\left[\left\{F(t-\tau_1)-F(t-\tau_2)\right\}\sqrt{L^2-x^2}\left(1+\frac{dx}{2}\right)\right]- \\ 4W_z\left[\left\{F(t-\tau_2)\right\}\sqrt{\left(L+\frac{\Delta\ell}{2}\right)^2-\left(x-\frac{\Delta\ell}{2}\right)^2}\left\{1+\frac{d\left(x-(\Delta\ell/2)\right)}{2}\right\}\right] \qquad [3.62]$$

for $x \le L$ and $t \ge \tau_2$.

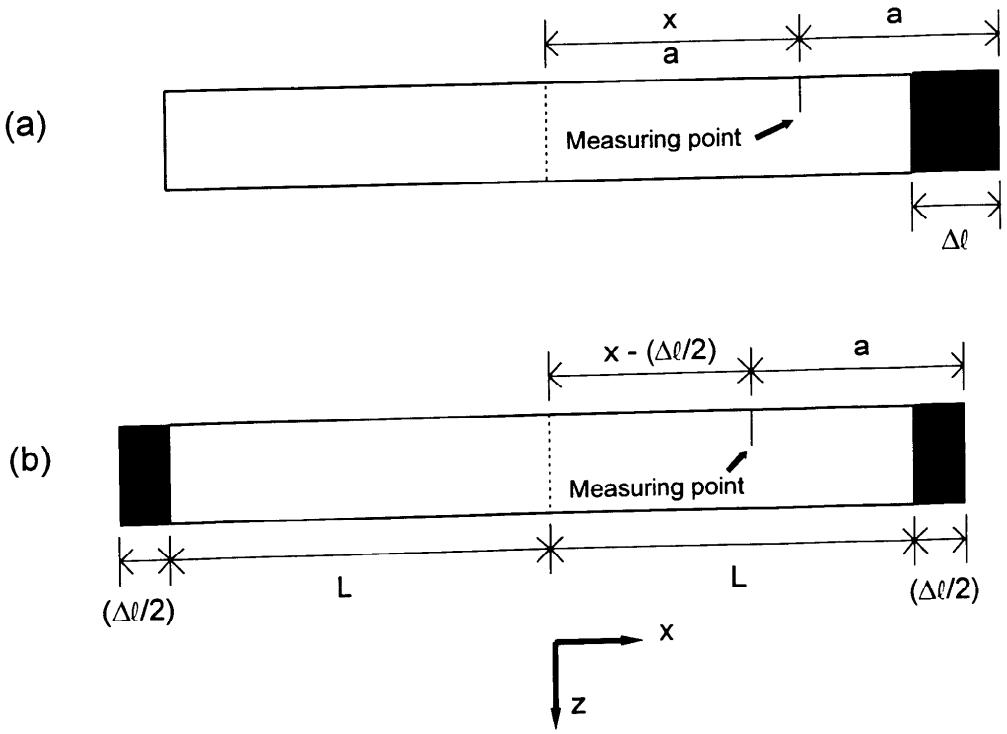

Figure 3.12. The equivalent stope principle.

3.6 Numerical modelling of incremental viscoelastic stope problems using the displacement discontinuity approach

The analytical solution in the previous section is only valid for an isolated panel. A displacement discontinuity approach to solve incremental viscoelastic problems is developed

in this section to simulate more complex geometries such as multi-reef or pillar scenarios. To simulate the time-dependent behaviour of rock, Crawford and Curran (1983) used an extended displacement discontinuity technique to solve problems in linear viscoelasticity. The advantage of the method is that the solution can be obtained explicitly as a function of time and hence a time stepping procedure becomes unnecessary. However, when modelling a mining excavation developed in several steps, the time when each of these increments was mined becomes important. Therefore a further extension of the technique is required. Such an extension is developed below using the superposition principle given in equation [3.58a]. As a first step, the mathematical relationships for one step problems are derived. This is done for the two element Kelvin model as analytical solutions for this model are readily available to test the accuracy of the numerical technique.

Single step problems

Consider a linear elastic problem and K displacement discontinuity elements used to solve this problem. The relationship between stresses and discontinuity displacements are given by

$$\{\sigma\} = [k]\{D\} \qquad [3.63]$$

where $\{D\} = \{D_N, D_S\}^T$ denotes the 2K displacement discontinuity components, $\{\sigma\} = \{\sigma_N, \sigma_S\}^T$ represents the stresses in the discontinuities and $[k]$ is the matrix of influence coefficients which depends on the geometry of the problem and the material properties.

When solving a two-dimensional problem using constant elements, matrix $[k]$ may be expressed as

$$[k] = \left(\frac{E}{4\pi(1-\nu^2)}\right)[k^*] \qquad [3.64]$$

where $[k^*]$ contains only geometric terms and the multiplier accounts for the material properties. (See Crouch and Starfield (1983) for the derivation of the geometric terms $[k^*]$.)

Solving equation [3.63] for $\{D\}$ and substituting $[k]$ using equation [3.64] gives

$$\{D\} = \left(\frac{4\pi(1-\nu^2)}{E}\right)\left[k^*\right]^{-1}\{\sigma\} \qquad [3.65]$$

When this equation is subjected to the correspondence principle, it follows that

$$\{\tilde{D}(s)\} = \left(\frac{4\pi(1-\tilde{\nu}^2)}{\tilde{E}}\right)\left[k^*\right]^{-1}\{\tilde{\sigma}(s)\} \qquad [3.66]$$

When solving the problem for constant applied stresses (therefore the creep problem), it follows that

$$\{\tilde{\sigma}(s)\} = \frac{\sigma}{s} \qquad [3.67]$$

When transforming equation [3.66] back to the time domain and making the assumption that the rock behaves elastically in dilatation and like a Kelvin model in distortion it follows that (see Appendix B1 for finding the inverse Laplace transform of this function)

$$\{D(t)\} = \left(4\pi g_2\left(1 + ce^{-\alpha_1 t} - (c_1+1)e^{-\alpha_2 t}\right)\right)\left[k^*\right]^{-1}\{\sigma\} \qquad [3.68]$$

where

$$g_2 = \frac{1-\nu^2}{E} \qquad [3.69]$$

$$\alpha_1 = \frac{E}{\eta(1+\nu)} \qquad [3.70]$$

$$\alpha_2 = \frac{3E}{\eta(1-2\nu)(1+\nu)} \qquad [3.71]$$

$$c_1 = -\frac{1}{2(1-\nu)} \qquad [3.72]$$

and η is the viscosity coefficient of the dashpot in the Kelvin model.

The displacements at a point in the field are related to the displacement discontinuity components by

$$\{u_f\} = [M]\{D\} \qquad [3.73]$$

where $[M]$ contains geometric and material property terms. (See Crouch and Starfield (1983) for the definition of $[M]$.) When inserting equation [3.65] it follows that

$$\{u_f\} = \left(\frac{4\pi(1-\nu^2)}{E}\right)[M]\left[k^*\right]^{-1}\{\sigma\} \qquad [3.74]$$

The time-dependent components in the field can therefore be found by applying the correspondence principle to equation [3.74] and taking the inverse Laplace transformation. Because $[M]$ also contains material parameters, finding the inverse Laplace transformation is reduced to finding the inverse Laplace transformation of the following expressions

$$L^{-1}\left[\frac{(1-2\tilde{\nu})(1+\tilde{\nu})}{\tilde{E}}\right], \quad L^{-1}\left[\frac{2(1-\tilde{\nu}^2)}{\tilde{E}}\right] \text{ and } \quad L^{-1}\left[\frac{1+\tilde{\nu}}{\tilde{E}}\right] \qquad [3.75]$$

The inverse transformation for the second expression has been given in equation [3.68]. Making the assumption that the rock behaves elastically in dilatation and like a Kelvin model in distortion, the other two expressions can be solved as

$$L^{-1}\left[\frac{(1-2\tilde{\nu})(1+\tilde{\nu})}{\tilde{E}}\right] = \frac{(1-2\nu)(1+\nu)}{E}\left[1-e^{-\frac{3Et}{\eta(1-2\nu)(1+\nu)}}\right] \qquad [3.76]$$

$$L^{-1}\left[\frac{(1+\tilde{\nu})}{\tilde{E}}\right]=\frac{(1+\nu)}{E}\left[1-e^{-\frac{Et}{\eta(1+\nu)}}\right] \qquad [3.77]$$

Multi-step problems

When applying this viscoelastic displacement discontinuity technique to mining problems, the analysis above assumes that the complete excavation is created at once. This is not the case in practice where excavations are usually developed in steps. The problem can however be solved by using the superposition concept, proposed by Salamon (1974) for the analytical solutions of incremental mining in viscoelastic ground and discussed in Section 3.4.

Postulate that the first increment is created at time τ_1, and that it is represented by K displacement discontinuity elements. To avoid confusion, the following notation will be introduced: The displacement discontinuity components will be represented by $D_i(t-\tau_i)$ with the subscript denoting the step number mined at time τ_i. For example $D_2(t-\tau_2)$ represents the displacement discontinuity components at time $t-\tau_2$ for the complete problem geometry after the elements of the second step have been added. The 2K time-dependent displacement discontinuity components $\{D_1(t-\tau_1)\}$ for the first increment can be obtained from equation [3.68] for any time $t>\tau_1$. However if the second step is developed at time τ_2 (L elements added), the method of superposition must be applied to give the time-dependent displacement discontinuity components at time $t>\tau_2$ as

$$\{D(t)\}=\{D_1(t-\tau_1)\}-\{D_1(t-\tau_2)\}+\{D_2(t-\tau_2)\} \qquad [3.78]$$

After the second increment, the total number of elements is (K+L). Note that $\{D_2(t-\tau_2)\}$ contains 2(K+L) components whereas $\{D_1(t-\tau_1)\}$ and $\{D_1(t-\tau_2)\}$ contain only 2K components. When doing the summation, the extra 2L components for the second increment is zero for $\{D_1(t-\tau_1)\}$ and $\{D_1(t-\tau_2)\}$. This

follows as the displacement discontinuity components for any element which does not yet exist must be zero.

For n number of steps

$$\{D(t)\} = \sum_{i=1}^{n-1}\left[\{D_i(t-\tau_i)\} - \{D_i(t-\tau_{i+1})\}\right] + \{D_n(t-\tau_n)\} \qquad [3.79]$$

which is valid for time $t > \tau_n$.

Equation [3.79] implies that to obtain a numerical solution for a viscoelastic problem consisting of n increments at time $t > \tau_n$, (2n-1) displacement discontinuity solutions need to be calculated. For two-dimensional constant displacement discontinuity elements, this can be reduced to finding just n solutions. This is possible as the material properties can be separated from the kernel table as a multiplier (see equations [3.64] and [3.68]). From equation [3.68]

$$\frac{\{D(t)\}}{\left(4\pi g\left(1 + ce^{-\alpha_1 t} - (c+1)e^{-\alpha_2 t}\right)\right)} = \{D_{ml}\} = \left[k^*\right]^{-1}\{\sigma\} \qquad [3.80]$$

Therefore only one $\{D_{ml}\}$ needs to be solved for every step and multiplied by the correct time-dependent multiplier to obtain $D_i(t-\tau_i)$ and $D_i(t-\tau_{i+1})$ for the particular step. This is however not possible for three dimensional displacement discontinuity kernels and (2n-1) DD solutions will have to be calculated. The individual solutions need not be stored as the summation can be done in a temporary array as soon as each solution is calculated. A flow chart for the solution of incremental viscoelastic problems using displacement discontinuities is given in Figure 3.13.

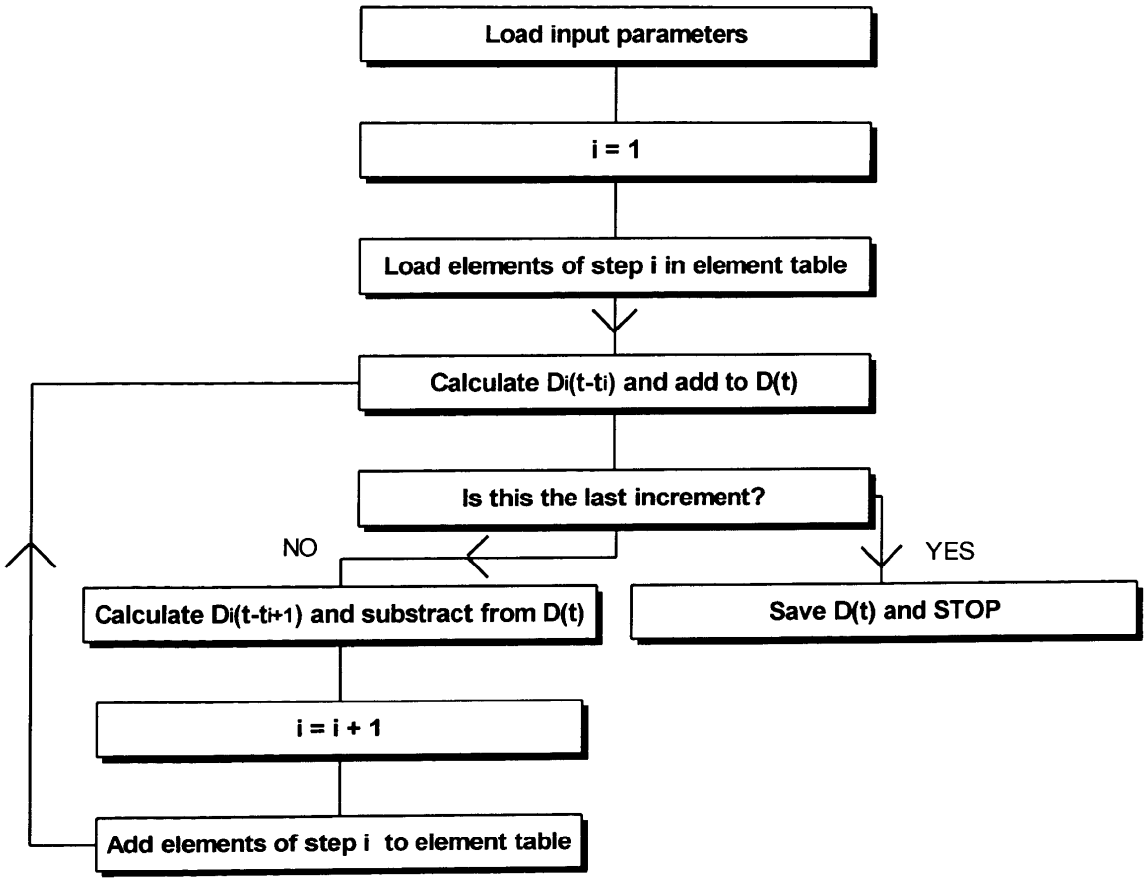

Figure 3.13. A flow chart for the calculation of the displacement discontinuity components for incremental viscoelastic problems.

The same principle applies when calculating displacements at a field point. A procedure similar to Figure 3.13 can therefore be used. As the creep and not the relaxation problem is solved, the stress is not a function of time. The stress will change in step-like fashion between mining increments. The preceding concepts have been incorporated in a computer code given in Appendix D1. The following examples are presented to compare the accuracy of the numerical technique with analytical solutions. Although the first problem is not mining related, an analytical solution for this problem is available and it is therefore useful to verify the accuracy of the numerical code for one step problems.

Example 1 : Thick-walled tube

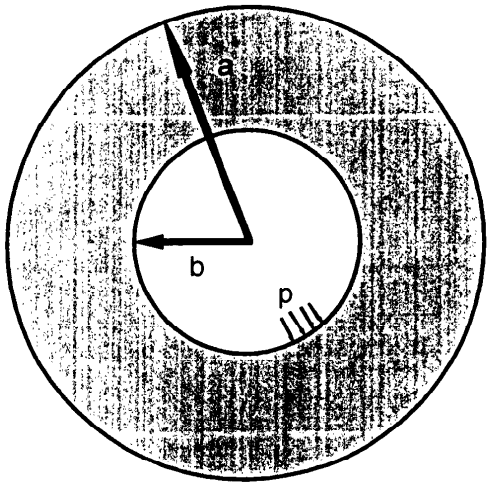

Figure 3.14. Thick-walled tube.

Flügge (1975) derived the viscoelastic displacement solution for a thick-walled tube (Figure 3.14) if an internal pressure p is applied. If the tube material is elastic in dilatation and shows viscoelastic Kelvin behaviour in distortion, the radial displacement u is given by

$$u(r,t)=\frac{pb^2}{a^2-b^2}\left\{\frac{3r}{6K+2G}\left[1-e^{-\frac{6K+2G}{\eta}t}\right]+\frac{a^2}{2Gr}\left[1-e^{-\frac{2G}{\eta}t}\right]\right\} \qquad [3.81]$$

where G is the shear modulus, K is the bulk modulus, η is the viscosity coefficient and r is the radial position with $b \leq r \leq a$.

This problem was solved using the numerical technique (constant strength displacement discontinuity elements) with a 64 element approximation for the inner boundary and a 128 element approximation for the outer boundary using quarter symmetry. Other values used were E = 1 GPa, ν = 0.2, η = 5 GPa.s, p = 100 MPa, a = 1 m, b = 0.5 m. The radial displacement was calculated along the x-axis midpoint between the two boundaries. The analytical and numerical solutions as a function of time are given in Figure 3.15. A good approximation of the solution can be obtained with the numerical method.

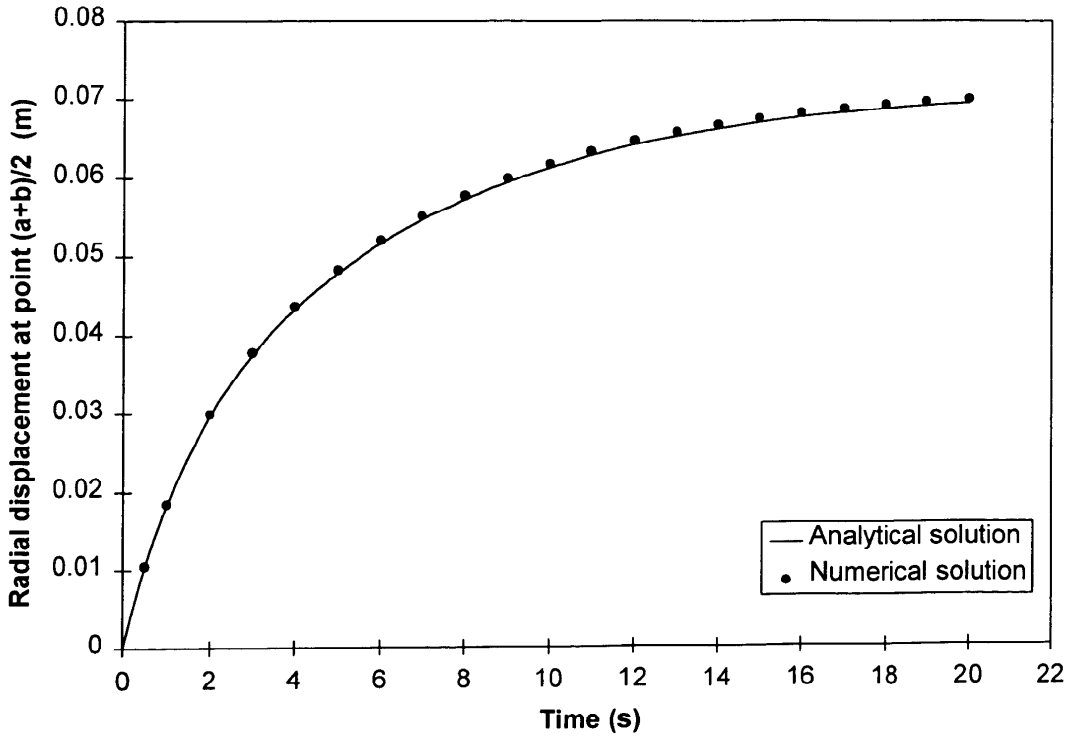

Figure 3.15. Radial displacement for a pressurised thick-walled tube at point (a+b)/2.

Example 2 : Incremental enlargement of a two-dimensional stope

The convergence in a two-dimensional horizontal stope where the stope is incrementally enlarged (Figure 3.16) will be solved using the numerical technique. The surrounding material is assumed to behave elastically in dilatation and like a viscoelastic Kelvin model in distortion. It is postulated that increment 1 is a stope of 10 m created at time τ_1 = 0 hours. This is followed by two increments at time τ_2 = 24 hours and time τ_3 = 48 hours when the length of the stope is both times increased by 1 m on both sides. Other values used are Young's modulus = 70 GPa, Poisson's Ratio = 0.2, viscosity coefficient = 500 GPa.h and the vertical stress = 60 MPa. The convergence is calculated 0.125 m from the centre of the stope.

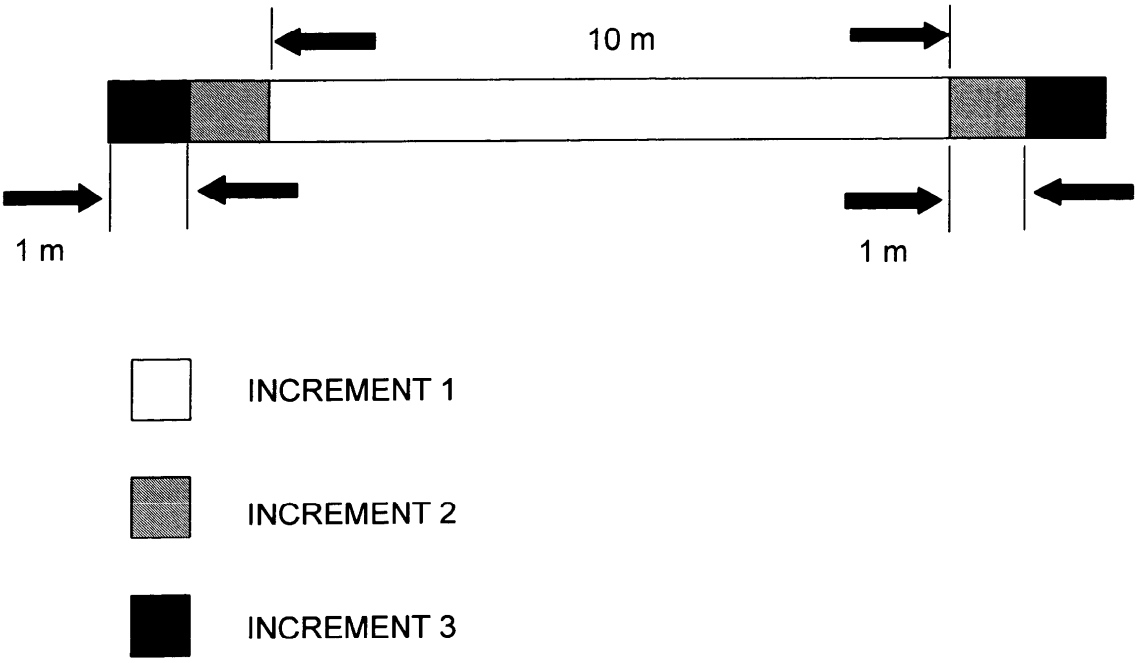

Figure 3.16. Incremental enlargement of a two-dimensional stope.

The analytical convergence solution for this problem is obtained from equation [3.58b] for n = 3 and Appendix B1 where

$$S_z(x,t-\tau_i) = -4W_z\sqrt{\ell_i{}^2 - x^2}\; g_2\left[1 + c_1 e^{-\alpha_1(t-\tau_i)} - (c_1+1)e^{-\alpha_2(t-\tau_i)}\right] \qquad [3.82]$$

with

$$g_2 = \frac{3K + 2q_0}{q_0(6K + q_0)} \qquad [3.83]$$

$$\alpha_1 = \frac{q_0}{q_1} \qquad [3.84]$$

$$\alpha_2 = \frac{6K + q_0}{q_1} \qquad [3.85]$$

$$c_1 = -\frac{6K + q_0}{6K + 4q_0} \qquad [3.86]$$

S_z = viscoelastic convergence

W_z = vertical stress (compressive stress is negative)

ℓ = half span of the stope

x = distance from the centre of the stope (origin of co-ordinate system)

K = bulk modulus

q_0 = 2G where G is the shear modulus

q_1 = viscosity coefficient of the viscous element

The numerical problem was solved using a 40 element approximation for increment 1. This was extended by 4 elements on each side for both increments 2 and 3. The input file for this problem is given in Appendix D2. Figure 3.17 illustrates both the analytical and numerical solutions for convergence at a distance of 0.125 m from the centre of the slit. It is clear that the numerical solution is a good approximation. It, however, slightly overestimates relative to the analytical solution as constant displacement discontinuity elements are used (see Ryder and Napier, 1985).

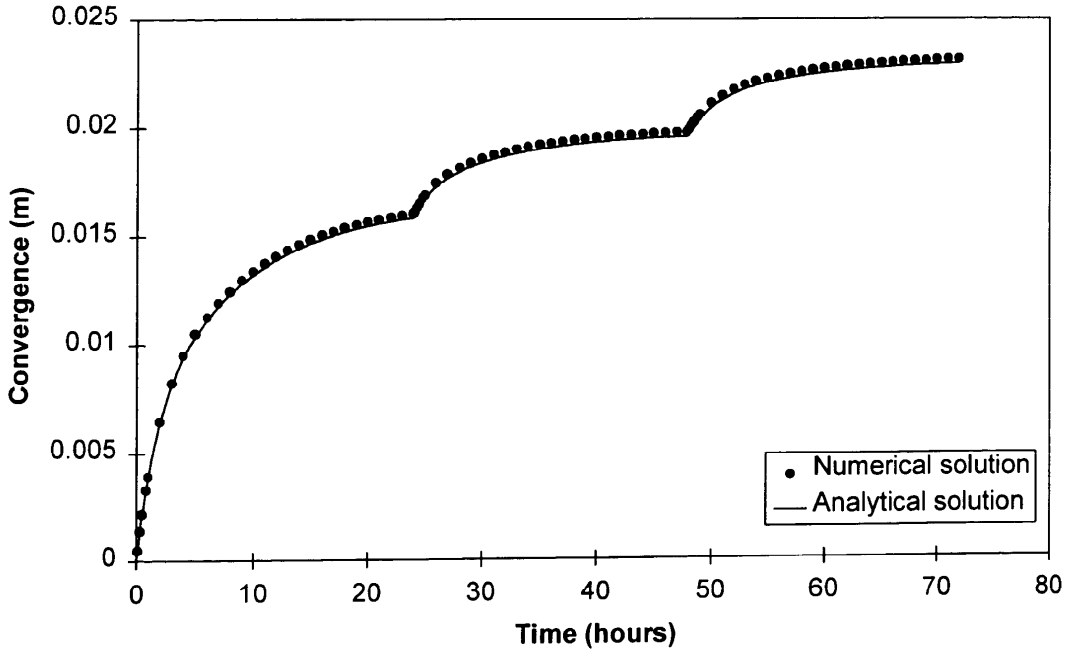

Figure 3.17. Numerical and analytical solution of the convergence at a distance of 0.125 m from the centre of the stope for the problem illustrated in Figure 3.16.

As the creep and not the relaxation problem is solved, the stress in the surrounding material is expected to remain constant between successive increments. The elastic solution for the vertical stress ahead of the stope is given by Salamon (1968) as

$$\sigma_z = \frac{qx}{\sqrt{x^2 - \ell^2}} \qquad [3.87]$$

where q = virgin vertical stress, x = position along x-axis and ℓ = half span of the stope. The stress is not a function of the material parameters and therefore not a function of time in the viscoelastic domain. Figure 3.18 illustrates the magnitude of vertical stress 6 m ahead of the original face position (increment 1) as a function of time. Both the analytical and numerical solutions vary in step-like fashion after each increment.

The displacements in the surrounding rock calculated by the numerical technique vary as a function of time as illustrated in Figure 3.19. This figure gives the numerical solution of displacements 6 m and 10 m above the centre of the slit. Note that the numerical technique was derived using the Kelvin model and therefore there is no instantaneous response after any of the mining increments.

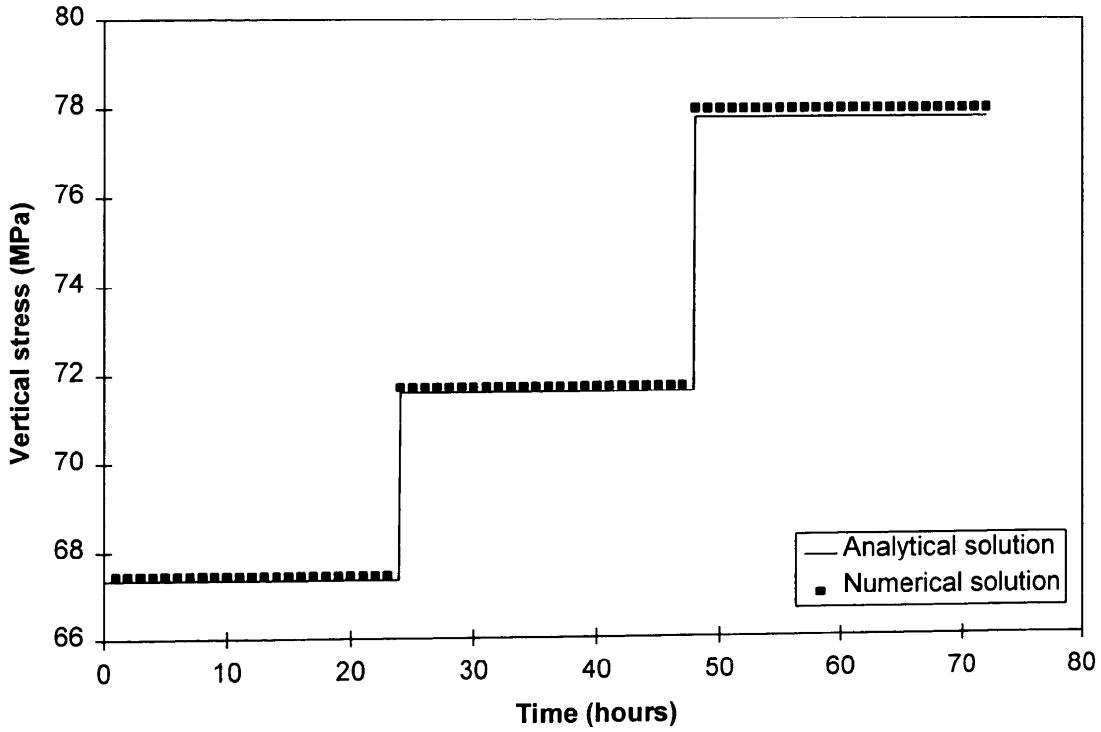

Figure 3.18. Vertical stress 6 m ahead of original stope face.

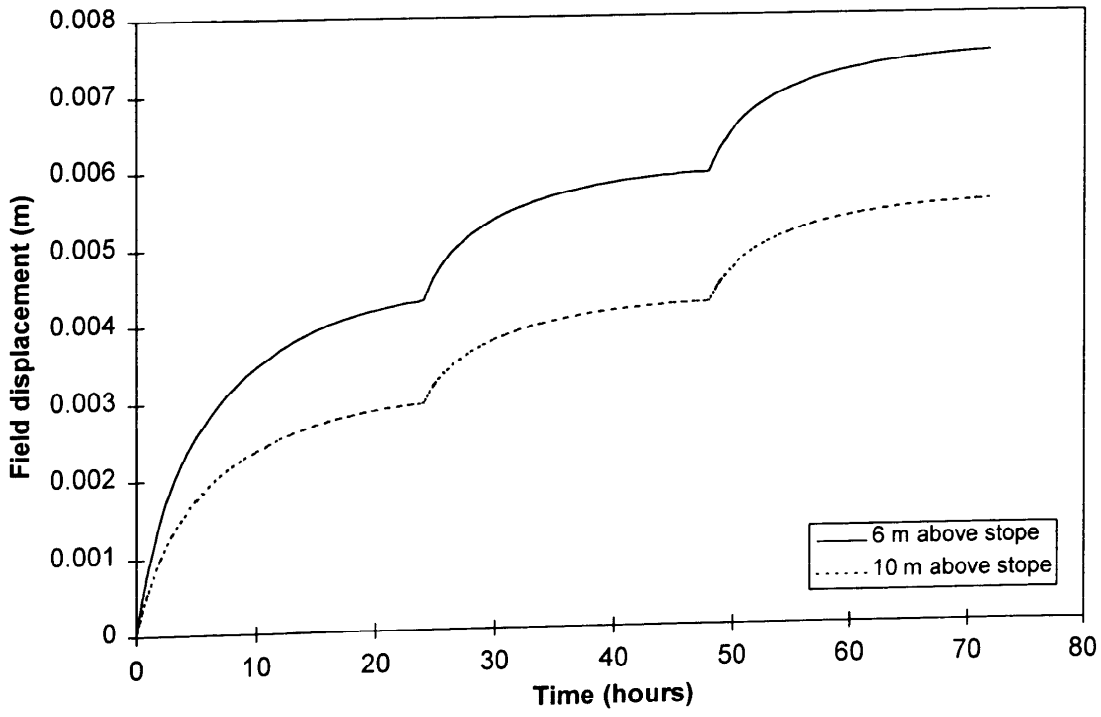

Figure 3.19. Displacements in the material above the stope.

The example above illustrates that the displacement discontinuity technique can be extended to solve incremental problems in viscoelasticity. The solutions can be obtained explicitly as a function of time and therefore there is no need for a time stepping procedure. The method however requires that (2n-1) solutions (or n solutions for two-dimensional displacement discontinuities) be calculated for a viscoelastic problem consisting of n increments. If the number of increments and elements becomes very large, the method can become time consuming.

Although this technique was illustrated using the Kelvin model, it can be easily modified for a Burgers assumption. Further work is also required to investigate how the non-linear effects of contact between the hangingwall and footwall can be incorporated. More important, however, is to test whether the viscoelastic assumption is an adequate representation of the time-dependent behaviour observed underground. This is explored in the next chapter.

Chapter 4

Time-dependent closure measurements

4.1 Introduction and previous work

Analysis of the rock mass at depth requires some knowledge about the response of the rock to enlargement of the excavations. Limited techniques are available to characterise the *in situ* behaviour of the rock. Seismic data has been used extensively in an attempt to characterise the rock in the deep gold mines in South Africa (Legge and Spottiswoode, 1987; Mendecki, 1997). Another potential source of valuable data is the closure behaviour of excavations. Continuous time-dependent closure data is a good reflection of the localised rock response and can provide important information which may be more difficult or even impossible to obtain with other methods. Unfortunately this source of data has been largely neglected in the South African industry since the early seventies. Apart from the reasons mentioned in Chapter 1, the lack of appropriate time-dependent models to analyse this data has contributed to the problem. Although a large number of closure measurements have been recorded (Wiggill, 1965; Gürtunca et al., 1989; King et al. 1989; Güler, 1997), these measurements usually consisted of measurements with a 24 hour interval or longer between successive data points. Data collected by Walsh et al. (1977) at West Driefontein Mine had an interval of a week between measurements. All these measurements will be collectively termed *long period* measurements. Figure 4.1 illustrates typical closure versus time curves obtained from long period measurements. This is for closure stations at a fixed location in a panel and, with time, the face moves away from the measurement point due to regular blasting. The results plotted in Figure 4.1 can be misleading as the curves are not only indicative of the true time-dependent behaviour of the rock but the complex result of a) enlargement of the excavation, b) the face moving away from the measurement position and c) the true time-dependent behaviour of the rock.

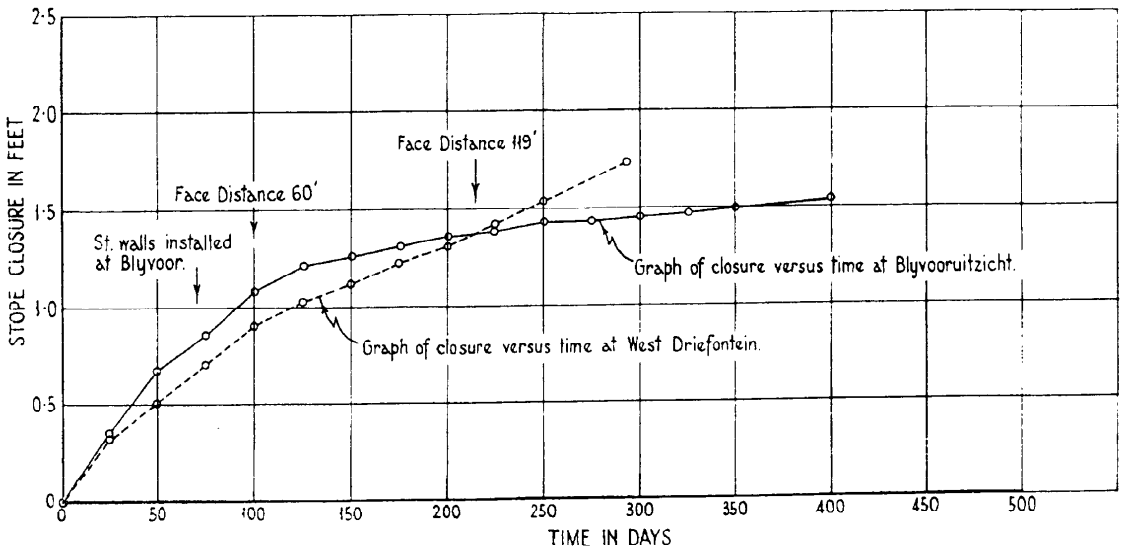

Figure 4.1. Typical closure curves obtained from long period measurements (after Wiggill, 1965).

As will be shown in this chapter, much of the useful information, especially after blasting, is lost with these long period measurements. In spite of this limitation, significant time-dependent rock behaviour was noted by several researchers. King et al. (1989) measured closure behaviour in two adjacent panels at Hartebeestfontein Mine. After blasting activity had stopped in one of the panels, the closure rate in this panel continued at a constant rate of 6 mm/day for 37 days. Only after this period did the rate gradually start to decrease. Mining however continued in the second panel (and probably in other nearby panels) and it is unclear what the effect of these geometrical changes was on the first panel. After mining stopped in the second panel, the closure rate in this panel persisted for thirteen days and then gradually declined. Closure data collected by Gürtunca (1989) in the Klerksdorp area to quantify the effect of backfill also exhibited significant time-dependent effects. Daily closure rates varied from panel to panel and were in some instances as high as 30 mm/day. The study showed that closure rates are significantly lower in backfilled panels than in partially filled panels.

As mentioned above, the true time-dependent behaviour of the rock mass is difficult to identify from long period measurements as the data also reflects the effect of changes in the mining geometry. This problem can be overcome by taking closure measurements with instruments that record in a continuous fashion. From this the time-dependent closure behaviour between successive blasts (when there is no change in mining geometry) can be

identified. The following observations and analyses of continuous closure measurements are described in the literature.

Leeman (1958) used closure recorders to measure time-dependent closure profiles in a tabular stope at East Rand Proprietary Mines (E.R.P.M.). The nature of the recorders was such that they recorded the deformation of the rock strictly on the surface of the excavation and not some distance inside the fracture zone. He observed profiles similar to Figure 4.2 where the rate of closure suddenly increases just after blasting time. This high rate of closure decreases within hours to give a gradual steady-state closure until the next blast occurs and the pattern is repeated. On Sundays no blasting took place and, as expected, no incremental jump is visible in the data. The rate of gradual steady-state closure was usually also a minimum on Sundays. He concluded that the effect of blasting is to accelerate the gradual closure in a stope. Unfortunately, Leeman did not give any explanation for the observed closure profiles and he did not attempt to simulate this using either analytical or empirical approaches. He did note that the amount of closure caused by blasting diminishes with distance from the working face. The rate of closure also varied greatly from one point to the next and was affected by the position of the measuring point in relation to the support in the stope. He found no conclusive evidence that the rate of closure either increases or decreases just before a rockburst, but emphasized that further measurements were necessary to verify this.

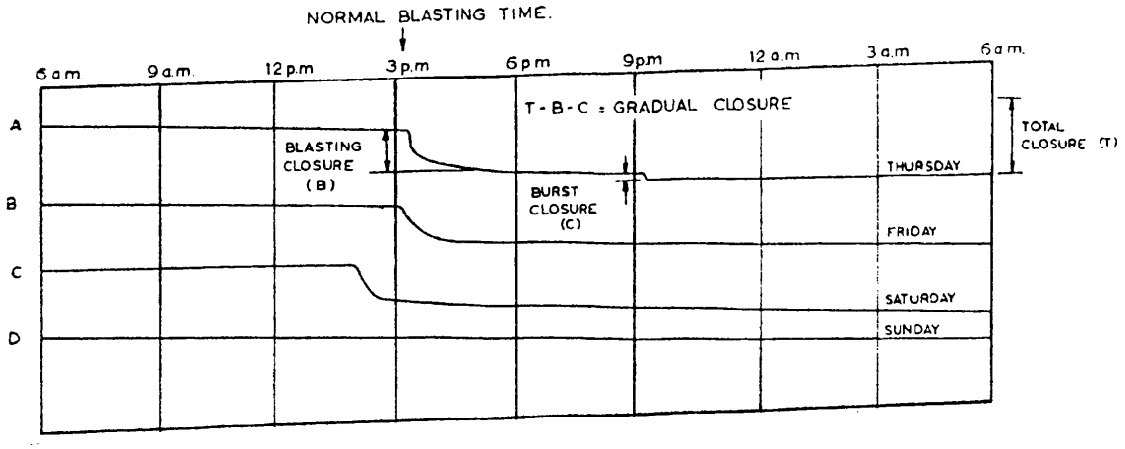

Figure 4.2. Typical time-dependent closure profiles measured at East Rand Proprietary Mines (after Leeman, 1958). Note that the closure is increasing downwards on the vertical axis.

Hodgson (1967) also measured time-dependent closure at E.R.P.M. His experimental technique differed slightly from that of Leeman (1958) as his convergence meters were anchored 15 m into the hangingwall and footwall. He stated that over a long period of time, convergence measured by these anchored instruments corresponded to the elastic displacements resulting from changes in geometry. A more detailed examination of the manner in which the convergence takes place indicated however that the closure is in fact time-dependent. He explained the gradual steady-state closure as being caused by the time-dependent migration of the fracture zone ahead of the face resulting in the effective stope span becoming bigger. Hodgson predicted that if the face advanced faster than the migration of the fracture zone, less energy would be released in a stable manner thereby increasing the incidence of rockbursts. This is in agreement with the statistical analysis of Cook et al. (1966) which indicated an increase in rockbursts for a face advance rate of more than 4 m a month, for small abutments, to 8 m a month, for large abutments.

The first quantitative attempt to analyse time-dependent closure profiles of tabular stopes was made by McGarr (1971) using data from E.R.P.M. He used an empirical approach to represent the closure δ as

$$\delta = \frac{B}{C} \sum_{n=0,n\neq 7m}^{\infty} \left(1 - e^{-DC(t-24n)}\right) H(t-24n) \qquad [4.1]$$

where B, C and D are positive constants, n and m are integers and H is the Heaviside unit function (H(t) = 1 for $t \geq 0$ and 0 for $t < 0$). The unit of time t in the equation is hours. At the time of this study no blasting on Sundays was allowed and n = 7m corresponds to those days. Obtaining the rate of closure from equation [4.1] by differentiating gives

$$\dot{\delta} = DB \sum_{n=0,n\neq 7m}^{\infty} e^{-DC(t-24n)} H(t-24n) \qquad [4.2]$$

After the last blasting period of the week on Saturday, the closure and the rate of closure become

$$\delta = a\left(1 - e^{-\frac{t}{\tau}}\right) \qquad [4.3]$$

and

$$\dot{\delta} = be^{-\frac{t}{\tau}} \qquad [4.4]$$

respectively where a and b are constants and $\tau = 1/DC$. McGarr (1971) suggested that the relaxation time τ may be used as a parameter to describe the ability of the rock mass to form a fracture zone in response to the face advance. High values of τ might be associated with mines that are prone to rockbursts.

As these earlier results focused entirely on measurements at E.R.P.M., several experimental sites were established in other mines for this study. This was necessary to address the following questions.

a) How does the time-dependent closure behaviour vary for different spatial positions in the stope?

b) Does the time-dependent closure vary significantly in different geotechnical areas?

c) Is there a link between the time-dependent closure behaviour and seismicity?

d) Can the time-dependent closure be simulated using a viscoelastic approach?

4.2 Experimental equipment and methodology

The time-dependent closure data was collected using clockwork closure meters designed for the CSIR. Although an old mechanical design, it was still useful as a research tool as it was inexpensive, easy to install and intrinsically safe for use in mines. The mechanism of this instrument is illustrated in Figure 4.3.

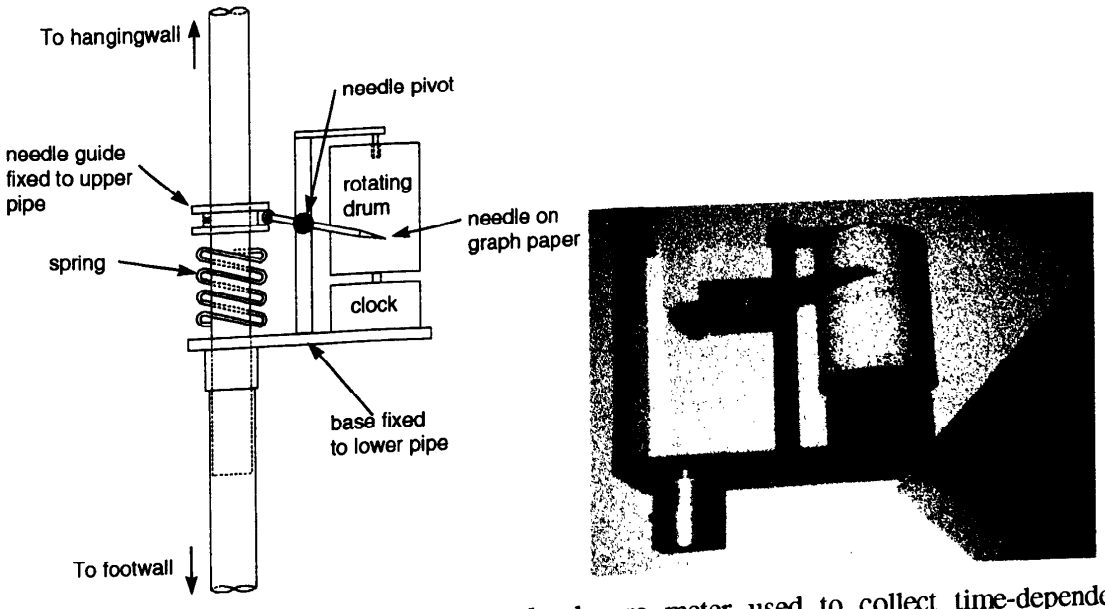

Figure 4.3. Mechanism of the clockwork closure meter used to collect time-dependent closure data.

It consists of two pipes, one which slides inside the other against the pressure of a spring. The base of the instrument is fixed to the lower pipe with the needle being moved by a guide fixed to the upper pipe. The instrument is installed with the needle point close to the bottom of the graph paper on the drum. Stope closure moves the upper pipe further into the lower with the needle point moving upwards on the paper. The clock gives one rotation every seven days resulting in a continuous record of the closure over this period. The needle arm is designed with various possible pivot points to allow for different amplification factors of the closure magnitude. Unfortunately this design is inherently flawed as instantaneous closure is recorded as an arc, thereby distorting the time axis (see Appendix E). The data needs to be corrected before use and the approach developed by the author for these instruments is given in Appendix E. An example of the raw data recorded on the graph paper is given in Figure 4.4. Figure 4.5 illustrates the same data after it was digitised and corrected according to the developed procedure. Note that no attempt was made to smooth any of the closure data in this chapter, although large digitisation intervals will have some smoothing effect. The typical digitisation interval used is illustrated in Figure 4.5.

When installing the instruments underground, it is important that the two pipes make contact with solid rock in the hangingwall and footwall. The top pipe was secured to the hangingwall using quick-setting putty. When installed close to the face, the instrument should be protected from blast damage. This was done by installing the meter behind one of the timber support packs. Figure 4.6 illustrates a typical installation underground.

In dipping stopes the instruments were installed normal to the plane of the reef to measure the closure component (see Figure 4.7). As defined in Chapter 1, *closure* refers to the relative hangingwall and footwall movement normal to the plane of the reef while *ride* is the component parallel to the reef plane. It should be noted that with time, a significant ride component will tilt the instrument resulting in a composite measurement. In the instrumented panels the ride component was small (less than 3 mm day in the panels at Western Deep Levels Mine; Toper, 1997) and this effect was ignored.

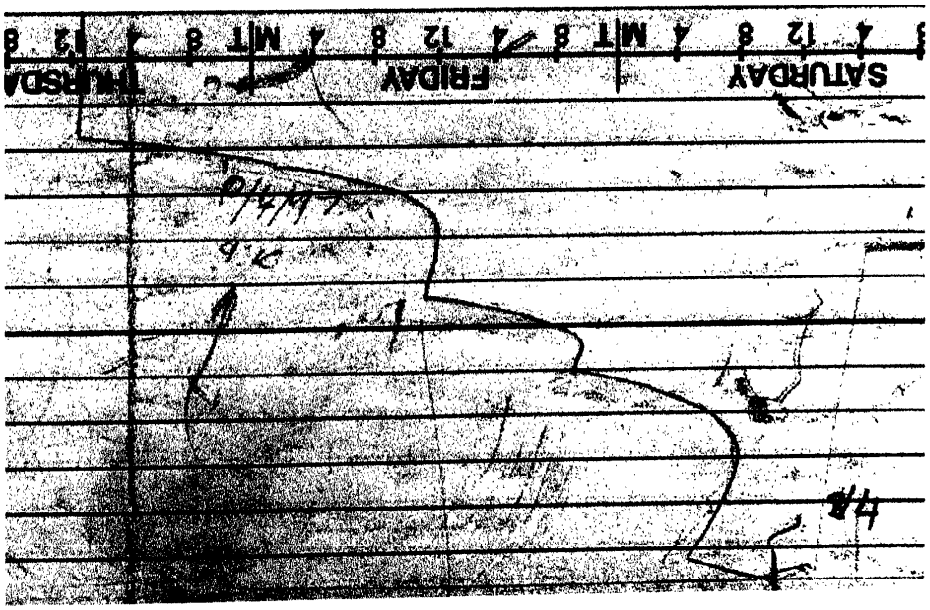

Figure 4.4. An example of continuous closure data recorded using the clockwork closure meter (see comments in the text above regarding the corrections needed). This figure only shows a small section of the graph paper sheet and is not printed to scale. (The horizontal grid lines are separated by a vertical distance of 5 mm.) Note that the horizontal axis represents time, which increases to the left. (The days printed on the paper indicate an increase of time to the right, but this is incorrect as the paper was mounted upside down on the drum.) The vertical axis represents closure magnitude which increases upwards. The pivoting needle arm resulted in the actual closure magnitude being multiplied by a factor of 1.86 on the graph paper.

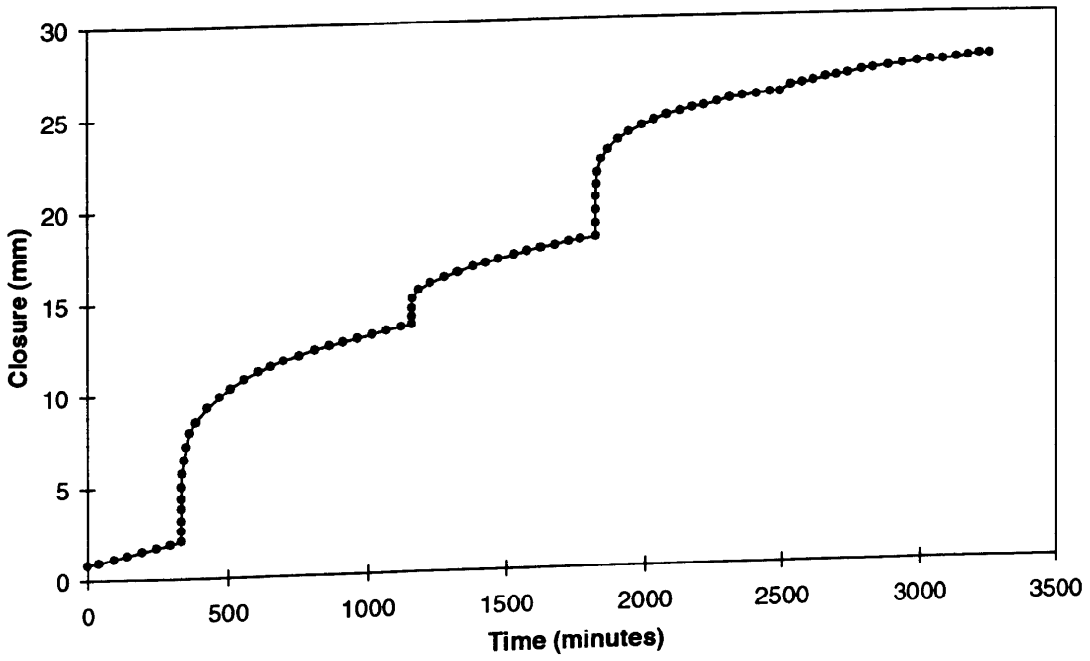

Figure 4.5. The corrected closure data for the measurements depicted in Figure 4.4. The data points give an indication of the digitisation interval used.

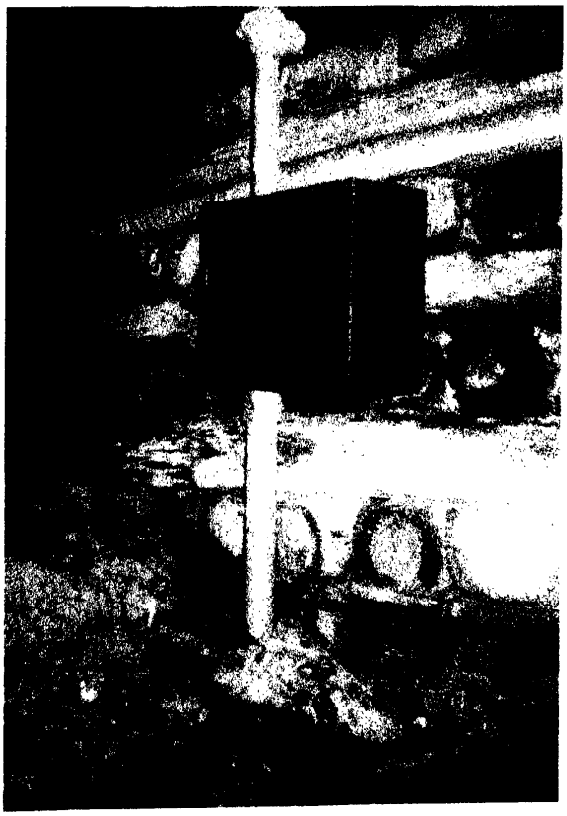

Figure 4.6. Installation of the clockwork closure meter in a stope. During installation it is important that all rubble is cleared from the footwall to ensure that the lower pipe makes contact with solid rock. The loose material in the photograph accumulated after installation.

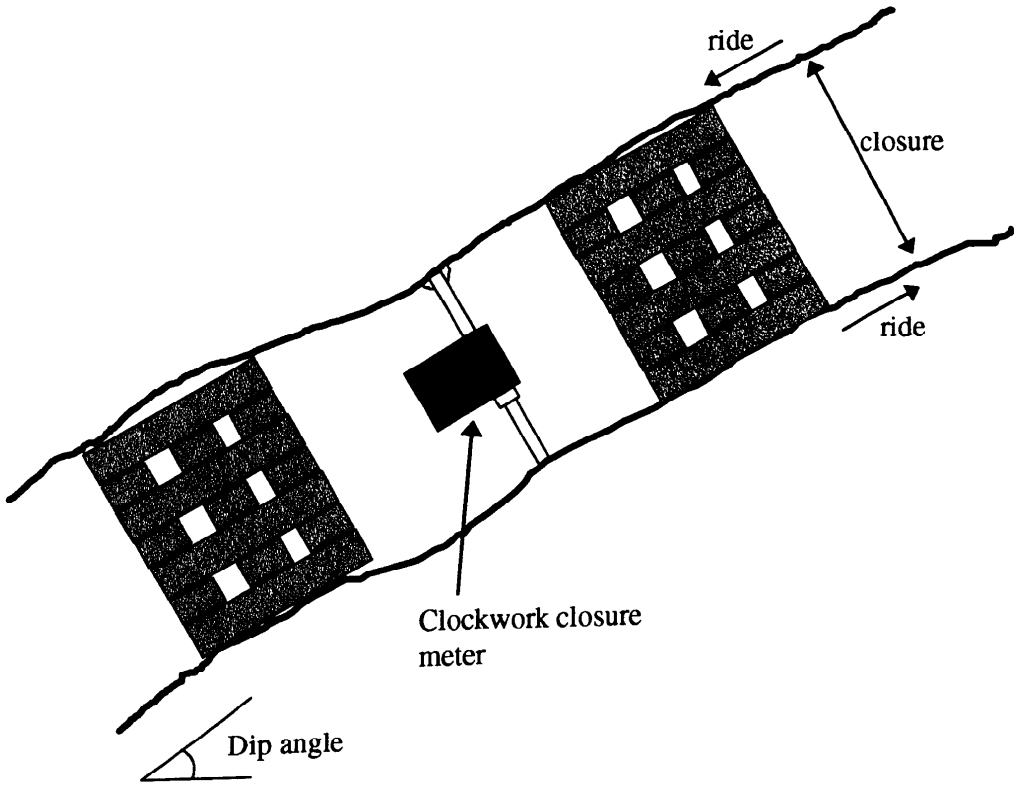

Figure 4.7. Installation of the clockwork closure meter normal to the plane of the excavation.

Unfortunately the mechanical clocks in the closure meters were unreliable. The extremely harsh conditions (heat, humidity, fine dust) resulted in frequent stoppages. For the five instruments installed in the up-dip Ventersdorp Contact Reef panel for a period of 45 days, there were only 16 days when all five instruments where in simultaneous operation. It is also very time consuming to digitise the data. It is suggested that as these measurements become more routine in future, alternative instrumentation should be developed.

4.3 Experimental results - Ventersdorp Contact Reef

Experimental sites were established in two panels in the South Shaft of Western Deep Levels Mine in the Carletonville area. In both panels the reef type mined was Ventersdorp Contact Reef (see Section 1.3) with the hangingwall consisting of the hard Alberton lava and the footwall of quartzite. In some areas of the mine the lava can be very hard with uniaxial compressive strength values of more than 400 MPa (Table 2.1, Chapter 2). In the section of the mine where the experimental sites were located, electrical detonators are used for blasting. These detonators are activated from a centralised control station which records the exact blasting time. This data proved invaluable for the analysis of the closure data. Seismic data for this area was obtained from the mine's seismic network. The general mining layout in this area is given in Figure 4.8.

Site 1: Updip panel - Ventersdorp Contact Reef

The instrumentation was installed in the W3 panel of the 87-49 longwall. An enlarged view of this panel is given in Figure 4.9. This includes the face positions during the period of the experiment. The dip of the reef is 22° and the depth below surface is approximately 2570 m. Timber packs are used as permanent support in this panel.

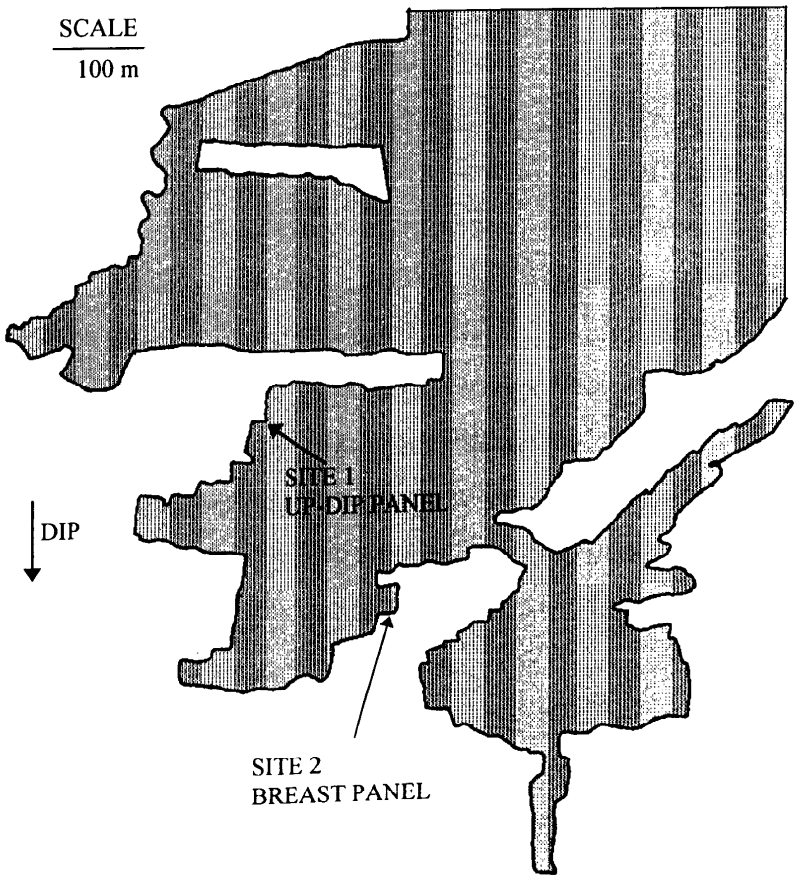

Figure 4.8. Plan view of the mining geometry in the area where the closure data was collected at Western Deep Levels Mine.

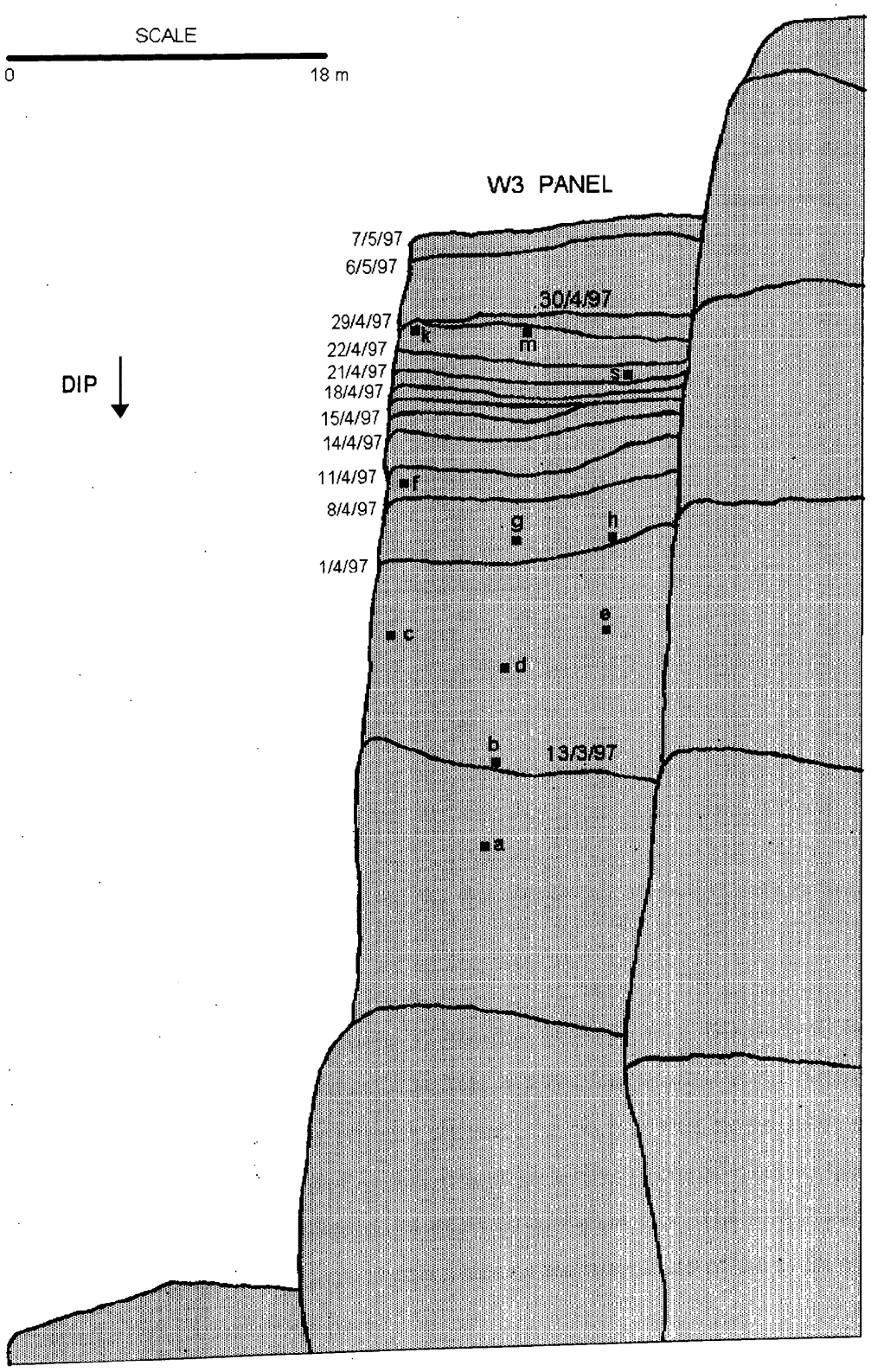

Figure 4.9. Enlarged plan view of the W3 up-dip panel in the 87-49 longwall with the positions of the closure meters indicated. As the distance to face became excessive, some meters were moved forward. The period of installation at each position was a: 3/4/97-14/4/97, b: 2/4/97-5/5/97, c: 3/4/97-14/4/97, d: 2/4/97-15/5/97, e: 2/4/97-14/4/97, f: 15/4/97-5/5/97, g: 15/4/97-15/5/97, h: 15/4/97-5/5/97, k: 6/5/97-14/5/97, m: 6/5/97-15/5/97, s: 5/5/97-14/5/97.

Five clockwork closure meters were installed in this panel at any one time, with their positions illustrated in Figure 4.9. A simplification of these positions is depicted in Figure 4.10. to denote the numbering convention. Initial installation of the row parallel to the face (no. 1, 2 and 3) was done as close as possible to the face (±6 m). As the distance to the face for this row became excessive with time (> 14 m), the instruments were moved forward.

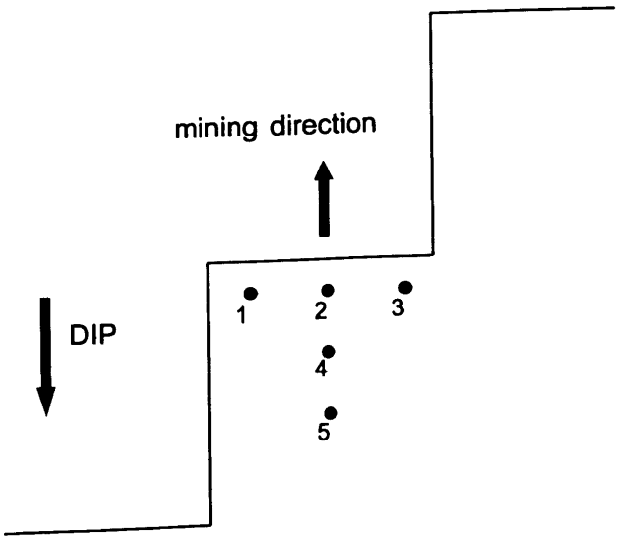

Figure 4.10. Numbering convention used for the clockwork closure meters in the up-dip panel.

Typical recorded time-dependent closure is illustrated in Figure 4.11. Similarly to the work discussed in the introduction (Section 4.1), there is a sudden increase in the closure after the blast. This will be called the primary closure. This is followed by the more gradual steady-state closure rate. Of interest is that if seismic events occurred close to the panel, similar closure behaviour was observed as depicted in Figure 4.11. The magnitude of the primary closure after a seismic event is dependent on the magnitude of the event and how close its source was located to the panel.

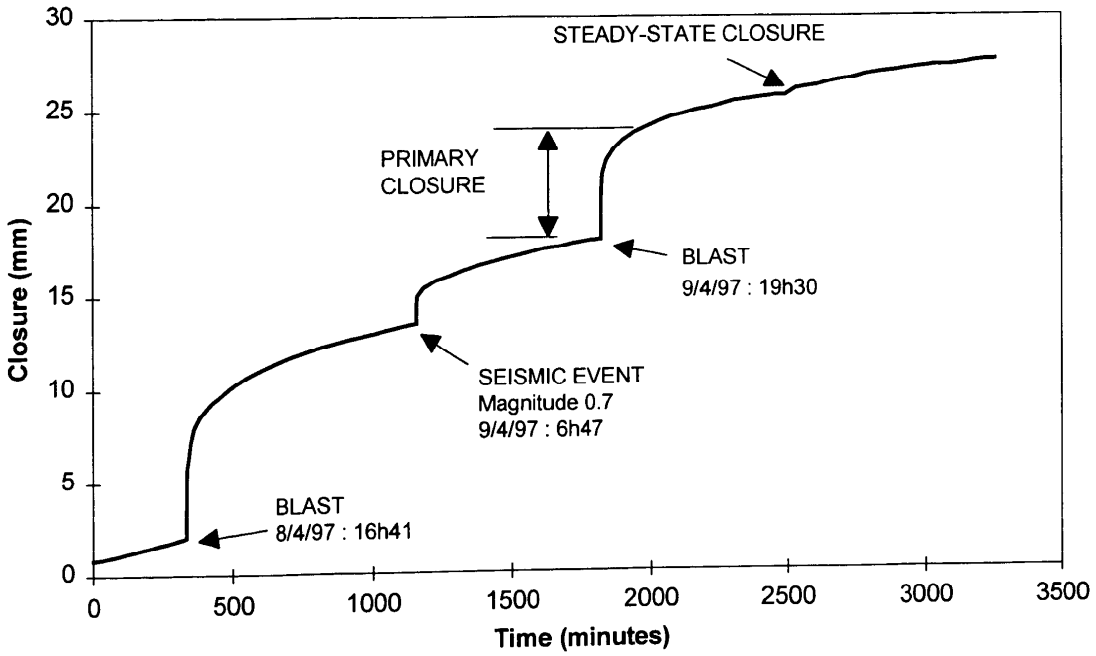

Figure 4.11. Typical time-dependent stope closure for the Ventersdorp Contact Reef at Western Deep Levels Mine. This was for closure station no. 3 at a distance of 8.7 m from the face before the blast on 8/4/97.

After any particular blast, the increase in closure is a function of the distance to face and length of face advance. Figure 4.12 illustrates the incremental closure for stations no. 2, 4 and 5 after the blast on 15/4/97. The primary closure is large close to the face, but smaller as the distance to the face increases. The rate of steady-state closure also decreases into the back area. Figure 4.13 compares the behaviour after the same blast for the row of stations parallel to the face (no. 1, 2 and 3). Although the steady-state closure rate is essentially similar for these three stations, the magnitude of primary closure increases from the tight (no. 1) to the loose ends (no. 3) of the panel. As it is difficult to determine the onset of the steady-state closure phase, the closure rates given in Figures 4.12 to 4.15 were calculated for a period from 800 minutes after the blast to the end of the data set.

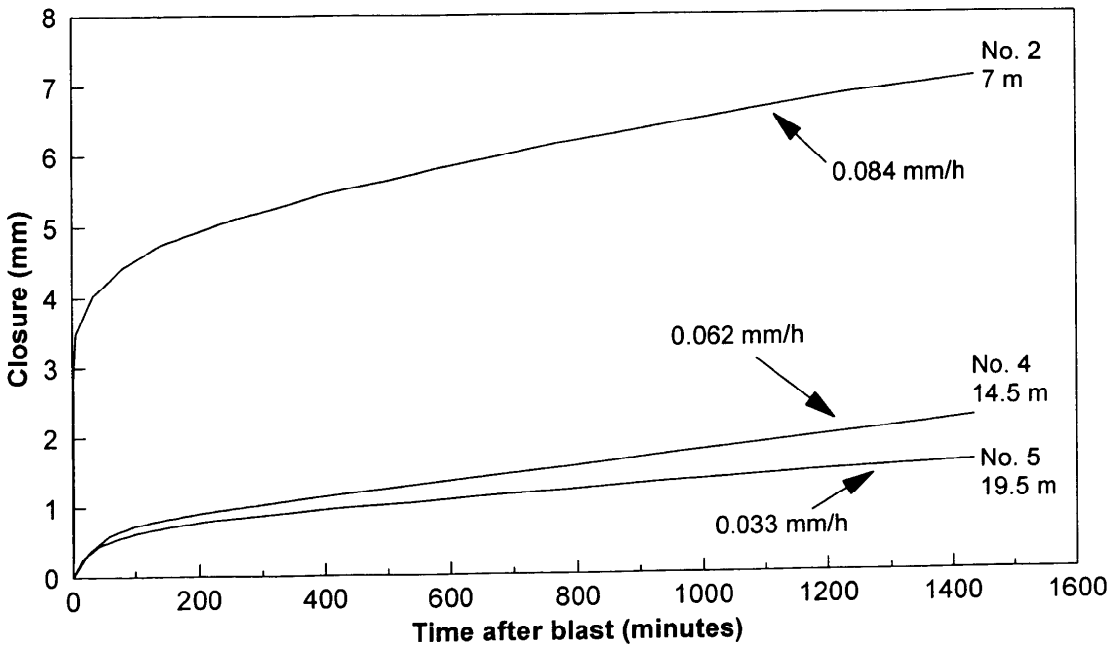

Figure 4.12. Closure as a function of time for different positions in the panel following the blast on 15/4/97. The distances given in the graph are the distances from the measuring instruments to the face before the blast.

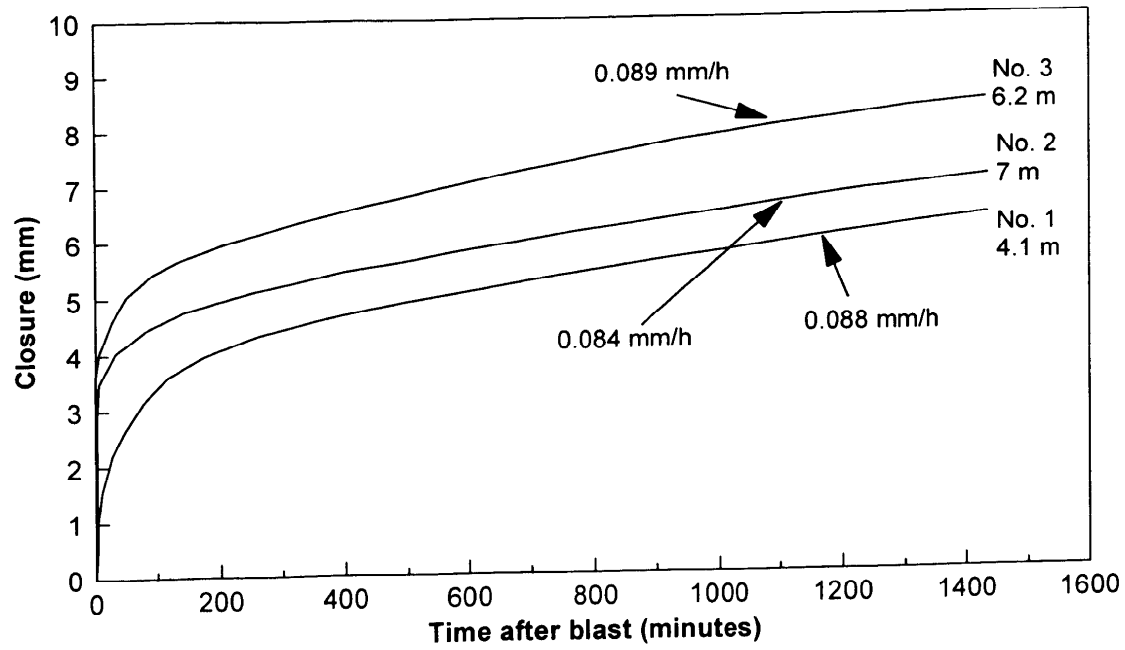

Figure 4.13. Closure as a function of time for different positions parallel to the face following the blast on 15/4/97. No.1 was installed in the tight end and no. 3 on the loose end of the panel.

To further illustrate the dependence of closure behaviour on spatial position, the incremental closure recorded after the blast on 16/4/97 is given in Figures 4.14 and 4.15. The blast was preceded by 15 minutes by a seismic event of magnitude 1.2. This event may have been triggered by blasting in another longwall and was located approximately 110 m away from the panel face. Again it is noted that the magnitude of primary closure and steady-state closure rate decreases into the back area (Figure 4.14). The effect of the seismic event in addition to the blast increases the magnitude of the primary response recorded for some stations (for example compare no. 4 in Figures 4.12 and 4.14 and no. 1 in Figures 4.13 and 4.15). The steady-state closure rate for stations close to the face (except no. 1) also seems to be slightly increased (Figure 4.15) when compared with Figure 4.13.

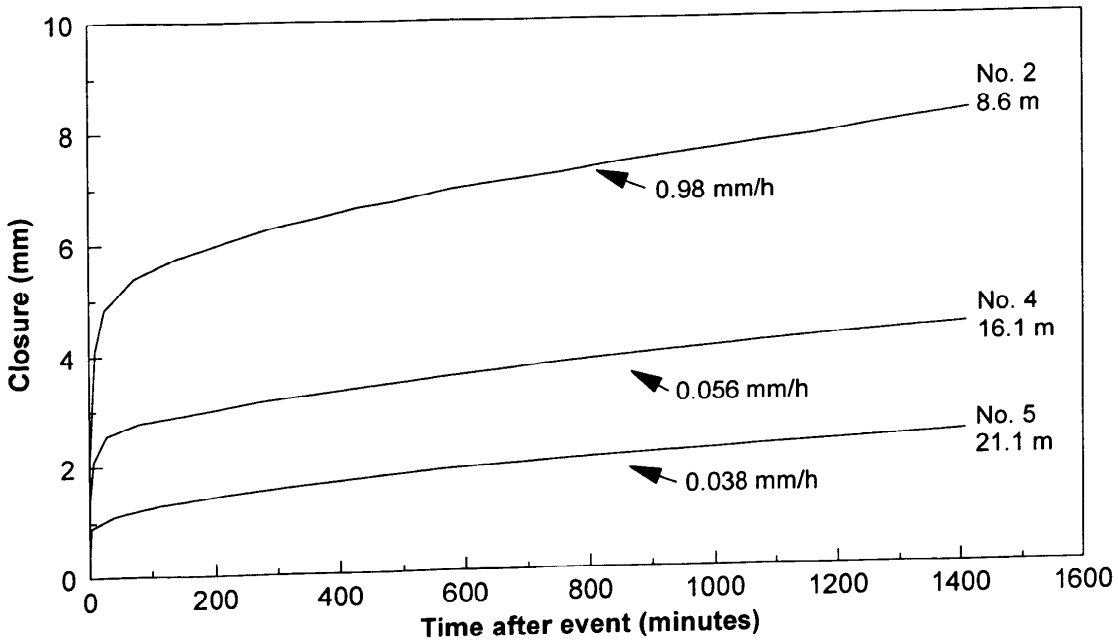

Figure 4.14. Closure as a function of time for different positions from the face following a seismic event of magnitude 1.2 (followed 15 minutes later by the blast) on 16/4/97.

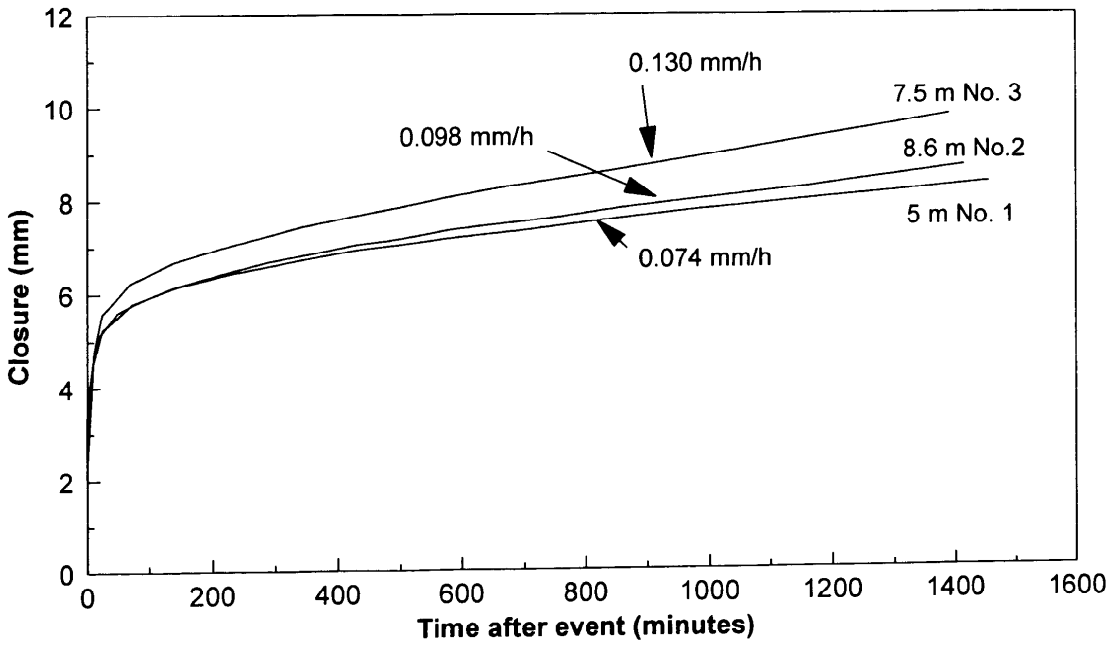

Figure 4.15. Closure as a function of time for different positions parallel to the face following a seismic event of magnitude 1.2 (and the blast 15 minutes later) on 16/4/97. The distances given in the graph are the distances to the face before the blast.

Of interest is the decay of the steady-state closure rate if all mining activity stops. Over the long weekend from Friday 25/4/97 to Monday 28/4/97, no mining took place. Although there was a slight decrease in steady-state closure rate, measurements taken over this weekend indicated that a significant rate of closure can persist for many days (Figure 4.16). This behaviour was explored further at the second experimental site.

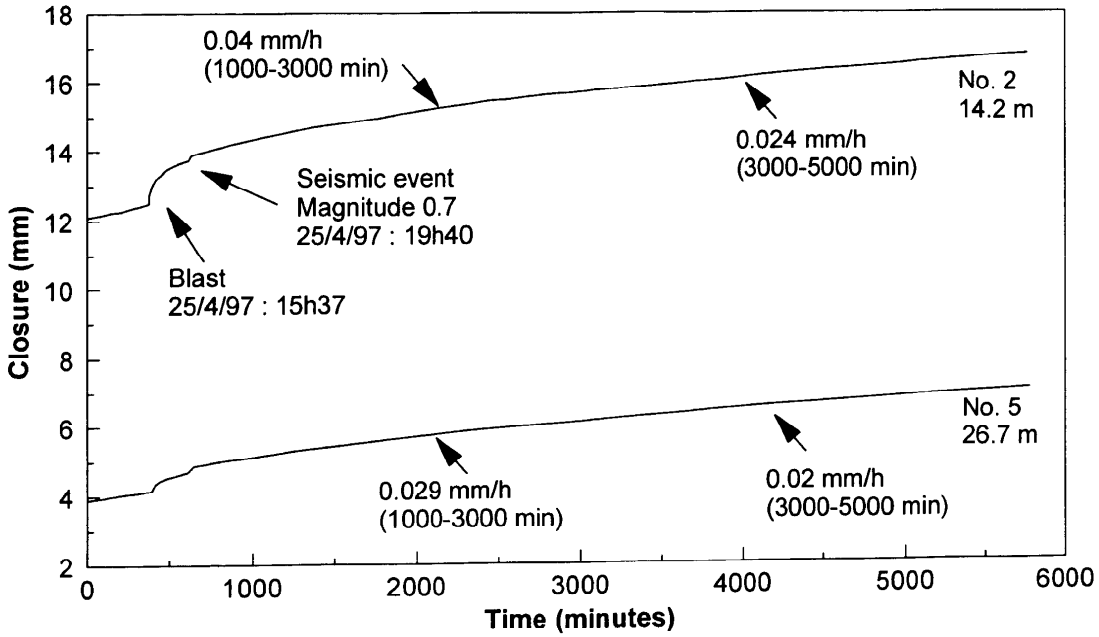

Figure 4.16. Closure measured when there was no mining activity for a period of 4 days from 25/4/97 to 29/4/97. The time periods in brackets indicate the intervals used to calculate the closure rates.

Effect of seismic events on the closure behaviour

As mentioned above, the effect of seismic events on the closure behaviour is similar to that of blasting, namely a primary closure response followed by steady-state closure (Figure 4.11). For some of the larger events, the closure meters recorded an instantaneous response significantly larger than that caused by blasting operations (Figure 4.17). Note that the large dynamic overshoot is a response of the equipment and not true rock movement. As the bottom pipe was not secured to the footwall, it could be thrown upwards and lose contact with the rock under dynamic conditions. This would result in a recorded overshoot which is larger than the actual rock response. This was confirmed by testing the instrument in the laboratory under dynamic conditions. If the bottom pipe is accelerated to a velocity of 1.5 m/s with the top pipe held stationary, an overshoot of 7 mm is recorded when the driving force is suddenly removed. A further example of this behaviour can be seen in Figure 4.26 in Section 4.6. The overshoot behaviour was however not recorded for all seismic events as seen in Figure 4.11.

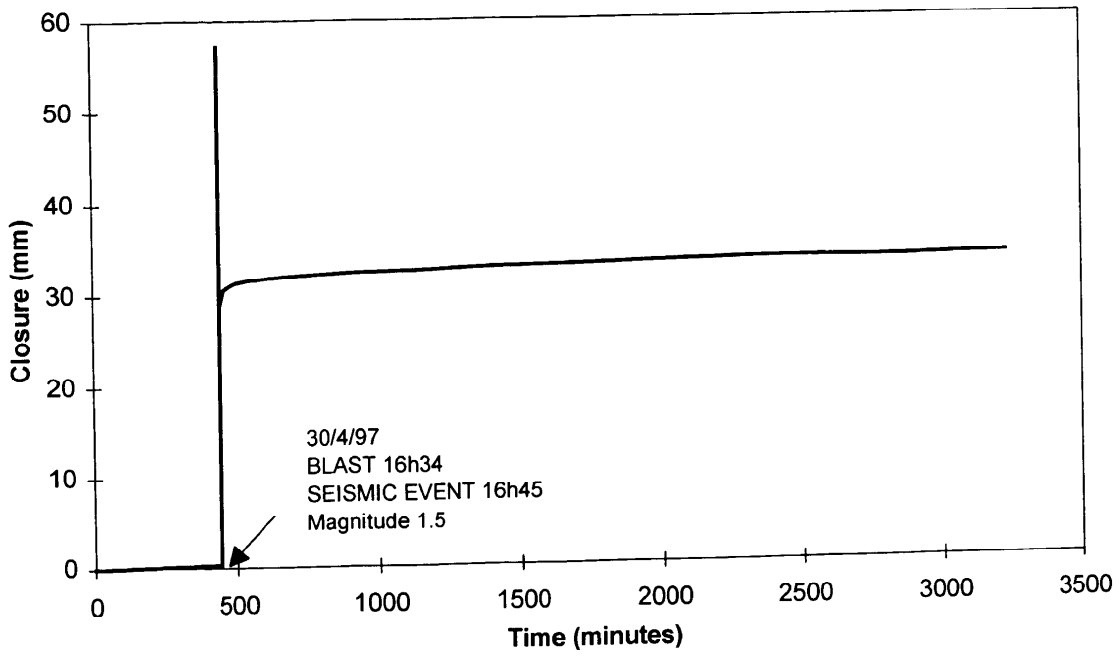

Figure 4.17. Closure behaviour including the typical overshoot recorded for some seismic events. This was measured by instrument no. 1 which was 10.9 m from the face. The seismic event occurred approximately 60 m in front of the longwall in the solid rock.

Site 2: Breast panel - Ventersdorp Contact Reef

To obtain a better understanding of the time-dependent closure behaviour if mining activity stops for an extended period of time, an isolated breast panel was instrumented (see Figure 4.8). The mining depth was approximately 2670 m below surface. This panel was approaching a dyke and therefore mining was planned to stop when the face was within a certain distance of this dyke. The geometry of the panel and the location of the meters are illustrated in Figure 4.18. Instruments no. 1 and 2 were moved forward to the new positions on the 10/6/97 and 11/6/97 respectively. No mining was taking place in the adjacent panels. The last blast in this panel occurred on 13/6/97.

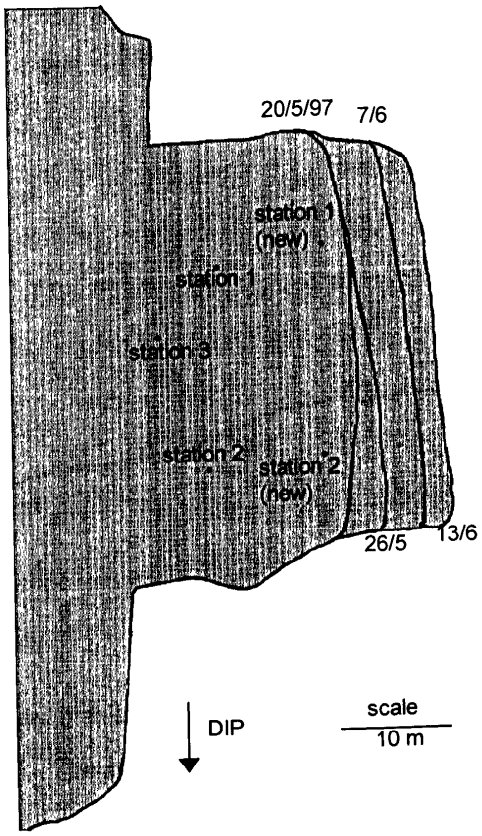

Figure 4.18. Installation of the closure meters in the breast panel.

Closure recorded by instrument no. 3 is shown in Figure 4.19. After the last blast on 13/6/97, the closure rate remained approximately constant for another 7 days and then gradually decreased to a level below the sensitivity of the instrument. The station closer to the face recorded a higher rate of closure for a much longer period as illustrated in Figure 4.20. Note that Figure 4.19 and 4.20 should not be directly compared as the time periods of the two graphs are different. This was unfortunately due to equipment failures and overlapping data for the different positions is not available. The experiment was stopped on 30/6/97 owing to conditions becoming too dangerous to enter the panel. At this time (17 days after the last blast in the panel), instrument no. 1 still recorded a steady-state closure rate of approximately 0.009 mm/h (216 μm/day). This value for hard rock is appreciable as it is for example more than the 130μm/day measured for the time-dependent movement of salt in the New Brunswick Mine in Canada at a depth of 850 m (Euverte et al., 1994).

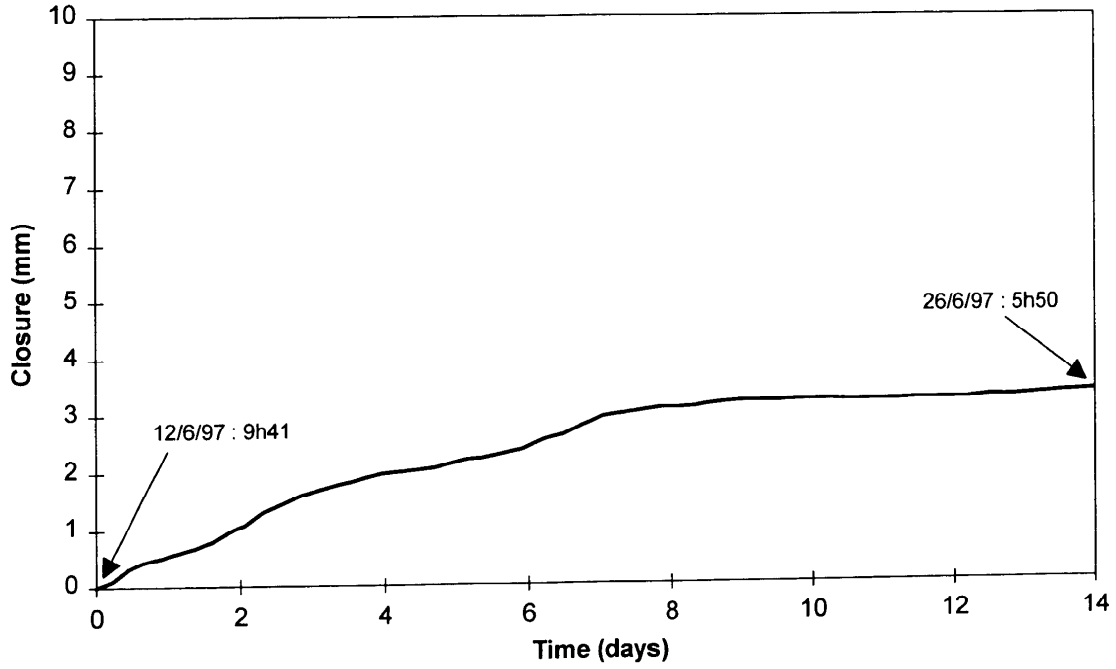

Figure 4.19. Closure as a function of time for closure station no. 3. The last mining activity in the panel was on 13/6/97. The instrument was 26 m from the face on this date.

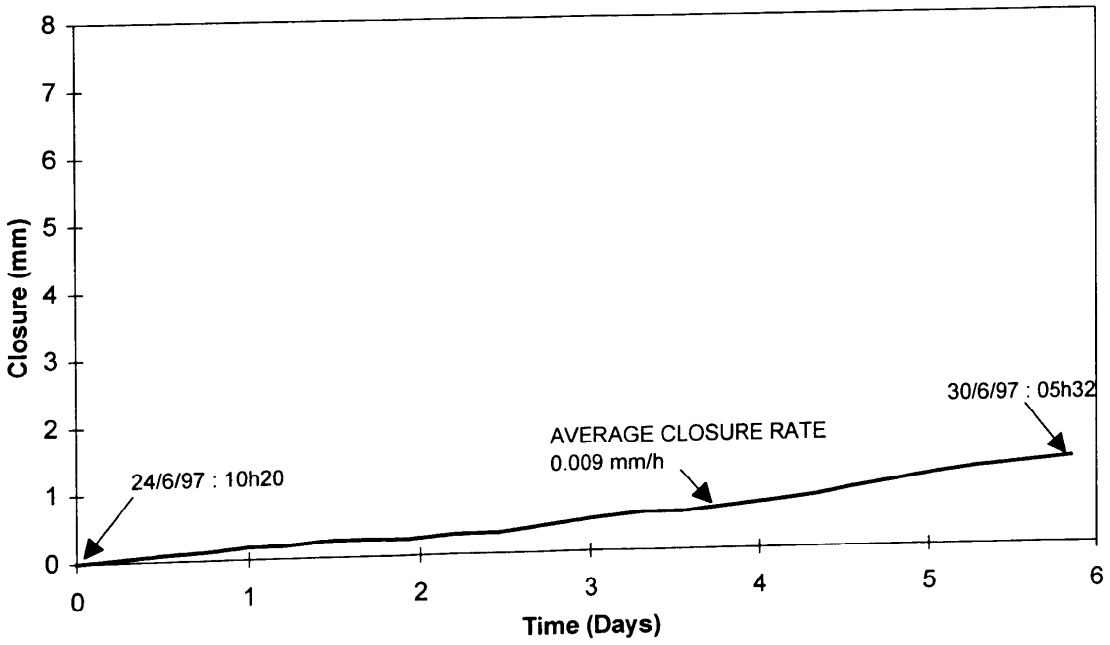

Figure 4.20. Closure as a function of time for closure station no. 1. The distance to face was 8.3 m. Note that the time period covered by this graph is different to that of Figure 4.19 and they should not be directly compared. The closure rate given is an average for the period from 24/6/97 to 30/6/97.

4.4 Experimental results - Vaal Reef

To contrast the relatively low closure rates of the Ventersdorp Contact Reef with areas experiencing significant closure, data was collected from the No. 6 shaft pillar area at Hartebeestfontein Mine. The Vaal Reef is mined in this area with both the hangingwall and footwall consisting of argillaceous quartzites (see Section 1.3). A schematic diagram of the shaft pillar area is given in Figure 4.21. This area is known to have some of the highest closure rates in the industry. The squeezing conditions described in Section 1.2 are encountered in this area. Of significance are the well-defined bedding planes in the quartzite. The nature of infilling of these discontinuities makes conditions less favourable for stable mining excavations. The overall competency of the rock mass and its ability to provide stable mining excavations for prolonged periods appears to be less favourable than the rock types encountered in Ventersdorp Contact Reef mining operations. The quartzites of the Ventersdorp Contact Reef appear to be less bedded and substantially more siliceous than those present at Hartebeestfontein Mine. As a result of this greater strength, the rock in other mines would appear to be more susceptible to strain bursting under high stress conditions.

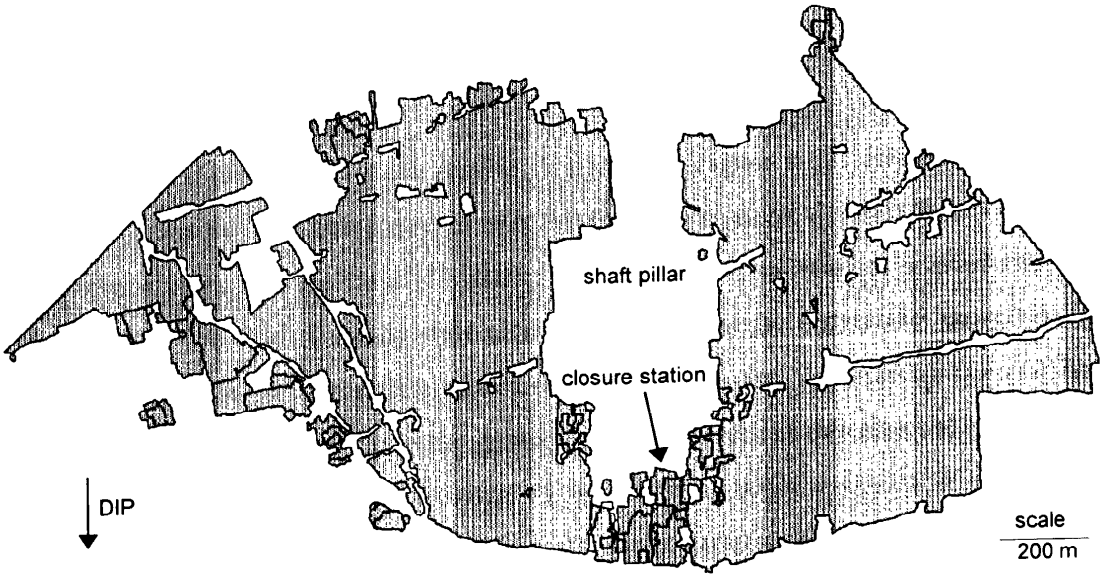

Figure 4.21. Plan view of the mining geometry at No. 6 shaft pillar area, Hartebeestfontein Mine where the closure data was collected.

Stoping operations at Hartebeestfontein Mine are unique in the South African gold mining industry as back area caving is used. Only the face area of the panels is supported with the

back area allowed to cave through natural processes or blasting. It should however be noted that for the panel in which the closure data was collected, caving was not allowed with timber packs used as permanent support units. A single closure meter was installed in the position illustrated in Figure 4.22. The dip in this area was 7° and the depth approximately 2350 m.

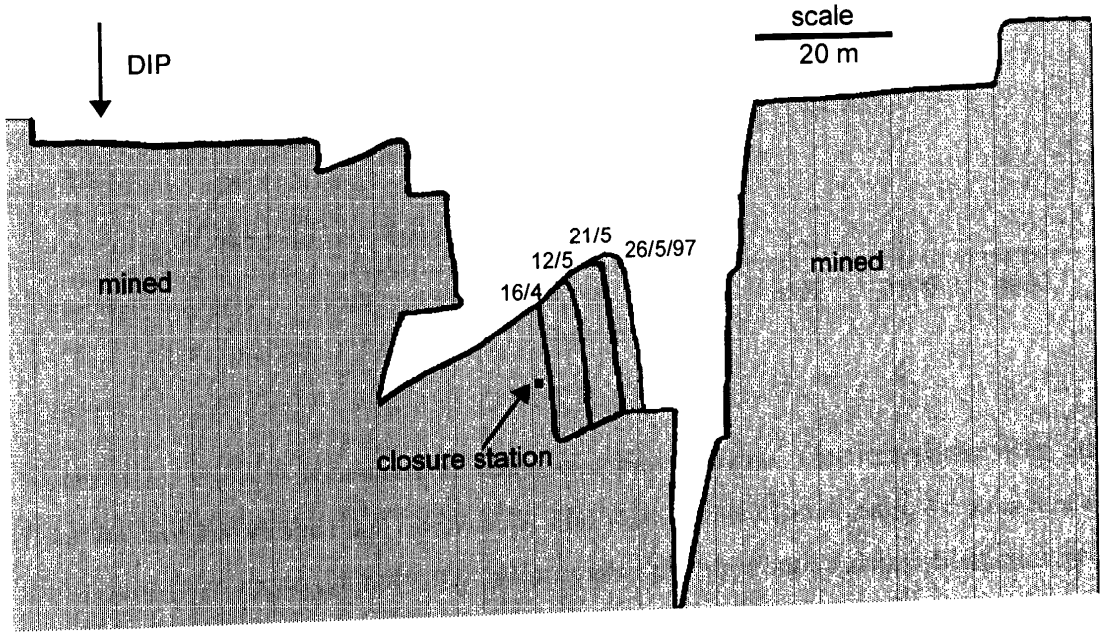

Figure 4.22. Location of the clockwork closure instrument in the 78N23 longwall.

A typical time-dependent closure profile is given in Figure 4.23. Evident is the high steady-state closure rate compared to that of the Ventersdorp Contact Reef, while the instantaneous closure at the time of blasting is small. A second data set is given in Figure 4.24. Note that the rate of steady-state closure increased as the instrument moved further away from the face. This is unlike measurements taken in the Ventersdorp Contact Reef stopes. A significant difference in the geotechnical properties of this area compared to the Ventersdorp Contact Reef is the presence of well-defined bedding planes. It appears that slip and dilation of these bedding planes is an important mechanism controlling the closure behaviour. This, coupled with the rapid deterioration of the hangingwall due to time-dependent fracture processes, may explain the increase in steady-state closure rates for larger distances from the face. Control of the hangingwall strata is difficult in these areas and risks of falls of ground are pronounced.

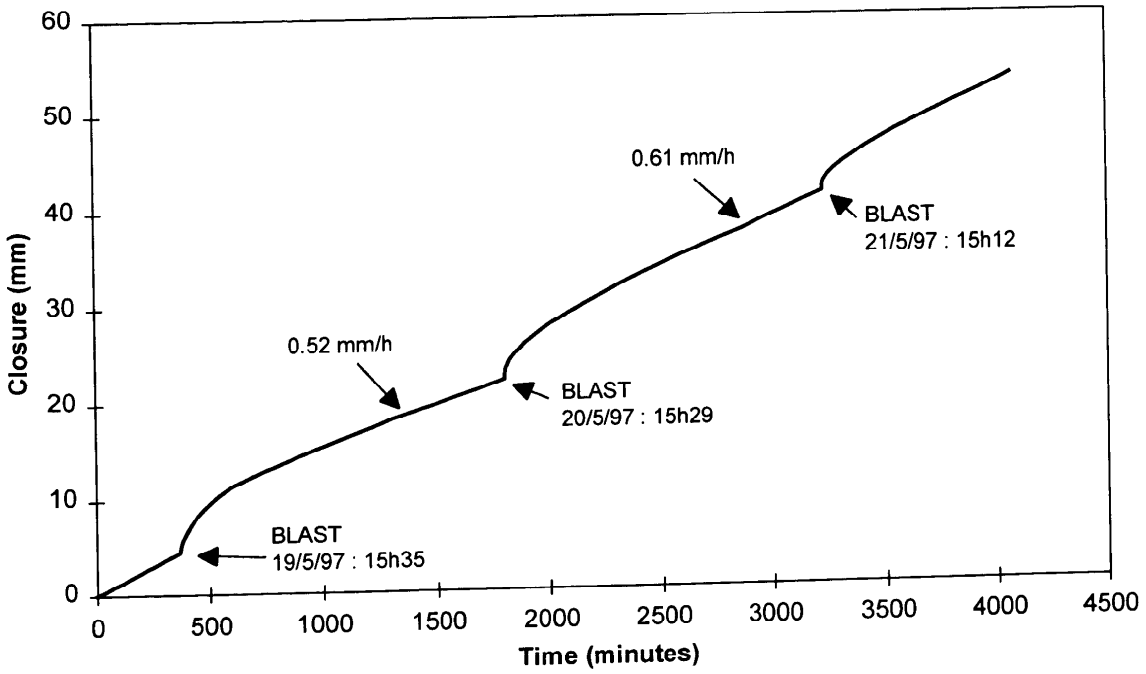

Figure 4.23. Closure measured at Hartebeestfontein Mine. The instrument was 10.9 m from the face before the blast on 19/5/97. The steady-state closure rates were calculated for the periods from approximately 800 minutes after the blast until the next blast occurred.

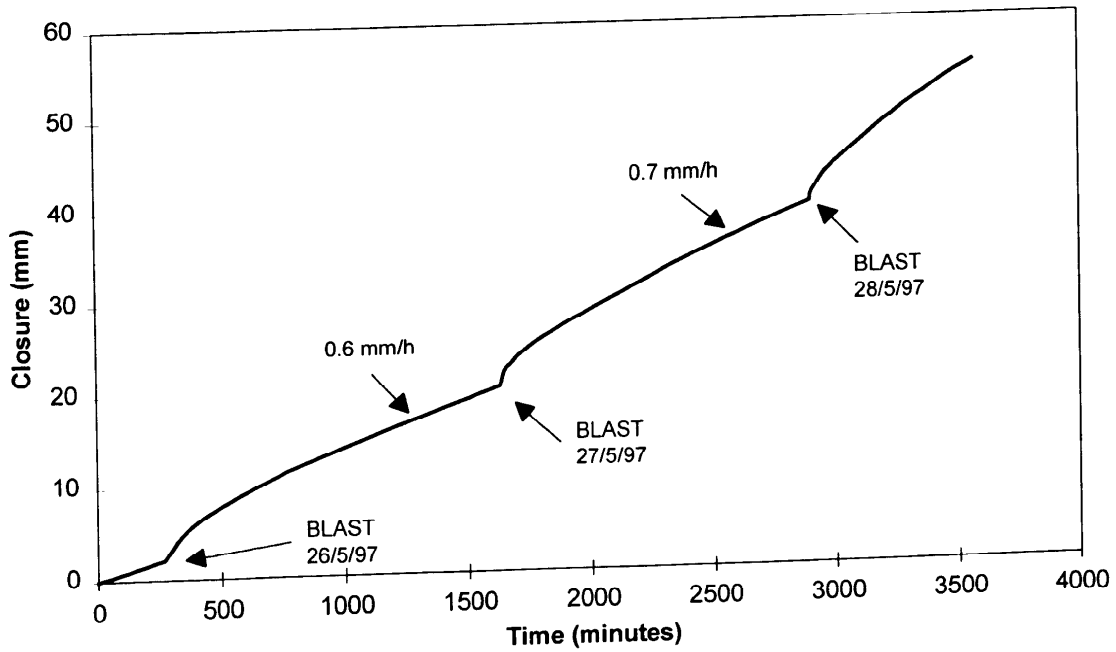

Figure 4.24. Closure measurements at Hartebeestfontein Mine for a larger distance to face than those in Figure 4.23. The instrument was 14.2 m from the face before the blast on 26/5/97.

4.5 Comparison between typical closure profiles of the Ventersdorp Contact Reef and Vaal Reef

When comparing typical results for the Vaal Reef in Figure 4.23 with those for the Ventersdorp Contact Reef in Figure 4.11, it is clear that significant differences exist between the continuous closure profiles of these different geotechnical areas. For a more direct comparison, typical closure increments after blasts for these two areas are plotted in Figure 4.25. The two experimental sites are approximately at the same depth and for these specific data sets, the closure instruments were approximately the same distance from the face. Although care should be taken when comparing these sites directly owing to different mining geometries, the following important differences are noted. The closure behaviour observed in areas of the Ventersdorp Contact Reef is characterised by a large instantaneous jump after blasting followed by a low closure rate. These areas are also prone to face bursting. In contrast, in this particular region of the Vaal Reef, the closure is characterised by a small instantaneous jump after blasting followed by a high rate of closure. Face bursting is virtually absent in these areas, although the risk of falls of ground is pronounced.

The instantaneous jump after blasting is the result of the immediate redistribution of stress following the removal of an increment of rock in the face. The more significant the disturbance to the stress field, the more pronounced the immediate response will be. If the increment of rock removed by blasting carries no load (in essence loose rock lying at the face) no change in the stress field will take place and no change will be noticed in the closure behaviour. The instantaneous closure response after blasting is therefore an indicator of the role the removed rock plays in maintaining the stress equilibrium before blasting. For the Ventersdorp Contact Reef, the significant instantaneous closure after blasting is probably an indicator of a high stress peak closer to the face than for the Vaal Reef. This may explain why face bursting is more pronounced on this reef than some areas of the Vaal Reef. This is further explored in Section 5.4, Chapter 5.

A further difference in behaviour between these areas is the high rate of steady-state closure of the Vaal Reef stopes compared to the Ventersdorp Contact Reef stopes. The high steady-state closure rate may be an indication of efficient stress redistribution through

mobilization and growth of the fracture zone and slip on discontinuities such as bedding planes. This in turn may result in low face stresses. Although the face bursting hazard might be low in areas with high steady-state closure rates, the more mobile fracture zone leads to rapid deterioration of hangingwall conditions leading to a fall of ground hazard. This should be confirmed through further studies.

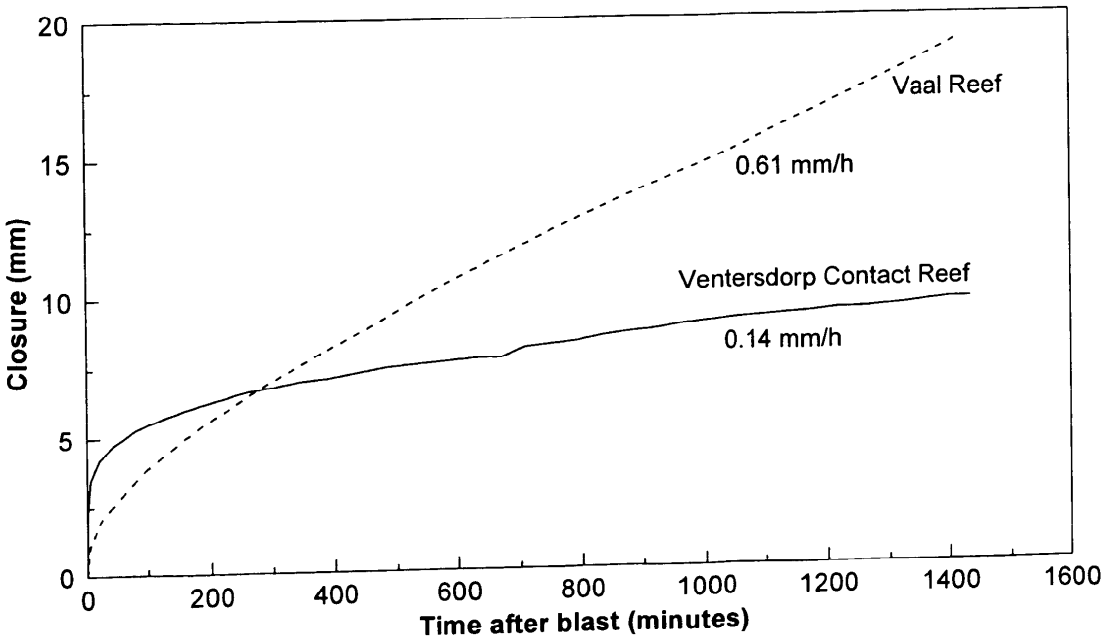

Figure 4.25. Comparison of typical closure profiles of the Ventersdorp Contact Reef and Vaal Reef. For the Vaal Reef measurements the instrument was 11.5 m from the face before the blast while it was 10 m from the face for the Ventersdorp Contact Reef measurements.

4.6 Continuous closure data versus long period measurements

As discussed in Section 4.1, when taking long period closure measurements at a fixed location in a stope and plotting the results as a function of a number of days, graphs similar to Figure 4.1 are obtained. Some researchers refer to these plots as "time-dependent closure". Long period measurements have provided the most commonly reported closure data in recent years. As a result of this, continuous closure data can easily be confused with these long period measurements. The material in this section is included to clarify this issue. The important differences between continuous closure measurements and long period measurements are summarised in Table 4.1.

Table 4.1. Differences between continuous closure measurements and long period measurements.

	Continuous measurements	**Long period measurements**
Time scale of typical graphs	Minutes to days	Weeks to months
Distinguish between instantaneous closure caused by blasting and true time-dependent behaviour	Yes	Not possible. Closure rates calculated are an average value of both.
True time-dependent behaviour	Steady-state closure rate visible between individual blasts.	Steady-state closure rate visible provided mining stops for several days or closure station sufficiently far away from any working faces.
Additional closure due to seismicity	Easily quantified.	Difficult to distinguish from normal closure behaviour.

To illustrate the usefulness of continuous measurements, typical time-dependent closure measured in the up-dip panel at Western Deep Levels Mine, South Shaft will be contrasted with daily measurements at the same position. Figure 4.26 illustrates the continuous measurements. The instantaneous jump after each blast and the effect of seismic events are clearly visible. For example the primary response after the blast on 17/4/97 was approximately 2 mm while the large seismic event on 17/4/97 produced an incremental jump (ignoring the overshoot) of 4 mm. The steady-state closure rate following the blast on 16/4/97 was 0.082 mm/h. If only daily measurements were taken at the same location between 10h00 and 11h00 every morning, Figure 4.27 would be the resulting closure profile. Clearly a large proportion of the useful data is lost with these daily measurements. It is unknown whether this closure is the result of large primary closure followed by a small steady-state closure rate or vice versa. From Figure 4.27, the closure rate would now typically be calculated as an average of 6.5 mm/day. It is not clear if this rate will continue if mining stops. From the continuous closure measurements, the true steady-state rate is approximately 0.082 mm/h or 2 mm/day which is significantly less than the value calculated above. Another popular way of representing this rate is millimeter closure per meter of face advance. The face advance over this period was approximately 3 m and the total closure was 33 mm. The closure rate can therefore be calculated as 11 mm/m. This method is not acceptable as it implies that the closure will remain at a constant value if all mining activity stops.

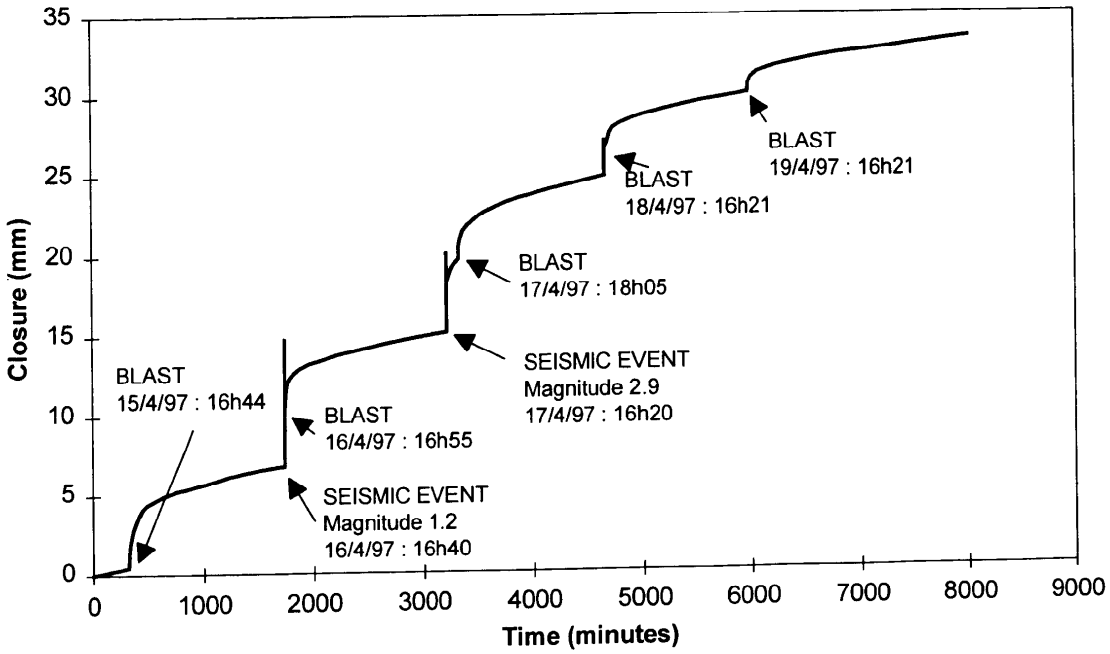

Figure 4.26. Continuous closure measured in the up-dip panel at Western Deep Levels Mine. This was for instrument no. 1 which was 4.1 m from the face before the blast on 15/4/97. The origin of the time axis is at 10h30 on 16/4/97. (See Section 4.3 for an explanation of the overshoot behaviour after the seismic events.)

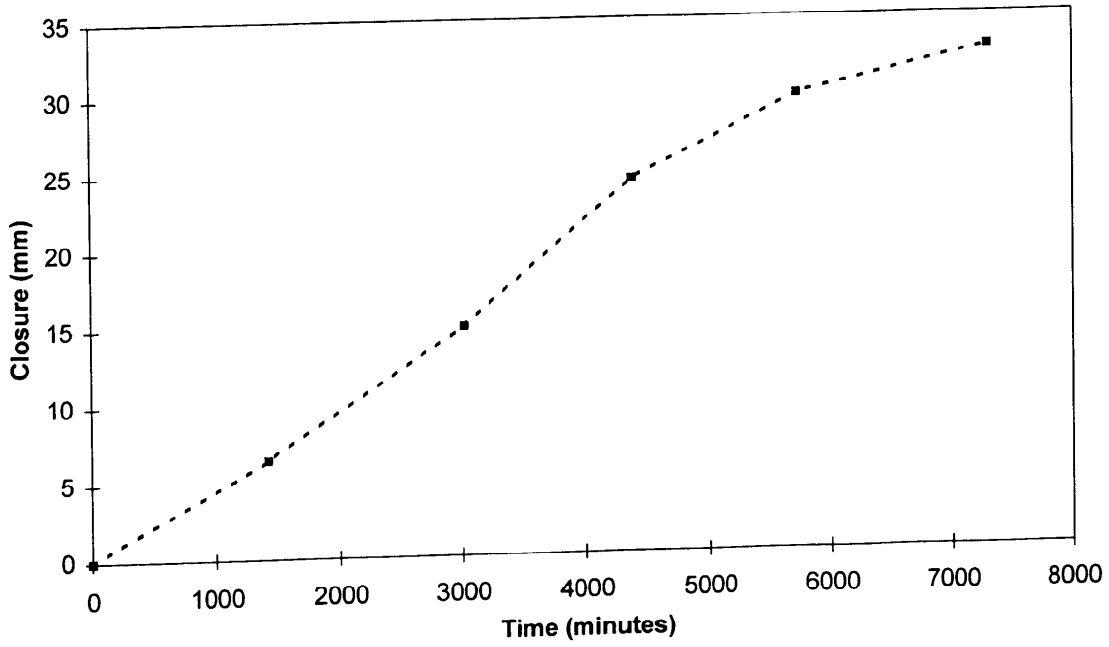

Figure 4.27. This is the resulting closure curve for the same data set as above, but with a sampling period of 24 hours. Each data point was taken between 10h00 and 11h00 every morning.

The example above is for measurements close to the face of the stope. It was however noted that the incremental jump after blasting becomes less as the measurement station moves into the back area (Figures 4.12 and 4.14). The difference between continuous closure profiles and daily measurements then becomes less pronounced. This is illustrated in Figure 4.28. With sufficient distance from the face (typically greater than 20 m for the experimental sites at Western Deep Levels Mine), daily closure measurements will therefore be sufficient. As continuous closure recorders are more expensive and difficult to maintain, the author would suggest that continuous recorders only be used close to the face while daily measurements would suffice for greater distances to face.

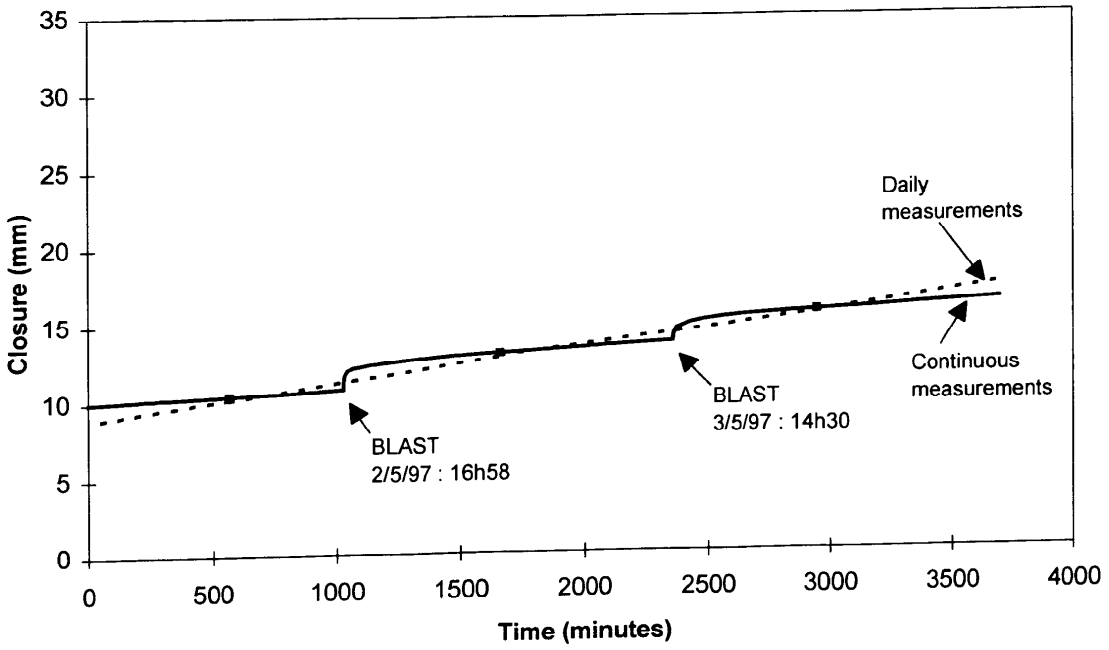

Figure 4.28. Comparison between continuous and daily closure measurements for the up-dip panel at Western Deep Levels Mine for measurements taken further from the face than in Figures 4.26 and 4.27. The continuous data was recorded by instrument no. 3 which was 16 m from the face before the blast on 2/5/97.

To illustrate the relationship between closure profiles from long period measurements (Figure 4.1) and continuous measurements, equations [3.24] and [3.42] were inserted in the structure of [3.58b] and plotted for n = 20 increments in Figure 4.29. Although the validity of this analytical model still needs to be verified (see next section), it is useful to illustrate the trend. Arbitrary values of model parameters were used namely H = 2000 m, E_2 = 1×10^{11} Pa, E_1 = 1×10^{11} Pa , η_2 = 1×10^{15} Pa.h, η_1 = 2×10^{11} Pa.h, x = 0 m, α = 0°, k = 0.5, g = 9.81 m/s^2 and ρ = 2700 kg/m^3. As the face moves away from the measurement position, the primary closure behaviour becomes smaller. When taking daily

measurements, this now results in the apparent rate of closure becoming less as the face moves away. This profile from the daily measurements is reminiscent of that seen in Figure 4.1.

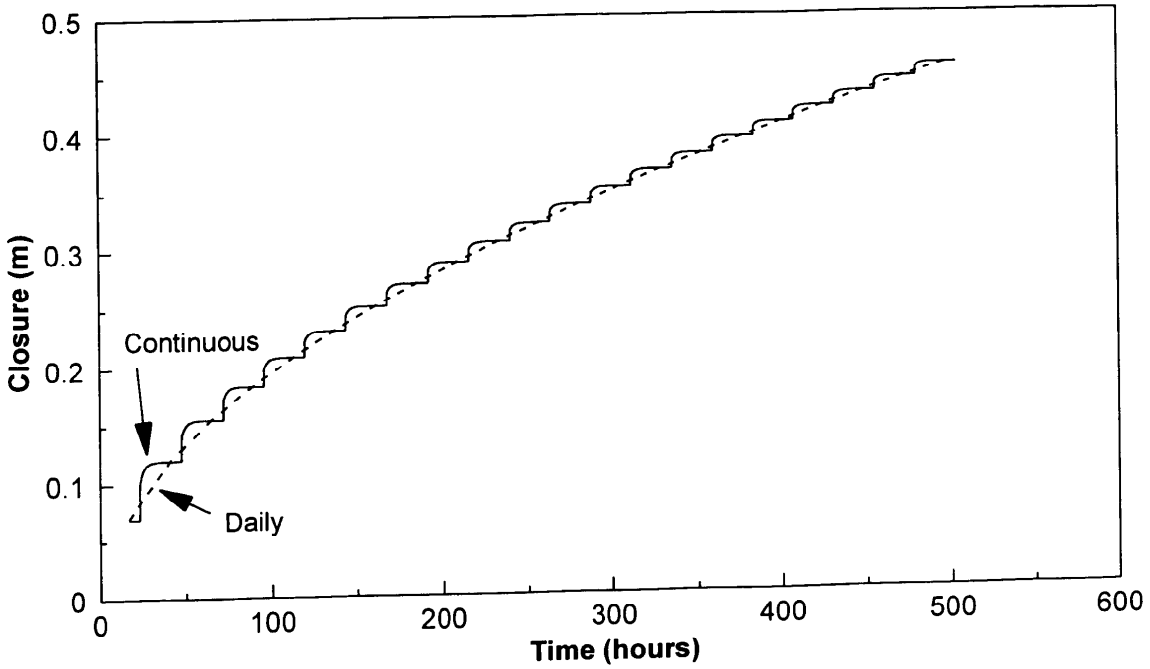

Figure 4.29. Postulated relationship between continuous and daily closure measurements.

4.7 Calibration and applicability of the developed viscoelastic stope closure model

From Figure 4.11, the stope closure after blasting displays a typical primary response (including an instantaneous component) followed by steady-state closure. From the developed viscoelastic convergence models, this behaviour is best represented by the Burgers convergence model (Chapter 3) giving an instantaneous response, primary convergence and steady-state convergence. Although the 3-parameter solid convergence model (Appendix B2) can simulate the instantaneous response and primary phase, the convergence approaches an asymptotic value which is clearly not the case for the measured data in the short term (Figure 4.16). The Kelvin convergence model (Appendix B1) is even worse as it cannot simulate the instantaneous response. The discussion in this section will therefore only focus on the Burgers convergence model.

The analytical solution for the Burgers convergence model developed in Chapter 3 is only valid for geometries where plain strain assumptions can be made and if there is no contact between the hangingwall and footwall in the back area. It is not possible to make these

assumptions for the data given in Sections 4.3 and 4.4 due to the complicated layouts. Therefore data from an experimental site at Deelkraal Gold Mine is used. The layout of the longwall is given in Figure 4.30. The dip of the reef is 27° and the depth at the closure station was approximately 2700 m below surface. For the analysis, a two-dimensional section was taken along strike. Although this will introduce some error due to the overhand configuration, it is deemed an acceptable approximation. Similar to the experimental sites at Western Deep Levels, Ventersdorp Contact Reef is mined in this area. The uniaxial compressive strength of the lava in the hangingwall and quartzite in the footwall was 237 MPa and 181 MPa respectively (Güler, 1997). Because of the low closure rate in this area, there was no contact between the hangingwall and footwall in the back area, although the span was already quite large.

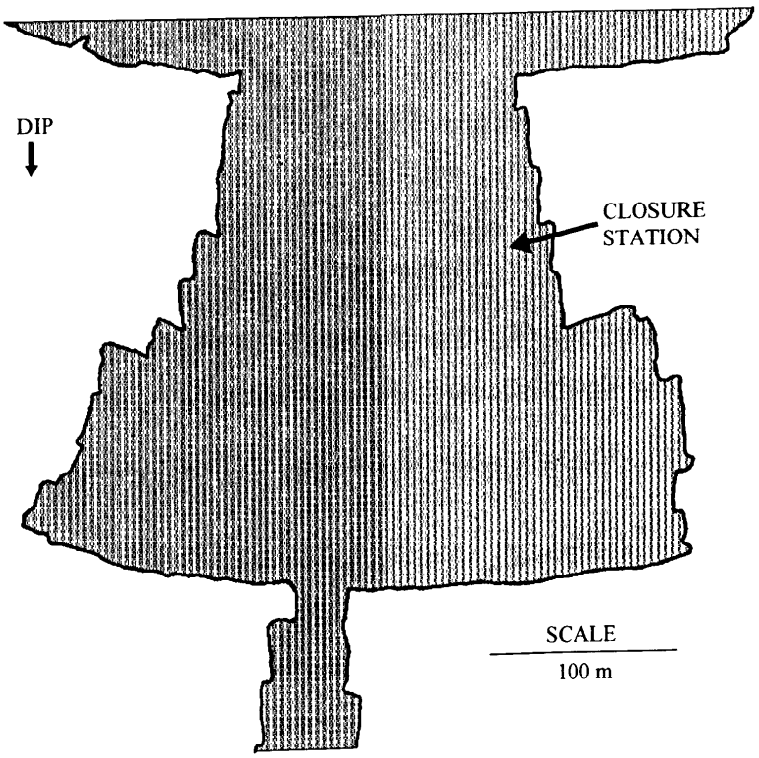

Figure 4.30. Position of the closure station in the 25-15E longwall at Deelkraal Gold Mine.

A single clockwork closure instrument was installed in this longwall in the position shown in Figure 4.30. The stope span at this position along strike was approximately 200 m. Figure 4.31 illustrates some of the closure data collected. Before the blast on 16/9/94, the instrument was 16.6 m from the face. After the blast (one side only), the increase in span was 1.4 m. Equation [3.62] was fitted to the data following this blast on 16/9/94. This was done using a spreadsheet and manipulating the parameters until a reasonable fit was obtained. Although more accurate methods, like non-linear least squares fitting, are available, these were not used as some subtle problems with the use of viscoelastic theory

to simulate the closure of tabular excavations were discovered, as explained below. The actual calibrated values are therefore of little significance. The fit is illustrated in Figure 4.32. The calibrated values are $E_2 = 4\times10^{12}$ Pa, $E_1 = 3\times10^{11}$ Pa, $\eta_2 = 6.5\times10^{15}$ Pa.min, $\eta_1 = 2.5\times10^{13}$ Pa.min.

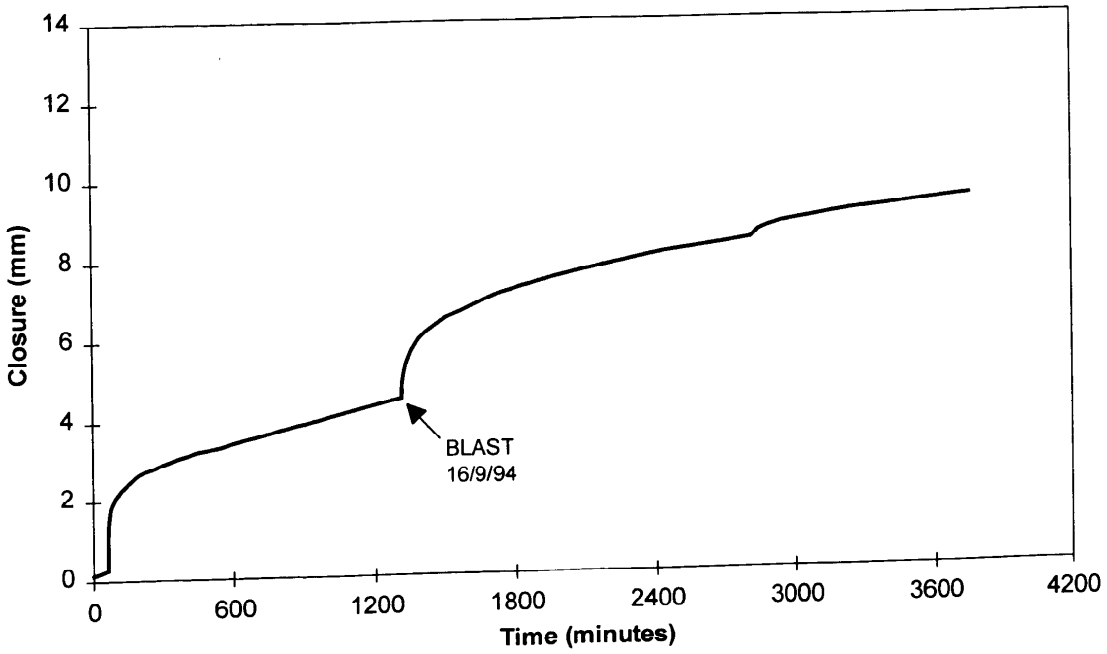

Figure 4.31. Time-dependent closure measured in the 25-15E longwall at Deelkraal Gold Mine.

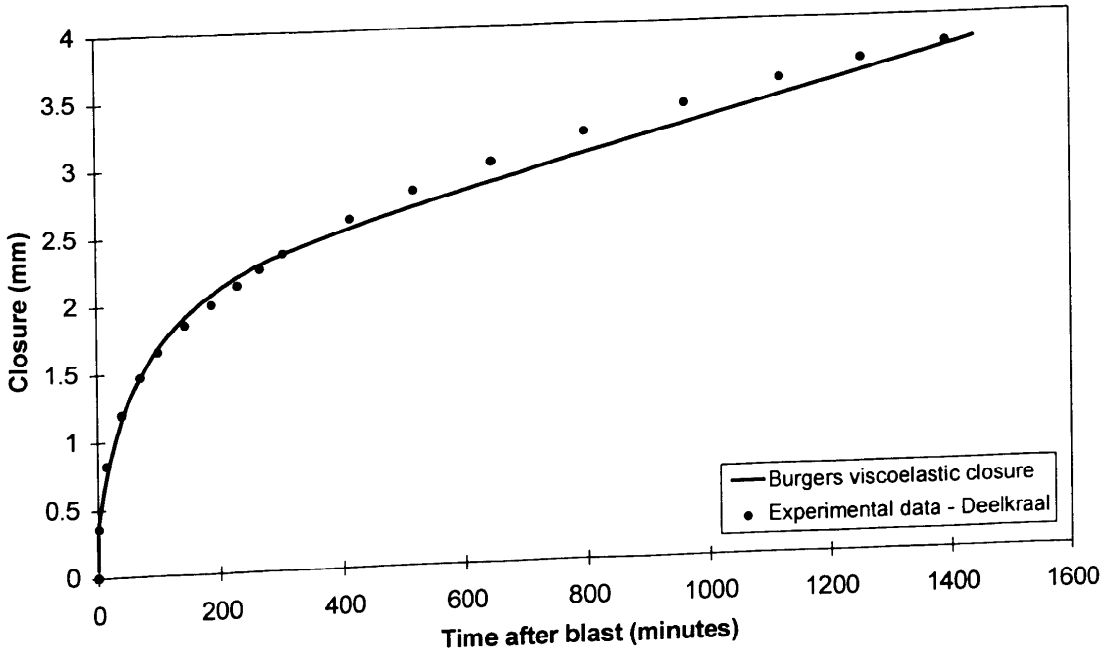

Figure 4.32. The Burgers viscoleastic convergence solution fitted to the experimental closure measured at Deelkraal. The experimental data is that which followed the blast on 16/9/94 (see Figure 4.31)

Because of the good fit obtained in Figure 4.32, it appears superficially that the time-dependent closure can be successfully simulated using a viscoelastic approach. Of interest is that for the closure data for the Ventersdorp Contact Reef, the magnitude of the instantaneous closure after blasting decreases with distance to the face (Figure 4.14). This behaviour is also shown by the Burgers viscoelastic model as illustrated in Figure 3.11 (Chapter 3). A drawback of the Burgers viscoelastic model is that the rate of steady-state convergence maintains a constant value even if all mining activity stops for lengthy periods. Although this is true for underground closure behaviour in the short term ($\leq$ 1 days, Figure 4.12), the closure rate in the longer term appears to gradually decrease in the absence of blasting (Figure 4.16). This can be simulated more accurately by adding another elastic component in parallel to the second dashpot of the Burgers model. This is illustrated in Figure 4.33. This is also known as a Kelvin chain (Flügge, 1975).

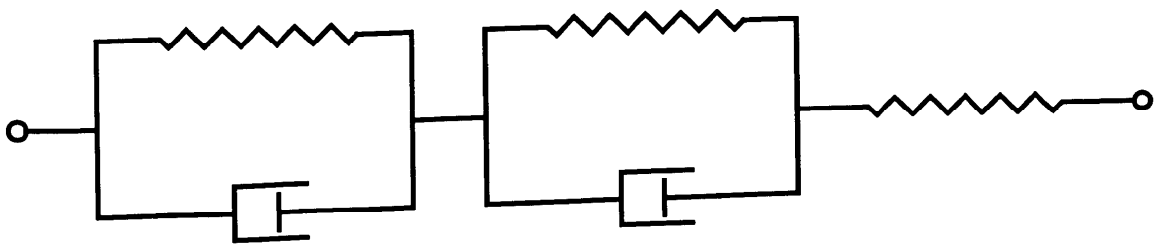

Figure 4.33. Proposed addition of a third elastic component to the Burgers model to simulate the gradual reduction in steady-state closure rate in the absence of mining activity.

It can be shown that the differential equation of this model is given by

$$\sigma + p_1\dot{\sigma} + p_2\ddot{\sigma} = q_0\varepsilon + q_1\dot{\varepsilon} + q_2\ddot{\varepsilon} \qquad [4.5]$$

The closure equation for tabular stopes using the model above will have to be derived using the methodology in Chapter 3. This solution was never derived as a more serious defect in the use of viscoelasticity in relation to the closure of tabular excavations was discovered. For the Burgers viscoelastic solution, the rate of steady-state closure increases when moving away from the face (Figure 3.10). Although this is noted for the Vaal Reef (Figures 4.23 and 4.24), it is not true for the Ventersdorp Contact Reef. From Figures 4.12 and 4.14 it is clear that for the Ventersdorp Contact Reef the highest rate of steady-state closure occurs close to the working faces and decreases into the back area. The calibrated

values obtained from Figure 4.32 are therefore only valid at the particular observation point. When using the calibrated model to obtain time-dependent closure behaviour at other distances from the face, errors will be introduced which will become progressively worse the further away from the point of calibration these are. It appears then that viscoelastic theory is not suitable to simulate the time-dependent closure behaviour of tabular excavations in hard rock. Increasing the number of elements in the viscoelastic model (for example Figure 4.33) will not help either. The fundamental equation for the viscoelastic closure of a tabular excavation was derived in Chapter 3 as equation [3.24]. Changing the specific viscoelastic model will only change the time-dependent component F(t). This is multiplied by the term $\sqrt{\ell^2 - x^2}$, of which the magnitude is increasing away from the face with a maximum value at the centre of the panel (x = 0). As any rate prescribed by F(t) is multiplied by this term, the highest rate of closure will always be in the centre of the panel.

This problem is a consequence of the inability of viscoelastic theory to simulate time-dependent failure processes and discontinuum displacements. The viscoelastic assumption implies that the rock mass behaves as a continuum material and is thus unable to represent the fracture envelope surrounding excavations in hard rock. From Chapter 2 it was concluded that the creep rate of the intact hard rock is low and cannot explain significant movements of the order of millimetres or centimetres per day. It is therefore accepted that time-dependent failure processes play a significant role in the observed closure behaviour. Recorded evidence of the time-dependent fracture processes has already been presented in Section 1.3. Due to the inability of viscoelasticity to simulate this process, a viscoplastic approach will be explored in the next chapter.

Chapter 5

The applicability of a continuum elasto-viscoplastic model

5.1 Introduction

As concluded in the previous chapter, a viscoelastic approach is not suitable to simulate the time-dependent behaviour of deep tabular excavations in hard rock. From the discussion in Section 1.3 and the results in Chapter 4, it is evident that the time-dependent failure processes in the rock play a prominent role in the underground closure behaviour. Any model used to simulate this time-dependent behaviour needs to include some representation of the delayed failure processes and the resulting time-dependent extension of the fracture zone. It appears as if the significant time-dependent effects are confined to the fracture envelope surrounding excavations. The far field behaviour has been shown to be adequately represented by elastic theory (Ryder and Officer, 1964). An idealisation of this concept is given in Figure 5.1. Note that the actual shape of the fracture envelope is not necessarily that depicted in the figure.

In reality the fracture zone consists of discrete fractures and other discontinuities as illustrated in Figure 1.3. There is no sharp boundary between this zone and the intact elastic material but a gradual transition zone as the density of fracturing decreases further away from the stope. It is in this transition zone where the creep of the intact material might play an important role in the time-dependent formation of new fractures. Although the tests in Chapter 2 were conducted under uniaxial conditions, there is evidence that the creep rate is dependent upon the magnitude of the deviatoric stress (σ_1-σ_3) and not the magnitudes of the individual principal stresses (Lama and Vutukuri, 1978). In certain areas of the fracture zone, the deviatoric stress might just be large enough to cause additional creep fracturing some time after blasting. Although the creep rate of the intact rock is low and therefore does not have a direct effect on the closure rate of the stope, it might result in the important effect of delayed fracturing.

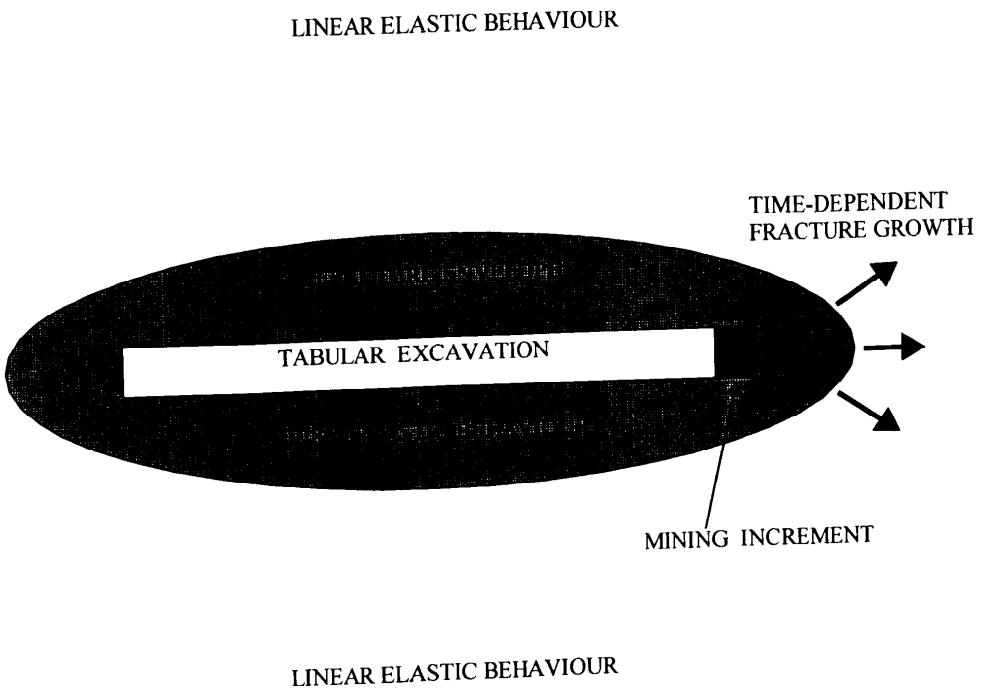

Figure 5.1. Conceptualization of the fracture zone surrounding tabular excavations and time-dependent extension of this zone following a mining increment.

The concept in Figure 5.1 is not entirely new as Jantzon (1965) proposed an essentially similar model. Unfortunately at that time, suitable time-dependent constitutive models, numerical tools and computer systems were not available to exploit these ideas further. In this chapter a continuum viscoplastic model with a novel cohesion weakening rule is proposed and implemented in a finite difference code. This is used to simulate typical stope closure behaviour and the squeezing conditions at Hartebeestfontein Mine.

To include failure processes in rheological models, slider elements (also called St. Venant elements) are typically added to the elastic and viscous elements of viscoelasticity. These slider elements have a specified failure strength and are immobilised below this strength. Commonly a dashpot is placed in parallel with the slider to control the strain rate if the slider is loaded above its failure strength. This is the so-called Bingham unit (Figure 5.2).

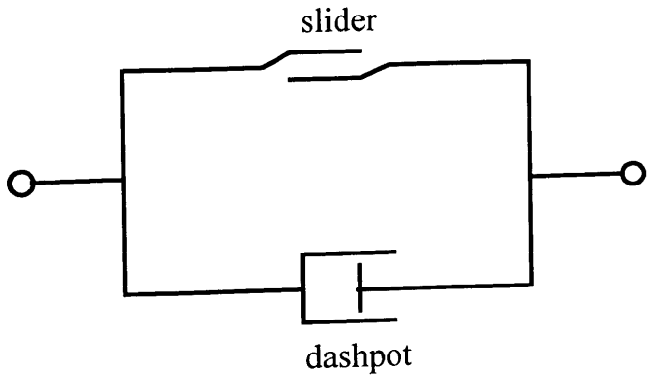

Figure 5.2. The Bingham rheological model.

Various combinations of elastic, viscous and St. Venant elements have been used by different researchers to simulate particular time-dependent problems. Gioda (1982) and Gioda and Cividini (1996) used a Kelvin unit in series with a Bingham unit to represent primary and secondary closure in squeezing tunnels. Tertiary movements can be considered by providing suitable laws relating the values of the mechanical parameters (such as viscosity) to the irreversible part of the time-dependent strain. These rheological models are particularly suited for analysis carried out through the finite element method. This allows the interaction between squeezing rock and support to be simulated. Other examples of the use of these rheological models can be found in Akagi et al. (1984), Song (1993), Lee et al. (1995), Euverte et al. (1994) and Sagawa et al. (1995).

Nawrocki (1995) developed a one-dimensional semi-analytical solution for the time-dependent behaviour of a coal seam. A Bingham type of material model was assumed. This study was initiated to investigate the rate of face advance on rockburst occurrence. The analysis showed that rapid ore extraction produces zones of high stress concentrations close to the longwall face. This situation is deemed to be hazardous as it increases the likelihood of rockbursting.

Since Perzyna (1966) proposed the general concept of elasto-viscoplasticity, a number of workers have applied this theory to geological materials. Elasto-viscoplasticity is essentially a modification of classical plasticity theory by the introduction of a time-rate rule in which the yield function and plastic potential function of classical plasticity are incorporated. In

comparison with viscoelasticy, a viscoplastic material shows viscous behaviour in the plastic region only. Desai and Zhang (1987) used this theory together with a generalised yield function to characterise the viscoplastic behaviour of a sand and rock salt. Sepehr and Stimpson (1988) used Perzyna's theory as a basis to develop a time-dependent finite element model to understand the time-dependent closure of excavations and seismicity in the potash mines in Saskatchewan. For a rheological analysis of tunnel excavations, Swoboda et al. (1987) developed a coupled finite element/boundary element approach to analyse the interaction of the rock with the viscoelastic properties of the shotcrete. The rock was assumed to behave in an elasto-viscoplastic fashion.

Fakhimi (1992) and Fakhimi and Fairhurst (1994) proposed a visco-elastoplastic constitutive model to simulate the time-dependent behaviour of rock. The model consists of an elasto-plastic Mohr-Coulomb model in series with a linear viscous unit. This model was implemented in an explicit finite difference code. A typical solution cycle would be to do an elasto-plastic analysis during which real time is frozen. After an equilibrium point is reached, the linear viscous unit is used to determine additional creep strain components for a specified period of real time. Control is then passed back to the elasto-plastic analysis to obtain a new equilibrium and the process is repeated. Although this model appeared successful in imitating the behaviour of uniaxial and triaxial tests and the stand-up time of excavations, the time dependent behaviour of the model is independent of the failure processes. The entire material (including the far field) also behaves in a viscous manner. This model is therefore not applicable to the conceptual model of deep excavations in hard rock (Figure 5.1) where the time-dependency is a direct consequence of the failure processes and the solid rock behaves essentially elastically.

5.2 Model formulation

For this study, classical elasto-viscoplasticity as defined by Perzyna (1966) is used as a basis for the model. Figure 5.3 shows the rheological analogue of the developed model. Similarly to elasto-plastic theory, the concepts of yield function and flow rule also apply. However, in viscoplasticity theory, stresses above the yield surface are admissible.

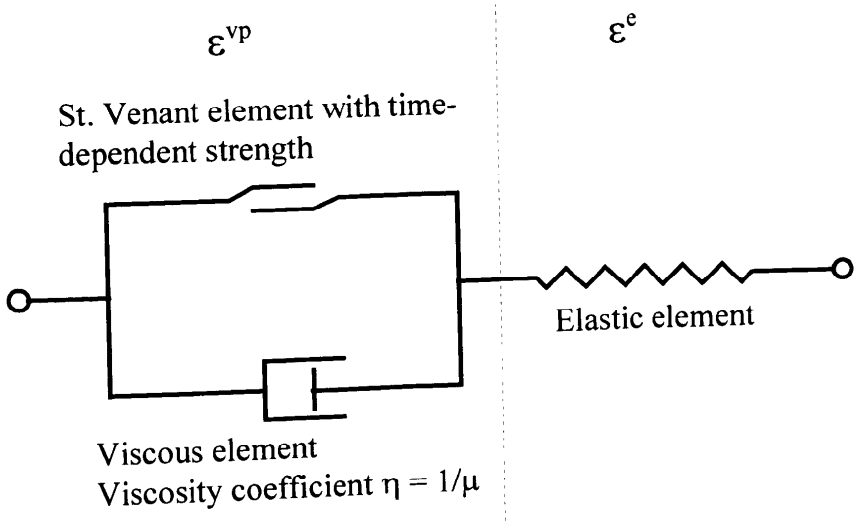

Figure 5.3. Representation of the developed elasto-viscoplastic model.

Yield surface

A time-dependent Mohr-Coulomb shear yield function is assumed and is given by

$$f_s(t) = \sigma_1 - \sigma_3 N_{\phi c} + 2C_c\sqrt{N_{\phi c}} \qquad [5.1]$$

where

$$N_{\phi c} = \frac{1+\sin\phi_c}{1-\sin\phi_c} \qquad [5.2]$$

ϕ_c = current value of friction angle

C_c = current value of cohesion

σ_1 = major principle stress

$\sigma_1 < \sigma_2 < \sigma_3$ for a compressive stress negative convention

Shear failure takes place for $f_s(t) \le 0$. For $f_s(t) > 0$, the rock behaves elastically. The cohesion C_c and friction angle ϕ_c will assume peak values C_p and ϕ_p for intact rock. Therefore for intact rock equation [5.2] becomes

$$N_{\phi p} = \frac{1+\sin\phi_p}{1-\sin\phi_p} \qquad [5.3]$$

Once the particular volume of rock fails, the friction angle assumes a residual value ϕ_r and the cohesion gradually decays to a residual value C_r. This cohesion softening process is simulated as a time-dependent process as described later. This is also depicted in Figure 5.4.

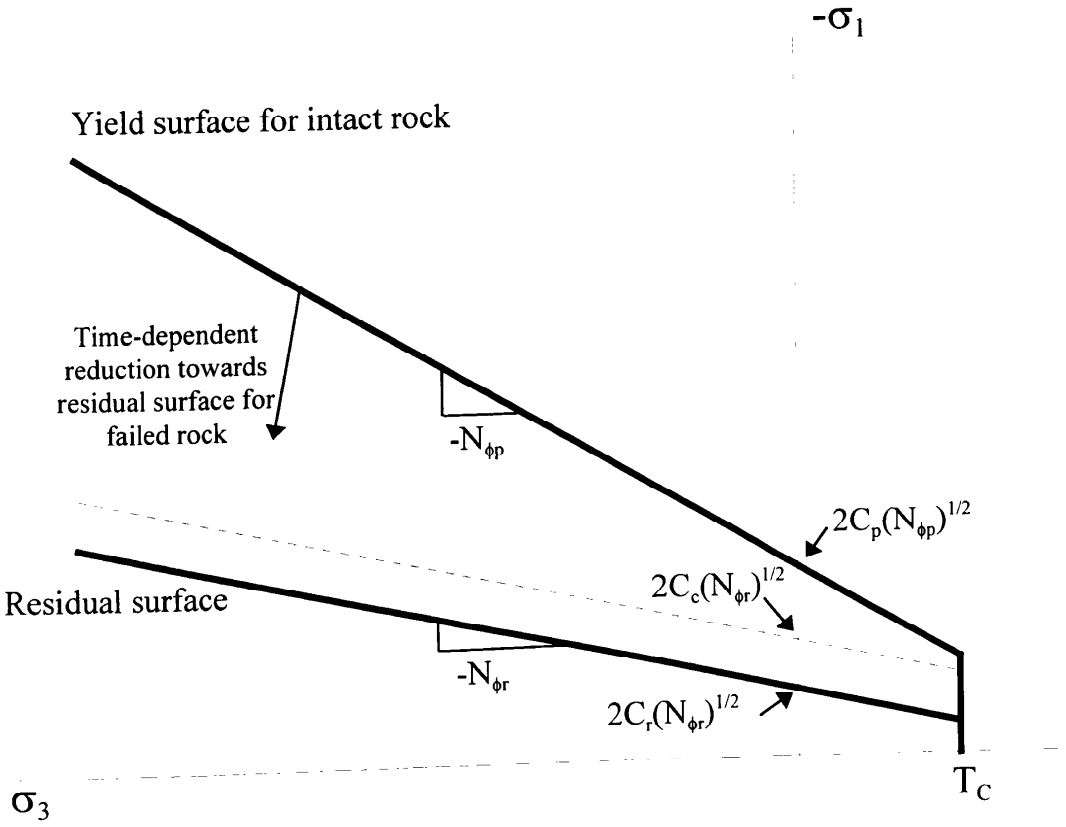

Figure 5.4. The evolution of the yield surface for intact rock to the eventual residual surface for failed rock. Note that compressive stresses are negative and that on the vertical axis the negative of the major principal stress is plotted to turn the figure upright. $N_{\phi r}$ is defined in equation [5.11]. T_C is the tensile strength of the material.

Flow rule

If shear failure is detected, the viscoplastic strain rate $\dot{\varepsilon}_i^{vp}$ is given by

$$\dot{\varepsilon}_i^{vp} = \mu\langle f_s(t)\rangle \frac{\partial g_s}{\partial \sigma_i} \qquad \text{for} \quad i = 1, 2, 3 \qquad [5.4]$$

where μ is the fluidity parameter and

$$\begin{aligned} \langle f_s(t) \rangle &= f_s(t) \quad \text{for} \quad f_s(t) \leq 0 \\ \langle f_s(t) \rangle &= 0 \quad \text{for} \quad f_s(t) > 0 \end{aligned} \qquad [5.5]$$

A non-associated flow rule is used (Vermeer and De Borst, 1984) where the plastic potential function is given by

$$g_s = \sigma_1 - \sigma_3 N_\psi + 2C_c \sqrt{N_\psi} \qquad [5.6]$$

with

$$N_\psi = \frac{1 + \sin\psi}{1 - \sin\psi} \qquad [5.7]$$

and ψ is the dilation angle. From equation [5.4] it follows that in the model the strain rate of the failed rock is proportional to excess stress above the yield surface. This is similar to observations made by Bieniawski (1970) when he investigated the time-dependent behaviour of fractured rock in the laboratory. For failed samples subjected to a constant loading, there was a further increase in strain with time until a specific value was attained. During this period, the rate of strain gradually decreased as it moved closer to the target level of deformation.

Time-dependent strength

A constitutive description of time-dependent rock behaviour should include the effect of strength degradation with time and/or deformation. Experimental evidence (Kranz et al., 1982) indicated that rock under load shows a decrease in strength with time. Fakhimi and Fairhurst (1994) modelled the time-dependent degradation of material strength by exponential friction and cohesion decay functions. The degradation of rock strength with time is another mechanism that can play an important role in squeezing conditions. Aydan et al. (1996) simulated the time-dependent behaviour of squeezing rocks as the degradation of strength properties as a function of time by utilising information obtained from creep tests. The uniaxial strength of rock (σ_C) is represented by the function

$$\frac{\sigma_c}{\sigma_c^{\,o}} = \frac{\sigma_c^{\,\infty}}{\sigma_c^{\,o}} + \left(1 - \frac{\sigma_c^{\,\infty}}{\sigma_c^{\,o}}\right) e^{-\frac{t}{\tau}} \qquad [5.8]$$

where σ_c^{∞} is the ultimate uniaxial strength, σ_c^{o} the short term strength and τ is a constant called the "retardation failure time" by Aydan et al. (1996).

As explained in Chapter 1, observations of time-dependent fracturing ahead of tabular stopes in the South African gold mines and especially in the haulages at Hartebeestfontein Mine show that the rock becomes progressively more fractured with time resulting in the gradual loss of cohesive strength in a particular volume of rock. This loss of strength will be modelled by assuming that the rate of cohesion reduction is proportional to the excess stress above the residual target surface

$$\dot{C}_c = k_c \langle f_{res} \rangle \qquad [5.9]$$

where k_c is the cohesion decay factor and

$$f_{res} = \sigma_1 - \sigma_3 N_{\phi r} + 2C_r \sqrt{N_{\phi r}} \qquad [5.10]$$

$$N_{\phi r} = \frac{1 + \sin\phi_r}{1 - \sin\phi_r} \qquad [5.11]$$

is the residual target surface. The principle embodied in equation [5.9] is based loosely on the observations in Chapter 2 that if rock specimens are loaded close to the uniaxial strength, the creep rate and eventual creep failure occur faster than for a low stress. For a particular volume of rock under high stress, creep fractures will therefore form more rapidly, resulting in a faster loss of cohesion in the rock than for low stress.

Implementation of the model in FLAC

The model developed above was implemented in a creep version of the computer program FLAC using the built-in FISH language. FLAC (Itasca, 1993) is a two-dimensional explicit finite difference code developed for geotechnical engineering applications. FISH is a programming language embedded within FLAC enabling the user to define new variables,

functions and constitutive models. The creep version of FLAC gives access and control over a timestep that represents real time.

Kirsten and Bartlett (1992) described squeezing conditions in rock as "indeterminate" plastic displacements and attempted to simulate this numerically using a non-creep version of FLAC. A Mohr-Coulomb yield function was used. Very weak material properties were chosen resulting in failure of the solution to converge because of ongoing plastic strain. The resulting displacement indeterminacy was used to represent squeezing behaviour. Time as a parameter was not explicitly included in the model. This is not an optimum solution as factors such as the deformation rate and the timing of support installation cannot be simulated. Therefore, the creep version of FLAC was used in this study.

When a new constitutive model is written for FLAC, the main task is to update the stress tensor in each timestep for the given old stress tensor and strain components. For the model developed above, the material behaves elastically if the failure strength is not exceeded. During each cycle in the program stepping, each element is tested for failure using equation [5.1]. For elements that have not failed, $C_c = C_p$ and $\phi_c = \phi_p$. Once the element fails, ϕ_c is set to ϕ_r while C_c is gradually reduced from C_p to C_r as explained below.

For elements where the stress exceeds the failure strength, the total strain increment is given by

$$\Delta\varepsilon_i = \Delta\varepsilon_i{}^{e} + \Delta\varepsilon_i{}^{vp} \qquad \text{for} \qquad i = 1, 2, 3 \qquad [5.12]$$

Writing equation [5.4] in incremental form gives

$$\Delta\varepsilon_i{}^{vp} = \mu\,\Delta t\langle f_s(t)\rangle\frac{\partial g_s}{\partial\sigma_i} \qquad \text{for} \qquad i = 1, 2, 3 \qquad [5.13]$$

where Δt is the timestep. Inserting equation [5.6] in equation [5.13] and then in equation [5.12] gives

$$\begin{aligned}\Delta\varepsilon_1 &= \Delta\varepsilon_1{}^{e} + \mu\,\Delta t\langle f_s(t)\rangle \\ \Delta\varepsilon_2 &= \Delta\varepsilon_2{}^{e} \\ \Delta\varepsilon_3 &= \Delta\varepsilon_3{}^{e} - \mu\,\Delta t\langle f_s(t)\rangle N_\psi\end{aligned} \qquad [5.14]$$

The stress increments $\sigma_i' - \sigma_i^0$ are related to the elastic strain increments by the elasticity equations

$$\begin{aligned}\sigma_1' &= \sigma_1^0 + A\Delta\varepsilon_1^e + B\left(\Delta\varepsilon_2^e + \Delta\varepsilon_3^e\right)\\ \sigma_2' &= \sigma_2^0 + A\Delta\varepsilon_2^e + B\left(\Delta\varepsilon_1^e + \Delta\varepsilon_3^e\right)\\ \sigma_3' &= \sigma_3^0 + A\Delta\varepsilon_3^e + B\left(\Delta\varepsilon_1^e + \Delta\varepsilon_2^e\right)\end{aligned} \qquad [5.15]$$

where

$$A = K + \frac{4G}{3} \qquad [5.16]$$

$$B = K - \frac{2G}{3} \qquad [5.17]$$

K = bulk modulus

G = shear modulus

The initial estimate of new stresses (before testing for failure) is also derived from the elasticity relations

$$\begin{aligned}\sigma_1^I &= \sigma_1^0 + A\Delta\varepsilon_1 + B\left(\Delta\varepsilon_2 + \Delta\varepsilon_3\right)\\ \sigma_2^I &= \sigma_2^0 + A\Delta\varepsilon_2 + B\left(\Delta\varepsilon_1 + \Delta\varepsilon_3\right)\\ \sigma_3^I &= \sigma_3^0 + A\Delta\varepsilon_3 + B\left(\Delta\varepsilon_1 + \Delta\varepsilon_2\right)\end{aligned} \qquad [5.18]$$

This can be written as

$$\begin{aligned}\sigma_1^0 &= \sigma_1^I - A\Delta\varepsilon_1 - B\left(\Delta\varepsilon_2 + \Delta\varepsilon_3\right)\\ \sigma_2^0 &= \sigma_2^I - A\Delta\varepsilon_2 - B\left(\Delta\varepsilon_1 + \Delta\varepsilon_3\right)\\ \sigma_3^0 &= \sigma_3^I - A\Delta\varepsilon_3 - B\left(\Delta\varepsilon_1 + \Delta\varepsilon_2\right)\end{aligned} \qquad [5.19]$$

When inserting equation [5.14] this gives

$$\sigma_1^0 = \sigma_1^I - A\left[\Delta\varepsilon_1^e + \mu\Delta t\langle f_s(t)\rangle\right] - B\left[\Delta\varepsilon_2^e + \Delta\varepsilon_3^e - \mu\Delta t\langle f_s(t)\rangle N_\psi\right]$$
$$\sigma_2^0 = \sigma_2^I - A\Delta\varepsilon_2^e - B\left[\Delta\varepsilon_1^e + \Delta\varepsilon_3^e + \mu\Delta t\langle f_s(t)\rangle\left(1 - N_\psi\right)\right] \qquad [5.20]$$
$$\sigma_3^0 = \sigma_3^I - A\left[\Delta\varepsilon_3^e - \mu\Delta t\langle f_s(t)\rangle N_\psi\right] - B\left[\Delta\varepsilon_1^e + \Delta\varepsilon_2^e + \mu\Delta t\langle f_s(t)\rangle\right]$$

This in turn can be inserted in equation [5.15] to give

$$\sigma_1' = \sigma_1^I - \mu\Delta t\langle f_s(t)\rangle\left[A - BN_\psi\right]$$
$$\sigma_2' = \sigma_2^I - B\mu\Delta t\langle f_s(t)\rangle\left[1 - N_\psi\right] \qquad [5.21]$$
$$\sigma_3' = \sigma_3^I - \mu\Delta t\langle f_s(t)\rangle\left[B - AN_\psi\right]$$

Writing equation [5.9] in incremental format

$$\Delta C_c = k_c\langle f_{res}\rangle\Delta t \qquad [5.22]$$

At timestep (j+1) the value of cohesion is given by

$$C_c^{j+1} = C_c^j - \Delta C_c \quad \text{if} \quad C_c^{j+1} > C_r$$
$$C_c^{j+1} = C_r \quad \text{if} \quad C_c^{j+1} \le C_r \qquad [5.23]$$

The FISH implementation of this model is given in Appendix F.

5.3 Simulation of time-dependent fracture zone behaviour

To illustrate the behaviour of the model described above, the time-dependent fracture zone formation surrounding a 4 m square tunnel subjected to constant field stresses was simulated. The model parameters are given in Table 5.1. Note that these parameters were arbitrarily chosen to illustrate the model behaviour.

Table 5.1. Model parameters used to simulate time-dependent fracture formation surrounding a tunnel.

Parameter	Value
Vertical stress	70 MPa
Horizontal stress	40 MPa
Bulk modulus	27.7 GPa
Shear modulus	20.8 GPa
Density of the rock	2700 kg/m^3
Cohesion of intact rock	22 MPa
Friction angle (peak and residual)	30°
Residual cohesion	15 MPa
Cohesion decay	0.001 day^{-1}
Dilation angle	25°
Fluidity coefficient	1×10^{-11} $Pa^{-1}.day^{-1}$

The extent of the fracture zone at different times is illustrated in Figure 5.5. Soon after development of the tunnel, the failed zone covers those areas where the stresses exceeded the failure strength of the intact rock ($f_s(t) \leq 0$). Time-dependent processes lead to a gradual loss of residual strength in the fractured rock, transferring stress to the unfailed rock. This then also becomes fractured resulting in a time-dependent increase in the extent of the fracture zone as illustrated in Figure 5.5. The resulting horizontal closure of the tunnel is illustrated in Figure 5.6. The initial behaviour, soon after development, is dominated by the viscous response (equation [5.4]) of the rock to changing stress conditions, which in this case are the induced stresses caused by the tunnel development. In the longer term the behaviour is governed by the processes leading to a reduction in rock strength (equation [5.9]). This leads to the steady-state closure regime visible in Figure 5.6 between 50 and 300 days. The effect of different rates of cohesion decay on the steady-state closure rate is illustrated in Figure 5.7. If the field stresses remain constant, the closure will not continue indefinitely as an eventual equilibrium position is attained (unless very weak properties are used). This approach to the equilibrium position is visible in Figure 5.6 as the gradual reduction in closure rate at the end of the data set. If the field stresses however continually increase over a period of time, the steady-state closure will also continue over this period.

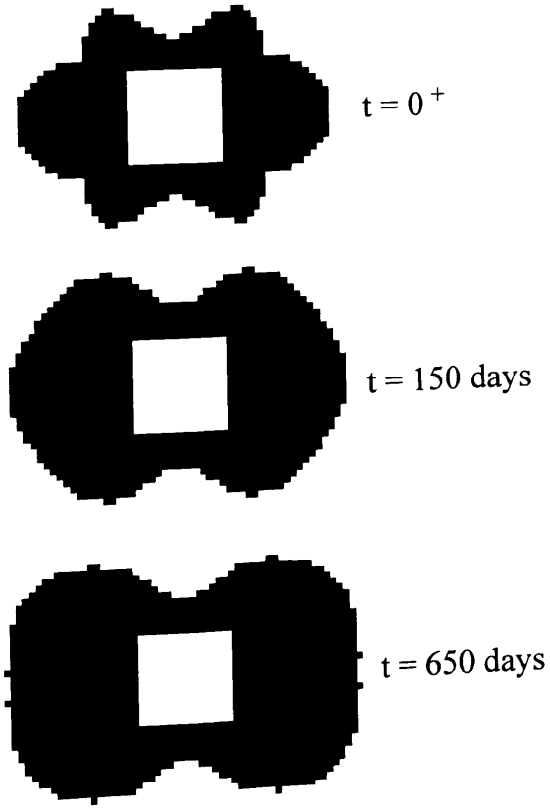

Figure 5.5. Simulated time-dependent fracture zone formation surrounding a tunnel in elasto-viscoplastic rock subjected to constant field stresses.

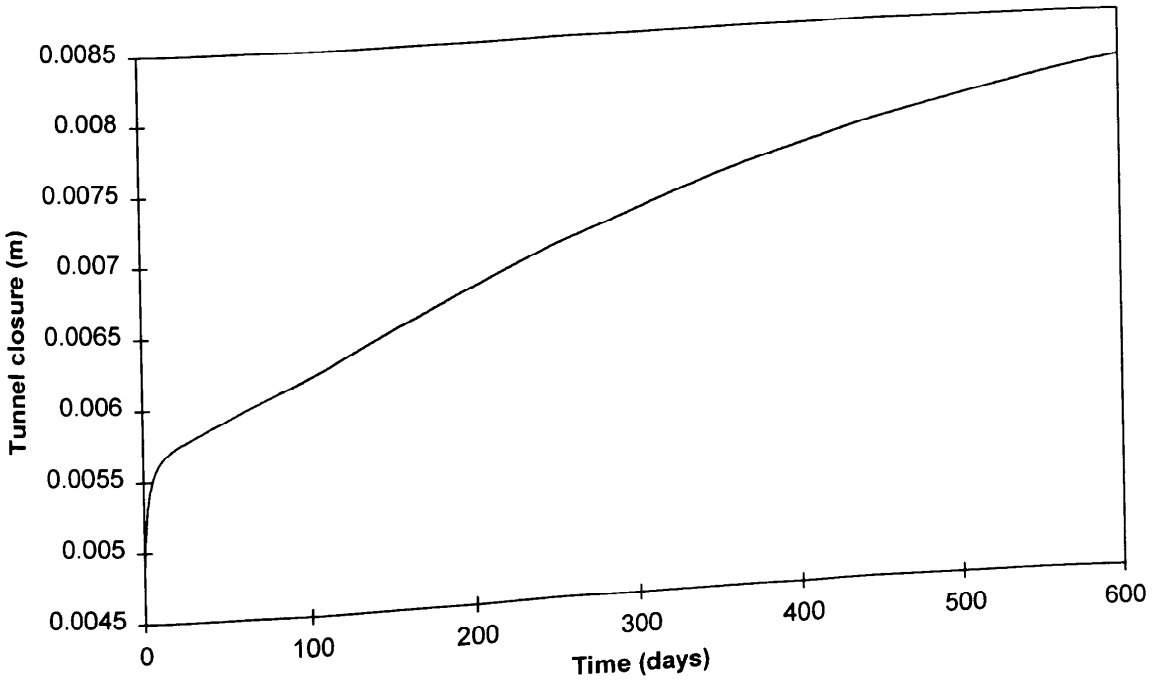

Figure 5.6. Simulated tunnel closure (sidewall - sidewall) as a function of time caused by the time-dependent fracture zone formation described above.

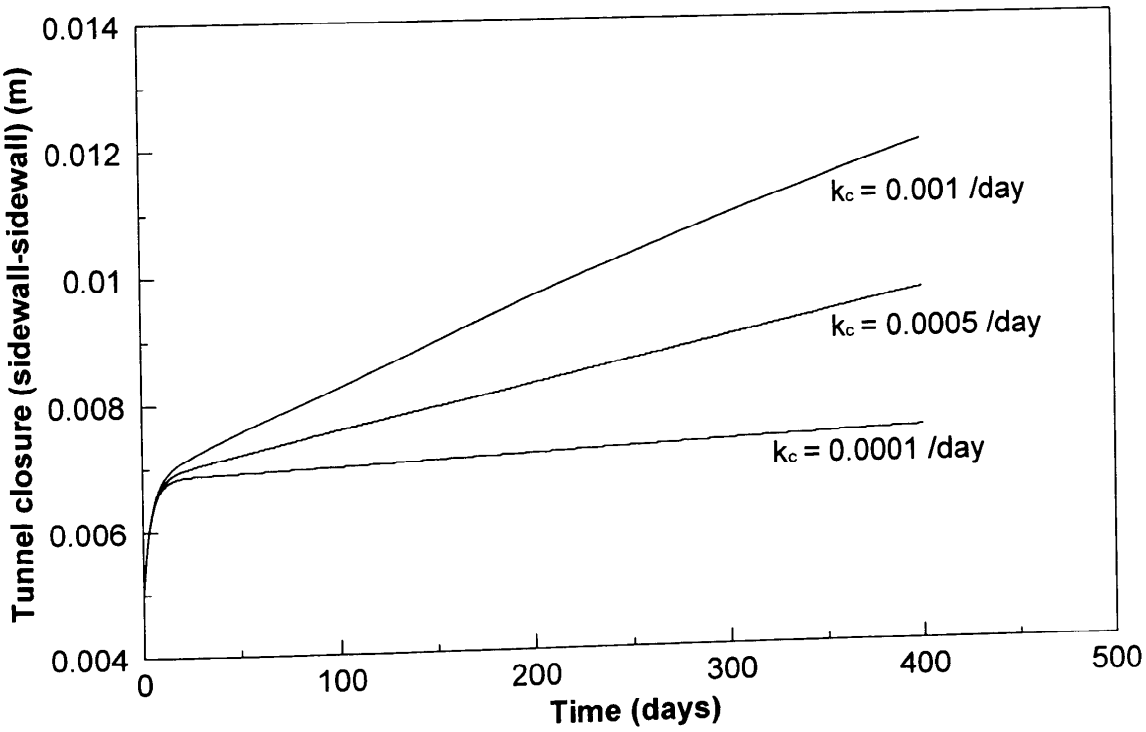

Figure 5.7. Effect of different rates of cohesion decay on the closure behaviour of the tunnel.

5.4 Simulating time-dependent closure of tabular excavations

To investigate the applicability of the model for simulating time-dependent stope closure, the incremental mining of a panel was investigated. Figure 5.8 illustrates the geometry used with three increments mined. The size of the finite difference mesh was 100 × 80 elements, appropriately graded to ensure that the boundaries were sufficiently far away from the stope. The size of the elements in the area of the stope was 0.2 m while the size of each mining increment was 1 m. Quarter symmetry was used to save on the number of elements. The stoping width was 1 m although only 0.5 m is shown in Figure 5.8 because of the imposed symmetry. Although the model appeared successful in replicating the closure behaviour as explained below, excessive computer run-times were recorded. The explicit solution scheme of FLAC requires a small timestep to ensure stability. After a large instantaneous stress change (for example after a mining increment), the timestep needs to be very small. Only as a new equilibrium is attained, can the timestep be progressively enlarged. The run-time for ten mining increments in the simulation of Figure 5.8 with weak rock properties can easily exceed 72 hours on a 200 MHz Pentium computer. This currently prohibits the simulation and calibration of incremental stope behaviour if the span is large. It should be noted that these

restrictions only apply to the incremental mining of tabular stopes and not to the simulation of tunnel behaviour where only one mining increment needs to be considered. For some of the illustrative stope problems in this section, a low number of mining increments was used with high field stresses to obtain the required high stresses ahead of the face.

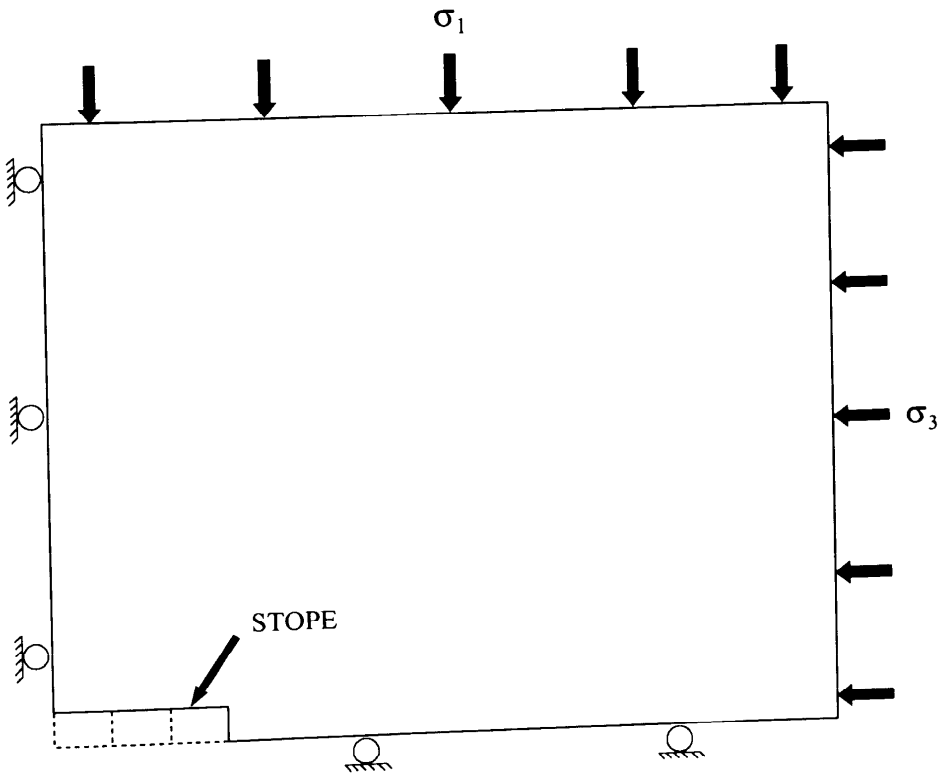

Figure 5.8. Geometry and boundary conditions used for simulating tabular excavations (not drawn to scale).

To investigate the closure behaviour of tabular excavations predicted by the model, eight increments were mined (giving a total span of 16 m) using the model properties given in Table 5.2. Typical closure results are given in Figure 5.9 as a function of time after mining the 8th increment. For the two distances from the face, behaviour similar to that noted for the experimental results of the Ventersdorp Contact Reef is obtained. The incremental jump after blasting is reduced as the distance to face increases. Furthermore, the closure rate of the steady- state phase also decreases into the back area. This is significant as this behaviour cannot be simulated with a viscoelastic model as explained in Chapter 4. The viscoplastic model approximates the time-dependent failure processes and therefore gives an improved closure response.

Table 5.2. Properties used for the incremental mining of the tabular stope to obtain the results in Figure 5.9.

Parameter	Value
Vertical stress	90 MPa
Horizontal stress	45 MPa
Bulk modulus	38.9 GPa
Shear modulus	29.2 GPa
Density of the rock	2700 kg/m^3
Cohesion of intact rock	22 MPa
Friction angle (Both peak and residual)	30°
Residual cohesion	10 MPa
Cohesion decay	0.005 h^{-1}
Dilation angle	0°
Fluidity coefficient	1×10^{-10} $Pa^{-1}.h^{-1}$

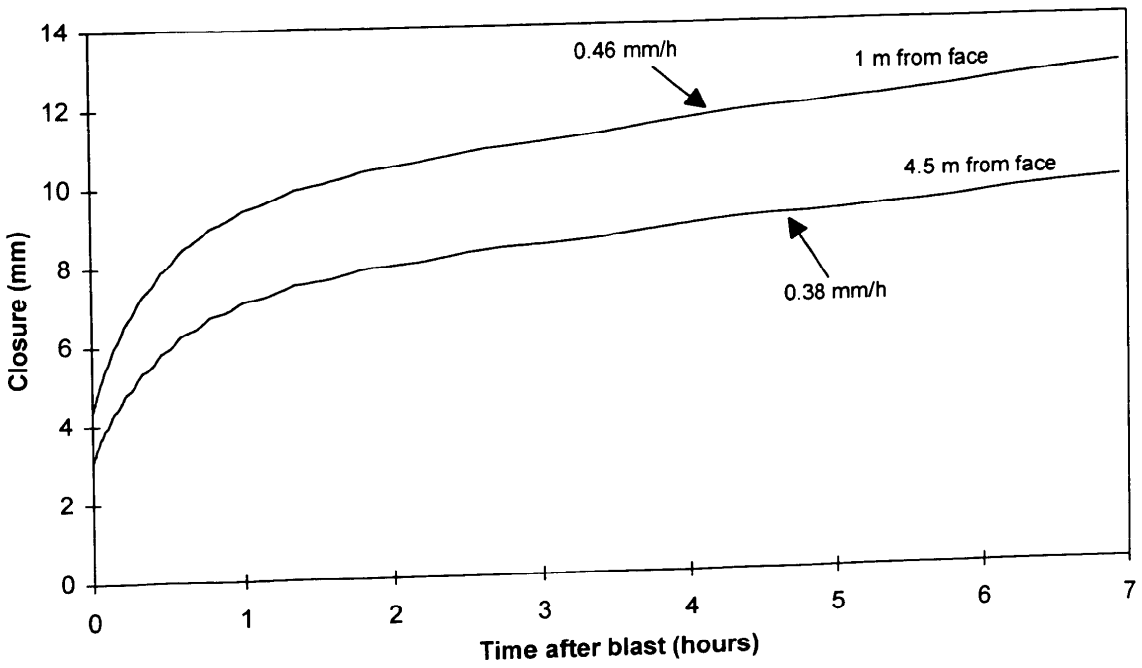

Figure 5.9. Simulated time-dependent closure. The distances were the original distance to face before mining the increment. The steady-state closure rate was calculated between 2 hours and the end of the data set.

In Chapter 4 (Section 4.5) it was suggested that the instantaneous closure after blasting is an indication of the proximity of the stress peak to the face. This hypothesis was tested by numerically mining two stopes (two increments each) in rock with different properties. These properties are given in Table 5.3. The only difference in properties for these stopes is the

different rates of cohesion decay. This resulted in the rock ahead of the face of Stope B losing its strength much faster than ahead of Stope A and therefore carrying less load. This is illustrated in Figure 5.10 where the major principle stress is plotted as a distance ahead of the original face position just before the second increment is mined. Visible in this figure is the stress peak for both stopes some distance ahead of the face. With sufficient distance from the face, the stress magnitude is reduced to the virgin value. For Stope A with the stronger rock, the peak is closer to the face. The next increment of mining will remove the first metre of rock thereby forcing the stress carried by this increment to be instantaneously redistributed. As the average stress in this increment of rock is larger for Stope A than Stope B, it is expected that the instantaneous closure will be bigger for A. This is confirmed by the closure that followed this increment in Figure 5.11. For Stope A the instantaneous closure was 3.7 mm compared to the 2.5 mm for Stope B. This confirms the hypothesis that the instantaneous closure underground can be used as an indication of the proximity of the stress peak to the face and therefore an indicator of face bursting hazard. Following the instantaneous closure, the steady-state closure for Stope B is larger as the failed rock loses its strength faster resulting in greater time-dependent deformation.

Table 5.3. Parameters used in the simulation to obtain the results in Figure 5.10 and 5.11.

Parameter	**Value**
Vertical stress	110 MPa
Horizontal stress	55 MPa
Bulk modulus	38.9 GPa
Shear modulus	29.2 GPa
Density	2700 kg/m^3
Cohesion of intact rock	10 MPa
Friction angle (Both peak and residual)	30°
Residual cohesion	3 MPa
Cohesion decay	Stope A : $1x10^{-10}$ h^{-1} Stope B : 0.01 h^{-1}
Dilation angle	15°
Fluidity coefficient	1×10^{-10} $Pa^{-1}.h^{-1}$

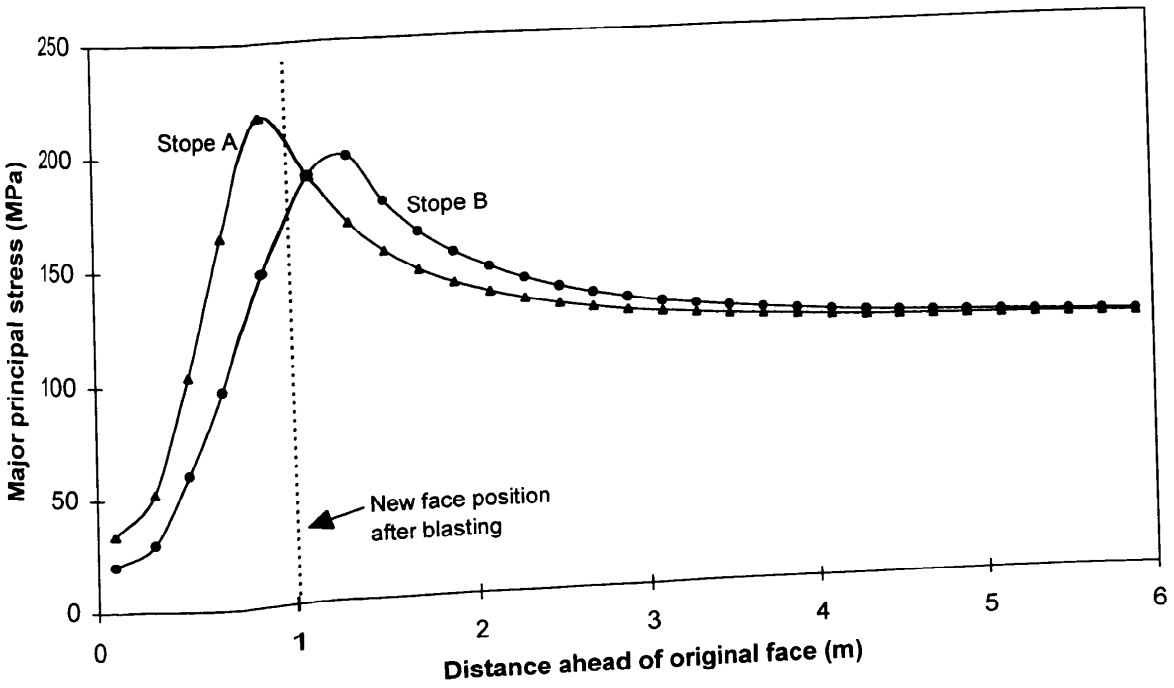

Figure 5.10. Comparison of the major principal stress as a function of distance ahead of the face. These stresses were calculated in the centre of the reef (midway between the future hangingwall and footwall).

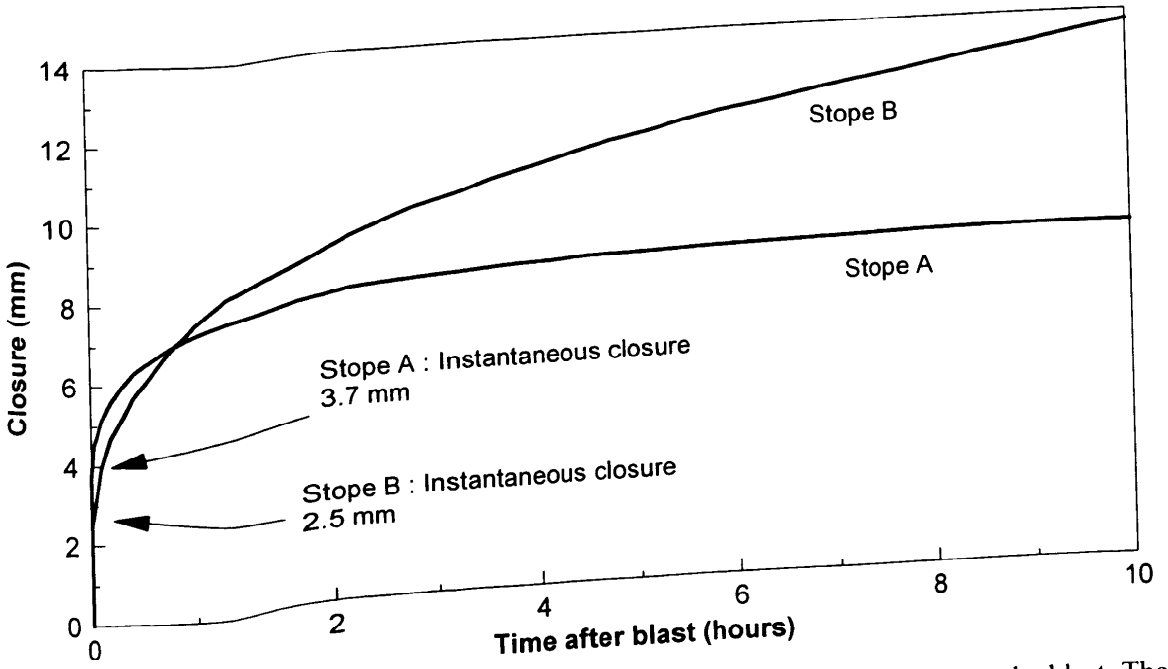

Figure 5.11. Comparison of the closure behaviour as a function of time after the blast. The measurement position was 0.5 m behind the original face.

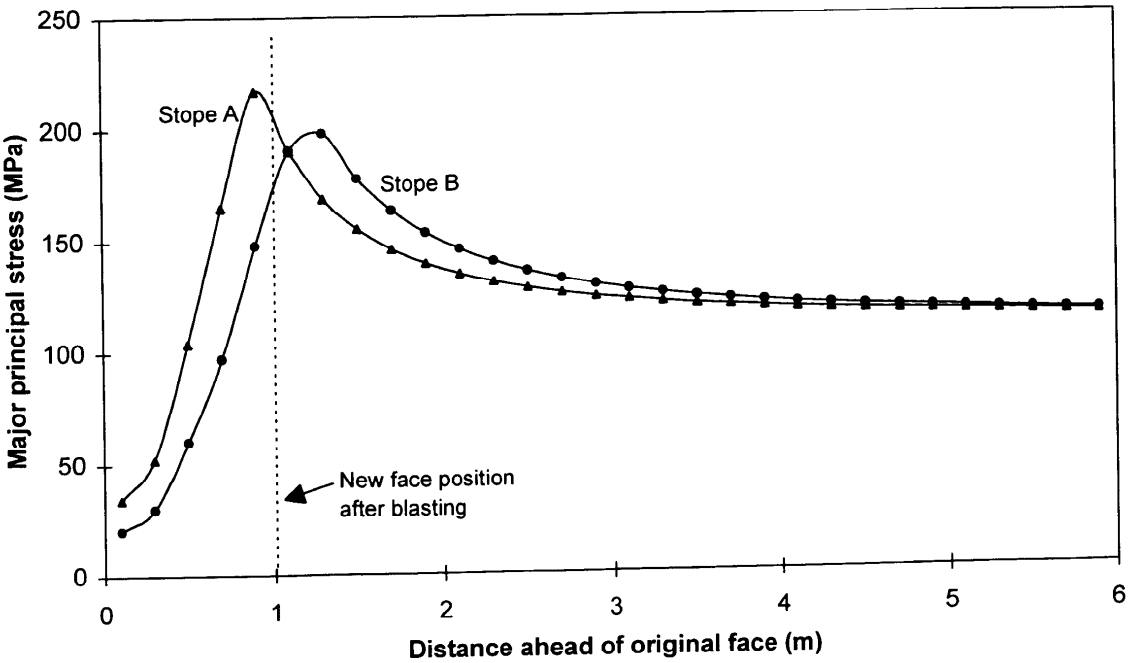

Figure 5.10. Comparison of the major principal stress as a function of distance ahead of the face. These stresses were calculated in the centre of the reef (midway between the future hangingwall and footwall).

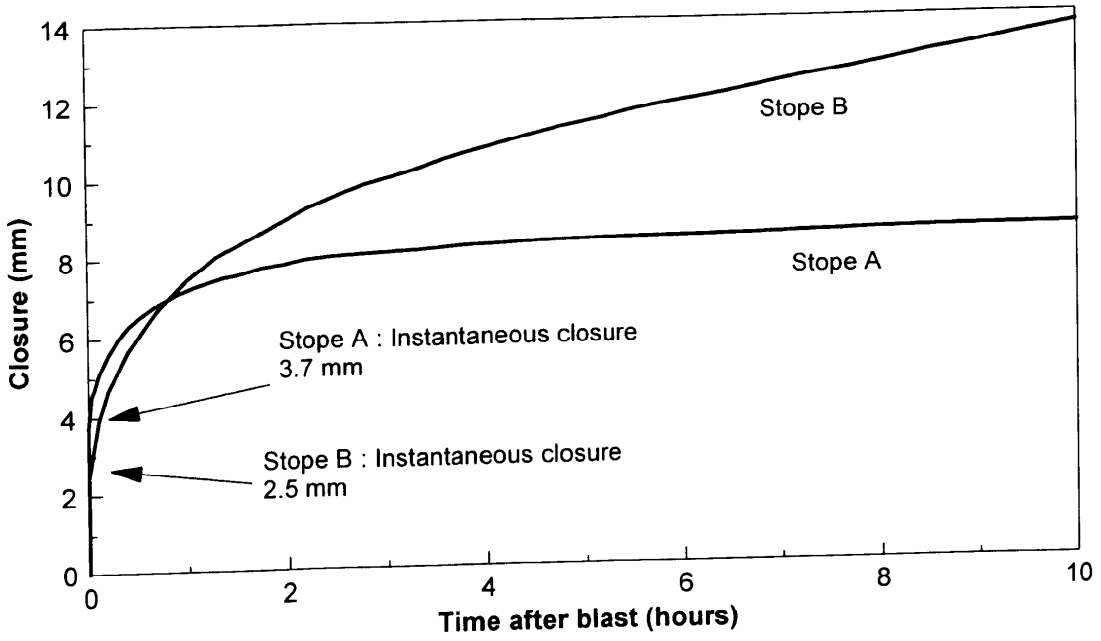

Figure 5.11. Comparison of the closure behaviour as a function of time after the blast. The measurement position was 0.5 m behind the original face.

Figure 5.10 illustrates the position of the peak stress 24 hours after mining an increment. This position is not stationary but moves as the time-dependent fracture processes occur in the rock. To illustrate this, Figure 5.12 illustrates the stress peak for various times after mining the increment of Stope B. Soon after the blast the peak is high and located close to the face. With time it moves away, due to the fracture processes, and gradually becomes smaller. Of significance is that the biggest stress change happens within the first five hours. This may explain why the majority of seismic events underground occur in the short period after blasting.

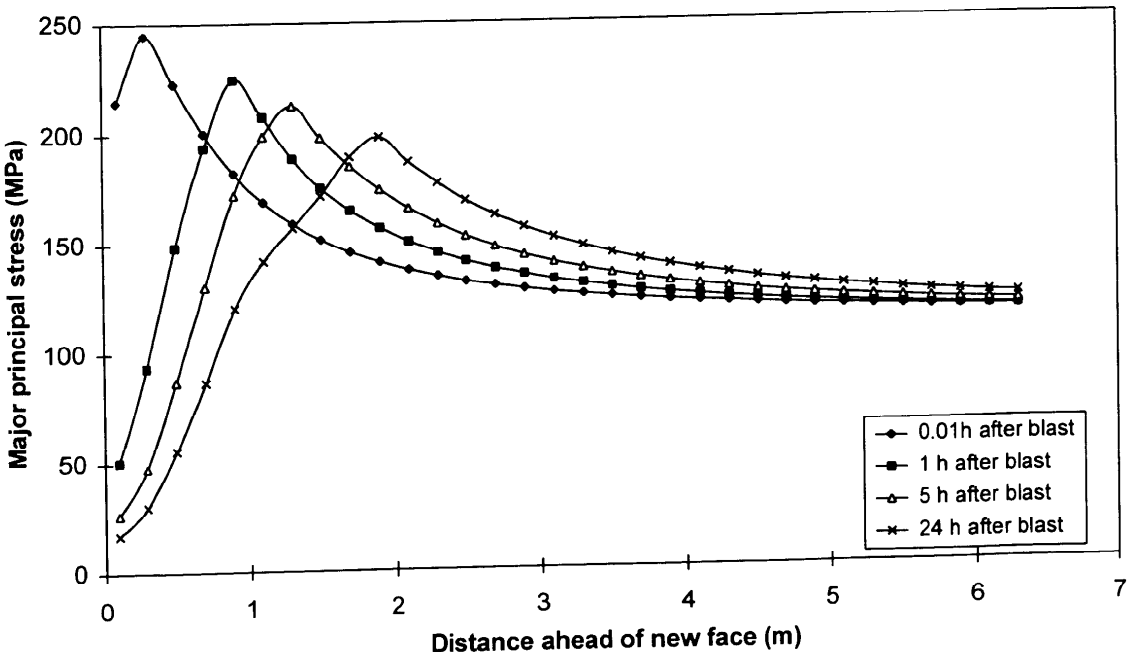

Figure 5.12. Simulated time-dependent movement of the major principal stress peak ahead of the face after blasting.

In the examples above, arbitrary model parameters were used to illustrate the processes. Due to the success of this model in simulating the time-dependent fracture process, it is desirable to calibrate these parameters using underground closure data. The two-dimensional plain strain version of FLAC was used and therefore only geometries where these assumptions can be made are appropriate. In Chapter 4 such data from Deelkraal Mine was used to calibrate the viscoelastic model. Unfortunately the span of this stope was 200 m. As the results obtained from viscoplasticity theory are path dependent, this span cannot be simulated in one mining increment. Mining 100 increments (using symmetry) is however impractical as explained earlier in this section. Therefore data was needed where the span of the stope was small. Closure data collected by Kersten (1995) at Hartebeestfontein Mine in 1965 was used. The

experimental site consisted of two isolated breast panels that were being ledged from a raise and a two-dimensional approximation could be made. The instrumented panel was situated at a depth of 1850 m with a span of 20 m. The actual stress conditions and rock parameters are not known accurately and therefore the objective of this simulation was not exact parameter calibration, but an attempt to replicate the observed profiles. The closure fitting process was found to be very arduous as ten mining increments (using symmetry) had to be mined. An initial guess of parameters was used and after the 10th increment, the closure was compared with the experimental values. This process was repeated many times and it was found that the path dependence made it virtually impossible to achieve the desired closure by making small changes in the parameter values before the first increment. In spite of these problems, it should be noted that the closure behaviour of the viscoplastic model gives similar trends to that of the underground measurements. Figure 5.13 shows the experimental data and numerical results for a fluidity coefficient of $1x10^{-10}$ $Pa^{-1}h^{-1}$ and a cohesion decay rate of 0.005 h^{-1}. Other parameters used were bulk modulus = 38.8 GPa, shear modulus = 29 GPa, cohesion = 22 MPa, residual cohesion = 15 MPa and friction angle (peak and residual) = 30°. In the model the stope was mined incrementally to the required span using 1 m increments. The numerical result shown in Figure 5.13 was obtained after six increments and not the required ten.

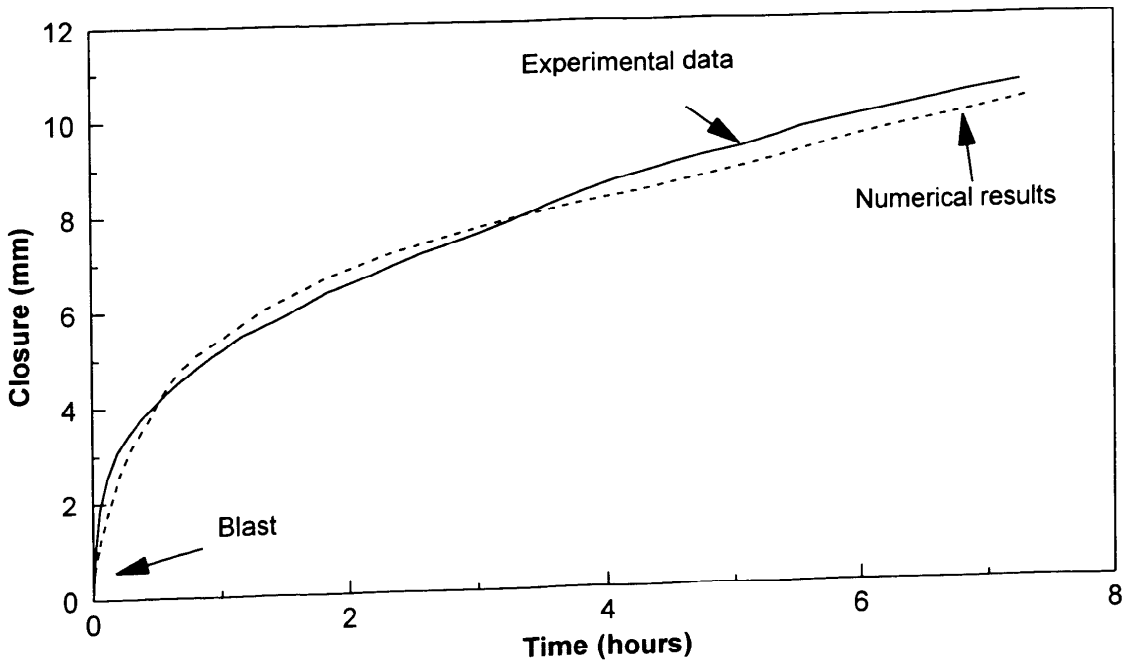

Figure 5.13. Experimental and simulated stope closure after blasting.

As a result of these calibration problems, it is suggested that experimental data should be collected from a panel where the span is still small (< 10 m).

5.5 Analysis of pump chamber deformation at Hartebeestfontein Mine

As described in Chapters 1 and 4, the rock at Hartebeestfontein Mine experiences significant time-dependent rock behaviour. The problems caused by these movements were highlighted in a research study (Piper and Wagner, 1982) to evaluate the long term stability of an underground refrigeration complex at No. 6 shaft of the mine. It was suggested in this study that the long term stability of the refrigeration chamber could not be assured even with the upgrading of the support system. Further measurements and extensometer data showed an acceleration of chamber closure as the No. 6 shaft pillar became progressively more isolated (Roberts and Jager, 1988). It was unclear at that stage how much of this behaviour was caused by true time-dependent rock behaviour and how much by an increase in stress due to far-field mining activity. With deteriorating conditions, the refrigeration chamber was eventually relocated to overstoped ground.

A pump chamber situated in the shaft pillar on 71 level at No. 6 shaft was instrumented by the mine staff as part of an ongoing programme to monitor rock behaviour in the shaft area. The data was made available to the author to examine the applicability of the developed viscoplastic model to simulate this behaviour. The extent of the mining surrounding this shaft pillar is illustrated in Figure 4.21 (Chapter 4). The pump chamber was developed in argillaceous quartzites having similar properties for the hangingwall and footwall. The properties of these rocks were given in Table 2.1 in Chapter 2. The dimension of the chamber was 18.5 m × 6 m × 3.5 m. Support consisted of 6 m, 40 ton cable anchors in a diamond pattern and 2.2 m (16 mm diameter) smooth bar shepherd crooks in a 1 m square pattern. The entire excavation was meshed and laced using the shepherds crook reinforcing units as anchors. The footwall was unsupported. Figure 5.14 is a schematic diagram of the excavations surrounding the chamber. On the south side of the chamber the rock is undisturbed, while a haulage intersects the chamber obliquely to the north. To monitor any vertical stress change, a vibrating wire stress meter was installed in the south sidewall at a depth of 9 m. This measured an increase of 3 MPa over a period of nearly 600 days from December 1994 to June 1996 (Figure 5.15). This increase was caused mainly by stoping operations in the area surrounding the shaft pillar. The increase in stress predicted by an elastic MINSIM analysis (see Napier and Stephansen, 1987 for a description of MINSIM) over this period is also plotted. The windows used in the MINSIM analysis included all of the mined areas illustrated in Figure 4.21. The trend in Figure 5.15 for the measured and simulated stress is similar, although the magnitude predicted by MINSIM is smaller. It should be noted that none of the service excavations in

Figure 5.14 was simulated in the MINSIM analysis. It is not clear what effect these excavations and the growing fracture zone surrounding these excavations have on the stress measured by the vibrating wire stress meter.

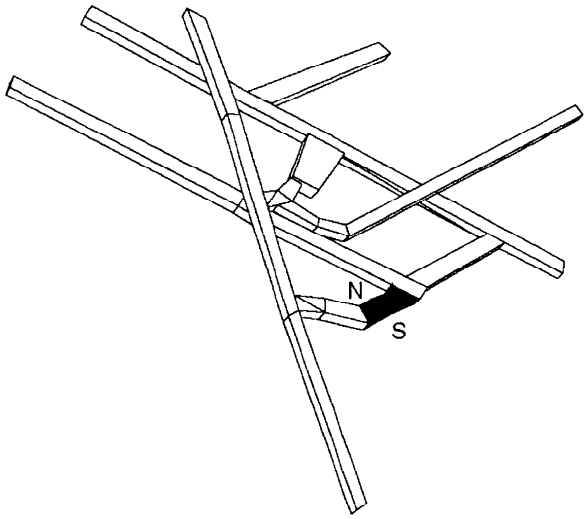

Figure 5.14. View of the excavations surrounding the pump chamber. The letters indicate the north and south sidewalls of the chamber.

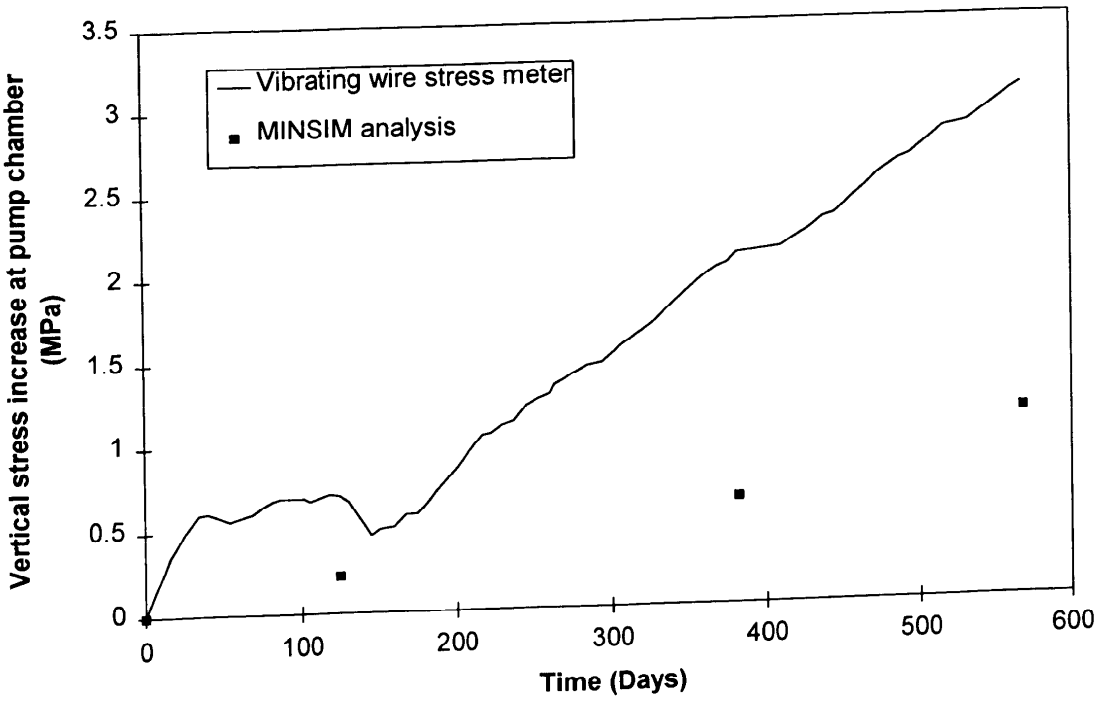

Figure 5.15. Increase in vertical stress measured at the pump chamber. The increase in stress calculated from an elastic analysis (MINSIM) due to progressive mining of the area surrounding the shaft pillar is also plotted.

Deformation of the rock was measured by installing rod extensometer stations in the footwall, hangingwall and sidewalls. Each measuring station consisted of five rods of different lengths anchored at depths of 2, 3, 4, 5 and 6 m. The resulting measurements therefore gave the relative movement between the surface of the excavation and the rock at different depths. All measurements showed strong time-dependent behaviour, although some of the deformation can be attributed to the slight increase in stress. The footwall measurements are given in Figure 5.16. These indicate large rock deformation at a depth of 3 m to 4 m. This can probably be ascribed to opening on bedding planes at that depth. In comparison the data from the hangingwall shows less movement (Figure 5.17). Most of the movement occurs within the first two metres with very little deformation deeper in the rock. As the rock properties in the hangingwall and footwall are identical, it appears that the absence of support in the footwall leads to enhanced deformation.

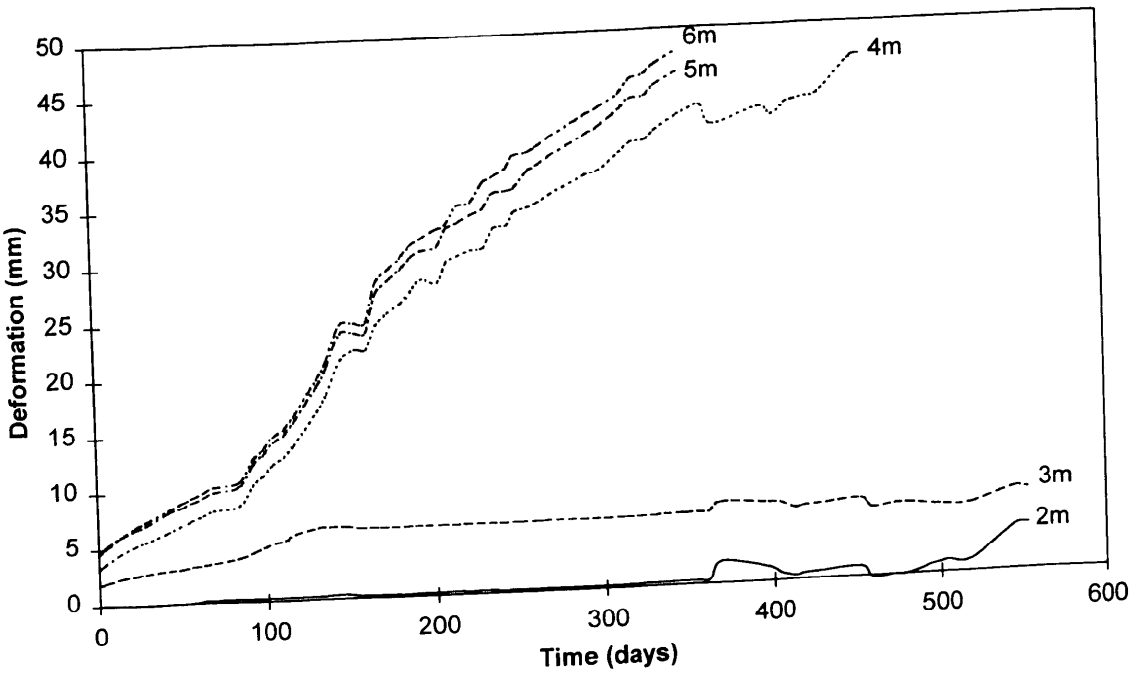

Figure 5.16. Footwall deformation of the pump chamber measured with rod extensometers anchored at different depths.

In the south sidewall (Figure 5.18), behaviour similar to the hangingwall is experienced with most of the movement taking place within the first two metres and very little between 2 m and 6 m. The north sidewall (Figure 5.19) experienced larger deformations and significant differences between the various extensometers. A three-dimensional elastic stress analysis using the code MAP3D (Mine Modelling Limited, 1995) indicated higher vertical stress conditions on the north side of the chamber, caused by the nearby haulage. Figure 5.20

displays the contours of maximum principal stress. The higher stress conditions may explain the difference in behaviour between the two sidewalls.

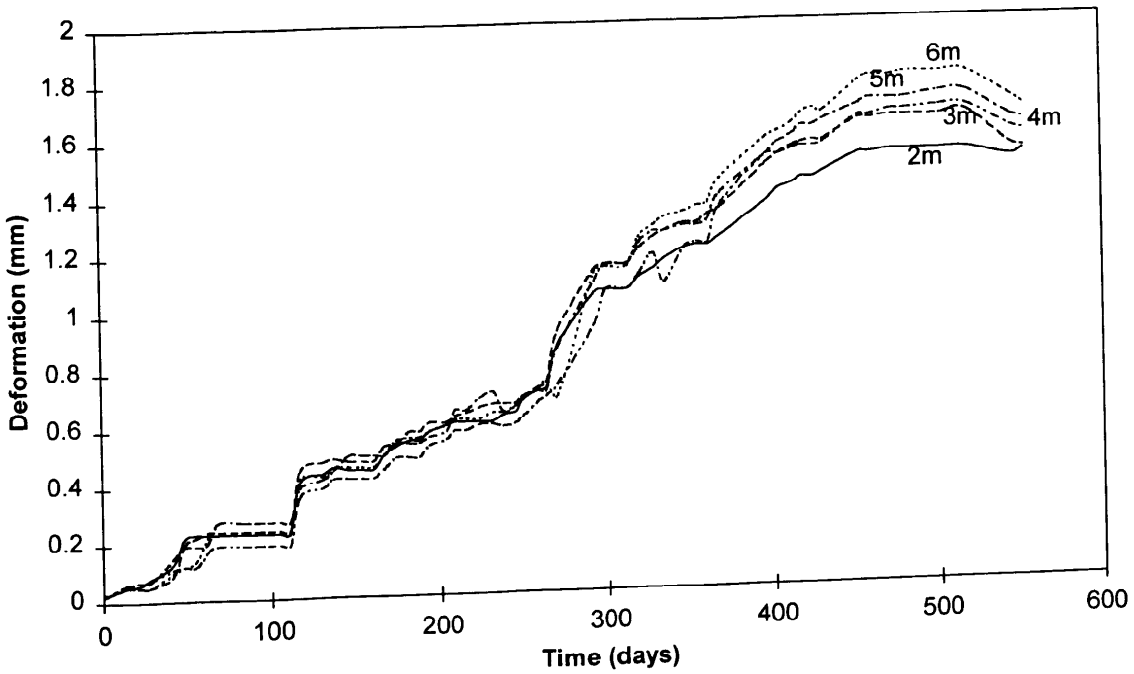

Figure 5.17. Hangingwall deformation of the pump chamber measured with rod extensometers anchored at different depths.

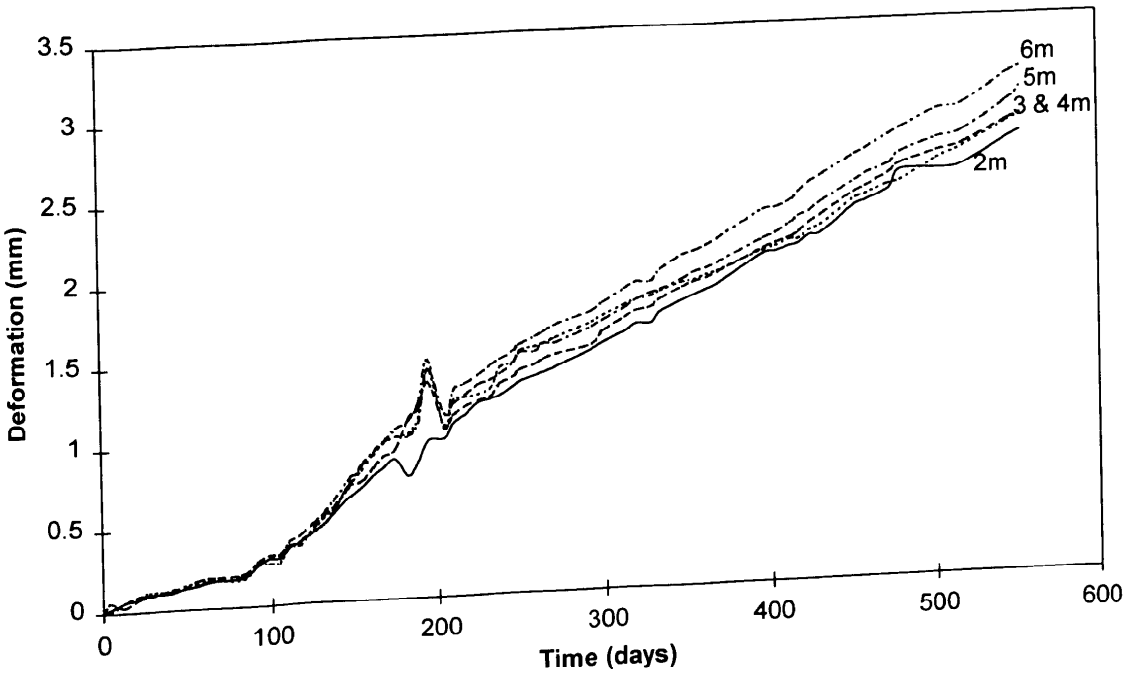

Figure 5.18. Sidewall deformation on the south side of the pump chamber measured with rod extensometers anchored at different depths.

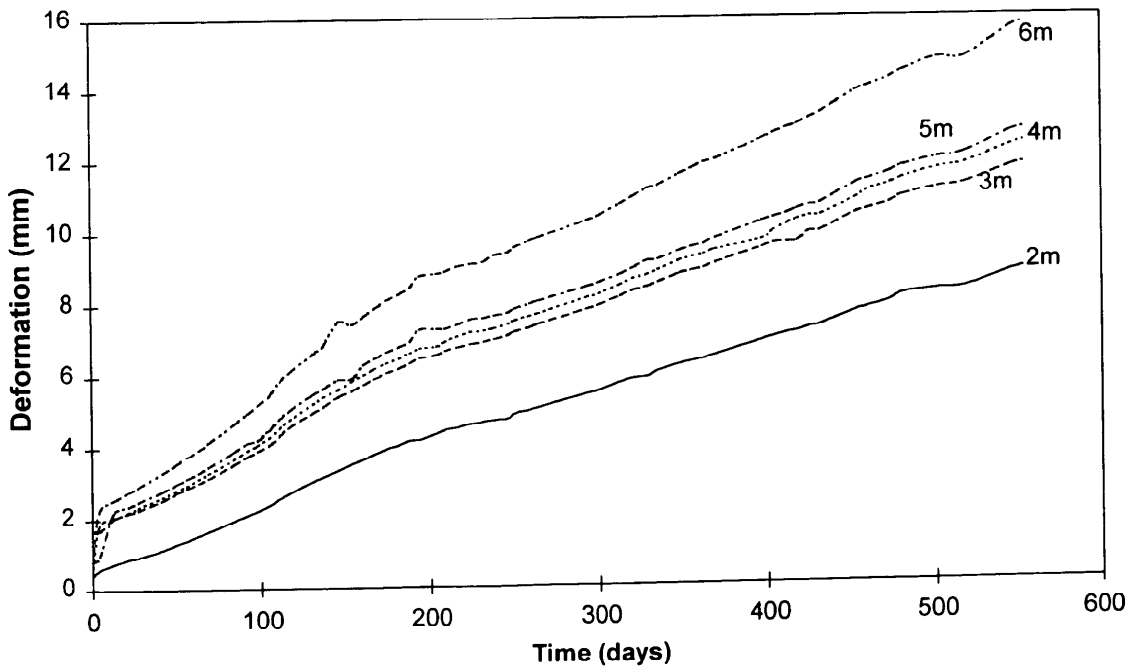

Figure 5.19. Sidewall deformation on the north side of the pump chamber measured with rod extensometers anchored at different depths.

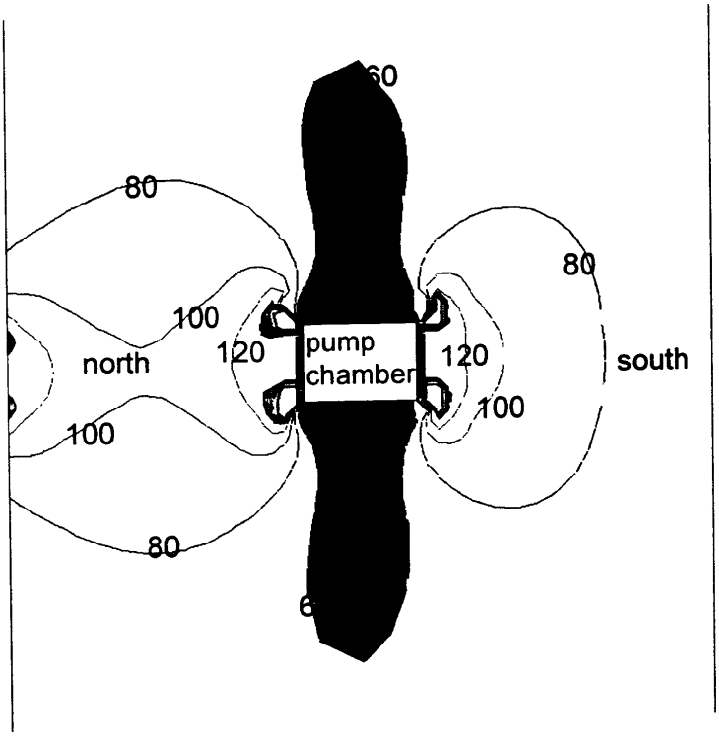

Figure 5.20. Major principal stress contours (MPa) surrounding the pump chamber on a plane normal to the long axis of the excavation. In the third dimension, the plane is situated at the centre of the chamber. These elastic values were calculated using the three-dimensional elastic solver MAP3D.

In an attempt to simulate the higher stresses on the north side of the chamber in the two-dimensional FLAC model, a second excavation was modelled on this north side. The major principal stress contours are plotted in Figure 5.21. Compared to Figure 5.20, adding the second excavation appears to give more representative values for the major principal stresses on the north side. This is however only true for a plane in the centre of the excavation in the three-dimensional case. Furthermore, the intermediate and minor principal stresses on the north side are probably not an accurate representation of reality in the two-dimensional model.

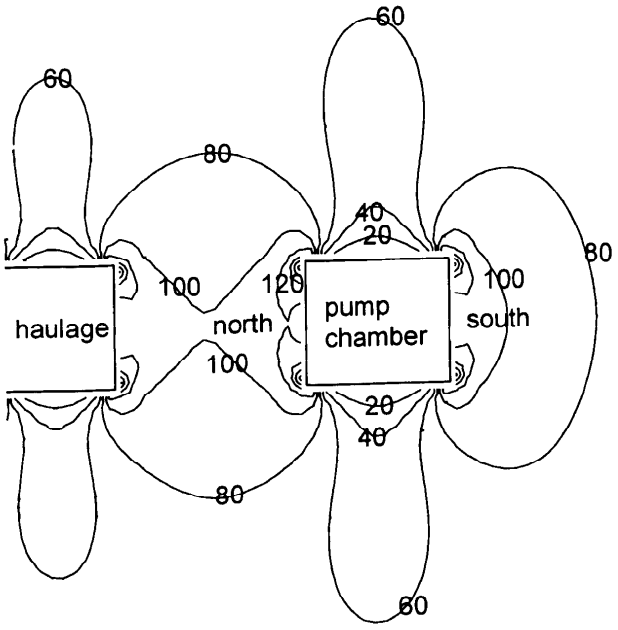

Figure 5.21. Major principal stress contours (MPa) before failure using the developed two-dimensional elasto-viscoplastic code. The haulage on the left was included to obtain a more representative magnitude of major principal stress on the north side of the pump chamber.

In the model the 6 m cable anchors were simulated using the pattern illustrated in Figure 5.22. The parameters used for these cables were an elastic modulus of 100 GPa and a tensile yield strength of 4×10^5 N. The 2.2 m anchors and the wiremesh and lacing were not simulated. The other parameters used in the simulation are given in Table 5.4. Note that the vertical stress was linearly increased by 3 MPa and the horizontal stress by 1.5 MPa over the period of the simulation to model the increase in stress as illustrated in Figure 5.15. To simulate the extensometer data, the relative displacements between the surface of the excavation and node points at the appropriate depth were calculated. Figure 5.23 illustrates the results for the 2 m anchor in the south sidewall. Although a good fit is obtained, the model underestimates the deformation at the north sidewall (Figure 5.24). This can possibly be attributed to the poor representation of minor and intermediate principal stresses on the north side of the model.

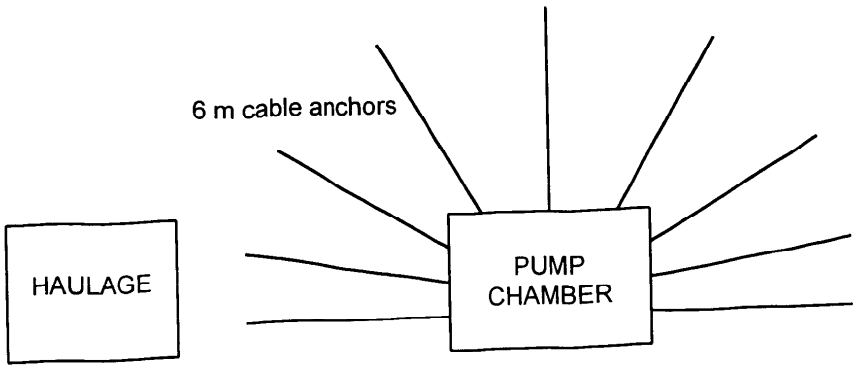

Figure 5.22. Pattern of cable anchor support simulated in the model.

Table 5.4. Parameters used to simulate the pump chamber deformation. The vertical and horizontal stresses were increased as discussed above.

Parameter	**Value**
Initial vertical stress	70 MPa
Initial horizontal stress	35 MPa
Bulk modulus	27.7 GPa
Shear modulus	20.8 GPa
Density	2700 kg/m^3
Cohesion of intact rock	23 MPa
Friction angle	30°
Residual cohesion	15 MPa
Cohesion decay	0.0005 day^{-1}
Dilation angle	20°
Fluidity coefficient	2.4×10^{-10} $Pa^{-1}.day^{-1}$

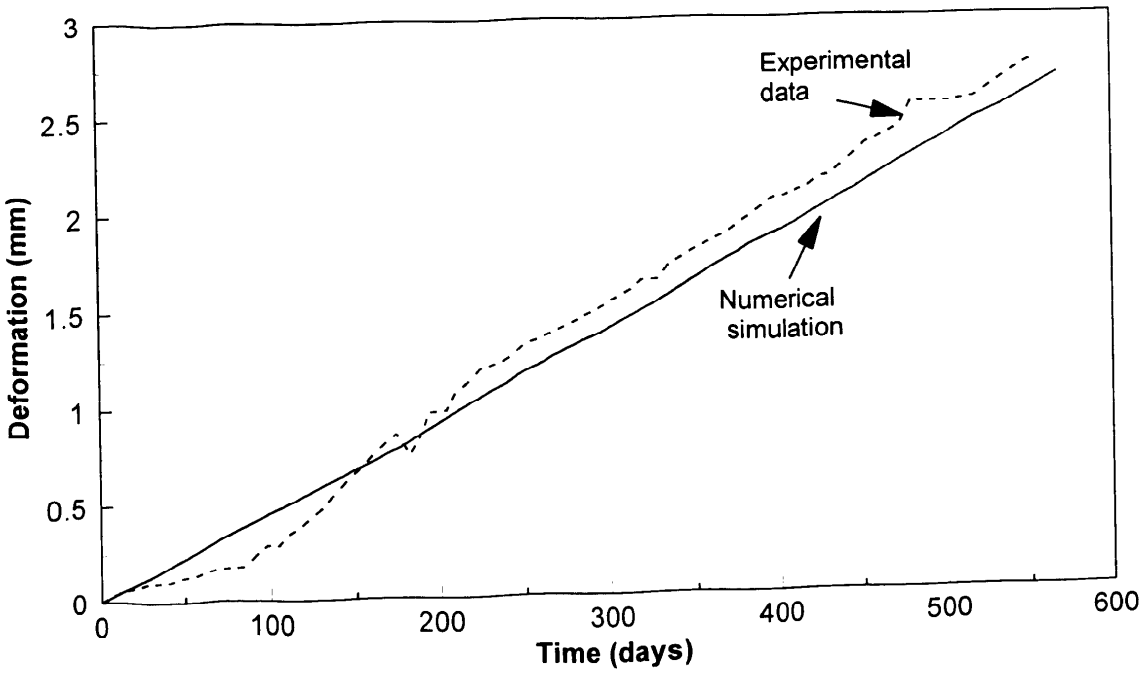

Figure 5.23. Comparison between the numerical simulation and experimental data for the 2 m extensometer on the south side of the pump chamber.

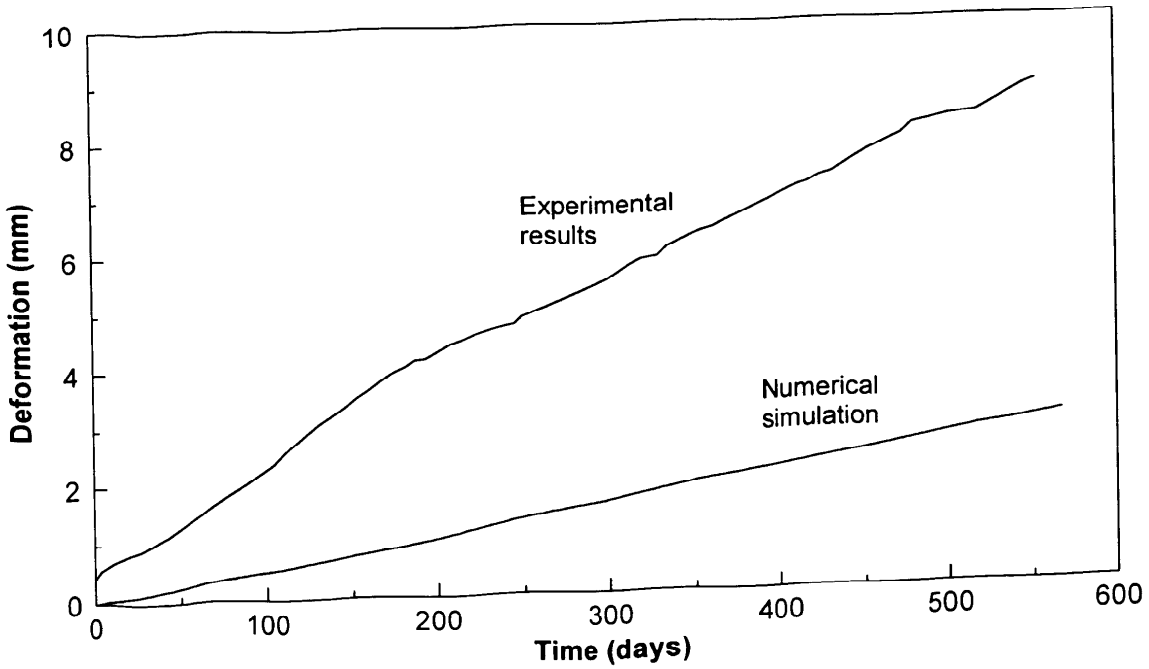

Figure 5.24. Comparison between the numerical simulation and experimental data for the 2 m extensometer on the north side of the pump chamber.

In the model most deformation tends to occur within the first 2 m of the excavation surface. This is similar to the observations for the underground data of the south sidewall. The data fit was poor for the extensometer data in the hangingwall and footwall. This is not unexpected for the footwall as the continuum approximation cannot simulate behaviour dominated by prominent discontinuities like opening displacements on bedding planes. Of significance is the difference between surface deformation of the hangingwall and footwall. As with the real chamber, the cable anchor support in the model was not installed in the footwall, leading to enhanced deformations (Figure 5.25).

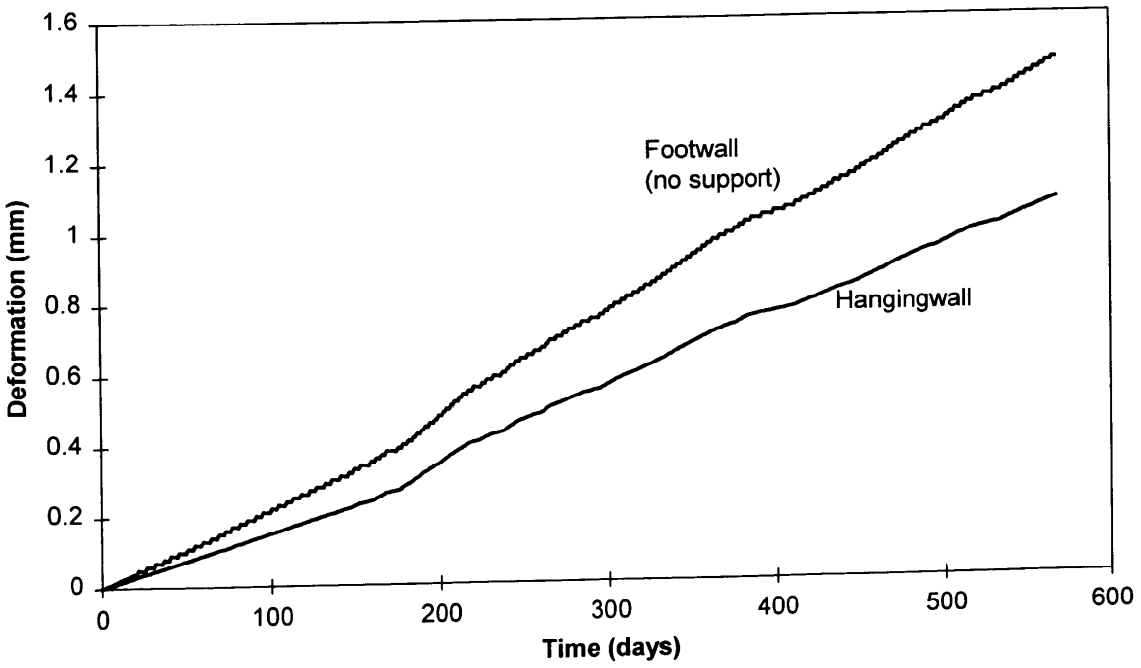

Figure 5.25. Numerical results for the surface deformation of the footwall and hangingwall.

5.6 Effect of support in the squeezing conditions at Hartebeestfontein Mine

As explained in Chapter 1 (Section 1.2), the significant time-dependent deformation of the rock at Hartebeestfontein Mine leads to severe support problems. Figure 5.26 illustrates the typical bulging of haulage support caused by slow time-dependent fracture processes. Significant footwall heave is also noticeable. Eventually the support fails entirely leading to the destruction illustrated in Figure 1.1 in Chapter 1.

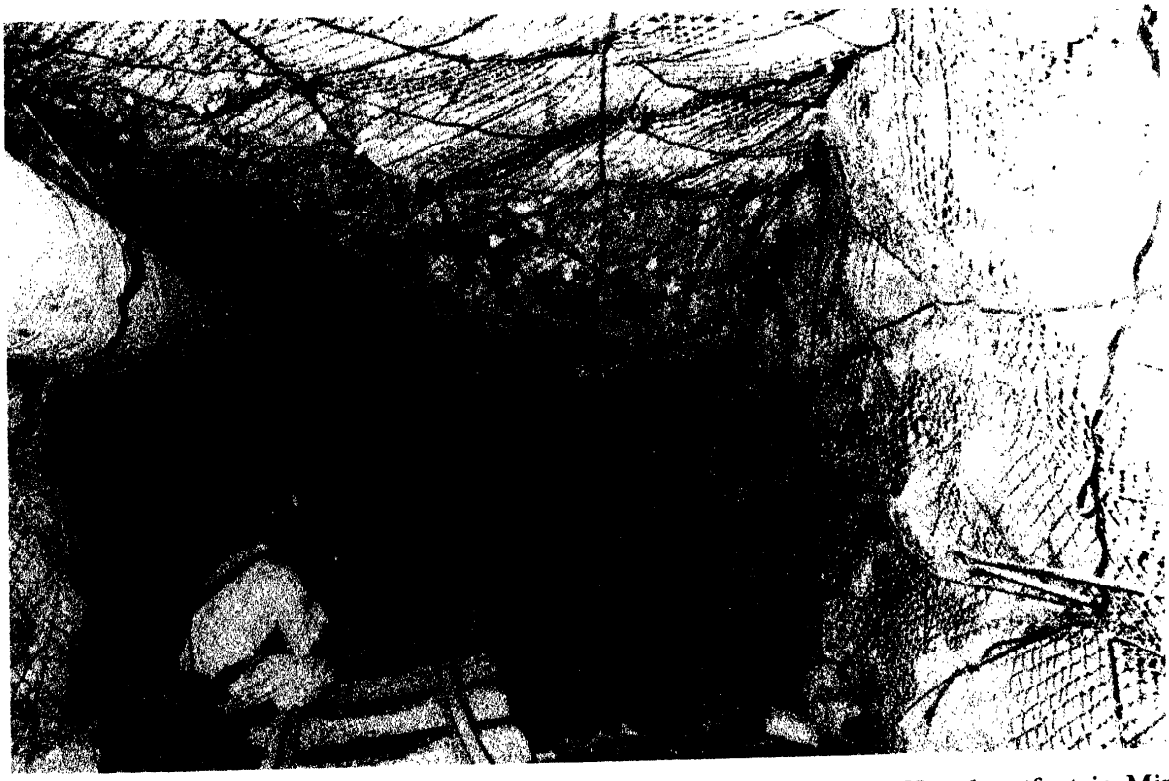

Figure 5.26. Haulage conditions experienced in the squeezing rock at Hartebeestfontein Mine (courtesy W.D. Ortlepp). Note that this is not rockburst damage.

It is clear from the squeezing tunnels at Hartebeestfontein Mine that typical haulage support consisting of anchors and wiremesh and lacing is not effective in controlling the massive time-dependent deformations (Malan and Bosman, 1997). From observations and closure measurements, it nevertheless appears that 2.2 m anchors with areal support, such as wiremesh and lacing, bind the fracture zone surrounding the excavation into a quasi-coherent structure which, to some degree, resists and abates the massive deformation. Once this structure is broken, either by massive support failure or intentional bleeding to increase the cross-sectional area of the excavation, deformation becomes uncontrollable. Unfortunately failure of the structure is a reality at some point in the life of the excavation. Once failure has taken place and support rehabilitation is complete, the process has been observed to repeat itself. Investigations of numerous massive collapses have revealed that only approximately 50 % of the anchors fail. Anchors predominantly fail in tension, although occasional shear failure is observed. The effect of support on excavation stability is shown by the fact that deformation in most cases is evident in the footwall first, where no support is installed. In areas where 6 m long 400 kN anchors have been installed, the closure rate appears to be less than in areas where only 2.2 m smooth bars have been used. Yielding anchors have been installed in excavations without significant benefit. It appears that any support that is capable of binding the fracture zone into a more coherent structure, delays catastrophic failure, but not indefinitely.

To illustrate the effect of support, a 4 m square tunnel was numerically simulated using properties similar to those given in Table 5.1. Cable anchors with a failure strength of $4x10^5$ N were installed using the pattern illustrated in Figure 5.27. An artificially high cable modulus of 150×10^{11} Pa was used to illustrate the effect of support failure within a reasonable period of modelling time. The cable anchor formulation in FLAC is such that before yield, the modelled anchors behave in a linearly elastic fashion and, after yielding, in a perfectly plastic fashion. The effect of the support is illustrated in Figure 5.28. As the axial forces build up in the cables, the closure rate of the tunnel decreases slightly. This is caused by the introduction of extra confining forces on the rock, reducing the rate of the time-dependent weakening process. The rate increases again after the failure strength of the anchors has been reached, but is still less than the original closure rate. Although the support is yielding, it maintains a confining force on the rock.

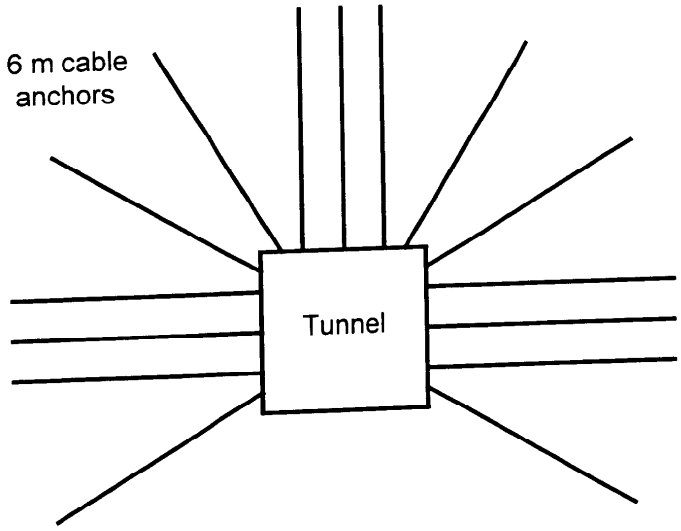

Figure 5.27. Cable anchor support used in the simulation.

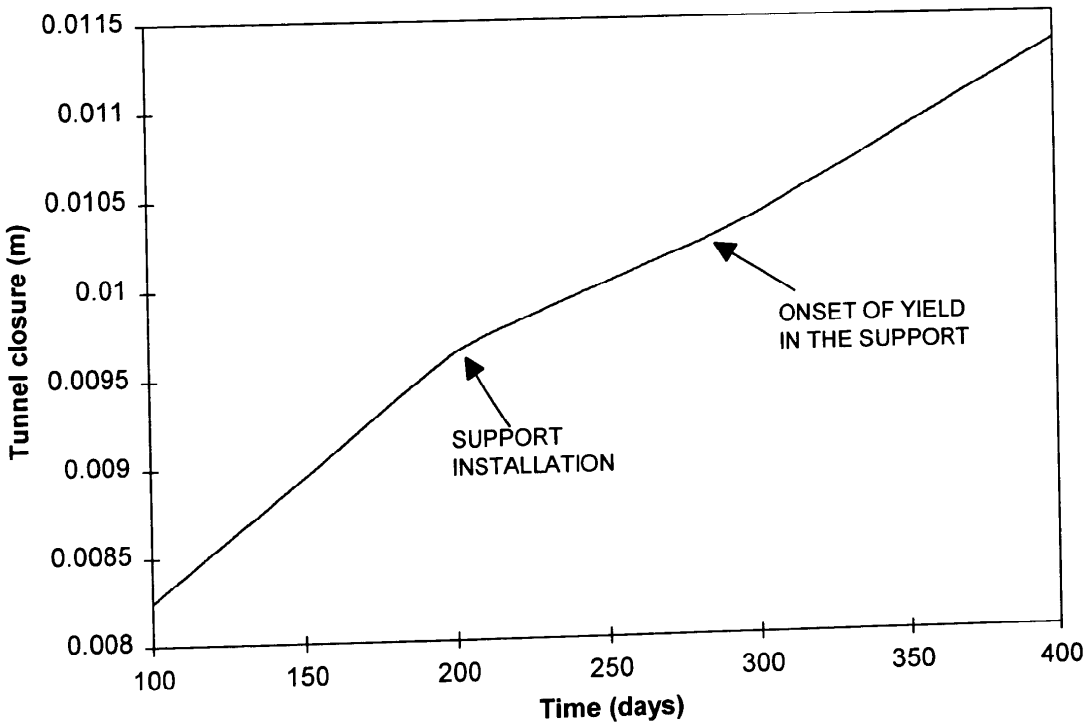

Figure 5.28. Typical effect of the cable anchor installation on the closure rate in the tunnel.

To summarise this chapter, a continuum viscoplastic model with time-dependent weakening of the rock was investigated to simulate the rheology of the fracture zone in deep mines. Superficially it appears that the model is successful in simulating the time-dependent formation of the fracture zone and the closure behaviour of stopes mined in an incremental fashion. This model was successfully used to test the hypothesis that continuous closure measurements of tabular excavations may be used to give an indication of the proximity of the stress peak ahead of the face.

Back analysis of the closure behaviour of a pump chamber at Hartebeestfontein mine showed that the continuum approach is unable to simulate the time-dependent behaviour if it is governed by prominent discontinuities such as the opening of bedding planes or shear creep along large discontinuities. As the time-dependent behaviour of the bedding planes may play a prominent role in the rock behaviour, a laboratory testing programme to investigate the shear creep of these discontinuities was initiated and is described in the next chapter.

Chapter 6

Laboratory investigation of discontinuity creep

6.1 Previous work

As explained in Chapter 2, a large amount of data for the laboratory creep of intact rock is available. As shown in Chapter 4, however, the closure rate of deep level excavations in hard rock is much greater than that of intact rock and significant time-related movements can be observed within a period of hours or days. This is an indication that the time-dependent behaviour of hard rock on an engineering scale is dominated by other mechanisms. Tan and Kang (1980) suggested that time-dependent deformation surrounding excavations may be governed mainly by the rheological properties of discontinuities. In this study *discontinuity creep* will be defined as the time-dependent relative displacement of opposing discontinuity surfaces, caused by a shear stress smaller than the shear strength of the discontinuity. The term *discontinuity* will be used as a collective term for all fractures, joints and bedding planes. Unfortunately very limited research has been done on the creep behaviour of discontinuities. This lack of experimental work is ironic in view of the possible importance of this mechanism. The following four factors have probably contributed to this dilemma.

a) Creep experiments can be very expensive as testing equipment may be required for weeks at a time to complete a single test. If the same equipment is used for short duration tests which are income generating, this income will be lost during the creep testing. The long duration of the tests does not make this an attractive subject for post graduate studies either.

b) Suitable equipment to measure shear creep is not widely available. Most rock engineering laboratories are equipped with uniaxial and triaxial equipment for the testing of intact cylindrical samples. This partially explains the wealth of experimental evidence for the creep of intact rock samples. Direct shear equipment suitable for the creep testing of discontinuities is less common.

c) Empirical approaches to and viscoelastic approximations of the creep behaviour of rock are successful in fitting existing in situ data (examples can be seen in Chapter 4; McGarr, 1971; Pan and Dong, 1991). These approaches, however, do not give an understanding of the underlying deformation mechanisms. Knowledge of these mechanisms is vital for an improved understanding of time-dependent behaviour and eventually for a better support strategy to ensure long term excavation stability.

d) The difficulty in describing the characteristics of discontinuities constitutes the last factor. Investigators are faced with problems such as whether to use natural or artificial discontinuities and whether to include gouge or not. In a testing programme many "identical" samples are required to investigate the effect of changing a particular experimental parameter. To obtain these discontinuity specimens in the field is extremely difficult.

In the past a number of studies of time-dependent discontinuity behaviour have been related to the investigation of earthquake mechanisms and have focused on time-dependent friction (Dieterich, 1978). Other studies (Crawford and Curran, 1981) investigated the rate-dependent behaviour of rock discontinuities to displacement controlled boundary conditions. Although indirectly related to the time-dependent behaviour, these tests give no information about the creep behaviour under constant stress conditions. The following studies investigated the stress-controlled creep behaviour of discontinuities.

Wawersik (1974) conducted triaxial creep tests on cylindrical samples of Westerly granite. Three samples were used which had an artificially induced tension fracture inclined at 30° relative to the direction of greatest compression. Tests were carried out under 20.68 MPa confinement at two levels of principal stress difference. The result of axial strain versus time shows a high initial creep rate that decays with time (see Figure 6.1). An important observation made is that rock specimens containing discontinuities are much weaker and

compliant than intact specimens. Owing to the low number of samples tested, no further conclusions are possible. Using a triaxial machine to test cylindrical samples with inclined discontinuities is not ideal as the actual value of shear stress along the discontinuity is calculated and not measured. The elliptical discontinuity contact area can also be criticised as there is a non-uniform loss of contact during shearing.

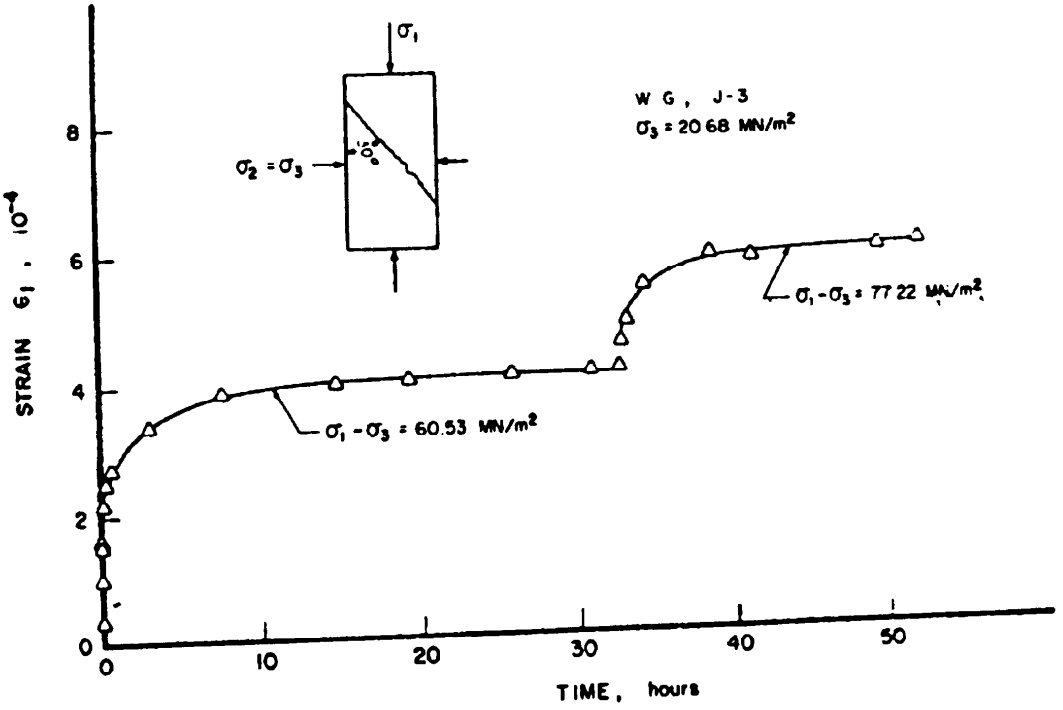

Figure 6.1. Axial creep strain versus time for a cylindrical water-saturated Westerly granite sample with an inclined discontinuity (after Wawersik, 1974).

Solberg et al. (1978) investigated the time-dependent deformation of Westerly granite specimens containing a sawcut separated by crushed Westerly granite fault gouge. The authors also used a triaxial testing machine with cylindrical samples and a confining pressure of 400 MPa. The sawcut was inclined at 30° to the axis of the specimen. Results indicated that the displacement rate across the discontinuity decayed to a constant rate after several hours. If the differential stress was high enough, accelerated creep was observed leading to sudden violent slip (Figure 6.2).

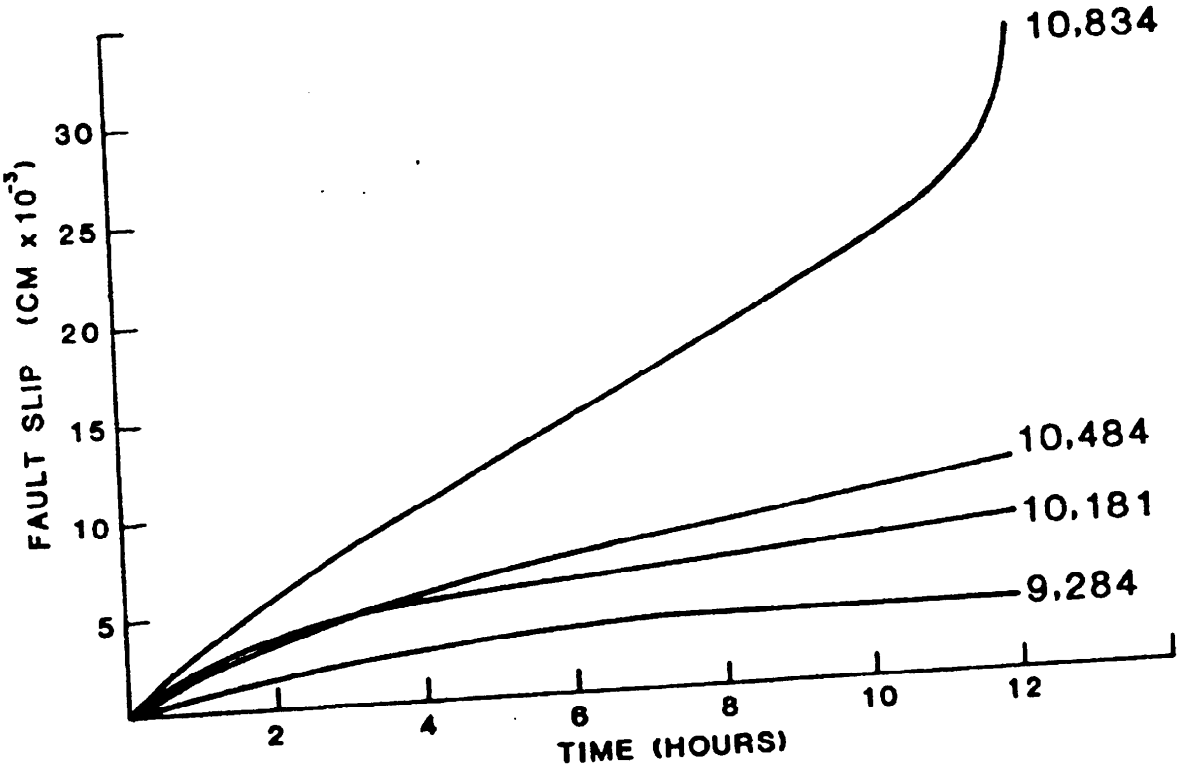

Figure 6.2. Time-dependent deformation of cylindrical Westerly granite samples with inclined discontinuities at different values of deviatoric stress (stress values in 10^{-1} MPa) (after Solberg et al., 1978).

Schwartz and Kolluru (1984) investigated the influence of stress level on the creep of unfilled rock discontinuities. Uniaxial creep tests were conducted on synthetic samples consisting of gypsum plaster that contained inclined discontinuities. The authors felt it was advantageous to use synthetic material as it gives higher creep rates, lower strength, easy specimen preparation and more controlled and consistent properties. The specimens were rectangular. The discontinuities were prepared by sawing through the intact samples and sanding the surfaces with 60 grit paper. Various samples with discontinuities inclined at different angles to the loading direction were used. This was done to test Amadei's (1979) hypothesis that the ratio of the applied shear stress to the peak shear strength was the critical factor governing discontinuity creep: the higher this ratio, the more pronounced is the creep effect. The data obtained extended this hypothesis. At small discontinuity inclinations, increasing the angle of inclination increased discontinuity creep, reaching a peak at 15° to 20°. Thereafter, increasing the angle, decreased the amount of creep. The authors concluded that discontinuity creep appears to depend both on the applied shear

stress to shear strength ratio and the absolute stress level across the discontinuity. An asperity mechanism was proposed to explain the experimental observations. It must be emphasised that artificial material was used in this study and the results may not be universally applicable to rocks.

Curran and Crawford (1980) and Crawford and Curran (1983) suggested that creep deformation along discontinuities may be appreciable, especially at loads near the peak strength. They developed a numerical technique based on the displacement discontinuity method to model time-dependent rock behaviour. Owing to a lack of experimental evidence on discontinuity creep behaviour, a simple 3-parameter solid viscoelastic model was used (similar to the model used in Appendix B2 to derive the convergence solution). Numerical experiments showed that discontinuity creep is only important when discontinuity surfaces are relatively free to move. Although the boundary element method proved to be useful in simulating the time-dependent rock behaviour, more experimental evidence is necessary to develop an accurate discontinuity creep model.

Bowden and Curran (1984) suggested that discontinuity creep can account for a significant proportion of the total deformation of a rock mass and investigated the creep behaviour of discontinuities in shale. A single surface bi-directional direct shear machine with a specimen size of 200 mm × 300 mm was used for the tests. It was possible to vary the shear and normal loads independently. Only artificially prepared discontinuities were used. The surfaces were sanded with 16 grit paper until it was planar and uniform in appearance. The important conclusion drawn from the study is that the shear creep rate is non-linearly proportional to the shear stress ratio (applied shear stress/shear strength). The creep rate is small for small shear stress ratios (Figure 6.3) and very large for large shear stress ratios. For shear stress ratios > 0.9, the creep rate is very sensitive to the shear stress ratio. At high values of shear stress ratios, time-dependent displacements are significant and may amount to centimetres in a matter of hours (Figure 6.4). Unfortunately only artificial discontinuities were used. It is also not clear what the effect of different levels of normal stress is.

A summary of the important discontinuity creep tests is given in Table 6.1.

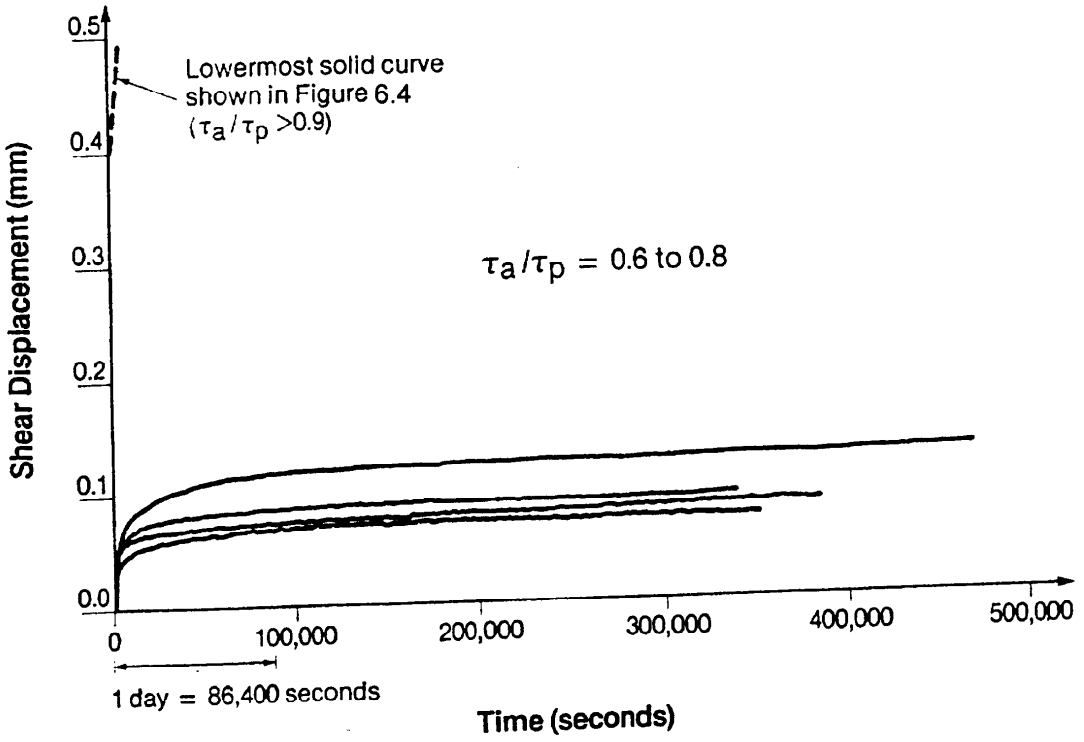

Figure 6.3. Shear creep of shale discontinuities for low shear stress/shear strength (τ_a/τ_p) ratios (after Bowden and Curran, 1984).

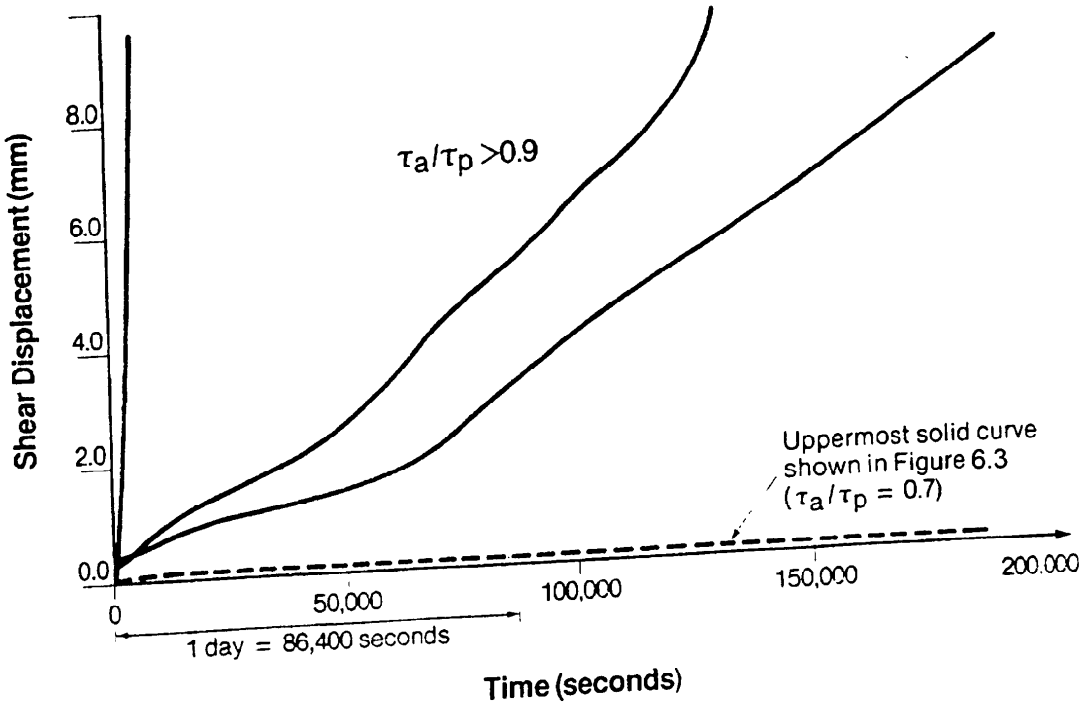

Figure 6.4. Shear creep of shale discontinuities for high shear stress/shear strength (τ_a/τ_p) ratios (after Bowden and Curran, 1984).

Table 6.1. Summary of discontinuity creep tests described in the literature.

	Rock Type	Discontinuity	Test Methodology	Boundary conditions
Wawersik (1974)	Westerly granite	Artificially induced tensile fracture.	Inclined discontinuity (0° to 30° from vertical) in triaxial equipment.	$\sigma_2 = \sigma_3$ = 6.89, 34.47, 68.95 MPa. σ_1-σ_3 varied between 60 % and 90 % of failure strength.
Solberg et al. (1978)	Westerly granite	Sawcut with simulated fault gouge.	Inclined discontinuity (0° to 30° from vertical) in triaxial equipment.	$\sigma_2 = \sigma_3$ = 400 MPa. σ_1-σ_3 raised in steps of 200 MPa every 12 hours.
Schwartz and Kolluru (1984)	Synthetic rock - Gypsum plaster	Sawcut - sanded with 60 grit paper - Friction angle 42°.	Inclined fracture 0° to 40° from horizontal - Uniaxial compression of sample.	σ_1 varied to obtain different discontinuity shear stresses.
Bowden and Curran (1984)	Shale	Sawcut - sanded with 16 grit paper.	Direct shear box	Normal stress 1 MPa and 2 MPa. Shear stress varied to obtain different shear stress to strength ratios.

As the existing information is limited, it was decided to initiate a testing programme of some typical discontinuities found in the South African mining industry. Of particular interest was the creep behaviour of discontinuities with gouge infilling and a substantial part of this chapter is devoted to these discontinuities.

6.2 Development of testing equipment and methodology

As no creep data for discontinuities in the South African mining industry existed, it was difficult to formulate specifications for the equipment required. After an extensive search at different South African research institutes, no suitable shear equipment was found. Although a shear box was available at CSIR Miningtek, the design of this equipment was such that a constant shear displacement is applied to the sample. This is not suitable for creep testing where a constant shear load is required. As a preliminary step, it was decided to modify this equipment with the addition of an air cylinder to maintain a constant shear load. Preliminary tests were carried out on fracture planes in lava specimens. Important observations gained from these tests were:

a) It is important to take measurements of the displacements as close as possible to the actual discontinuity surface. In the preliminary tests the specimens were cast in a resin mixture to enable mounting in the box. Due to the very low creep rate of some specimens, the effect of creep of this resin mixture and even the shear box itself obscured the true discontinuity creep data.

b) As the creep rate of some specimens is low, the amplification factor used by the instrumentation needs to be high. This makes the instrumentation very sensitive to changes in temperature. For the preliminary tests, the equipment was not housed in a temperature controlled laboratory and the diurnal cycle of temperature was clearly visible in the data. Good climate control is therefore a necessity (this should be the case for any creep experiment anyway!).

With these requirements known, the existing shear box was found to be unsuitable as the required modifications could not be made. New equipment for this study was therefore developed with the assistance of Mr. U.W. Vogler and is also described in more detail by Vogler et al. (1998).

Equipment development

The test equipment was developed from an existing 'Wykeham Farrance' shear box normally used for shear tests on soil. This proved to be a cost-effective solution that allows easy duplication of the equipment. The upper and lower halves of the box were designed to give unrestricted access to the two sides of the specimen. This allowed for the mounting of four vertical LVDT's (linear variable differential transformers) and two horizontal LVDT's, in special machined attachments, directly to the sample. This is illustrated in Figure 6.5. These mountings are glued to the surface of the rock. As there is no shear stress applied to these attachments, they will not creep relative to the rock surface. The only forces acting on these attachments are their own weight and the force exerted by the compressed springs of the LVDT's. The six LVDT's can be used to resolve the complete three-dimensional spatial movement. As the range of the horizontal LVDT's was quite small, another horizontal LVDT with larger range was used outside the box to measure any large scale shear displacement.

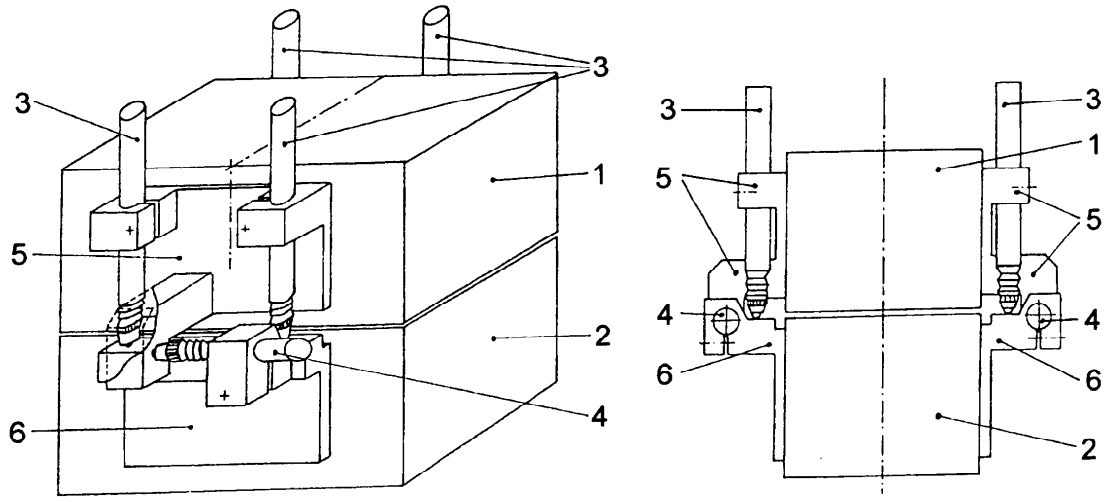

Figure 6.5. Attachment of the LVDT's to the discontinuity sample. The components are 1) Top half of the shear specimen, 2) Bottom half of the shear specimen, 3) LVDT's for measuring vertical displacements, 4) LVDT's for measuring horizontal displacements, 5) Upper fixing plates, 6) Lower fixing plates.

The deadweight method of applying constant normal force was retained as it is an ideal method of maintaining a constant load over a long period of time. Constant shear forces were applied using a developed air cylinder and a system of regulating valves. The complete system is illustrated in Figure 6.6.

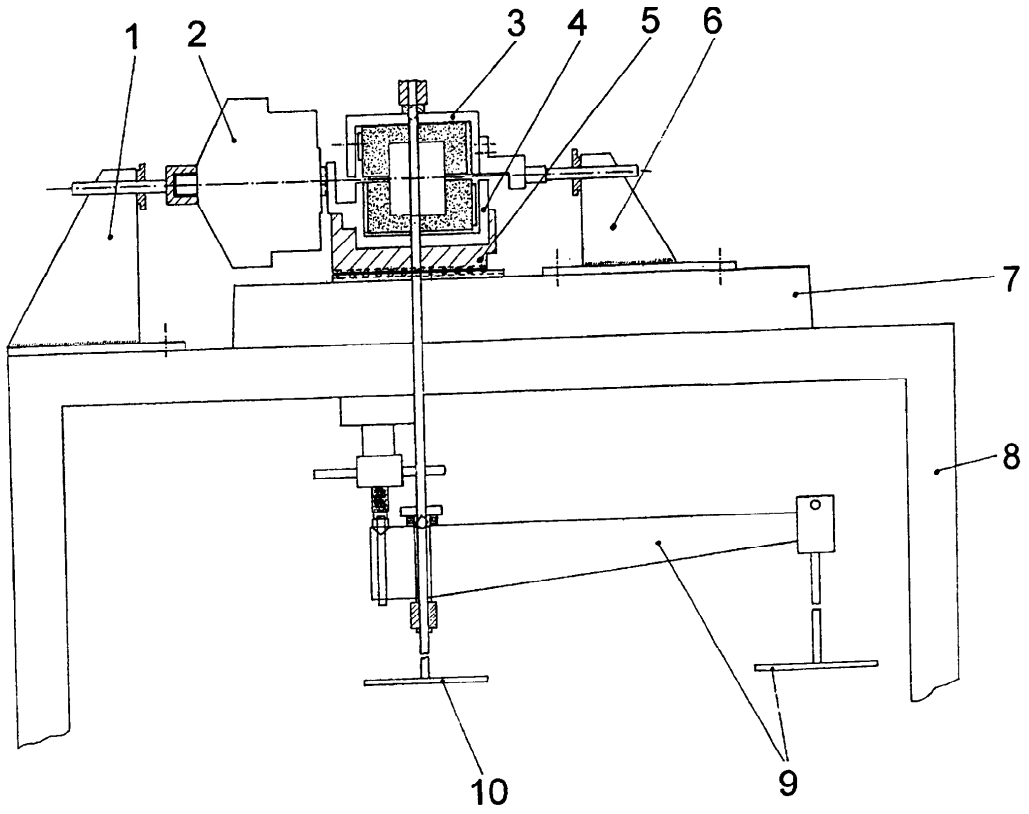

Figure 6.6. Shear box developed for the testing of discontinuity creep. The components are 1) Mounting bracket for air cylinder, 2) Air cylinder to apply shear load, 3) Upper half of box for mounting specimen, 4) Lower half of box for mounting specimen, 5) Lower half of original soil specimen mounting box, 6) Bracket with adjusting screw, 7) Support block, 8) Frame of existing Wykeham Farrance soil shear testing apparatus, 9) Existing 10:1 lever vertical loading device for deadweights and 10) Existing direct loading device for deadweights.

Figures 6.7 and 6.8 are photographs of the shear box and the LVDT's attached to the sample.

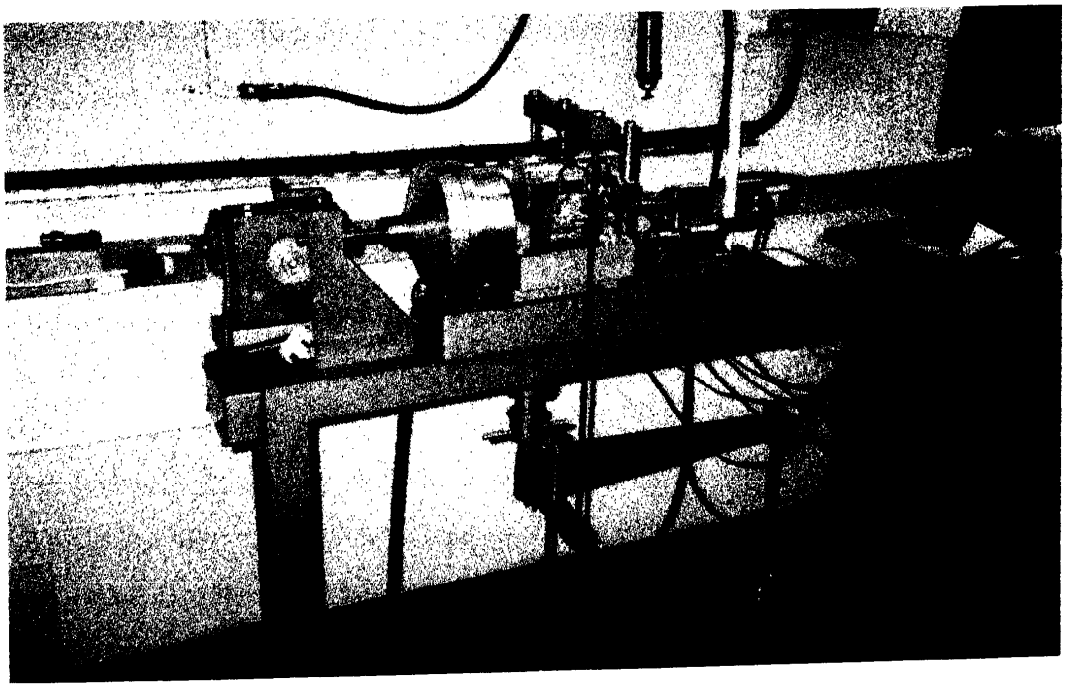

Figure 6.7. Shear box developed to investigate the creep of discontinuities in hard rock.

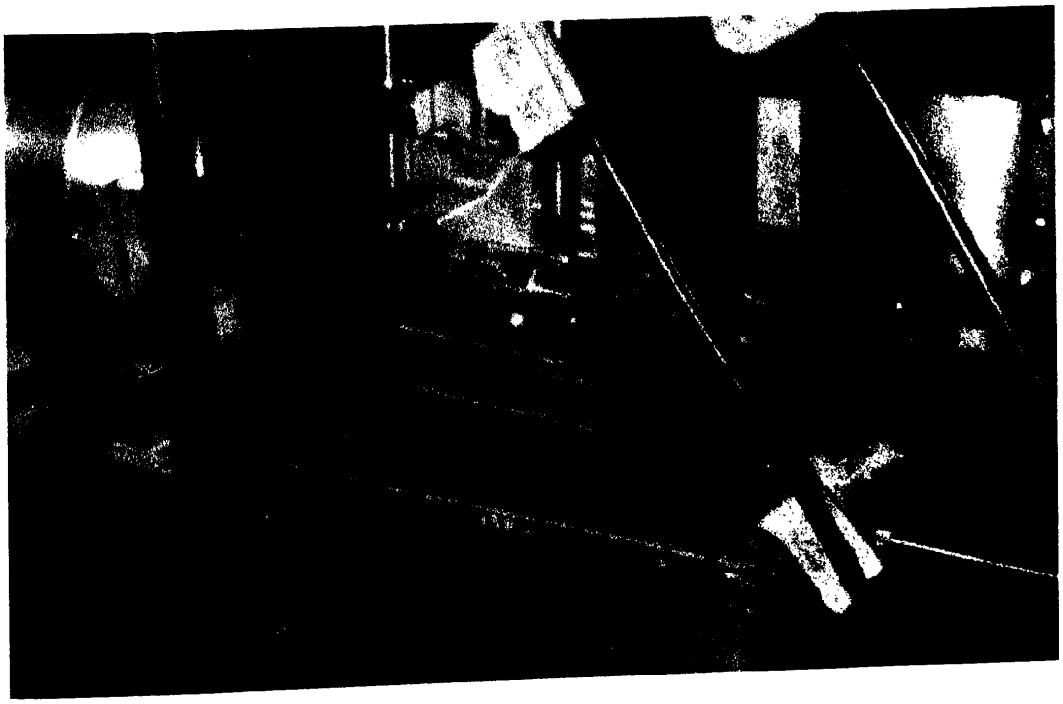

Figure 6.8. Details of the LVDT's and attachments glued to the surface of the rock. The rock specimen is hidden behind the attachment plates (also see Figure 6.9).

This equipment is housed in a climate controlled laboratory where the humidity is maintained at 50 % and the temperature at 22° C. Slight variations in temperature (±1° C) were recorded. Although very small creep measurements are possible with this system, a drawback is the more complex specimen preparation procedure. Natural discontinuities can be obtained by drilling cores parallel to the bedding or fracture planes underground. With care, the plane of the discontinuity will run parallel to the axis of the specimen. These cores can then be cut to suitable lengths and cast in any suitable resin to fit the shear box. The open sides should ground flat. It is important that the LVDT attachments are glued to the rock surfaces only and not the resin casting. Even though the resin might creep, the LVDT's only record the relative movement of the actual discontinuity. When preparing the specimens, care should be taken that enough rock material is available to attach the LVDT mountings. Figure 6.9 illustrates the lower half of a discontinuity specimen mounted in a resin cast.

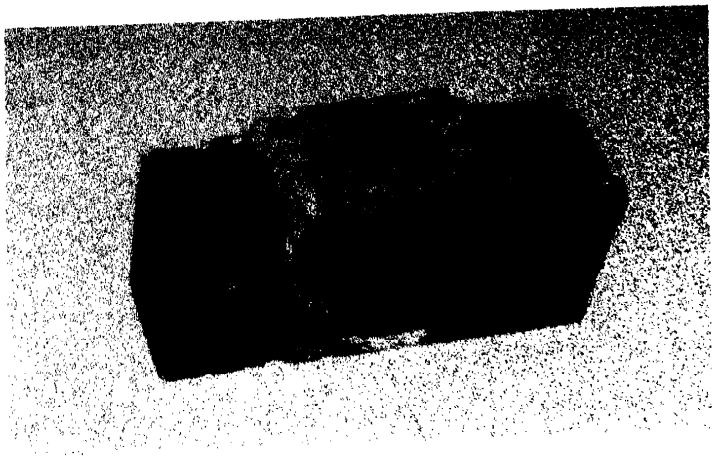

Figure 6.9. The lower half of a natural discontinuity obtained from a drill core and cast in a resin mixture. The LVDT mountings are only glued to the rock and not the resin.

After sample preparation, the specimen is mounted in the shear box. The appropriate normal stress is applied by choosing the appropriate amount of deadweight. The shear stress is then increased to certain magnitudes with a period of typically 48 hours between load increases. This is continued until the shear strength of the discontinuity is exceeded and the rate of shear displacement becomes uncontrolled. The air cylinder and regulator valves ensure that a constant air pressure and therefore a constant shear stress is maintained between load increases. The shear stress is increased manually by carefully adjusting a regulator valve to obtain the correct air pressure for the next shear stress level. The duration of this process typically lasts between 60 and 180 seconds. Due to the gradual nature of the shear stress increases, the shear strength of the specimen can be reasonably

accurately determined by noting the shear stress when the sample starts to slip in an uncontrolled fashion.

6.3 Creep of discontinuities with gouge infilling

Initial tests were conducted on discontinuities containing gouge infilling as these were expected to have a high creep rate and play a prominent role underground. Artificial gouge was used for the first tests to examine the effect of parameters such as gouge thickness and effect of normal and shear stress. Artificial gouge was preferred as it could be manufactured in sufficient quantities and allowed for comparative testing as its properties (particle size distribution, material) were consistent between different tests. These tests were followed by tests using natural gouge material obtained underground. From these tests it was clear that the behaviour of the artificial gouge was essentially similar to that of the natural material.

6.3.1 Artificial gouge

The gouge was obtained by crushing quartzite from Western Deep Levels Mine. The quartzite was the Type C (Table 2.1) described in Chapter 2. The broken material was sieved to obtain particle sizes less than 500 μm. The size distribution for this material is given in Figure 6.10. The result of a petrographic analysis of the quartzite before crushing is given in Table 6.2 and a microscope photograph of the resulting gouge is shown in Figure 6.11. The same quartzite was used to prepare two blocks containing a sawcut discontinuity for mounting in the shear box. The sawcut was ground flat to prepare a surface that appeared smooth to the naked eye. A typical test would involve mounting the lower quartz block in the shear box, adding gouge uniformly on the discontinuity to a particular thickness and then adding the top half of the specimen. Owing to compaction, the thickness of the gouge is reduced slightly when the normal load is applied. As the creep behaviour of intact rock is strongly influenced by the presence of water, the influence of moisture content in the gouge on discontinuity creep was also investigated. The climate control system in the laboratory maintained the humidity at 50 %. This would therefore also be the humidity of gouge tested in the room. To obtain 100 % humidity, the gouge in the specimen was kept soaked by filling the bottom specimen tray with water and wrapping water absorbing cloth around the discontinuity. This method proved successful

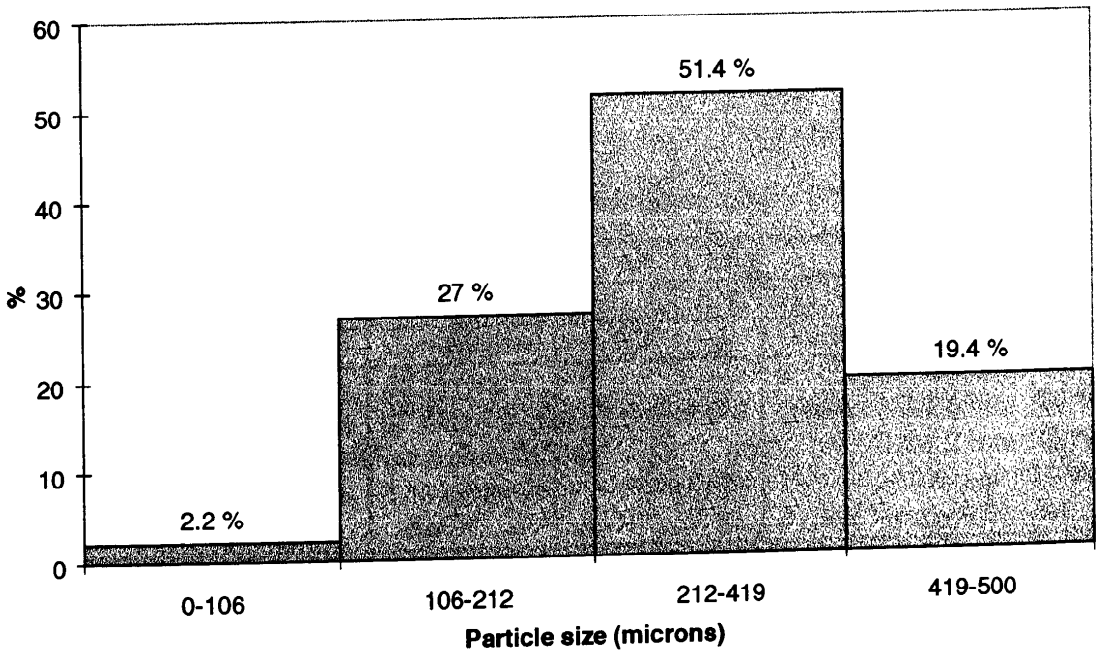

Figure 6.10. Particle size distribution (% weight) of the artificially prepared gouge material.



Figure 6.11. Grains of the artificially prepared gouge material. The scale is 1 mm from end to end. Note that the grains are angular and that the larger particle sizes are dominant. There is not an abundance of very fine material (also see Figure 6.10).

as, after completion of these tests, visual examination of the opened discontinuity confirmed that the gouge was wet over the entire surface.

Table 6.2. Petrographic analysis of the quartzite before crushing.

PETROGRAPHIC ANALYSIS		
QUALITATIVE	QUANTITATIVE	
	Composition (vol. %)	Grain size distribution
Dense quartzite containing pyrite with strong bonds between grains. Grains are surrounded by a thin amorphous matrix.	67 % quartz 32 % muscovite, chlorite and amorphous silica 1 % pyrite	0.1-2.6 mm diameter Quartz: 1.2-2.6 mm 60 % 0.6-1.2 mm 30 % < 0.6 mm 10 % Pyrite: Mostly 0.06 mm

Creep behaviour

As a first test, the creep behaviour of the artificial surface containing no gouge was investigated. A normal stress of 1 MPa was applied. The shear displacement for an increase in shear stress after fixed periods is illustrated in Figure 6.12 (the average of the two horizontal LVDT's). Again note that the shear stress increases were applied in a gradual fashion (see Section 6.2) to prevent any dynamic loading of the specimen. The deadweight loading arrangement also ensured that the normal load remained perfectly constant even during these shear stress increases. At the scale of the graph no creep behaviour is visible apart from the small increases in the shear displacement during the shear stress increases. The displacement became quite significant during the 0.5 MPa application. While increasing the shear stress during the last increment, the discontinuity failed at a shear stress of 0.53 MPa. This gave a friction angle of 28° for the unfilled discontinuity.

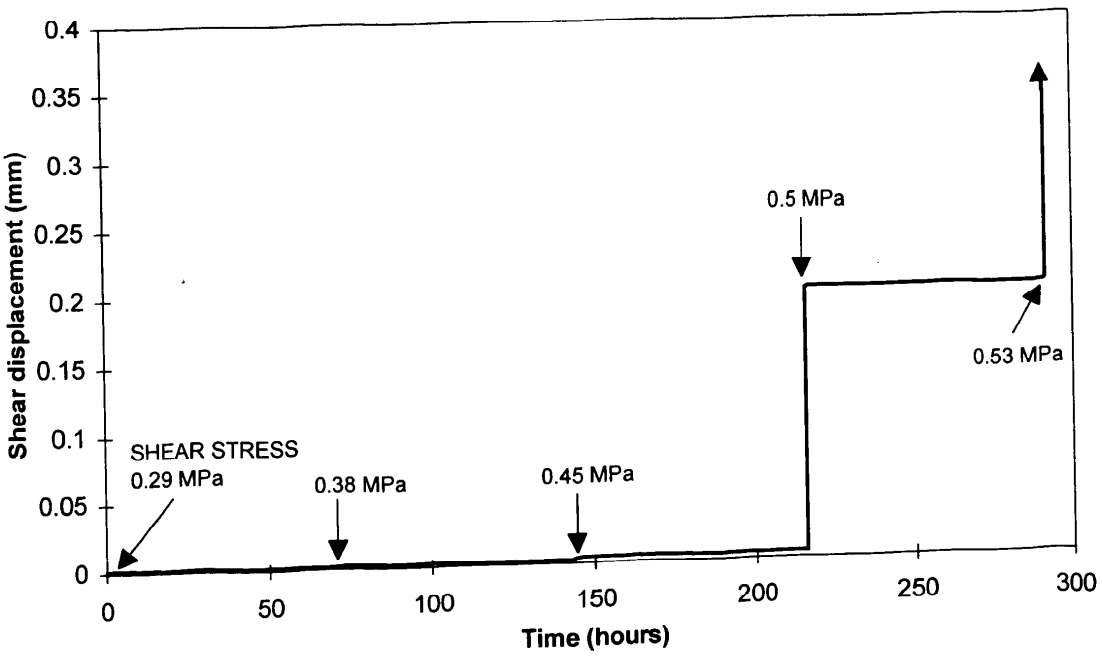

Figure 6.12. Shear behaviour of the unfilled sawcut discontinuity in quartzite. The shear stress was increased after fixed periods as indicated in the figure. The normal stress was 1 MPa.

In comparison, the effect of gouge infilling in the same discontinuity is illustrated in Figure 6.13. This was for a gouge thickness of 2 mm. The normal stress was again chosen to be 1 MPa. This data is the average of the two small horizontal LVDT's. Note that the interval between load increases was 72 hours for Figure 6.12 and 48 hours for Figure 6.13. Some creep behaviour is clearly visible for the discontinuity with gouge infilling. The last creep phase (for a shear stress of 0.517 MPa) is not plotted on this graph as the small LVDT was out of range. The specimen eventually failed at a shear stress of 0.533 MPa giving the same friction angle as the unfilled specimen. Of interest is that a cumulative shear displacement of 1.8 mm was recorded before the specimen failed at the 0.533 MPa shear stress level. The average normal displacement measured by the four vertical LVDT's is given in Figure 6.14. A convention of dilation being positive and compaction being negative will be assumed. The negative displacement in Figure 6.14 indicates a reduction in the width of the gouge layer (compaction). The initial reduction is significant compared to the subsequent steps as this is the compaction due to the application of the normal load. It appears that a further increase in the shear stress leads to further compaction, even though the normal stress remains constant.

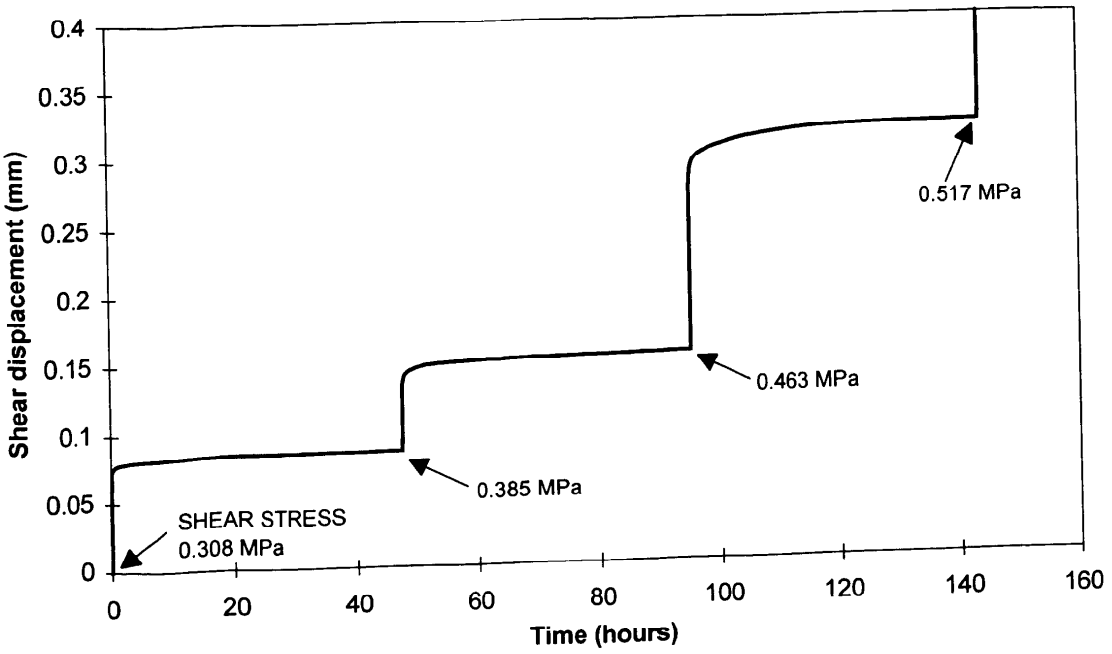

Figure 6.13. Typical shear creep behaviour of the discontinuity with gouge infilling and periodic increases in shear stress. The normal stress was 1 MPa. The gouge thickness was 2 mm and the specimen was tested at the ambient humidity of 50 %.

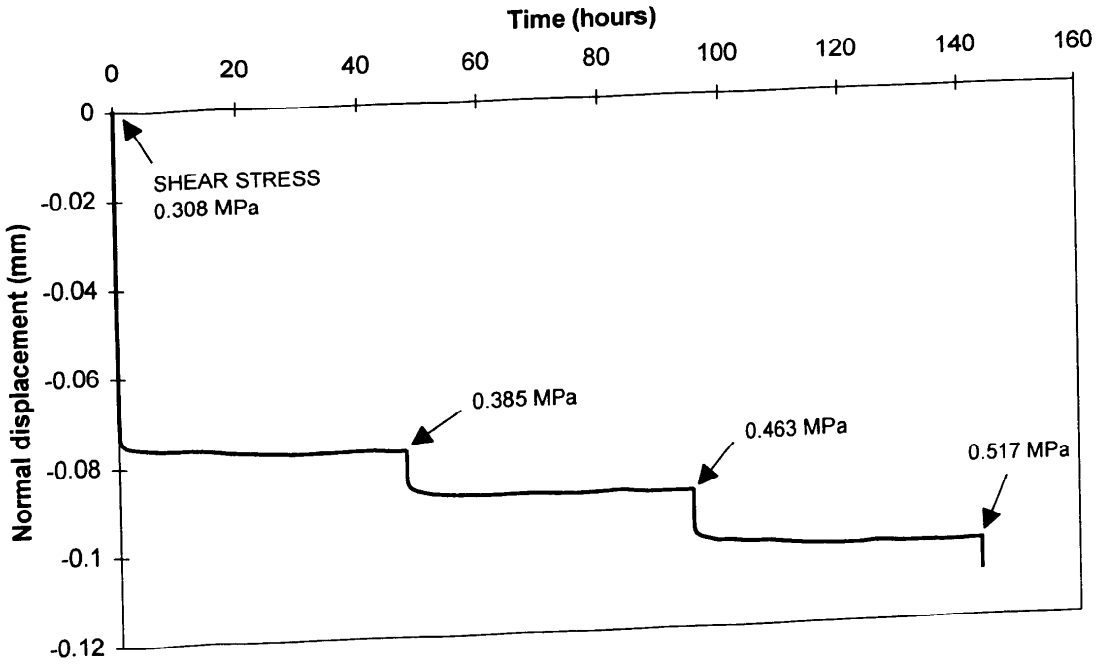

Figure 6.14. Normal displacement for the specimen in Figure 6.13.

Similar to the creep of intact rock, a primary and secondary creep phase can be distinguished. Figure 6.15 illustrates the shear creep curve for a discontinuity with a gouge thickness of 2 mm tested at 100 % humidity. The normal load was 1 MPa. The shear load

was adjusted to 0.48 MPa in one step which was 94 % of the shear strength. Primary and secondary creep phases are visible in the figure. Of interest is the large magnitude of the instantaneous response of approximately 0.63 mm. The creep rate of the secondary phase was calculated as 0.00045 mm/h. As it was difficult to determine the onset of the secondary phase, all creep rates in this chapter were calculated from 10 hours after application or increase of the shear load to the end of the particular creep increment.

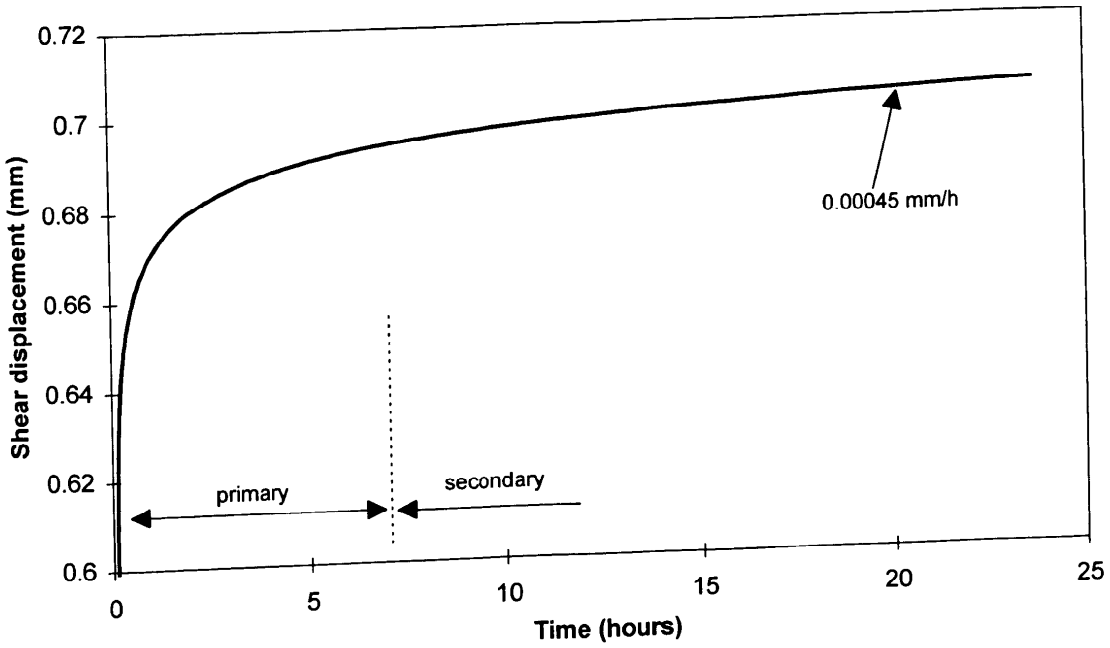

Figure 6.15. Typical shear creep behaviour of a discontinuity with gouge infilling. The gouge thickness was 2 mm and it was tested wet. Note that the y-axis is plotted from 0.6 mm to emphasise the profile of the curve, although the origin of the data is at 0 mm.

The normal displacement for this test also shows creep behaviour as illustrated in Figure 6.16. The magnitude of the primary phase and creep rate in the secondary phase is however significantly less.

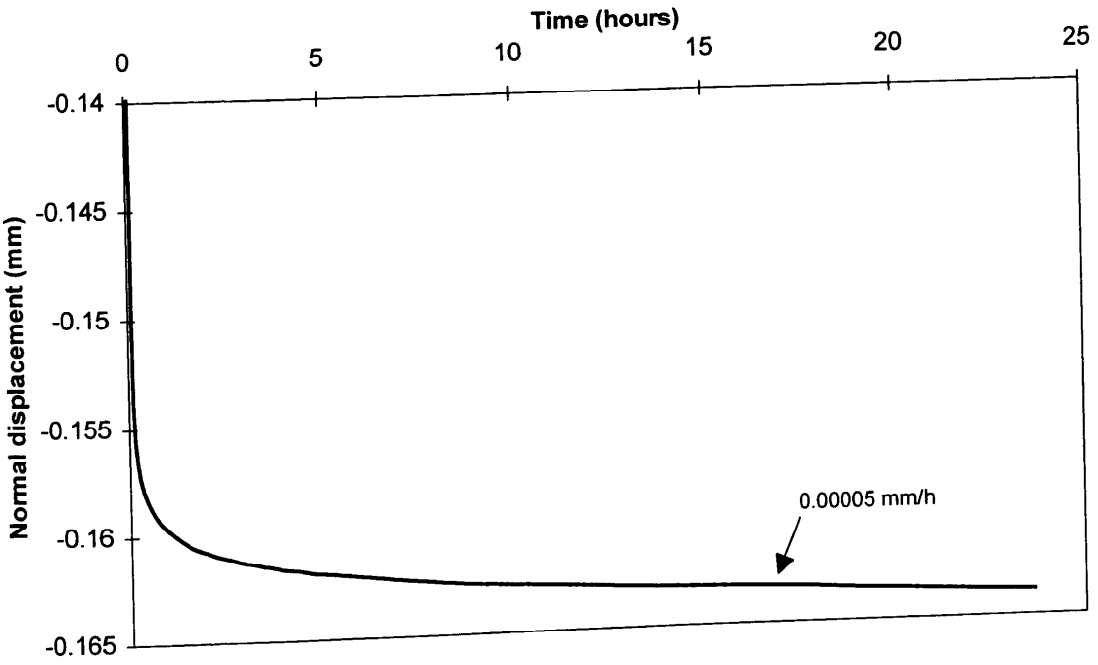

Figure 6.16. Normal creep behaviour for the specimen in Figure 6.15. The y-axis is plotted from 0.14 mm to emphasise the profile of the curve, although the origin of the data is at 0 mm.

Unloading behaviour

The large instantaneous shear response when applying or increasing the shear load is very prominent. There was some doubt whether this could be attributed entirely to plastic movements and some unloading tests were conducted. A gouge thickness of 2 mm was used and the shear load increased to 80 % of the shear strength in one step. In the first unloading test, the shear load was reduced to zero after 4 hours and in the second after 48 hours. These results are given in Figures 6.17 and 6.18. In both cases very little of the shear displacement was recovered after unloading.

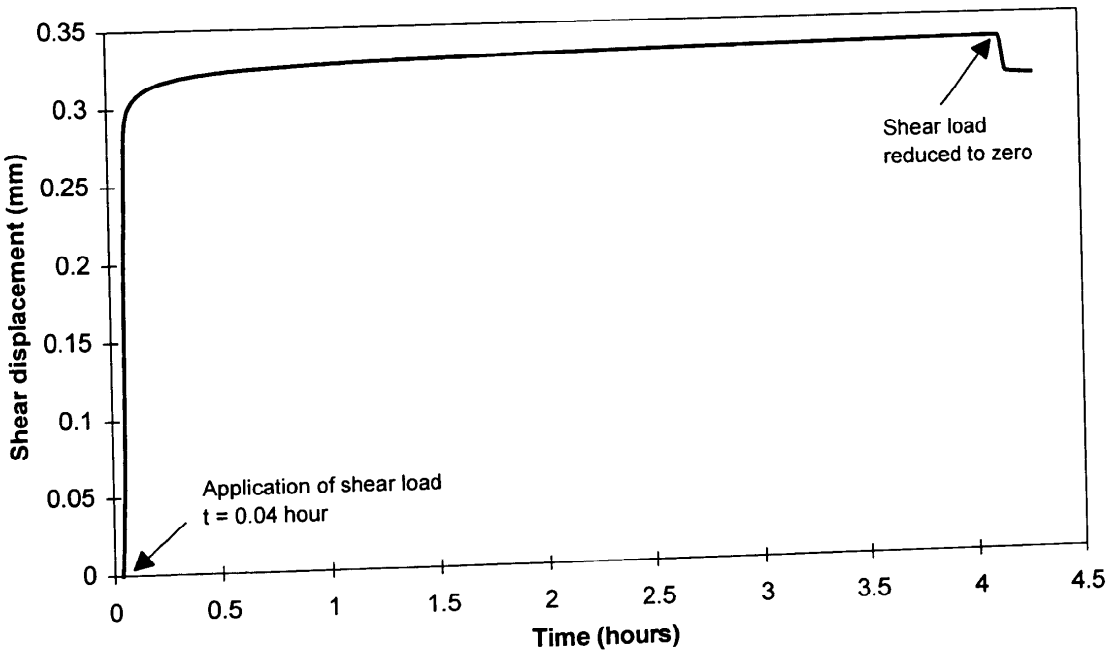

Figure 6.17. Shear displacement for a specimen with a gouge thickness of 2 mm. The shear load was removed 4 hours after application.

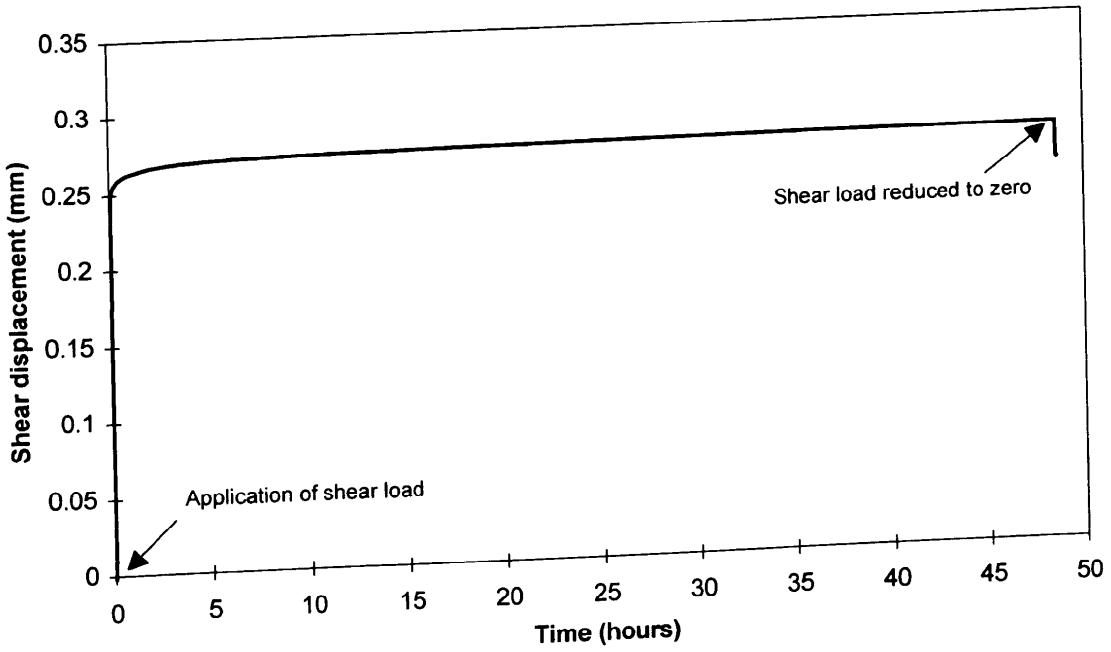

Figure 6.18. Shear displacement for a specimen with gouge thickness of 2 mm. The shear load was removed 48 hours after application.

Effect of shear and normal stress magnitude

To investigate the effect of the magnitude of the shear and normal stress, three different tests were conducted using a normal stress of 0.5 MPa, 1.0 MPa and 1.5 MPa. The tests were conducted by periodically increasing the shear load and therefore the effect of the shear stress/shear strength ratio could also be investigated. Figure 6.19 illustrates the incremental shear displacement for the different shear load increments and a normal stress of 0.5 MPa. Note that the magnitude of the instantaneous response increases with the shear stress/shear strength ratio. This is illustrated in Figure 6.20 where the cumulative instantaneous behaviour is plotted as a function of shear stress.

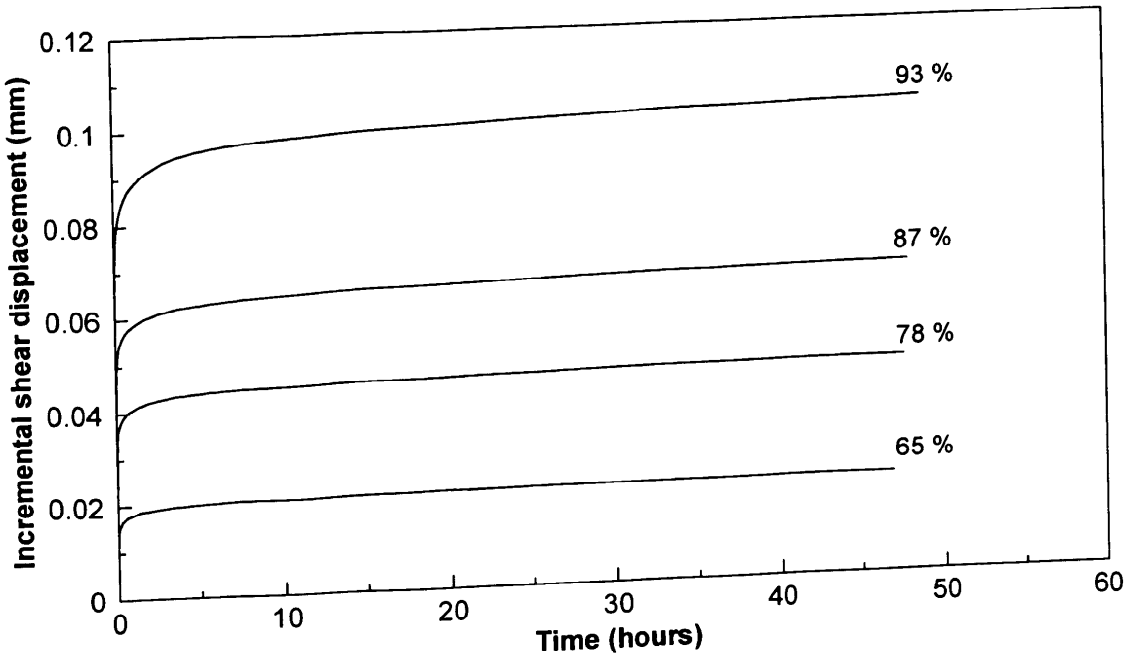

Figure 6.19. The effect of shear stress magnitude on the creep behaviour. The percentages indicate the magnitude of the shear stress relative to the shear strength (0.276 MPa). The normal stress was 0.5 MPa and the gouge thickness 2 mm. Note that this was not four different tests but the incremental creep for the different shear load increments of a single test.

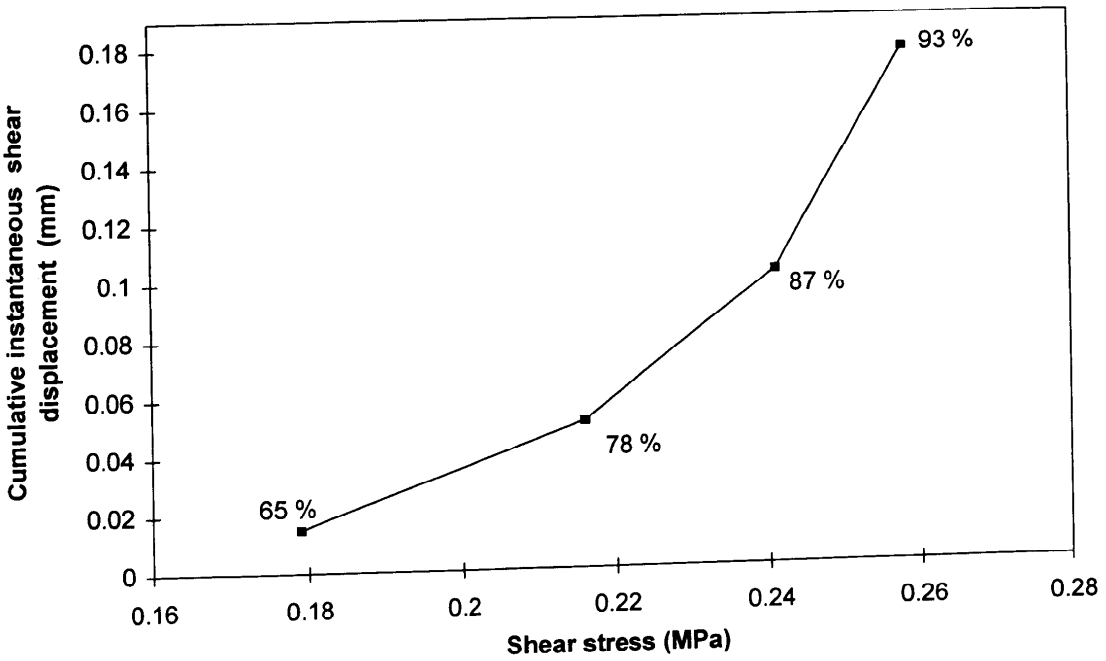

Figure 6.20. The effect of shear stress magnitude on the cumulative instantaneous shear displacement. The percentages indicate the magnitude of the shear stress relative to the shear strength (0.276 MPa). The normal stress was 0.5 MPa and the gouge thickness 2 mm.

The creep rate in the secondary phase also increases with the shear stress magnitude. This is illustrated in Figure 6.21.

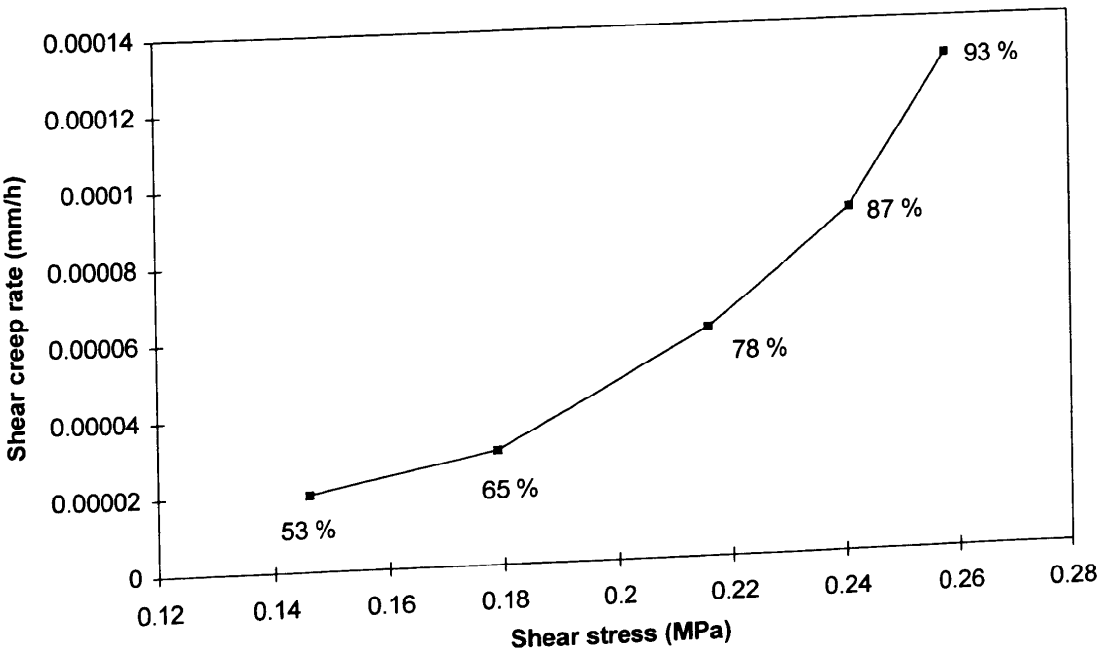

Figure 6.21. The effect of shear stress magnitude on the creep rate of the secondary phase. The percentages indicate the magnitude of the shear stress relative to the shear strength (0.276 MPa). The normal stress was 0.5 MPa and the gouge thickness 2 mm.

For the tests with normal loads of 1 MPa and 1.5 MPa, similar behaviour was observed as illustrated in Figures 6.22, 6.23 and 6.24. Note that the magnitudes of primary phase and shear creep rate in the secondary phase are not only a function of the shear stress/shear strength ratio, but are also dependent on the absolute value of shear and normal stress. For the 1.5 MPa normal load, the creep rate at 93 % of the shear strength was three times greater than for the 0.5 MPa normal load. This phenomenon has also been observed by Schwartz and Kolluru (1984) for unfilled discontinuities.

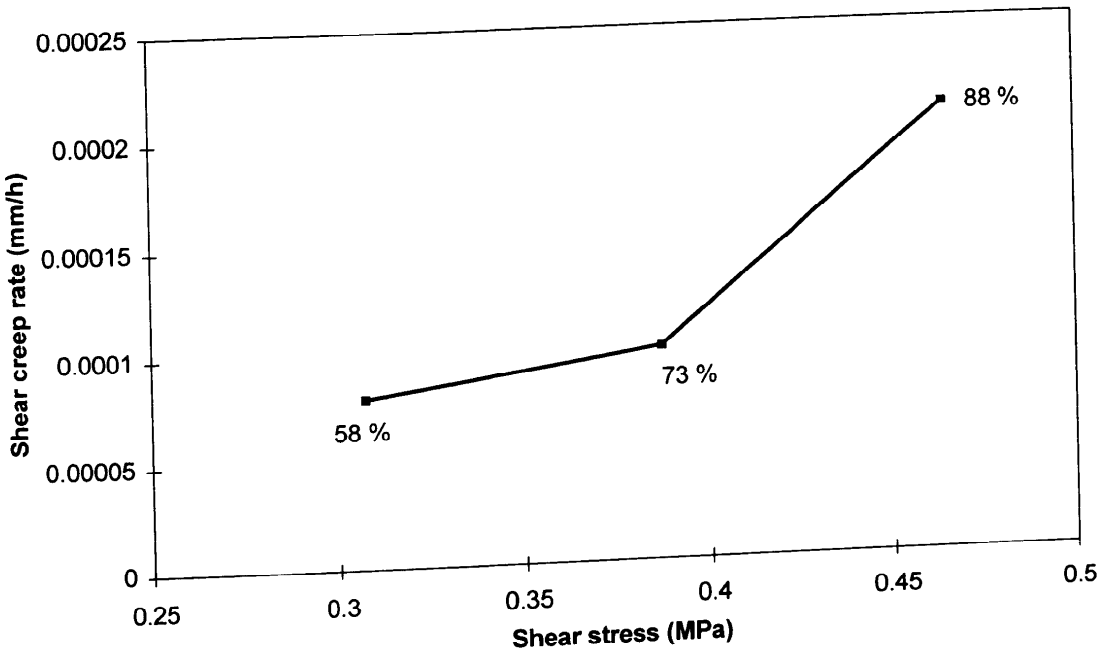

Figure 6.22. The effect of shear stress magnitude on the creep rate of the secondary phase. The percentages indicate the magnitude of the shear stress relative to the shear strength (0.53 MPa). The normal stress was 1 MPa and the gouge thickness 2 mm.

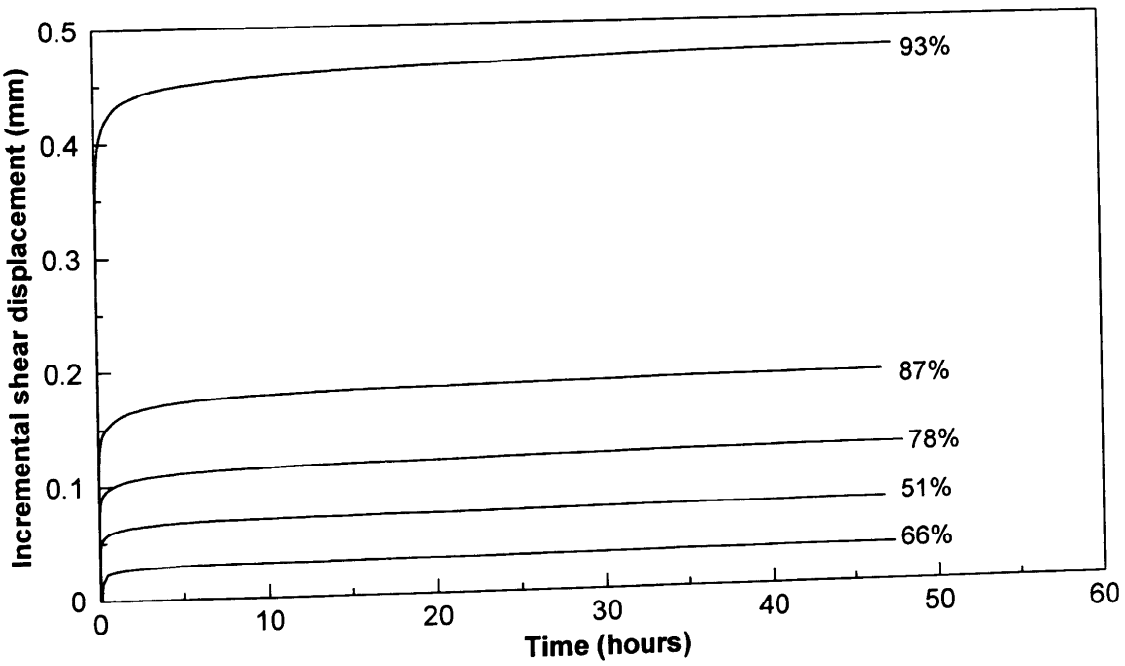

Figure 6.23. The effect of shear stress magnitude on the creep behaviour. The percentages indicate the magnitude of the shear stress relative to the shear strength (0.824 MPa). The normal stress was 1.5 MPa and the gouge thickness 2 mm.

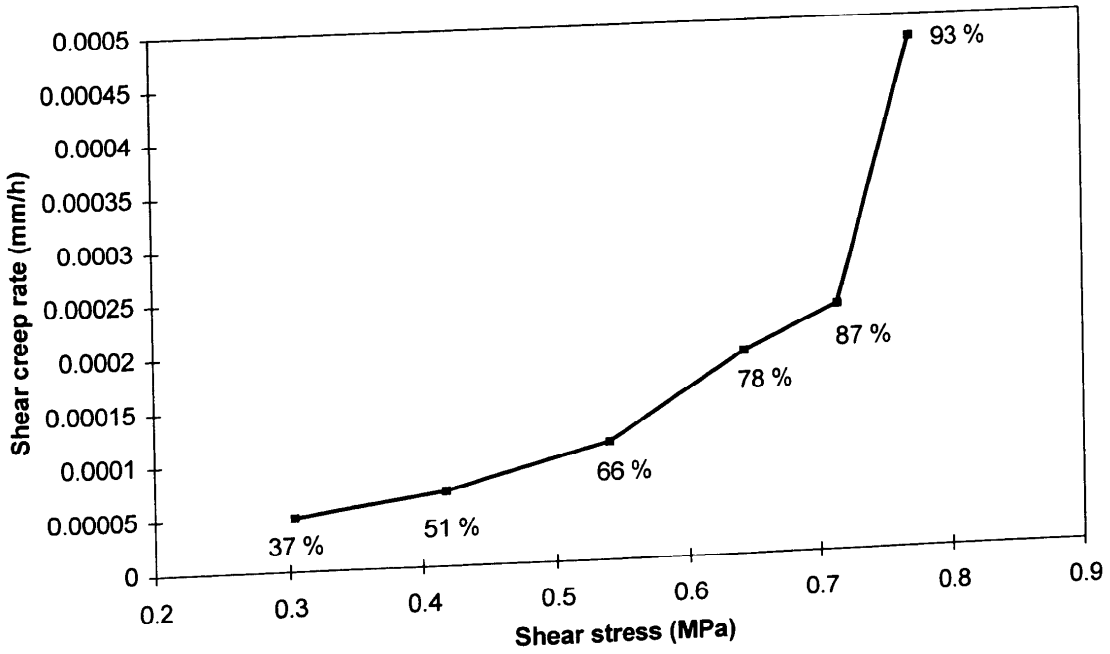

Figure 6.24. The effect of shear stress magnitude on the creep rate of the secondary phase. The percentages indicate the magnitude of the shear stress relative to the shear strength (0.824 MPa). The normal stress was 1.5 MPa and the gouge thickness 2 mm.

Effect of gouge thickness

The effect of gouge thickness was investigated by performing three tests with a thickness of 0.5 mm, 1 mm and 2 mm. The shear creep rate in the secondary phase as a function of gouge thickness is illustrated in Figure 6.25. Increasing gouge thickness leads to higher creep rates. This data illustrates that apart from the possible surface creep at the interface between the rock surface and the gouge, there is also a volumetric creep effect in the gouge.

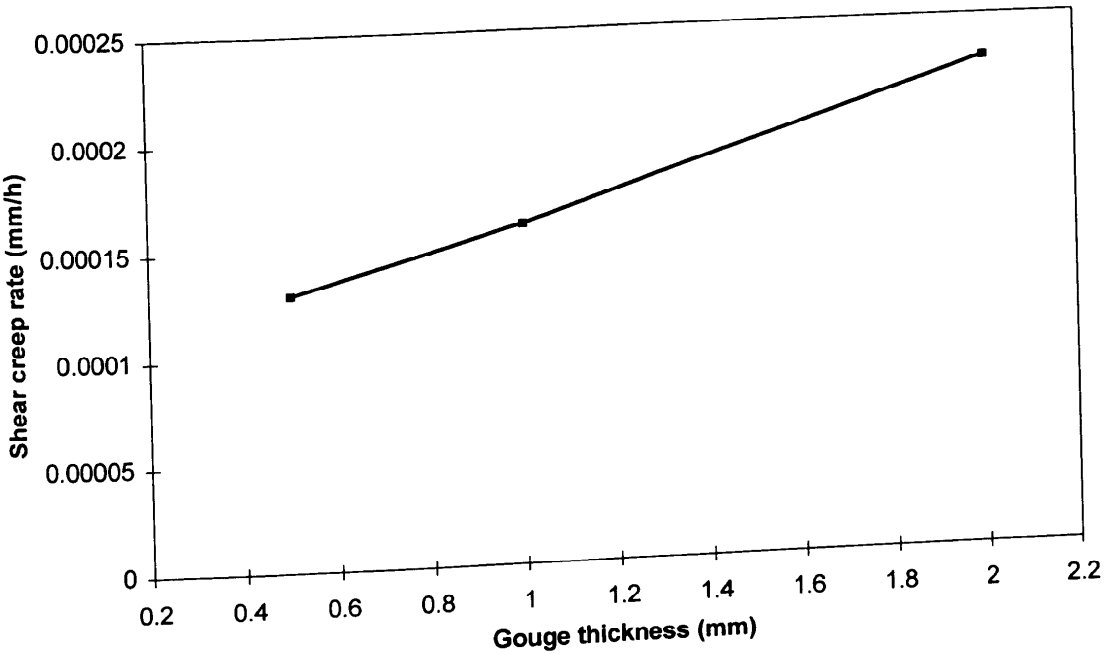

Figure 6.25. Shear creep rate of the secondary phase as a function of gouge thickness. For the 1 mm and 2 mm thickness, the shear stress magnitude was 87 % of the shear strength while it was 86 % for the 0.5 mm thickness. The samples were tested at 50 % humidity.

Effect of humidity

Figure 6.26 compares the creep of a filled discontinuity that was tested wet with another at the ambient humidity (50 %). As in other types of creep tests, water accelerates the creep rate.

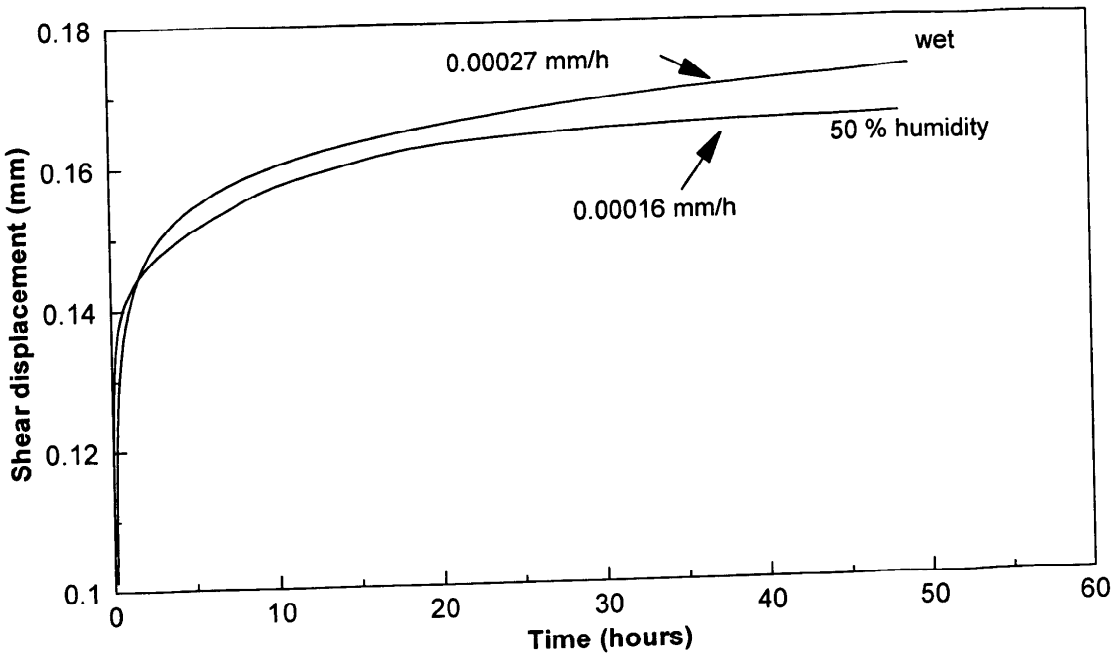

Figure 6.26. Effect of water on the creep rate of the discontinuity. The gouge thickness was 2 mm, the applied normal stress 1 MPa and the shear stress in both cases was 87 % of the shear strength.

Simulating the shear displacement rate in the secondary creep phase

Similar to findings by Amadei (1979) and Schwartz and Kolluru (1984), the discontinuity creep rate in the secondary phase depends on the applied shear stress/shear strength ratio (τ/τ_s). As a stress power law was successfully used in Chapter 2 to simulate the steady-state creep rate of intact specimens, a similar law is proposed for discontinuity creep, namely

$$\dot{D}_{SS} = A\left(\frac{\tau}{\tau_s}\right)^n \qquad [6.1]$$

where $\dot{D}_{SS}$ is the displacement rate of the secondary creep phase, τ is the applied shear stress and τ_s is the shear strength of the discontinuity. From the data above it follows that the parameter A will depend on the humidity, gouge thickness and absolute magnitudes of normal and shear stress. The coefficient n and parameter A can be determined from a $\log(\dot{D}_{SS})$ versus $\log(\tau/\tau_s)$ plot. This plot for the data in Figure 6.21 is illustrated in

Figure 6.27. The slope of this curve gives a value of n = 3.28. The linear nature of the curve illustrates the applicability of the model.

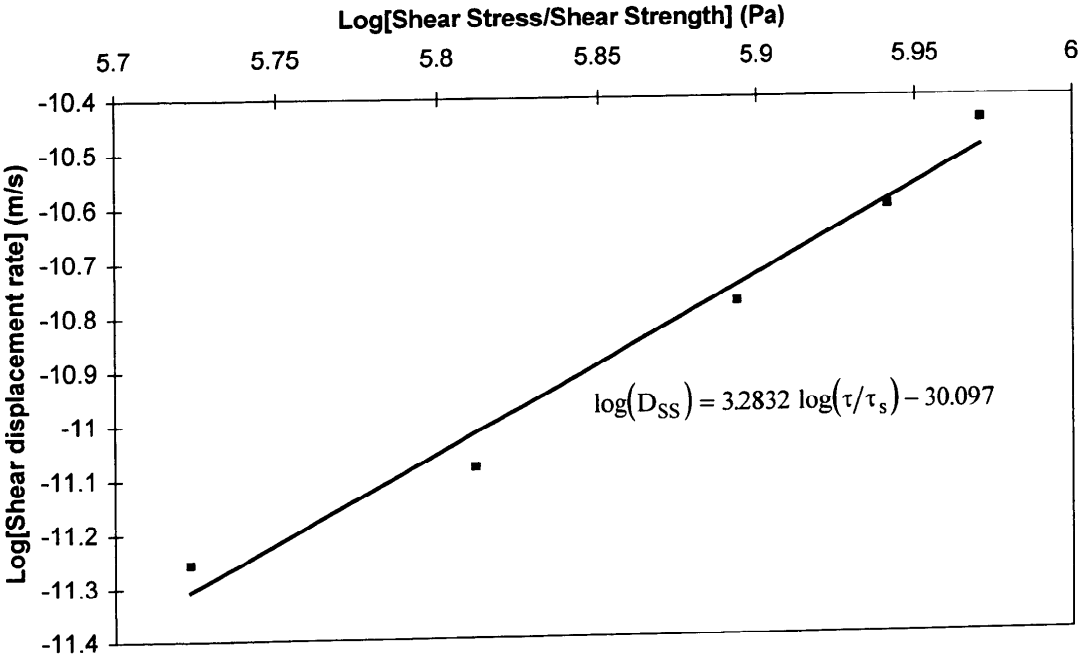

Figure 6.27. Log (shear displacement rate) versus log (shear stress/shear strength) for the data in Figure 6.21. The normal stress was 0.5 MPa and the gouge thickness 2 mm. The line was fitted using linear regression.

The parameters for the model in equation [6.1] were also calculated for the other tests with the higher values of normal stress. The calibrated parameters are given in Table 6.3.

Table 6.3. Calibrated values for the power law in equation [6.1]. All the tests were conducted at a temperature of 22° C.

Gouge type	Thickness (mm)	Humidity (%)	Normal stress (MPa)	n	Log(A)
Artificial	2	50	0.5	3.3	-30.1
Artificial	2	50	1	2.3*	-23.8*
Artificial	2	50	1.5	2.9	-27.1
Hartebeestfontein Mine (data in next section)	2	100	1	2.4*	-24.1*

*These values were calculated from only three data points and should be treated with caution.

6.3.2 Natural gouge - Bedding plane infilling at Hartebeestfontein Mine

To compare the behaviour of the artificial gouge described above with that found underground, gouge was collected from the site at Hartebeestfontein Mine described in Section 4.4 (Chapter 4). In this area the bedding planes in the quartzites are very prominent. In the instrumented panel illustrated in Figure 4.22 (Chapter 4), there was a significant fall of ground not far from the closure meter. This exposed the bedding planes and allowed the author to collect gouge material from between the layers. As the gouge contained some large particles which could not be accommodated by the small scale of the experiment, it was sieved to obtain particle sizes less than 850 μm. The size distribution (by percentage weight) of the remaining material is given in Figure 6.28 and a microscope photograph of this material in Figure 6.29. Compared to the artificial material described in the previous section, the abundance of very fine material is clear.

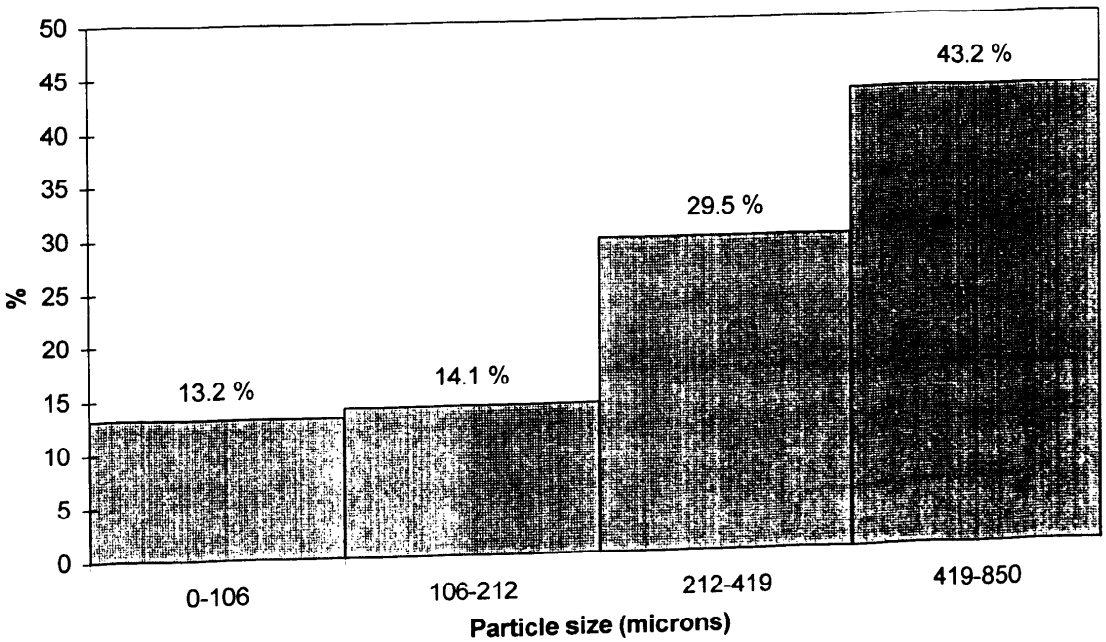

Figure 6.28. Size distribution of the particles (% weight) in the gouge collected from the bedding plane layers at Hartebeestfontein Mine.

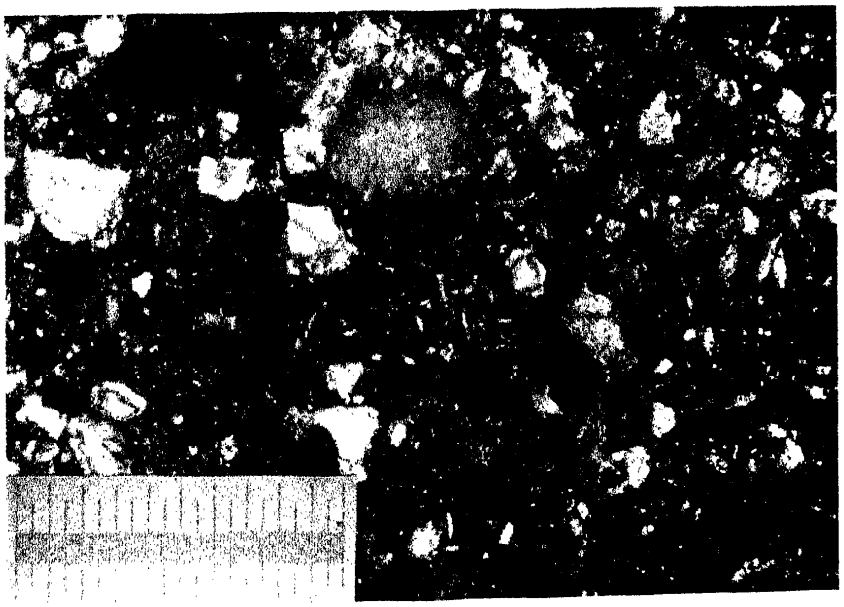

Figure 6.29. Microscope photograph of the natural gouge material collected at Hartebeestfontein Mine. The scale is 1 mm from end to end. Note the abundance of very fine material.

In spite of the differences in particle size distribution between this gouge and the artificial material, the experimental behaviour of the filled discontinuity was generally similar to the results presented above. Figures 6.30 and 6.31 illustrate shear and normal creep for a periodic increase in shear stress.

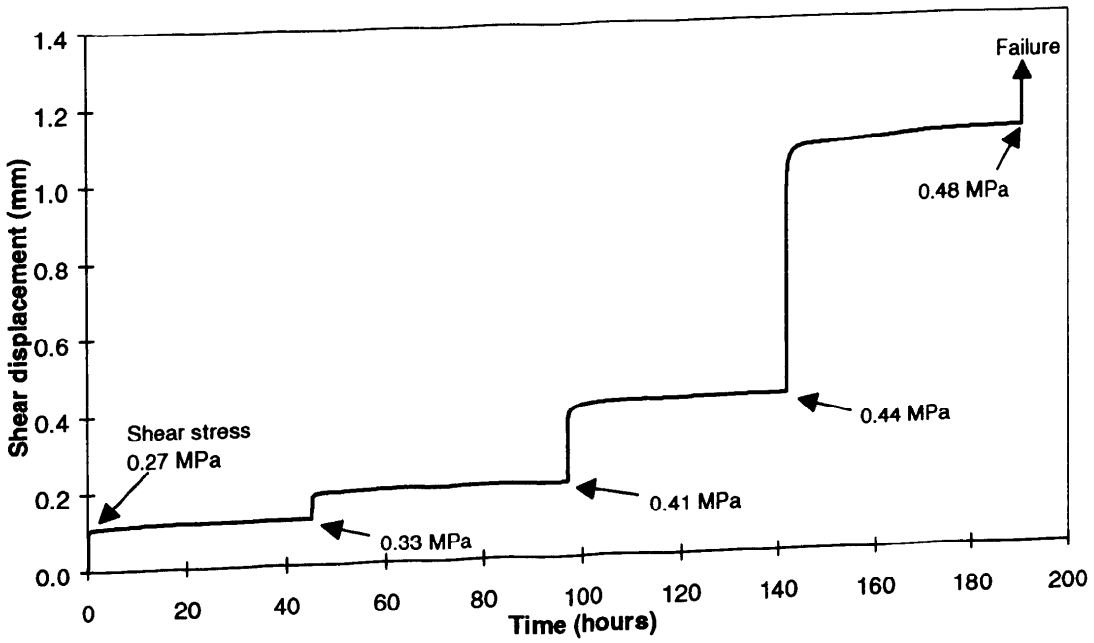

Figure 6.30. Shear creep behaviour of the discontinuity with gouge infilling from Hartebeestfontein Mine. The normal stress was 1 MPa. The gouge thickness was 2 mm and the humidity 50 %.

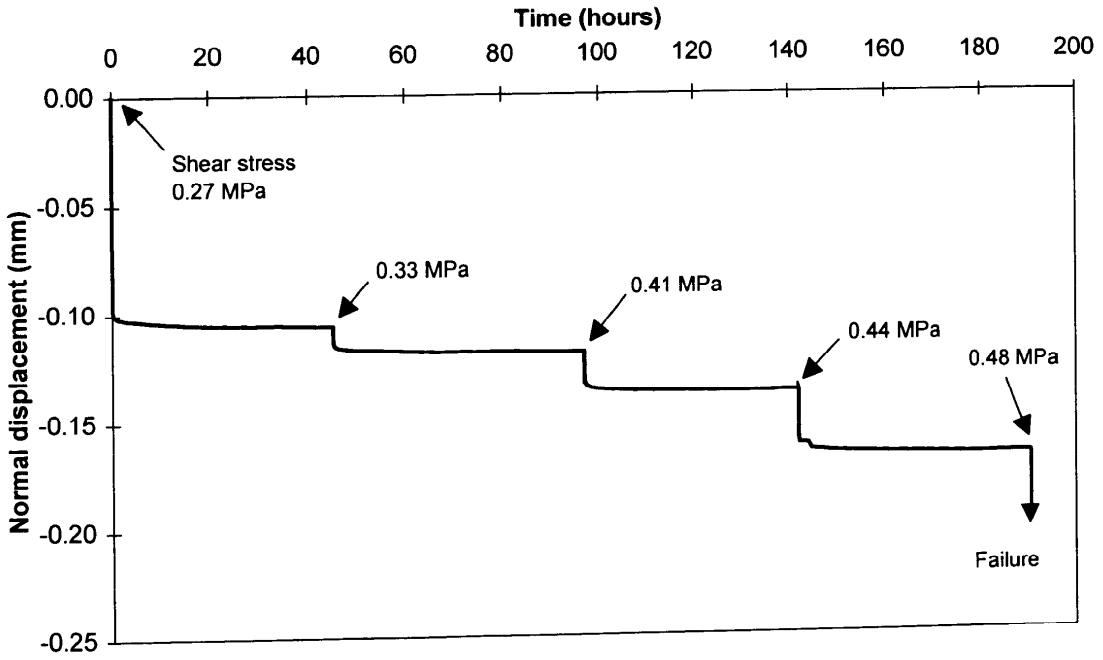

Figure 6.31. Normal displacement for the specimen in Figure 6.30.

Again the shear creep rate in the secondary phase increases with increasing shear stress. This is illustrated in Figure 6.32.

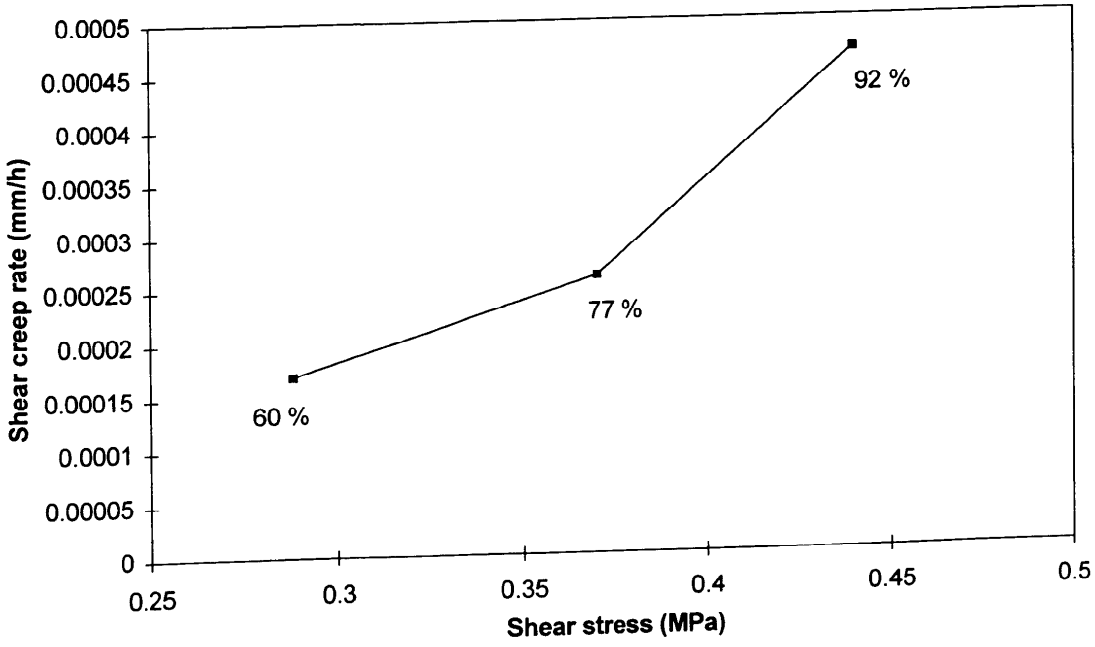

Figure 6.32. The effect of shear stress magnitude on the creep rate of the secondary phase for the Hartebeestfontein gouge tested at 100 % humidity. The percentages indicate the magnitude of the shear stress relative to the shear strength (0.48 MPa). The normal stress was 1 MPa and the gouge thickness 2 mm.

6.4 Creep of fractures with no gouge infilling

The results above were compared to the creep of mining induced fractures in Ventersdorp lava. The two opposing surfaces of the fracture were tightly fitting, were not subjected to any previous shear and contained no infilling. A similar testing procedure to that described above was used with periodic increases in the shear load. The normal load was 1 MPa. Figure 6.34 illustrates the shear creep behaviour of the last three loading increments. The sample eventually failed at a shear stress of 1.66 MPa giving a friction angle of 59°. Although some creep behaviour is visible in the last increments before failure, it should be noted that the magnitude of this creep is negligible compared to some of the discontinuities with gouge infilling. From Figure 6.33 accumulated displacements of the order of only 10 microns were observed before failure, while for a typical gouge-filled discontinuity (Figure 6.29), the accumulated creep movements could amount to 1.1 mm. As the creep displacement in Figure 6.33 was so small, the slight changes in the temperature (±1° C) and the effect of this on the instrumentation affected the recorded data. In Figure 6.33 the unexpected trends in the creep, in the secondary creep phase of the first two loading stages, were a result of this effect. Figure 6.34 illustrates the normal displacement accompanying the shear results of Figure 6.33. In comparison with the gouge-filled discontinuities, the discontinuity is dilating and not compacting. Also note that the magnitude of dilation is comparable to the magnitude of the shear displacement.

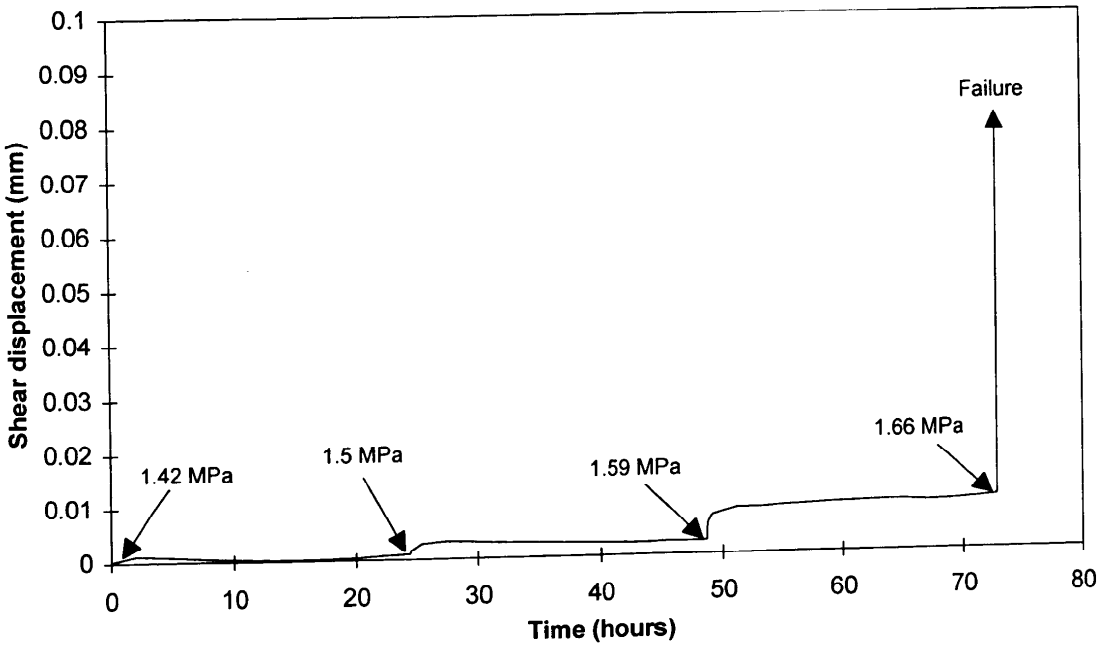

Figure 6.33. Shear creep behaviour of the extension fracture in Ventersdorp lava for a periodic increase in shear stress. The normal stress was 1 MPa. The sample was tested at the ambient humidity of 50 %.

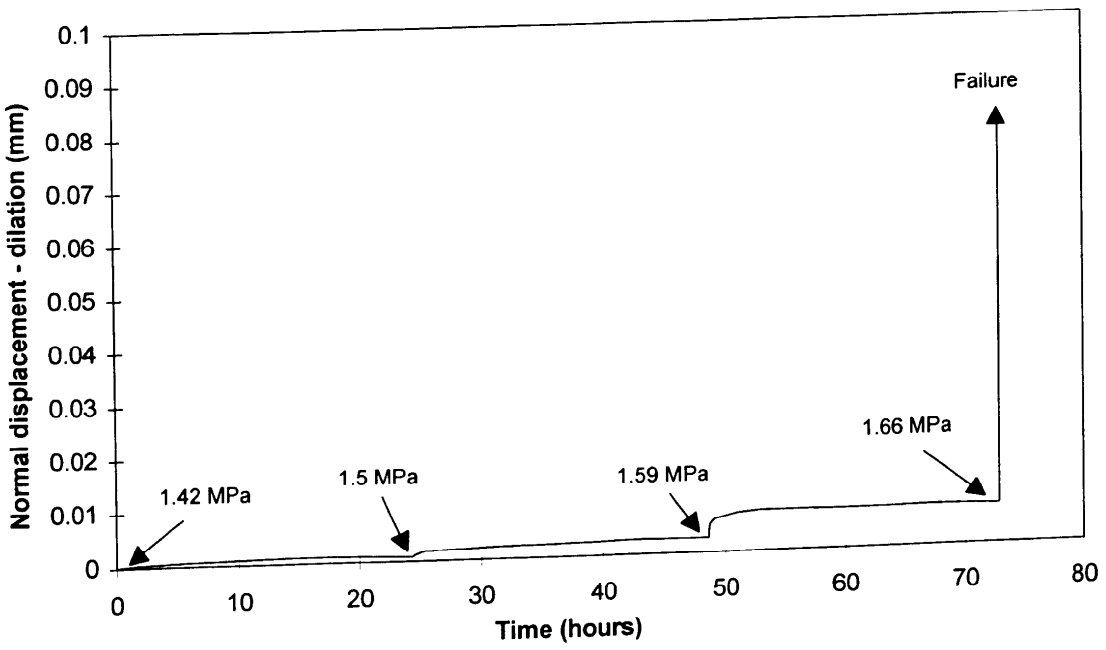

Figure 6.34. The dilation of the sample that accompanied the shear creep of Figure 6.33.

6.5 Summary : Shear creep of discontinuities

From the results above, it appears that in hard rock, discontinuity creep can be divided into two major classes namely i) creep of discontinuities with gouge infilling and ii) creep of discontinuities with matching opposing surfaces and no infilling. An example of the latter class is mining induced extensile fractures which have not been subjected to shear displacement (Type I fractures in Figure 1.3). No appreciable shear creep of these discontinuities was observed in the laboratory. For the first class, prominent creep behaviour was noted. It should however be noted that in these experiments the gouge thickness was significantly larger than the maximum asperity heights of the rock surface. If the asperity heights are larger than the gouge thickness, asperity locking and failure might become the dominant factor controlling the creep behaviour.

For discontinuities with gouge infilling thicker than the asperity heights, the following observations were made:

a) If a shear load is applied to the discontinuity that is also subjected to a normal clamping force, typical primary and secondary shear creep behaviour is noted.

b) The primary shear creep phase includes a prominent instantaneous response that increases for larger shear stress/shear strength ratios.

c) The magnitude of creep rate in the secondary phase also increases as the shear stress/shear strength ratio increases.

d) The magnitude of creep is not only a function of the shear stress/shear strength ratio, but also of the absolute stress magnitudes.

e) Creep normal to the discontinuity is also observed and reduces (compacts) the gouge thickness. With further increases in shear load (while keeping the normal load constant), further instantaneous compaction is observed.

f) The shear creep rate appears to depend linearly on the gouge thickness. The thicker the gouge, the faster the creep rate.

A power law was proposed to simulate the increase in steady-state creep rate for higher shear stress/shear strength ratios. This proved successful in simulating the data. The next chapter explores the use of a discontinuum viscoplastic formulation to simulate the rheology of discontinuities and the fracture zone surrounding tabular excavations.

Chapter 7

A proposed discontinuum viscoplastic model for the time-dependent behaviour of hard rock

7.1 Introduction

The central theme of this study is to understand and simulate the significant time-dependent deformations of deep excavations in hard rock. The creep rate of the intact hard rock is low and it appears that the time-dependent behaviour is governed mainly by the rheological properties of the fracture zone and prominent discontinuities. Other workers (Tan and Kang, 1980; Schwartz and Kolluru, 1984) emphasised the role that discontinuities might play in the time-dependent behaviour of excavations. Realistic modelling of the time-dependent rock behaviour therefore needs to simulate the rheological behaviour of discontinuities and the interaction between these discontinuities. Although a continuum viscoplastic model can simulate the time-dependent formation of the fracture zone as a volumetric effect (Chapter 5), it is not successful in simulating this behaviour where it is dominated by prominent discontinuities. Therefore, a discontinuous formulation is required. Samtani et al. (1996) developed a viscoplastic interface model for use in finite element programs. Interface elements in finite element programs can however cause numerical problems through ill-conditioning of the stiffness matrix and high stress gradients in the interface elements (Day and Potts, 1994). Further difficulties are experienced in generating multiple discontinuities in finite element meshes. These problems are not encountered in boundary element programs, although the number of elements is usually restricted to a fairly limited number in correspondence to the amount of computer memory available. Napier and Peirce (1995) developed a boundary element method for solving multiple interacting crack problems in which several thousand elements can be treated. Therefore a viscoplastic displacement discontinuity model was developed for use in this study.

The preliminary investigation of shear creep of discontinuities in the South African gold mining industry (Chapter 6) has illustrated two distinct classes of phenomena.

a) Discontinuities with gouge infilling may show noticeable shear creep behaviour for stresses below the failure strength.

b) Mining induced extension fractures with no infilling exhibit very long relaxation times if loaded below the failure strength. Their behaviour is therefore dominated by the post-failure response.

The initial sections in this chapter will focus on the second class although the effect of the discontinuities with infilling is also examined.

7.2 Seismicity and time-dependent deformation

As the discontinuum approach described in this chapter proved to be a useful tool to investigate stress transfer processes and seismicity effects of brittle rock, a brief overview of this link between seismicity and aseismic deformation is appropriate.

McGarr (1976) investigated the dependence of magnitude statistics on aseismic rock deformation in the East Rand Proprietary Mines. It was found that the level of seismicity is determined by the rate of aseismic deformation. That is, the time-dependence of the seismicity is the result of aseismic deformation that occurs over an extended period. It appeared that the rock was undergoing time-dependent deformation in response to stress changes due to either mine face advance or to seismic events. It was postulated that the aseismic deformation was due to progressive brittle failure as the rock temperature is too low to allow for continuum plastic deformation in the quartizites. Legge and Spottiswoode (1987) investigated the spatial, temporal and energy related aspects of fracturing ahead of a stope face with reference to microseismic activity. Locations of microseismic events showed the region of primary fracturing to be located 5 m to 10 m ahead of the mining faces. It was found that the total amount of seismic energy radiated during a typical face advance increment is a small portion of the total energy released on any individual day. Most energy is released in a stable manner by aseismic processes. Stewart and Spottiswoode (1993) discussed cumulative seismicity with time after blasting for data obtained from an experimental preconditioning site at Blyvooruitzicht Mine. The data

exhibits three clear trends namely an initial steep linear portion corresponding to the blast sequence itself, an intermediate portion in which the cumulative seismicity rate follows a trend that is inversely proportional with time and a final portion that corresponds to the background level of seismicity. The data set was, however, limited to the first hour after blasting. Kranz and Estey (1996) observed similar trends of seismicity. As the particular mine had ceased production, it was possible to determine the true background rate of seismicity. A Burgers model proved best to describe the rock rheology. It was shown that the cumulative number of events N as a function of time t could be described by

$$N(t) = a - be^{-st} + ct \qquad [7.1]$$

with the term ct included for the long term background seismicity.

In this thesis, mining-induced seismicity at the experimental preconditioning site at Blyvooruitzicht mine (Kullmann et al., 1996) was used for comparison with the numerical results. This is also described in Malan and Spottiswoode (1997). The faces were advanced by about 0.7 m by blasting in face-perpendicular holes drilled into the stope face. This is the normal form of production. In addition, face-parallel preconditioning blasts were set off 4 m to 5 m ahead of the face after every 4 m to 5 m of face advance. The purpose of these blasts was to help sustain the fracture zone that normally develops ahead of the face. If this fracture zone does not develop as expected, the resulting high stresses at the face can result in sudden stress release through face bursting. Kullmann et al. (1996) reported that these preconditioning blasts did indeed achieve these objectives.

The first face blasts and the preconditioning blasts on each day were individually marked in the data-base of 3 ½ years of data. It was therefore possible to select days with only face blasts or only preconditioning blasts and to study the rate of seismicity for comparison with modelled deformations.

7.3 Viscoplastic displacement discontinuity model for unfilled discontinuities

From the work in the previous chapter it follows that for mining induced extension fractures in hard rock, the creep of a discontinuity loaded below the shear strength is insignificant and will therefore be ignored. Above the yield strength, it is assumed that the rate of shear displacement is proportional to the excess shear stress. This is essentially

equivalent to assumptions made by Ida (1974) and Wesson (1988) about fault creep in earthquake studies.

Suppose that the local shear and normal components of the displacement discontinuity vector are denoted by D_S and D_N respectively. Analogous to Perzyna's (1966) theory of continuum viscoplasticity, the rates of change in normal and shear discontinuity are assumed to be given by

$$\begin{Bmatrix} \frac{\dot{D}_S}{d} \\ \frac{\dot{D}_N}{d} \end{Bmatrix} = \mu\langle F\rangle \begin{Bmatrix} \frac{\partial Q}{\partial \tau} \\ \frac{\partial Q}{\partial \sigma_n} \end{Bmatrix} \qquad [7.2]$$

where F is the yield criterion, Q the plastic potential function, τ the shear stress acting on the discontinuity and σ_n the normal stress. It is postulated that the viscoplastic effects are limited to a finite discontinuity thickness d. This thickness not only includes gouge width and asperity heights but also the thin layer of rock adjacent to the discontinuity wall controlling the strength and deformation properties (Barton and Choubey, 1977). The intact rock between discontinuities behaves elastically. The fluidity μ is a material constant with units $Pa^{-1}s^{-1}$. For ease of model calibration the parameters μ and d will be grouped as a discontinuity fluidity $\mu' = \mu d$ with units $Pa^{-1}s^{-1}m$. The Mohr-Coulomb model is adopted as yield criterion giving the following shear yield function

$$F = |\tau| - S_C + \sigma_n \tan\phi_C \qquad [7.3]$$

where S_C and ϕ_C are the current values of cohesion and friction angle respectively. For an unmobilised discontinuity, $S_C = S_P$ and $\phi_C = \phi_P$ where S_P and ϕ_P are the peak values of cohesion and friction angle respectively. A negative stress convention is used for compressive stresses. Shear failure takes place for $F \geq 0$. Below the yield surface ($F < 0$) the discontinuity is immobilised. The function $\langle F\rangle$ in equation [7.2] implies that

$$\begin{aligned} \langle F\rangle &= F \quad \text{for} \quad F \geq 0 \\ \langle F\rangle &= 0 \quad \text{for} \quad F < 0 \end{aligned} \qquad [7.4]$$

Roberts and Einstein (1978) showed that a non-associated flow rule should be adopted for rock discontinuities. The plastic potential function is given by

$$Q = |\tau| + \sigma_n \tan\psi \qquad [7.5]$$

where ψ is the dilation angle. Inserting equation [7.5] in [7.2] and writing in incremental format gives

$$\begin{aligned} \Delta D_S &= \mu' \ell \langle F \rangle \Delta t \\ \Delta D_N &= |\Delta D_S| \tan\psi \end{aligned} \qquad [7.6]$$

where Δt is the time increment. The variable ℓ is used as a slip direction indicator where (Napier and Malan, 1997)

$$\begin{aligned} \ell &= +1 \quad \text{for} \quad \tau < 0 \\ \ell &= -1 \quad \text{for} \quad \tau > 0 \end{aligned} \qquad [7.7]$$

The constitutive description of time dependent rock behaviour should also include the effect of strength degradation with time as discussed in Chapter 5. Stress corrosion (Atkinson, 1987) has been advanced as a possible mechanism to explain this type of rock behaviour. Similarly joint and fracture surfaces appear to undergo strength reduction due to weathering and water penetration. Unfortunately very limited data on time-dependent reduction of discontinuity strength is available. Strength reductions in the order of 5 % to 30 % have been noted by Barton (1976). Tan (1993) investigated the long term strength of very weak bedding planes in sandstone and mudstone. From his data (assuming a Mohr-Coulomb model) a 20 % reduction in friction coefficient and 70 % reduction in cohesion was observed after 20 days. Fakhimi and Fairhurst (1994) modelled the time-dependent degradation of material strength by exponential friction and cohesion decay functions. Similarly, to represent time-dependent discontinuity strength in this study, the following functions are introduced

$$S_C = S_r + \left(S_p - S_r\right)e^{-\alpha t} \qquad [7.8]$$

$$\phi_C = \phi_r + \left(\phi_p - \phi_r\right)e^{-\beta t} \qquad [7.9]$$

where α is the cohesion decay factor, β is the friction decay factor and S_r and ϕ_r the residual values of cohesion and friction angle. These conditions only hold for those discontinuities that are mobilised. Figure 7.1 illustrates the assumed yield surface and time-dependent reduction in strength of this surface. The time period t of strength degradation for a particular discontinuity is that time t accumulated for which the following condition is true

$$|\tau| \geq \gamma\left(S_C - \sigma_n \tan\phi_C\right) \quad \text{for} \quad 0 \leq \gamma \leq 1 \qquad [7.10]$$

The discontinuity should therefore be loaded to within a certain percentage (depending on γ) of its failure strength otherwise no strength degradation takes places. This condition is necessary as significant unloading of the discontinuity may suppress time-dependent microcracking of asperities preventing further decay of the strength properties. In view of the little experimental evidence available, the time-dependent weakening model described above should be considered as an initial assumption only.

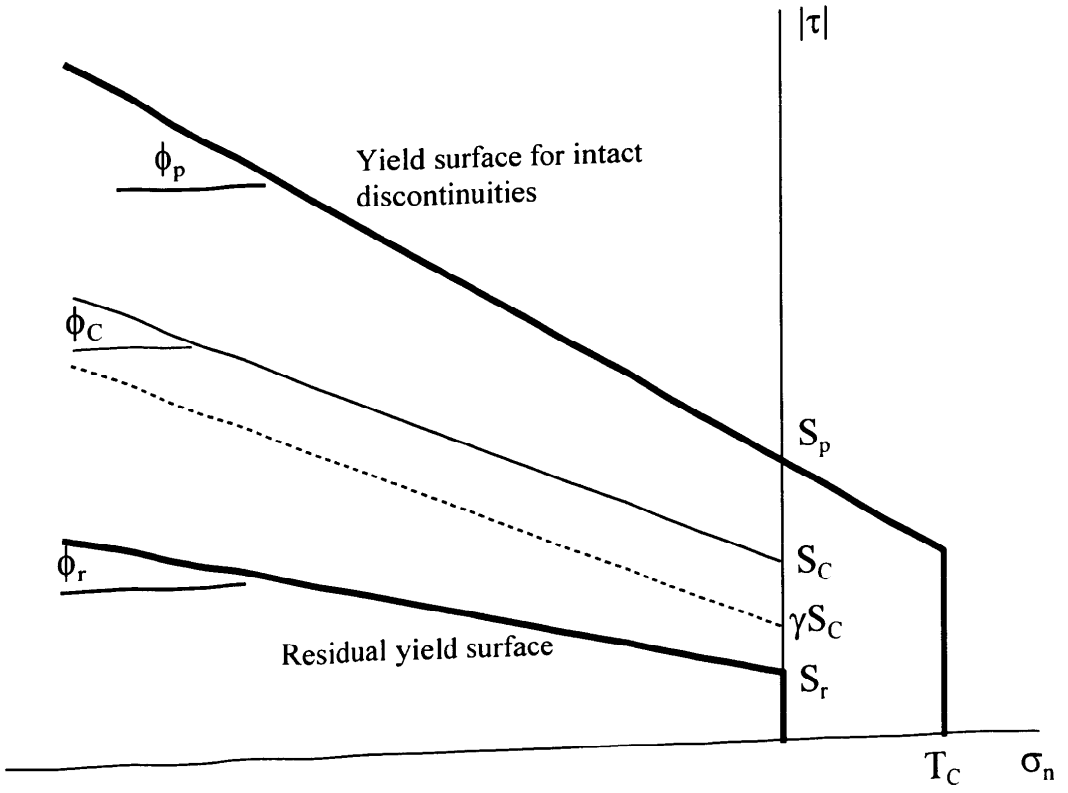

Figure 7.1. Evolution of the yield surface for intact discontinuities to the eventual residual surface.

7.4 Solution scheme

The viscous displacement discontinuity formulation described above was implemented as special elements in an existing plain-strain displacement discontinuity code. (See Napier, 1990 for a description of the code DIGS.) A time stepping routine similar to that devised by Napier and Malan (1997) to solve discontinuum viscoplastic problems was used. Figure 7.2 gives a flow chart explaining the time-dependent solution scheme. The reader is referred to Napier and Malan (1997) for a more detailed explanation. A typical problem might consist of a mixture of viscous elements to represent viscoplastic discontinuities and non-viscous elements representing excavation boundaries. An iteration procedure to estimate new discontinuity values for the non-viscous elements is nested inside the time-stepping loop. Each time increment is therefore accompanied by several iteration cycles. This can be an inefficient process unless accelerated iteration methods are used. A second order Lanczos minimisation algorithm (Ryder, 1991) was used as the iteration method in the numerical analysis described in Section 7.5.

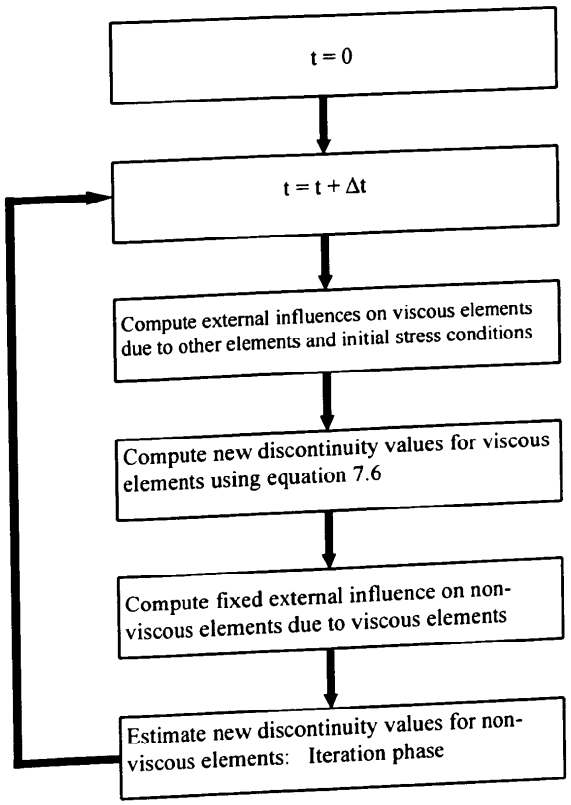

Figure 7.2. Time-stepping solution scheme.

7.5 Incremental mining of a tabular stope: Numerical results

Stope modelling was undertaken by covering the problem space with a random mesh of viscoplastic discontinuities. Figure 7.3 shows a typical distribution used. This distribution should be considered as potential fracture surfaces which are initially intact with a prescribed strength determined by the failure criteria described in equation [7.3]. For this preliminary modelling, no bedding planes were included. Mining was undertaken in an incremental fashion allowing the progressive evolution of the fracture zone. Owing to computer memory limitations, the number of elements is limited. The object of this modelling should therefore be seen as studying the effect of the time-dependent fracture process and not replicating observed fracture patterns. In future the viscous model will be implemented in the multipole boundary element method devised by Napier and Peirce (1995). As this allows for the solution of many more elements, more realistic fracture patterns may be obtained.

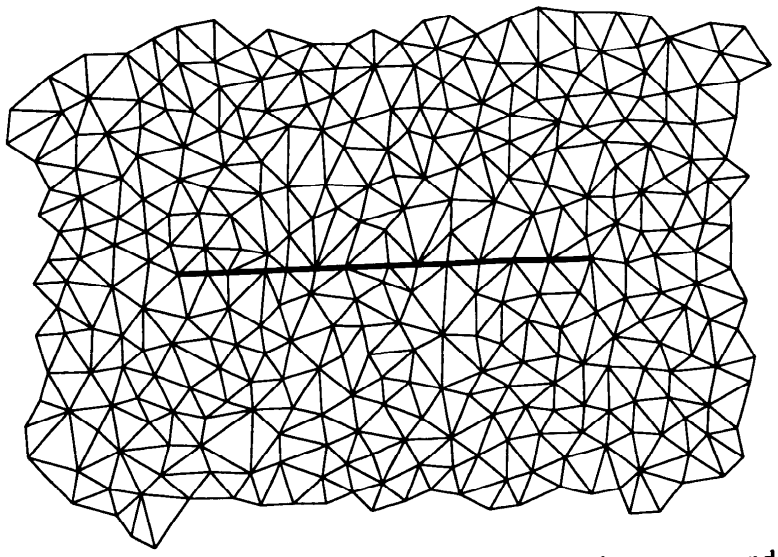

Figure 7.3. Initial random distribution of potential fracture planes surrounding the reef.

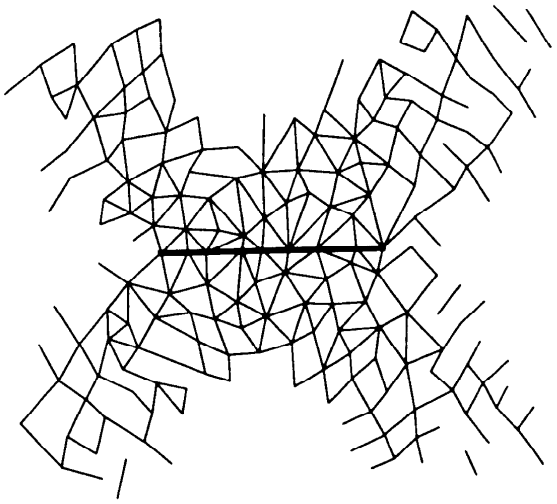

Figure 7.4. Development of the fracture zone 24 hours after the 9th mining increment. The stope is represented by the thick black line. The model parameters used are E = 70 GPa, $\nu = 0.2$, $\mu' = 1\times10^{-5}$ $MPa^{-1}h^{-1}m$, $S_p = 20$ MPa, $S_r = 0$ MPa , $\alpha = 0$ h^{-1}, $\beta = 0$ h^{-1}, $\phi_p = 30$, $\phi_r = 20$ and $\gamma = 0.8$. Note that both α and β are zero and therefore there was no reduction in strength of the failed discontinuities.

Figure 7.4 illustrates the development of the fracture zone 24 hours after the 9th mining increment. The discontinuities shown are all those mobilised up to that particular point in time. Owing to the low density of the initial tessellation, this fracture pattern is at best only a coarse approximation of that observed underground. This is especially noticeable in the immediate area of the stope faces where the density of fracturing is much lower than is expected for underground stopes. The model has nevertheless proved to be useful for simulating the time-dependent processes in the rock. An important consequence of the prescribed viscoplastic behaviour is that the additional fracturing caused by a sudden increase in stress occurs in a time-dependent fashion. After a mining increment, the existing discontinuities surrounding the stope are subjected to an increase in mining induced stress. Those discontinuities subjected to stresses above the yield surface relax in a time-dependent fashion according to equation [7.6]. This relaxation process causes a stress transfer to the solid rock at the edge of the fracture zone. New fractures then form in these positions as a time-dependent process. For the example above, the increase in cumulative fracture length as a function of time after a blast is illustrated in Figure 7.5. It should be emphasised that there are no changes in the excavation dimension during this time period. Similarly to Adams and Jager's (1980) observations, the majority of new fractures formed within a short period after the blast, and the rate of fracturing then diminished until the next blast.

Also plotted in Figure 7.5 is the rate of seismicity after production blasts and preconditioning blasts calculated by Malan and Spottiswoode (1997) for the site described by Kullmann et al. (1996). Events with magnitude greater than -1.5 were used. The seismicity following 304 production blasts and 62 preconditioning blasts was added, or "stacked", to obtain Figure 7.5. All recorded events within five minutes of the start of the face blast were excluded because face blasting took approximately five minutes and most events within this time appeared to be face blasts. Given that the preconditioning blasts do not actually change the mine geometry, the similarity in the shape of the time decay after preconditioning blasts and face blasts is evidence that the shape of the curve reflects the adjustment of the entire rock mass to changing stress conditions and not only for the removal of rock.

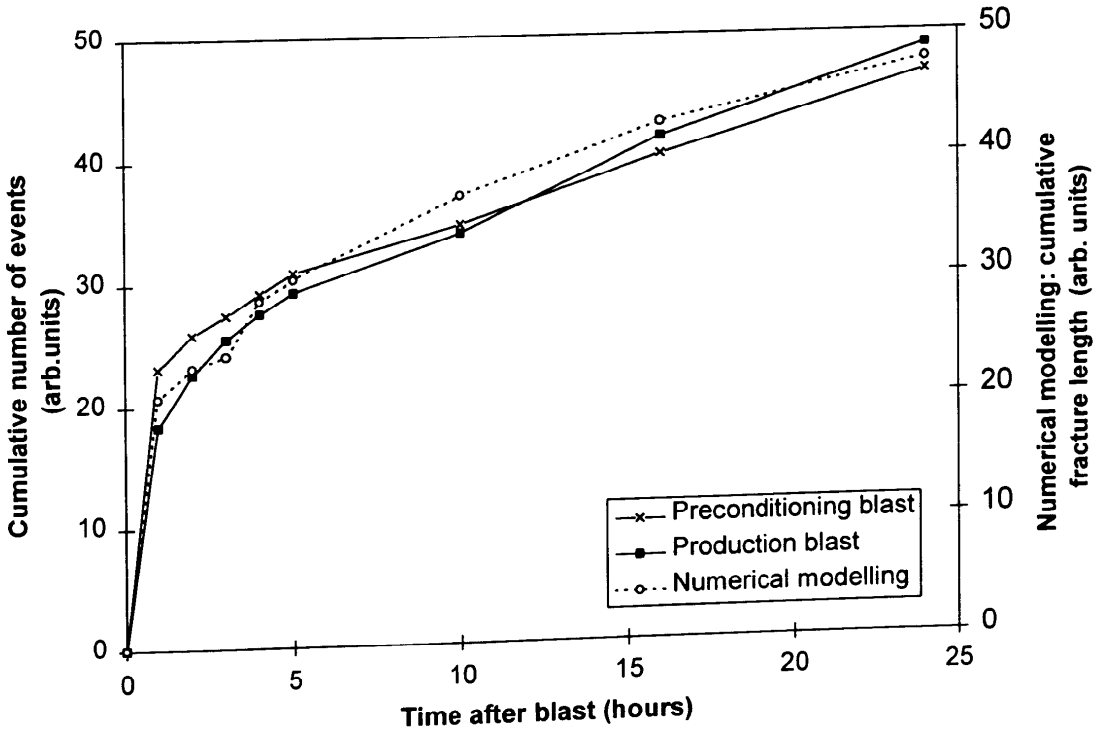

Figure 7.5. Increase in cumulative fracture length after the 9th increment. The same model parameters as given in Figure 7.4 were used. The rate of seismicity after production and preconditioning blasts is also plotted showing similar trends.

The time-dependent fracture process leads to the typical stope closure profile illustrated in Figure 7.6. Similar to the results in Chapter 4 (see Figure 4.26) the highest rate of closure occurs after blasting time and this decays until the next blast takes place. If the discontinuities are subjected to a time-dependent decrease in cohesive strength, an increase in closure is observed in the longer term.

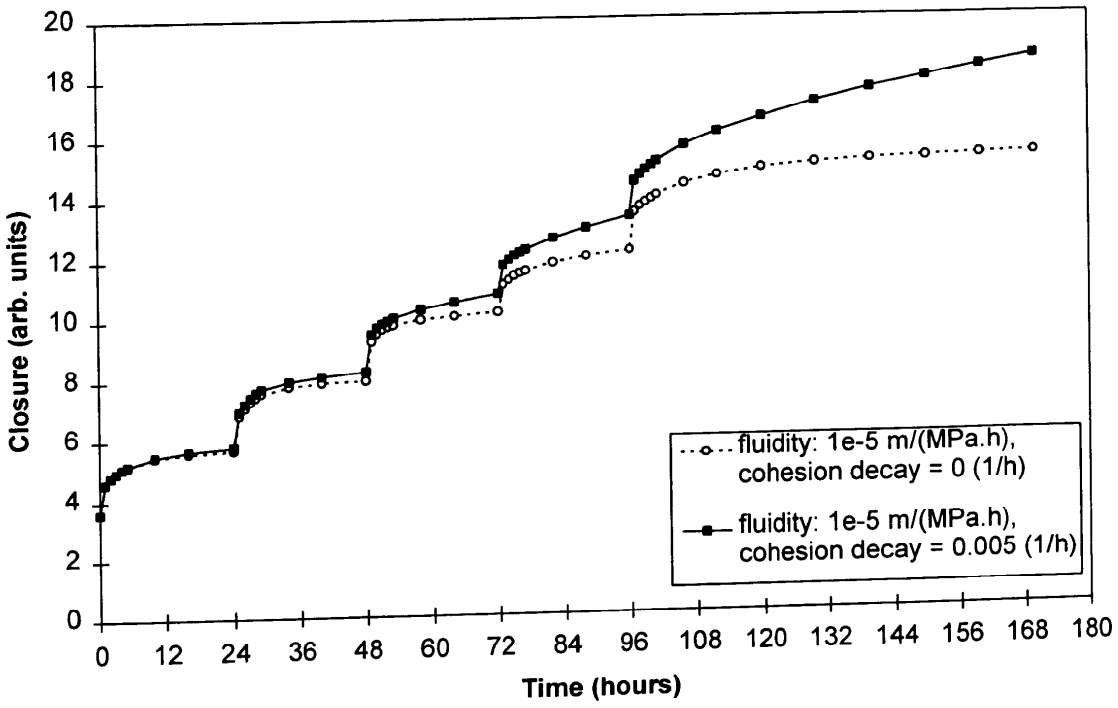

Figure 7.6. Numerical stope closure as a function of time. Blasting took place at 0, 24, 48, 72 and 96 hours.

As described in Chapter 4, McGarr (1971) investigated the stope closure rate throughout the week at East Rand Proprietary Mines (See Figure 7.7). The closure is given during six-hour intervals with the value at the middle of a given six hour period plotted in Figure 7.7. The experimental data has been averaged over 30 weeks. Results obtained from numerical modelling illustrates similar trends. The model parameters used are E = 70 GPa, $\nu = 0.2$, $\mu' = 1\times10^{-8}$ MPa^{-1}h^{-1}m , $S_p = 20$ MPa, $S_r = 0$ MPa , $\alpha = 0.005$ h^{-1}, $\beta = 0.005$ h^{-1}, $\phi_p = 30$, $\phi_r = 20$, $\gamma = 0.8$. The highest rate of closure occurs during the six hour interval that includes the times of face advance. The rate also increases throughout the week until Sunday when no blasting takes place and the rock is allowed to relax further. There is however a weak fit between the experimental data and numerical results for the periods of decreasing rate of closure after the blast. This is caused by the low density of fracturing ahead of the faces in the numerical model. Mining in this unfractured stressed rock results in relatively higher increases in convergence for the period that includes the blast. The peak values of the modelling results also show some erratic behaviour because of the discontinuous nature of the model. As the density of fractures in the tessellation is low, the rate of convergence is strongly influenced by the measurement position and the orientation of the new fractures activated by each mining step. If fractures with a favourable

orientation are activated in a particular step, higher rates of convergence are suddenly experienced. That this erratic behaviour almost follows the same trend as the peak values of the underground measurements is purely accidental. Other tessellation patterns and measurement positions will give different peak values for each step. If a number of different mesh patterns were analysed, one would expect a statistical trend with deviations from the mean value.

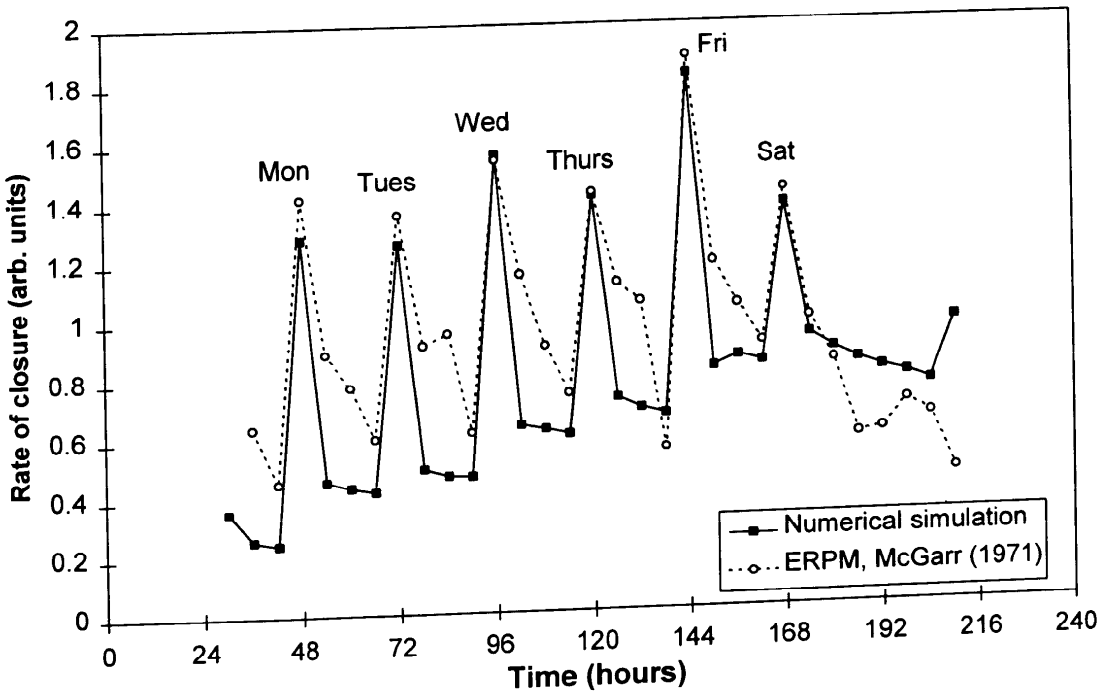

Figure 7.7. Numerical and experimental rate of closure as a function of time. The experimental data is from the East Rand Proprietary Mines (after McGarr, 1971, see text above).

7.6 Simulating the creep of gouge-filled discontinuities

A question remaining is what contribution is made by the creep of discontinuities subjected to shear stress below the failure strength. The discontinuity creep results in Chapter 6 showed that noticeable creep is experienced by discontinuities with gouge infilling. In a typical test where the shear load was incrementally increased, the cumulative shear creep displacement was 1.1 mm over a time period of 192 hours. This may be one possible mechanism explaining some of the displacement on shear fractures ahead of an

advancing face (see Figure 1.4 in Chapter 1). To enable numerical analysis, the author developed a simple model for implementation in a displacement discontinuity code. A complete understanding of the underlying mechanisms of the discontinuity creep in Chapter 6 is beyond the scope of this work. Therefore the model developed below only captures the most important features to enable the numerical study of fault creep where the fault is stressed below its failure strength and a stope face is advancing towards it.

For discontinuities with infilling, a similar yield function to that given in equation [7.3] is adopted. For $F \geq 0$ the behaviour is similar to that described in the previous section. Below the yield surface ($F < 0$) the discontinuity is not immobilised as assumed above, but is subjected to shear creep. The rheological model in Figure 7.8 is used to simulate this behaviour. It should be stated from the outset that this model is used as an approximation of the creep behaviour for shear loading in one direction. From the experiments above, the displacements are not recoverable on unloading and therefore K_{ds1} and K_{ds2} should be considered as pseudo-stiffness parameters.

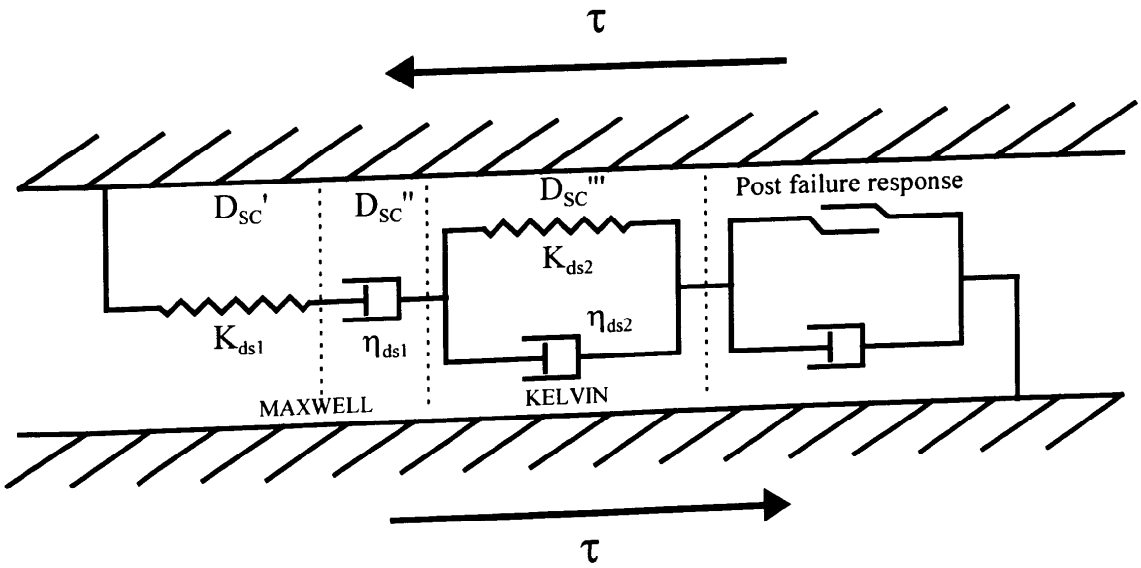

Figure 7.8. Rheological model to approximate the shear creep of discontinuities with infilling.

For $F < 0$, the total shear creep displacement D_{SC} is given by

$$D_{SC} = D_{SC}' + D_{SC}'' + D_{SC}''' \qquad [7.11]$$

For an applied shear stress τ, the first term is given by

$$D_{SC}' = \frac{\tau}{K_{dsl}} \qquad [7.12]$$

where K_{dsl} is the discontinuity shear stiffness of the Maxwell part of the model with units Pa/m. The lower this stiffness value, the larger the instantaneous response after applying or increasing the shear load.

The Maxwell dashpot (see Figure 7.8), controls the shear creep rate in the secondary phase and this is given by

$$\dot{D}_{SC}'' = \frac{\tau}{\eta_{dsl}} \qquad [7.13]$$

where η_{dsl} is the discontinuity viscosity with units Pa.s/m. After integration and imposing the condition $D_{SC}'' = 0$ at $t = 0$, it follows that

$$D_{SC}'' = \frac{\tau t}{\eta_{dsl}} \qquad [7.14]$$

For the Kelvin component in Figure 7.8 it follows that

$$\tau = D_{SC}''' K_{ds2} + \dot{D}_{SC}''' \eta_{ds2} \qquad [7.15]$$

When solving equation [7.15] through separation of variables and noting that at $t = 0$, $D_{SC}''' = 0$, it follows that

$$D_{SC}''' = \frac{\tau}{K_{ds2}}\left(1 - e^{\frac{-K_{ds2}t}{\eta_{ds2}}}\right) \qquad [7.16]$$

Inserting equations [7.12], [7.14] and [7.16] into equation [7.11] it follows that the total shear displacement for $F < 0$ is given by

$$D_{SC} = \tau\left[\frac{1}{K_{ds1}} + \frac{t}{\eta_{ds1}} + \frac{1}{K_{ds2}}\left(1 - e^{\frac{-K_{ds2}t}{\eta_{ds2}}}\right)\right] \qquad [7.17]$$

This model was fitted to some of the experimental results in Chapter 6. Figure 7.9 illustrates the fit obtained using the data of Figure 6.15. The applied shear stress was 0.48 MPa. The model parameters used were K_{ds1} = 0.675 MPa/mm, K_{ds2} = 7.5 MPa/mm, η_{ds1} = 1100 MPa.h/mm and , η_{ds2} = 14 MPa.h/mm.

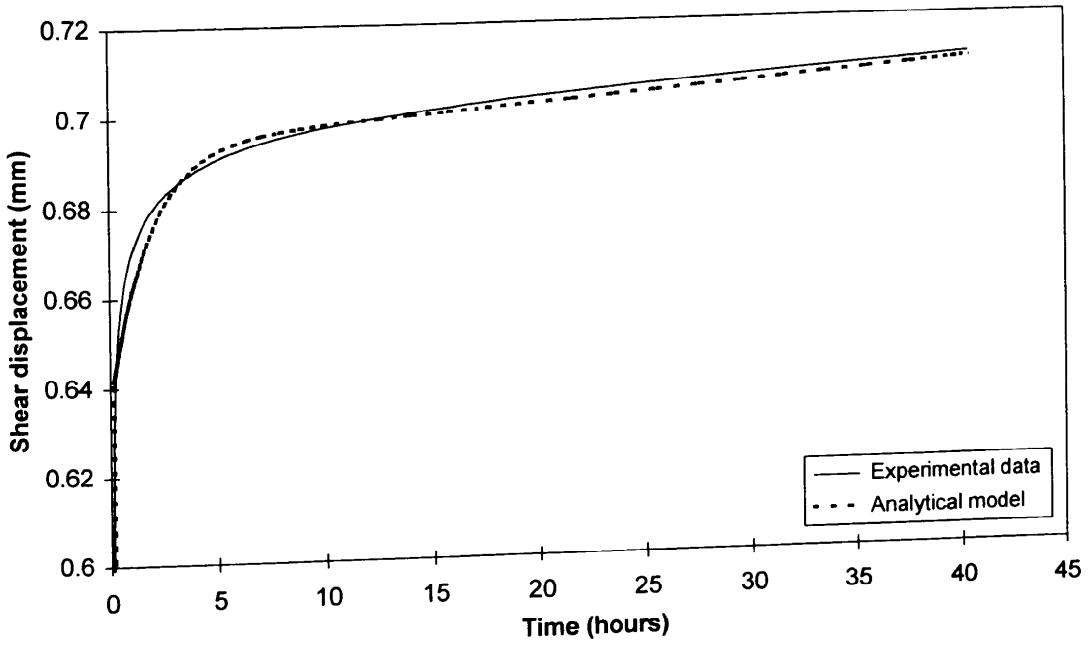

Figure 7.9. Simulating the experimental shear creep using the rheological model given in equation [7.17].

In Chapter 6 it was noted that the shear creep of discontinuities with thick gouge infilling is accompanied by a normal compaction. To simulate this compaction, D_{NC}, a function similar to the second one in equation [7.6] is used

$$D_{NC} = |D_{SC}| \tan\psi \qquad [7.18]$$

but now the dilation angle ψ is negative to simulate the compaction. Figure 7.10 illustrates the experimental compaction accompanying the shear displacement in Figure 7.9. Also plotted in this figure is the numerical approximation using equation [7.18] with a dilation

angle of -13°. The fit in the primary phase can be improved but as the compaction is normally quite small, the approximation of equation [7.18] will be deemed acceptable.

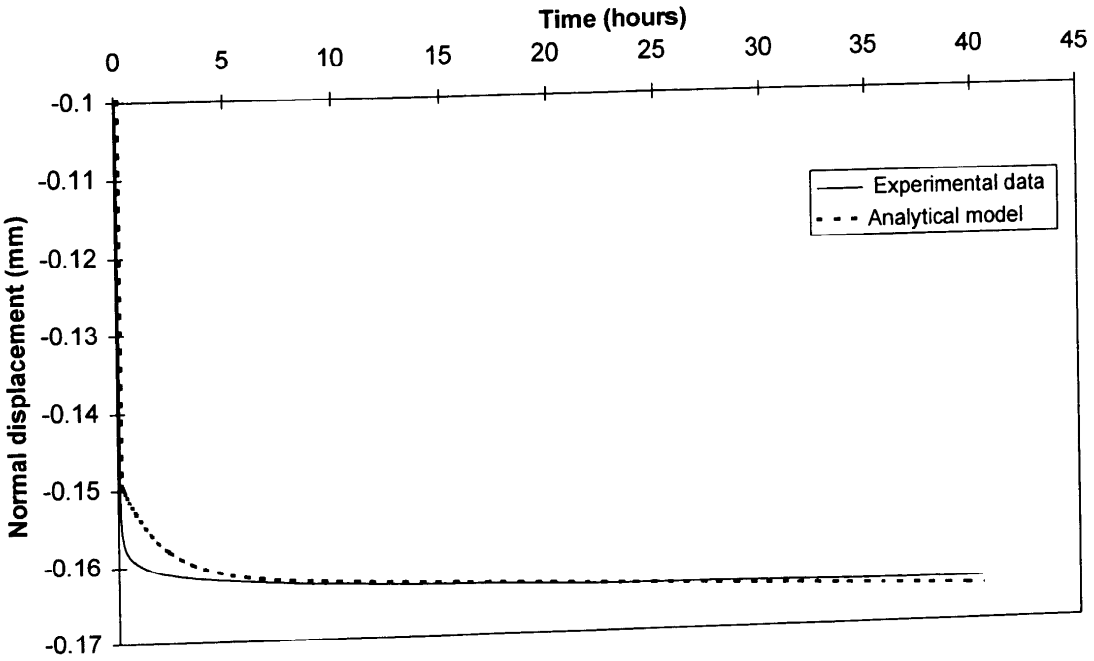

Figure 7.10. Experimental and simulated compaction accompanying the shear results in Figure 7.9.

From the fit in Figure 7.9 it appears that the model is an adequate representation of the discontinuity creep behaviour. It should be noted that the calibrated parameters are only valid at the applied stress of 0.48 MPa. In Chapter 6 it was noted that the magnitude of instantaneous response and steady-state creep rate increase with an increasing shear stress/shear strength ratio. The model parameters in equation [7.17] are therefore not constants but functions of the applied stress. To illustrate this, the results given in Figures 6.19, 6.20 and 6.21 in Chapter 6 will be examined in more detail.

From Figure 6.20 the Maxwell shear stiffness, K_{dsl} (controlling the instantaneous shear displacement) for the different loading steps can be calculated using equation [7.12]. These stiffness values are plotted in Figure 7.11 as a function of the shear stress/shear strength ratio (τ/τ_s) showing that K_{dsl} decreases for an increasing (τ/τ_s) ratio. In the model this will be simulated using the power law

$$K_{dsl} = A\left(\frac{\tau}{\tau_S}\right)^B \qquad [7.19]$$

The parameters A and B can be calculated from a $\log(K_{dsl})$ versus $\log(\tau/\tau_s)$ plot. This is illustrated in Figure 7.12 giving values A = 1.0387 MPa/mm and B = -5.6763.

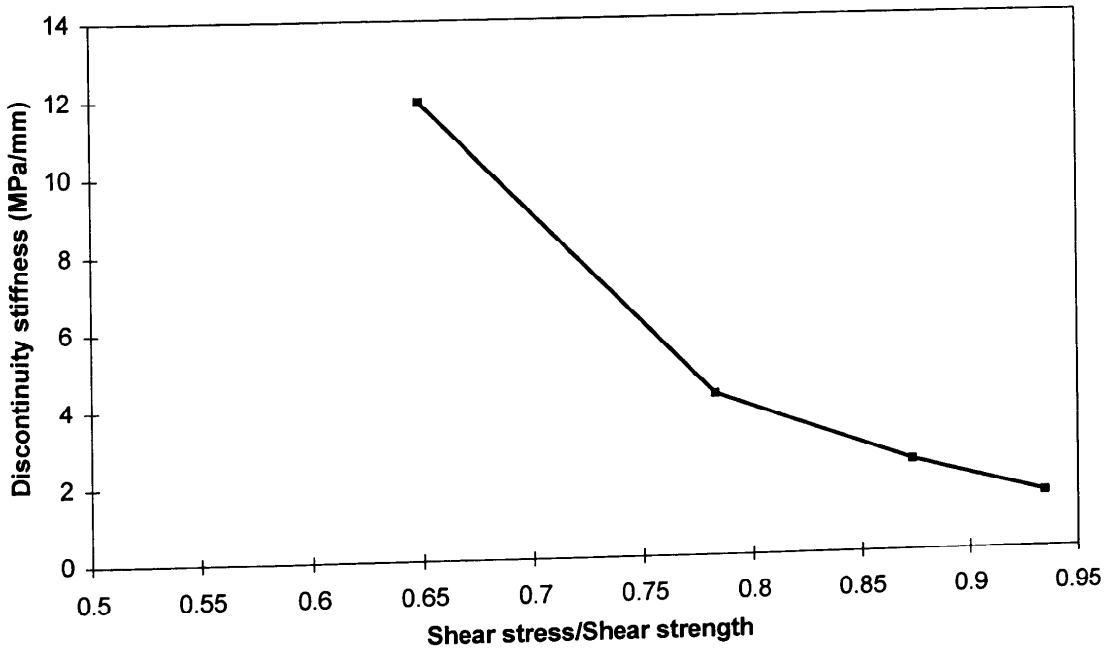

Figure 7.11. Relationship between the Maxwell stiffness, K_{dsl}, and the (τ/τ_s) ratio.

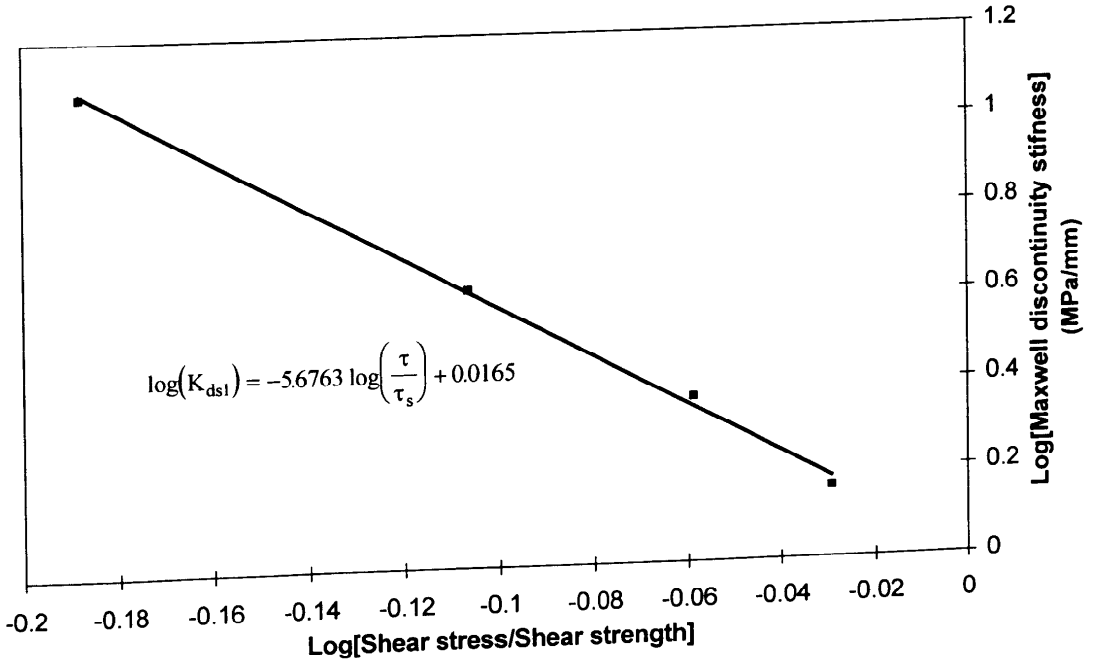

Figure 7.12. $\text{Log}(K_{dsl})$ versus $\log(\tau/\tau_s)$ plot.

From Figure 6.21 the Maxwell shear viscosity η_{dsl} (controlling the steady-state creep rate) could be calculated for the different loading steps using equation [7.13]. The resulting values are plotted in Figure 7.13 as a function of the (τ/τ_s) ratio. This viscosity also decreases with an increasing (τ/τ_s) ratio. In the model this will be simulated using

$$\eta_{dsl} = C\left(\frac{\tau}{\tau_S}\right)^D \qquad [7.20]$$

From the log-log plot in Figure 7.14, the parameters are calibrated as C = 1715.5 MPa.h/mm and D = -2.9262.

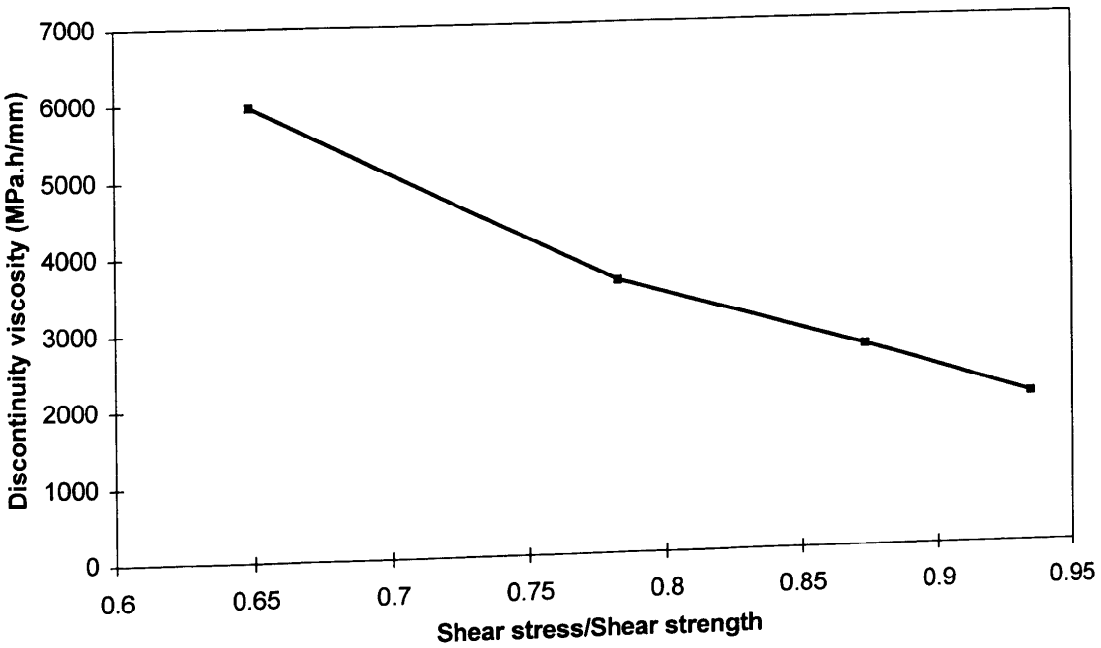

Figure 7.13. Relationship between the Maxwell viscosity, η_{dsl}, and the (τ/τ_s) ratio.

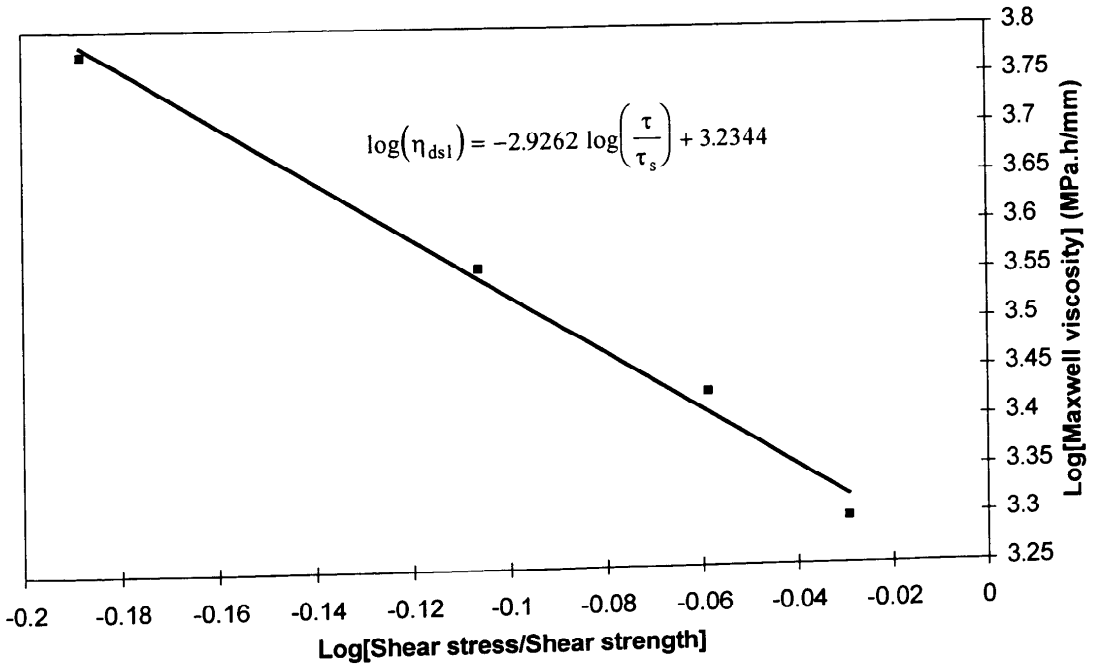

Figure 7.14. $\text{Log}(\eta_{ds1})$ versus $\log(\tau/\tau_s)$ plot.

To obtain the calibrated values of the Kelvin stiffness, K_{ds2}, equation [7.17] was fitted to the creep curves at the different stress levels in Figure 6.20. The calibrated values of K_{ds2} for each curve is plotted in Figure 7.15 as a function of the (τ/τ_s) ratio. Again the stiffness is decreasing with the (τ/τ_s) ratio. In the model this will be simulated using

$$K_{ds2} = E\left(\frac{\tau}{\tau_S}\right)^F \qquad [7.21]$$

From the log-log plot in Figure 7.16 the parameters are calibrated as E = 15.8 MPa/mm and F = -3.9414.

For simplicity in the model, the Kelvin viscosity η_{ds2} will be assumed a constant.

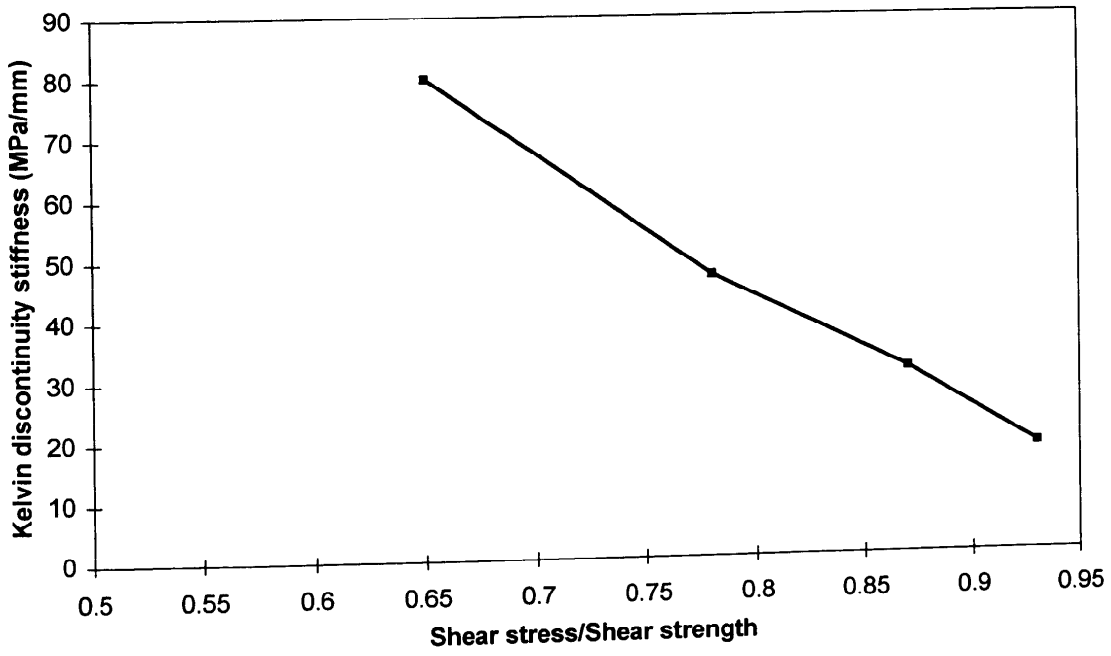

Figure 7.15. Relationship between the Kelvin stiffness, K_{ds2}, and (τ/τ_s) ratio.

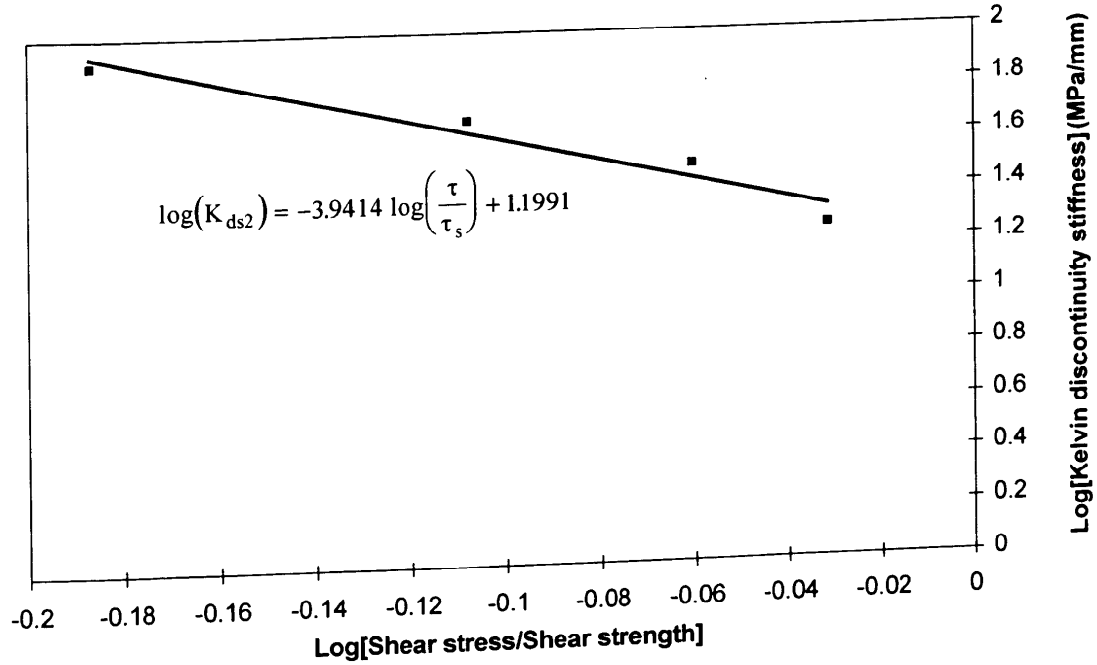

Figure 7.16. $\text{Log}(K_{ds2})$ versus $\log(\tau/\tau_s)$ plot.

In summary, it appears that the model given in equations [7.17] to [7.21] is successful in replicating the shear creep behaviour of discontinuities with gouge infilling. It should however be noted that in spite of the successful calibration of the parameters A, C and E above, these parameters also depend on factors like the gouge thickness and absolute values of shear and normal stress. Although the model is represented by the rheological

representation in Figure 7.8, the displacements are not recoverable during unloading as discussed in Chapter 6. In the modelling it is assumed that only for a reversal of shear stress direction (of equal magnitude) will the shear displacement be recovered.

Numerical analysis

The first term of the model given in equation [7.17] predicts an instantaneous response for a stepwise application or increase in shear stress. This is followed by the time-dependent creep components. To enable some preliminary modelling using the time-stepping structure of Figure 7.2, both components were included when updating the discontinuity values for the viscous elements. This is not ideal as the instantaneous response should be dealt with in the iteration phase to ensure a correct solution and numerical stability. This is especially important if multiple interacting viscous elements are present. Therefore this preliminary modelling will be limited to a single viscous fault ahead of an advancing stope where the displacements on the fault are small.

For the instantaneous response, the following scenarios are possible:
a) For an unloaded discontinuity or one where the direction of shear has changed, the instantaneous shear displacement after loading is given by

$$\Delta D_{Sinst} = \frac{\ell|\tau_i|}{K_{dsl}} \qquad [7.22]$$

where ℓ is the slip direction indicator defined in equation [7.6] and τ_i is the shear stress acting on the discontinuity in step i.

b) If the discontinuity is already loaded and subjected to an increase in shear stress while the sense of shear remains the same, the increment in instantaneous response is given by

$$\Delta D_{Sinst} = \ell\left[\frac{|\tau_i| - |\tau_{i-1}|}{K_{dsl}}\right] \qquad [7.23]$$

with τ_{i-1} the shear stress acting on the discontinuity in the previous step.

c) If the discontinuity is already loaded and subjected to a decrease in shear stress while the sense of shear remains the same, the increment in instantaneous response is given by

$$\Delta D_{Sinst} = 0 \qquad [7.24]$$

This increment is zero as the shear displacements are not recoverable.

The instantaneous response is followed by the creep components. Again the following scenarios can be identified.

a) For an unloaded discontinuity being subjected to a shear load τ_i in step i or one where the direction of shear changed in step i, the rate of creep displacement can be obtained by differentiating equation [7.17] to give

$$\dot{D}_{Screep} = \frac{|\tau_i|}{\eta_{ds1}} + \frac{|\tau_i|}{\eta_{ds2}}\left(e^{\frac{-K_{ds2}t'}{\eta_{ds2}}}\right) \qquad [7.25]$$

where t' is the time that elapsed since the shear stress τ_i was applied. Writing this equation in incremental format and adding the slip direction indicator gives

$$\Delta D_{Screep} = \ell\left[\frac{|\tau_i|}{\eta_{ds1}} + \frac{|\tau_i|}{\eta_{ds2}}\left(e^{\frac{-K_{ds2}t'}{\eta_{ds2}}}\right)\right]\Delta t \qquad [7.26]$$

where Δt is the timestep.

b) If the discontinuity is already loaded and subjected to an increase in shear stress while the sense of shear remains the same, the increment in creep components is given by

$$\Delta D_{Screep} = \ell\left[\frac{|\tau_i|}{\eta_{ds1}} + \frac{\left(|\tau_i| - |\tau_{i-1}|\right)}{\eta_{ds2}}\left(e^{\frac{-K_{ds2}t'}{\eta_{ds2}}}\right)\right]\Delta t \qquad [7.27]$$

where t' is the time that elapsed since the increase in shear stress.

c) If the discontinuity is already loaded and subjected to a decrease in shear stress while the sense of shear remains the same, there is not a primary creep response as the initial

displacements are not recoverable. Additional creep increments are given by the steady-state term although the creep rate will be reduced. The increment in shear creep is given by

$$\Delta D_{Screep} = \frac{\ell|\tau_i|\Delta t}{\eta_{dsl}} \qquad [7.28]$$

As mentioned above, this model was implemented in the displacement discontinuity code using a structure similar to Figure 7.2. The only difference was that instead of using equation 7.6 to compute new discontinuity values for the viscous elements, the equations above were used.

This model was used to investigate the creep of a fault with gouge infilling if a nearby stope was incrementally advanced towards this fault. This geometry is illustrated in Figure 7.17. This was simulated at a depth of 3000 m.

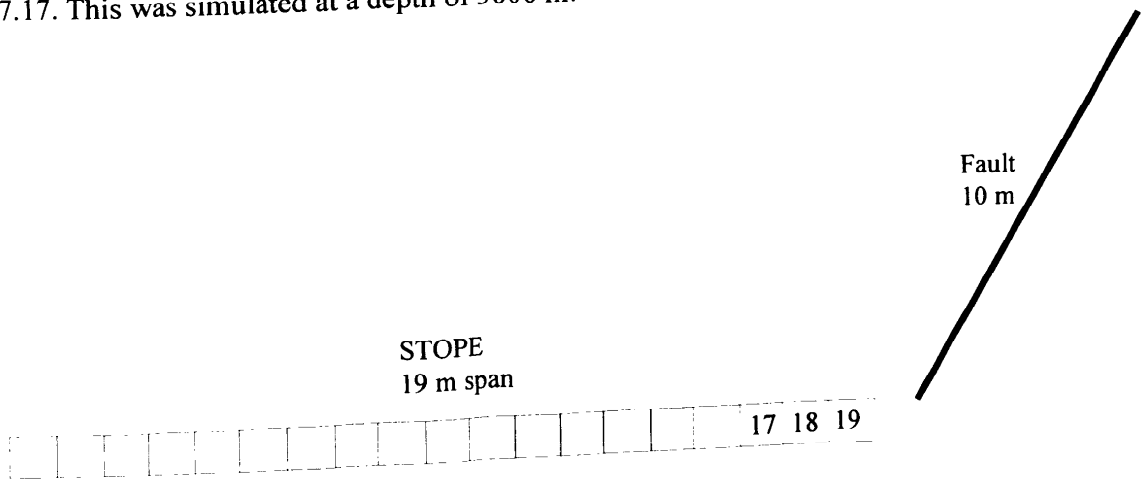

Figure 7.17. Incremental mining towards a fault with gouge infilling.

To simulate the fault strength, it was assigned a friction angle of 26° and a cohesion of 1 MPa. This ensured that for the maximum span of the stope, the fault was still stressed below its failure strength. Also used for the fault were the calibrated values of A, B, C, D, E and F given above. Other values were Young's modulus = 70 GPa and Poisson's ratio = 0.2. The stope was incrementally enlarged by mining 1 m increments. Figure 7.18 illustrates the fault creep for the last three increments. Note that a large percentage of the creep displacement occurs as an instantaneous movement at the time of each mining increment.

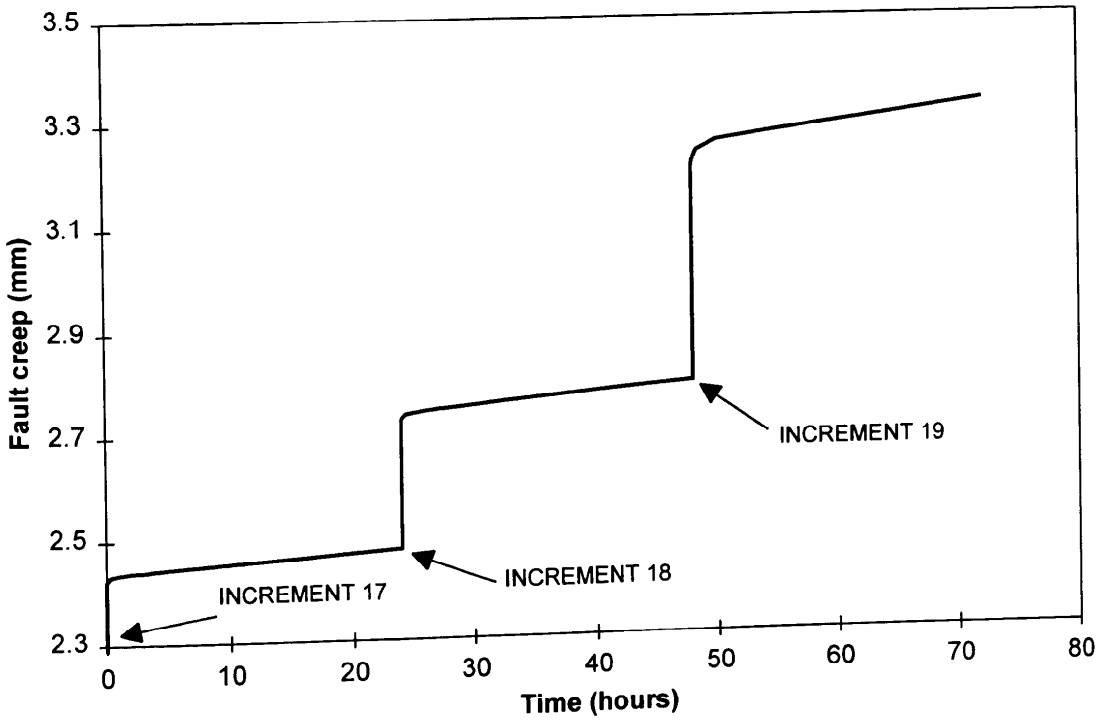

Figure 7.18. Simulated fault creep measured during the last three mining increments.

This example illustrates that in underground conditions, displacements may be observed from the creep of faults even when the shear stress does not exceed the shear strength of the discontinuity. In Chapter 1 it was noted that Legge (1984) observed shear displacements of about 5 mm to 40 mm on the large shear structures ahead of the face for a typical mining increment of 1 m. The creep mechanism explored in Chapters 6 and 7 may be responsible for some of this displacement. Further underground work is however necessary. A method should be devised to continuously monitor the fault creep displacements to verify the profile of Figure 7.18. These measurements are unfortunately difficult as they should include the monitoring of the fault while it is still some distance ahead of the face and therefore not easily accessible.

Chapter 8

Conclusions and recommendations

8.1 Conclusions

The objective of this study was to investigate the time-dependent behaviour of deep excavations in hard rock and develop appropriate numerical methods to simulate it. Although excavations in hard rock are not usually perceived to undergo significant time-dependent deformation, data from the deep gold mines in South Africa illustrates behaviour to the contrary. As these mines are also very prone to seismic activity, the study of time-dependent behaviour in hard rock is necessary to understand the conditions that are associated with the transition from stable time-dependent deformation to rock bursting. As there is some evidence that the rate of face advance affects the level of seismicity, a time-dependent constitutive model of hard rock on a mine scale is needed to determine optimum extraction rates to ensure both maximum production and safety of the workers.

A further motivation for this study is the observation of squeezing conditions (large time-dependent deformation) in some service excavations of the South African gold mining industry. Squeezing is almost exclusively associated with soft rocks like mudstone, but as a result of the great depths of the South African mines, large ongoing time-dependent deformation is occasionally noted in the hard rock. This is of concern as there are future plans for ultra-deep mining at depths between 3500 m and 5000 m which might increase the potential for squeezing conditions. To identify squeezing conditions in shallow tunnels in soft rock, the competency factor (ratio of uniaxial compressive strength to overburden stress) is frequently used. Squeezing conditions are usually associated with competency factors of less than two. In this study, a competency factor of 1.9 was calculated for the squeezing conditions investigated at Hartebeestfontein Mine. Of concern is the average strength of the Witwatersrand quartzites of 200 MPa. This implies that for the ultra-deep

mining levels, an increase in squeezing conditions can be expected. As this will put further strain on the profitability of these mines, further research on squeezing conditions in hard rock is required.

As almost no published data is available on the creep of intact hard rock from the South African mining industry, the initial part of this study focused on the uniaxial creep testing of quartzite and lava specimens in the laboratory. Although the strain rates were low, measurable room temperature creep was recorded. Typical primary, secondary and tertiary creep phases were noted. The strain rate of the secondary creep phase is strongly dependent on stress level and can be simulated with a stress power law. When loading samples to above 90 % of their failure strength, steady-state creep rates between 7.5×10^{-11} s^{-1} and 2×10^{-10} s^{-1} were observed for a variety of quartzite and Ventersdorp lava specimens. It should however be noted that the uniaxial compressive strength of the lava is significantly higher than that of the quartzites, therefore requiring a much higher applied stress to obtain a loading above 90 % of the failure strength. This has implications for the rock mass behaviour of the Ventersdorp Contact Reef stopes where the hangingwall consists of hard lava and the footwall of quartzite. As the ratio of deviatoric stress to failure strength at a particular distance from the excavation will be higher for the quartzite than the lava, creep failure may occur more readily in the quartzite.

The laboratory creep measurements were contrasted with continuous time-dependent closure measured in the tabular excavations of the South African gold mining industry. Unfortunately only limited data for continuous closure measurements is available and therefore experimental sites were established in different geotechnical areas. An important finding of this study is that continuous time-dependent closure data contains much information that is lost if only daily or longer period closure measurements are taken. Unfortunately daily measurements are the most popular method of monitoring closure in the South African industry. Future underground experiments involving the measurement of closure should be designed to include continuous measurements. The usefulness of these continuous measurements is explained below.

Continuous closure data typically illustrates an instantaneous response at blasting time followed by a primary closure phase lasting approximately four to five hours and a steady-state closure phase. After the next blast, this pattern is repeated. For tabular excavations in the Ventersdorp Contact Reef, the instantaneous response is very prominent, but it

decreases rapidly in magnitude as the distance from the face to the measurement position increases. The steady-state closure rate also decreases in magnitude with distance to the face. For a distance of 4 m to 5 m from the face in the up-dip panel described in this study, the steady-state closure rate is approximately 2 mm/day. If all mining activity stops, this rate gradually decreases, but can still be as high as 0.2 mm/day after two weeks. In contrast, for excavations in certain areas of the Vaal Reef, the steady-state closure rate can be as high as 15 mm/day. For these excavations, the instantaneous closure response at blasting time is virtually absent. Unlike the Ventersdorp Contact Reef, the steady-state closure rate of the experimental panel in the Vaal Reef increases with increasing distance to the face. This behaviour is probably caused by bedding plane separation in the hangingwall towards the back area of the panel. These steady-state closure measurements of tabular excavations in the Vaal Reef and Ventersdorp Contact Reef are important as the movements are much larger than typically expected for excavations in hard rock.

The laboratory creep rate of intact rock cannot explain the large time-dependent movements underground and it therefore appears that the rheology of the fracture zone and other prominent discontinuities like bedding planes play a dominant role. There is some evidence of the time-dependent extension of the fracture zone after a mining increment and this is confirmed by the cumulative distribution of microseismic events following a blast. Ideally, any model used to simulate the time-dependent behaviour of deep level excavations in hard rock should include some representation of delayed failure processes and the time-dependent extension of the fracture zone.

As a preliminary attempt to simulate the time-dependent closure measured underground, a viscoelastic approach was investigated. Although this theory is unable to simulate the fracture zone around excavations, it appears attractive owing to its simplicity, allowing for easy implementation in numerical codes. As viscoelastic theory is still frequently used in rock mechanics, it was necessary to investigate the potential of this theory for simulating the time-dependent closure of tabular excavations. As no analytical model for the closure of tabular openings in viscoelastic media is available, the author derived a two-dimensional closure solution for a parallel-sided tabular stope in a viscoelastic medium. This included the effect of an incremental enlargement of the stope. To complement the analytical solution, a displacement discontinuity method to solve incremental mining problems in a viscoelastic material was also developed. When deriving the analytical and numerical techniques, a particular viscoelastic model consisting of a certain combination

of elastic and viscous elements had to be selected as one of the building blocks. The Burgers viscoelastic model proved to be successful as a good fit with experimental closure data was obtained. It was however found that there are subtle problems with the use of this theory in simulating the behaviour of tabular excavations. For the viscoelastic solution, the rate of steady-state closure increases with an increase in the distance to the face. This is opposite to what is measured underground in the Ventersdorp Contact Reef stopes. The problem arises due to the inability of viscoelasticity to simulate the formation of the fracture zone. This is not readily apparent when applying the theory to circular tunnels as calibration of the model can be successfully achieved. For the special geometry of tabular excavations, however, calibration at a particular distance from the face does not give the correct closure rates at other positions. In spite of these problems, the viscoelastic solution might still be useful to simulate the closure rate at a particular point to assist in the design of appropriate support.

To allow for direct simulation of the time-dependent fracture zone behaviour, a continuum viscoplastic model was developed by the author and implemented in the finite difference code FLAC using the built-in programming language FISH. The model is based on classical viscoplasticity, with a novel time-dependent cohesion weakening rule to simulate the time-dependent failure of the rock. A Mohr-Coulomb failure law and a non-associated flow-rule were assumed. For an excavation in this material, the failure zone soon after development covers those areas where the stress exceeded the failure strength of the rock. The time-dependent processes lead to a gradual transfer of stress to the unfailed rock. This also becomes fractured leading to a time-dependent growth of the fracture zone. The process continues until an equilibrium position is attained. This model has proved to be successful in simulating the time-dependent closure behaviour of tabular excavations giving both the instantaneous response at blasting time and the primary and steady-state closure phases. Unlike the viscoelastic approximation, the steady-state closure rate decreases with increasing distance from the face. This is similar to the behaviour observed for the Ventersdorp Contact Reef stopes confirming the hypothesis that the time-dependent stope closure is mainly controlled by the fracture zone behaviour. Back analysis of the behaviour of a service excavation at Hartebeestfontein Mine, however, showed that the continuum approach is not successful if the local time-dependent behaviour is governed by prominent discontinuities such as bedding planes.

As the shear creep of bedding planes or other large discontinuities may play a role in the observed time-dependent behaviour, a laboratory testing programme was initiated to investigate this phenomenon. As no suitable testing equipment was available, a creep shear box was developed where the displacement transducers could be mounted directly on the sides of the rock specimen. This prevented the data from being obscured by creep components of the equipment or resin castings used to mount the samples. From the preliminary tests, it became clear that discontinuity creep of hard rock can be divided into two groups namely creep of discontinuities with gouge infilling and creep of discontinuities with matching surfaces and no infilling. Mining induced extension fractures that have not been subjected to previous shear displacements (belonging to the second group) do not undergo appreciable shear creep. For those discontinuities with thick infilling, significant creep displacement was observed. If a shear load is applied to these discontinuities, typical primary and secondary behaviour is noted. The primary shear creep phase includes a prominent instantaneous response that is not recoverable and increases for larger shear stress/shear strength ratios. (The shear strength considered here is for the complete system of discontinuity plus gouge infilling.) The instantaneous component is the dominant behaviour of the creep response and can be as large as 0.6 mm if the shear stress/shear strength ratio is increased from 0.85 to 0.92 (for a gouge thickness of 2 mm and a normal stress of 1 MPa). The magnitude of the creep rate in the secondary phase also increases for higher shear stress/shear strength ratios. A stress power law is proposed to simulate this behaviour. A typical steady-state creep rate was 0.00025 mm/h for a gouge thickness of 2 mm with a normal stress of 1 MPa and a shear stress/shear strength ratio of 0.9. The creep rate is, however, not only a function of the shear stress/shear strength ratio but also of the absolute stress magnitudes. The shear creep rate also depends on the gouge thickness with a faster creep rate for a thicker gouge infilling.

As the continuum viscoplastic model is unable to simulate the time-dependent behaviour of individual discontinuities, a viscoplastic displacement discontinuity formulation was developed. The displacement discontinuity technique was preferred as it provides a natural framework for the solution of multiple interacting crack problems as compared to finite element or finite difference methods. Implementing a discontinuum viscoplastic formulation in a distinct element method is also feasible but was not investigated in this study. As explained above, the laboratory studies indicated that mining induced extension fractures with no infilling do not undergo significant shear creep if subjected to stresses below the failure strength of the discontinuity. The viscoplastic model developed for these

discontinuities therefore assumed that they are immobilised below the failure strength. If the discontinuity fails, the rate of shear displacement is proportional to excess shear stress above the yield surface. Stope simulations were undertaken by filling the region of interest with a random tessellation of potential fractures. The tabular excavation was incrementally mined to allow the time-dependent formation of the fracture zone. As an increment is mined, new fractures form while the existing fractures are subjected to a change in stress. The excess stress on these fractures is gradually transferred to the unfailed discontinuites causing additional failure. The model gives a response similar to that observed underground where the majority of fractures form soon after blasting, followed by a gradual reduction in the number of new fractures as time progresses. The total simulated fracture length mobilised as a function of time gives similar trends to the cumulative seismicity measured underground after blasting. The time-dependent closure profiles measured underground can also be replicated by the model. This discontinuum viscoplastic formulation shows much promise for investigating parameters such as the effect of rate of face advance on the level of seismicity. Finally, some preliminary work was done to implement a rheological model in the code to replicate the creep of discontinuities with gouge infilling. From the modelling, it appears that for large shear structures underground, the majority of creep movements occur at times of stress changes.

Arguably, the most important finding of this study is that the time-dependent closure data can possibly be used to deduce important information about the stress in the fracture zone ahead of the face. This information may be used to identify areas with a high risk of face bursting. It appears that the instantaneous closure response at blasting time gives an indication of the magnitude of stress in the face area. The larger the stress, the bigger the instantaneous closure response following the mining increment. This hypothesis was tested by simulating two stopes with different rock conditions using the continuum viscoplastic approach developed in this study. As mentioned above, this approach is successful in simulating both the primary closure (including the instantaneous response) after a mining increment and the steady-state closure phase. For the numerical stope where the rock readily failed and weakened in a time-dependent fashion, the vertical stress peak was located further from the face than for a stope with little time-dependent fracturing. Following a mining increment, a larger instantaneous closure response was observed for the stope with the stress peak located closer to the face. The steady-state closure rate was higher for the stope with the more significant time-dependent behaviour. It should be noted that large steady-state closure rates may be undesireable as they indicate greater mobility

of the fracture zone that can lead to a higher risk of falls of ground. Some confirmation of the possible use of time-dependent closure data to determine a face burst/fall of ground hazard was obtained from the underground data. The Ventersdorp Contact Reef stopes are prone to face bursting events, but are characterised by a relatively stable hangingwall. The closure behaviour of these excavations typically includes large instantaneous responses at blasting time followed by low steady-state closure rates. In comparison, in some areas of the Vaal Reef, the instantaneous closure response after blasting is small, followed by a large steady-state closure rate. In these areas, face bursting events are virtually absent, but with an increased risk of possible falls of ground.

8.2 Recommendations for further work

1) The important concept of using time-dependent closure data to deduce information about the stress in the fracture zone should be tested with further underground experiments. It may be possible to develop a transfer function linking the time-dependent closure profile between blasts with the time-dependent evolution of stress distribution ahead of the face over this period. This function could be useful to define different geotechnical areas, identify areas prone to face bursting or a fall of ground hazard and to help determine optimum rates of face advance. The feasibility of routine continuous closure monitoring (similar to the monitoring of seismicity) to detect changes in the face conditions should be investigated.

2) From this study, the usefulness of continuous closure measurements to improve the understanding of the rock mass behaviour is evident. The current study only investigated closure behaviour (movements normal to the plane of the excavation). It is known that the ride component (movements parallel to the plane of the excavation) can be significant in certain stopes. Little is known about the time-dependent behaviour of the ride component. To the author's knowledge, no continuous ride measurements (not to be confused with daily measurements) have been made. Studying this behaviour would involve the design of suitable equipment to do the measurements.

3) Although significant progress was made by the author in understanding the mechanisms of shear creep of discontinuities, further testing of natural specimens is required. These

include mining induced extensile fractures in quartzites and the different types of joint and bedding plane discontinuities.

4) The increased understanding of time-dependent behaviour and the numerical models developed, allow the effect of rate of face advance to be investigated. Although some preliminary studies can be found in Napier and Malan (1997), further work is required. As the optimum rate of advance will depend on the particular geotechnical area, it is important that the numerical models be calibrated for the different areas.

5) The time-dependent behaviour of deep excavations in hard rock is a result of the rheology of the fracture zone. Of particular interest is the rate of fracture zone extension after mining increments as this will impact on the maximum rate of face advance that can be safely sustained. As direct underground measurement of the time-dependent fracture growth is very difficult, physical experiments using stope models in the laboratory should be conducted. This may shed light on the rate of fracture zone extension for the different types of hard rock and why some types are prone to face bursting.

6) In conjunction with the physical experiments suggested above, experimental methods should be developed to monitor the extension of the fracture zone underground. As continuous monitoring (including the period immediately after blasting, when entering the stope is forbidden) is necessary, an automated technique is required. As fracture mapping in boreholes using petroscopes or borehole cameras is not feasible, indirect methods such as acoustic emissions or sensitive seismic systems might be used. Ground penetrating radar may also be useful in this regard.

7) From the shear creep experiments and preliminary modelling of creep deformation on large shear structures, it appears that most of the creep displacement occurs as an instantaneous response during times of stress change. In underground stopes this is typically at blasting time or after large seismic events. Continuous measurements of displacement on large shear structures are required to confirm this behaviour and also to establish the magnitude of the displacements.

8) Conditions under which service excavations in hard rock undergo squeezing behaviour should be investigated. This is important for the projected ultra-deep mining projects and the likely response of the access tunnels. Knowledge of squeezing behaviour will enable

better estimation of the viability of extracting ore reserves that are very deep or in areas of high stress. It is unclear if the competency factor used for prediction of squeezing in soft rock is applicable to hard rock and this should be investigated further.

List of References

ADAMS, G.R. and JAGER, A.J. (1980) Petroscopic observations of rock fracturing ahead of stope faces in deep-level gold mines. *J. S. Afr. Inst. Min. Metall.*, vol. 44, pp. 204-209.

ADAMS, G.R., JAGER, A.J. and ROERING, C. (1981) Investigations of rock fracture around deep level gold mine stopes. In: EINSTEIN, H.H. (ed.) *Proc. 22nd U.S. Symp. Rock Mech.*, pp. 213-218.

AKAGI, T., ICHIKAWA, Y., KURODA, H. and KAWAMOTO, T. (1984) A non-linear rheological analysis of deeply located tunnels. *Int. J. Num. Anal. Meth. Geomech.*, vol. 8, pp. 457-471.

AMADEI, B. (1979) Creep behaviour of rock joints. *M.Sc. Thesis*, University of Toronto, Toronto, Canada.

ATKINSON, B. K. (1987) *Fracture mechanics of rock.* Academic Press, London.

AYDAN, Ö., AKAGI, T. and KAWAMOTO, T. (1996) The squeezing potential of rock around tunnels: Theory and prediction with examples taken from Japan. *Rock Mech. Rock Engng.*, vol. 29, pp. 125-143.

BARLA, G. (1995) Squeezing rocks in tunnels. *ISRM News Journal*, vol. 2, no. 3 & 4, pp. 44-49.

BARTON, N. (1976) The shear strength of rock and rock joints. *Int. J. Rock Mech. Min. Sci. & Geomech. Abstr.*, vol. 13, pp. 255-279.

BARTON, N and CHOUBEY, V. (1977) The shear strength of rock joints in theory and practice. *Rock Mech.*, vol. 10, pp. 1-54.

BIENIAWSKI, Z.T. (1967) Mechanism of brittle fracture of rock - Part III - Fracture in tension and under long term loading. *Int. J. Rock Mech. Min. Sci.*, vol. 4, pp. 425-430.

BIENIAWSKI, Z.T. (1970) Time-dependent behaviour of fractured rock. *Rock Mech.*, vol. 2, pp. 123-137.

BLACIC, J.D. (1981) Importance of creep failure of hard rock in the near field of a nuclear waste repository. In: *Proc. of workshop on nearfield phenomenon in geologic repositories for radioactive waste*, Seattle, pp. 121-132.

BLÜMEL, M. (1996) Performance of grouted bolts in squeezing rock. In: BARLA, G. (ed.) *Eurock '96*, Balkema, Rotterdam, pp. 885-891.

BOWDEN, R.K. and CURRAN, J.H. (1984) Time-dependent behaviour of joints in shale. In: *Proc. 25th Symp. Rock Mech.*, pp. 320-327.

CARTER, N.L. and KIRBY, S.H. (1978) Transient creep and semibrittle behaviour of crystalline rocks. *Pageoph*, vol. 116, pp. 807-839.

CARTER, N.L., ANDERSON, D.A., HANSEN, F.D. and KRANZ, R.L. (1981) Creep and creep rupture of granitic rocks. *Geophy. Monogr. Am. Geophys. Union*, vol. 24, pp. 61-82.

CHIN, H. and ROGERS, J.D. (1987) Creep parameters of rock on an engineering scale. *Rock Mech. Rock Engng*, vol. 20, pp. 137-146.

COOK, N.G.W., HOEK, E., PRETORIUS, J.P.G., ORTLEPP, W.D. and SALAMON, M.D.G. (1966) Rock mechanics applied to the study of rockbursts. *J. S. Afr. Inst. Min. Metall.*, vol. 66, pp. 435-528.

CRAWFORD A.M. and CURRAN J.H. (1981) The influence of shear velocity on the frictional resistance of rock discontinuities. *Int. J. Rock Mech. Min. Sci.*, vol. 18, pp. 505-515.

CRAWFORD A.M. and CURRAN J.H. (1981) Rate-dependent behaviour of rock joints: Black quartz syenite. *Proc. Int. Symp. Weak Rock*, Balkema, Rotterdam, pp. 291-296.

CRAWFORD A.M. and CURRAN J.H. (1983) A displacement discontinuity approach to modelling the creep behaviour of rock and its discontinuities. *Int. J. Num. Anal. Meth. Geomech.*, vol. 7, pp. 245-268.

CROUCH, S.L. and STARFIELD, A.M. (1983) *Boundary element methods in solid mechanics*. London, George Allen & Unwin.

CSIR, Rock Mechanics Research Group, National Mechanical Engineering Institute. (1963) Report on the non-elastic properties of rock from borehole number 3034 from Hartebeestfontein gold mine. *CSIR Report*, MEG 563.

CURRAN J.H. and CRAWFORD A.M. (1980) Comparative study of creep in rock and its discontinuities. *Proc. 21st Symp Rock Mech.*, Rolla, pp. 596-603.

DAY, R. A. and POTTS, D. M. (1994) Zero thickness interface elements - numerical stability and application. *Int. J. Num. Anal. Meth. Geomech.*, vol. 18, pp. 689-708.

DEIRING, J.A.C. (1980) An improved method for the determination, by a MINSIM type of analysis, of stresses and displacements around tabular excavations. *J. S. Afr. Inst. Min. Metall.*, vol. 81, pp. 425-430.

DEIST, F.H., GEORGIADIS, E. and MORIS, J.P.E. (1972) Computer applications in rock mechanics. In: *Application of Computer Methods in the Mineral Industry, 10th Int. Symp.*, Johannesburg.

DENKHAUS, H.G., HILL, F.G. and ROUX, A.J.A. (1958) A review of recent research into rockbursts and strata movement in deep-level mining in South Africa. *Ass. Min. Mngrs. S. Afr.*, pp. 245-268.

DESAI, C.S. and ZHANG, D. (1987) Viscoplastic model for geologic materials with generalised flow rule. *Int. J. Num. Anal. Meth. Geomech.*, vol. 11, pp. 603-620.

DIERING, D.H. (1997) Ultra-deep level mining - future requirements, *J. S. Afr. Inst. Min. Metall.*, vol. 97, pp. 249-255.

DIETERICH, J.H. (1978) Time-dependent friction and the mechanics of stick slip. In: BYERLEE, J.D. and WYSS M. (eds), *Rock friction and earthquake prediction*, pp. 791-806.

DUSSEAULT, M.B. and FORDHAM, C.J. (1993) Time-dependent behavior of rocks. In: HUDSON, J.A. (ed.) *Comprehensive rock engineering*, vol. 3, Pergamon Press, pp. 119-149.

EUVERTE, C., ALLEMANDOU, X. and DUSSEAULT, M.B. (1994) Simulation of openings in visco-elastoplastic media using a discrete element method. In: SIRIWARDANE and ZAMAN (eds), *Computer Methods and Advances in Geomechanics*, Balkema, Rotterdam, pp. 809-814.

FAKHIMI, A.A. (1992) The influence of time-dependent deformation of rock on the stability of underground excavations. *PhD thesis*, University of Minnesota.

FAKHIMI, A.A. and FAIRHURST, C. (1994) A model for the time-dependent behavior of rock. *Int. J. Rock Mech. Min. Sci.*, vol. 31, pp. 117-126.

FLÜGGE, W. (1975) *Viscoelasticity*. 2nd edition, New York, Springer-Verlag,

GAY, N.C. and JAGER, A.J. (1980) The influence of geological features on rock mechanics problems in Witwatersrand gold mines. *Chamber of Mines of South Africa Unpublished Research Report.*

GIODA, G. (1982) On the non-linear 'squeezing" effects around circular tunnels. *Int. J. Num. Anal. Meth. Geomech.*, vol. 6, pp. 21-46.

GIODA, G. and CIVIDINI, A. (1996) Numerical methods for the analysis of tunnel performance in squeezing rocks. *Rock Mech. Rock Engng.*, vol. 29, pp. 171-193.

GNIRK, P.F. and JOHNSON, R.E. (1964) The deformational behavior of a circular mine shaft situated in a viscoelastic medium under hydrostatic stress. In: SPOKES, E.M. and CHRISTIANSEN, C.R.(eds) *Proc .6th Symp. Rock Mech.*, University of Missouri, Rolla, pp. 231-259.

GRIGGS, D. (1939) Creep of rocks. *J. Geol.* vol. 47, pp. 225-251.

GÜLER, G. (1997) Analysis of the rock mass behaviour as associated with Ventersdorp Contact Reef stopes, South Africa. *M.Sc dissertation*, University of the Witwatersrand, Johannesburg.

GÜRTUNCA R.G. (1989) Results of a classified tailings monitoring programme at Vaal Reefs. *COMRO (now CSIR Miningtek) Internal Report*, no. 614.

GÜRTUNCA R.G., JAGER A.J., ADAMS D.J. and GONLAG M. (1989) The in situ behaviour of backfill materials and the surrounding rockmass in South African gold mines. In: HASSANI, F. (ed.) *Proc. 4th Int. Symp. of Mining with Backfill.*, Balkema, Rotterdam, pp. 187-197.

HANDLEY, M.F. (1996) Personal communication.

HODGSON, K. (1967) The behaviour of the failed zone ahead of a face, as indicated by continuous seismic and convergence measurements, *Chamber of Mines Research Report 31/61*, Transvaal and Orange Free State Chamber of Mines Research Organisation.

IDA, Y. (1974) Slow moving deformation pulses along tectonic faults. *Phys. Earth Planet. Inter.*, vol. 9, pp. 328-337.

ITASCA. (1993) FLAC - Fast Lagrangian Analysis of Continua: User's Manual.

JAEGER, J.C. and COOK, N.G.W. (1979) *Fundamentals of Rock Mechanics*. 3rd edition, London, Chapman and Hall, p. 320.

JANTZON, F.G.H. (1965) Discussion of paper: WIGGILL (1965) In: *Symposium on Rock Mechanics and Strata Control in Mines, J. S. Afr. Inst. Min. Metall.*, pp. 52-55.

JOHNSON, R.A. and SCHWEITZER, J.K. (1996) Mining at ultra-depth: Evaluation of alternatives. In: AUBERTIN, M. HASSANI, F. and MITRI, H. (eds) *Proc.2nd North Am. Rock Mech. Symp*: NARMS '96, Montreal, pp. 359-366.

JOUGHIN, N.C. and JAGER, A.J. (1983) Fracture of rock at stope faces in South African gold mines. In: *Rockbursts: Prediction and Control*, Inst. Min. Metall., London, pp. 53-66.

KING, R.G., JAGER, A.J., ROBERTS, M.K.C. and TURNER, P.A. (1989) Rock mechanics aspects of stoping without back-area support. *COMRO (Now CSIR Miningtek) Research Report*, no. 17/89.

KIRSTEN, H.A.D. and BARTLETT, P.J. (1992) Rigorously determined support characteristics and support design method for tunnels subject to squeezing conditions. *J. S. Afr. Inst. Min. Metall.*, vol. 92, pp. 195-214.

KERSTEN, R.W.O. (1995) Personal communication.

KOCH, P.S., CHRISTIE, J.M., ORD, A. and GEORGE, R. P. (1989) Effect of water on the rheology of experimentally deformed quartzite. *J. Geophys. Res.*, vol. 94, pp. 13975-13996.

KOVÁCS, I.K.A. (1971) An investigation of the time-dependent behaviour of solid rock in uniaxial compression. *CSIR Report*, MEG 1032.

KRANZ, R.L. (1979) Crack growth and development during creep of barre granite. *Int. J. Rock Mech. Min. Sci.*, vol. 16, pp. 23-35.

KRANZ, R.L. and ESTEY, L.H. (1996) Listening to a mine relax for over a year at 10 to 1000 meter scale. In: AUBERTIN, M. HASSANI, F. and MITRI, H. (eds) *Proc. 2nd North Am. Rock Mech. Symp*: NARMS '96, Montreal, pp. 491-498.

KRANZ, R.L. and SCHOLTZ, C. (1977) Critical dilatant volume of rocks at the onset of tertiary creep. *J. Geophys. Res.*, vol. 82, pp. 4893-4898.

KRANZ, R.L., HARRIS, W.J. and CARTER, N.L. (1982) Static fatigue of granite at 200° C. *Geophys. Res. Lett.*, vol. 9, pp. 1-4.

KULLMANN, D.H., STEWART, R.D. and GRODNER, M. (1996) A pillar preconditioning experiment on a deep-level South African gold mine, In: M. Aubertin, F. Hassani and H. Mitri (eds) *Proc. 2nd North Am. Rock Mech. Symp*: NARMS '96, Montreal, pp. 375-380.

LAMA, R.D. and VUTUKURI, V.S. (1978) *Handbook on mechanical properties of rocks - Testing techniques and results - Volume III.* Trans Tech Publications, Germany, pp. 209-320.

LEE, C., LEE, Y. and CHO, T. (1995) Numerical simulation for the underground excavation-support sequence in the visco-plastic jointed rock mass. In: FUJII, T. (ed.) *Proc. 8th Int. Cong. Rock Mech.*, ISRM, Balkema, Rotterdam, pp. 619-621.

LEEMAN, E.R. (1958) Some measurements of closure and ride in a stope of the East Rand Proprietary Mines. *Pap. Ass. Min. Mngrs. S.Afr.*, vol. 1958-1959, pp. 385-404.

LEGGE, N.B. (1984) Rock deformation in the vicinity of deep gold mine longwall stopes and its relation to fracture. *Ph.D Thesis*, University College, Cardiff.

LEGGE, N.B. and SPOTTISWOODE, S.M. (1987) Fracturing and microseismicity ahead of a deep gold mine stope in the pre-remnant and remnant stages of mining. In: *ISRM 6th Int.Congr.Rock Mech.*, Montreal, pp. 1071-1077.

LINKOV, A.M. (1995) Keynote lecture: Equilibrium and stability of rock masses. In: T. FUJII, T. (ed.) *Proc. 8th Int. Congress on Rock Mechanics*, ISRM, Japan, Balkema.

LINKOV, A.M. (1996) Rockbursts and the instability of rock masses - Schlumberger Award Lecture. *Int. J. Rock Mech. Min. Sci & Geomech Abstr.*, vol. 33, pp. 727-732.

LINKOV, A.M. (1997) Keynote lecture: New geomechanical approaches to develop quantitative seismicity. In: GIBOWICZ, S.J. and LASOCKI, S. (eds) *Proc. 4th Int. Symp. Rockbursts and Seismicity in Mines*, Balkema, Rotterdam, pp. 151-166.

LURIE, J. (1977) *South African geology for mining, metallurgical, hydrological and civil engineering*. McGraw-Hill, Johannesburg, pp. 72-78.

MALAN, D.F. (1995) A viscoelastic approach to the modelling of transient closure behaviour of tabular excavations after blasting. *J. S. Afr. Inst. Min. Metall.*, vol. 95, pp. 211-220.

MALAN, D.F. and BOSMAN, J.D. (1997) A viscoplastic approach to the modelling of time-dependent rock behaviour at Hartebeestfontein gold mine. In: GÜRTUNCA R.G. and HAGAN, T.O. (eds) *SARES97*, Johannesburg, pp. 117-130.

MALAN, D.F. and SPOTTISWOODE, S.M. (1997) Time-dependent fracture zone behaviour and seismicity surrounding deep level stoping operations. In: GIBOWICZ, S.J. and LASOCKI, S. (eds) *Proc. 4th Int. Symp. Rockburst and Seismicity in Mines*, Balkema, Rotterdam, pp. 173-177.

MATSUSHITA, Y., MIZOGUCHI, K., OHIRA, T., DOI, N. and OHTSUKA, M. (1995) The geological characteristics and the construction methods of heavy squeezing mudrock at the Nabetachiyama tunnel. In: FUJII, T. (ed.) *Proc. 8th Int. Cong. Rock Mechanics*, ISRM, Balkema, Rotterdam, pp. 491-495.

MCGARR, A. (1971) Stable deformation near deep-level tabular excavations. *J. Geophys. Res.*, vol. 76, no. 29, pp. 7088-7106.

MCGARR, A. (1976) Dependence of magnitude statistics on strain rate. *Bull. Seism. Soc. Am.*, vol. 66, no. 1, pp. 33-44.

MENDECKI, A.J. (1997) Keynote lecture: Principles of monitoring seismic rockmass response to mining. In: GIBOWICZ, S.J. and LASOCKI, S. (eds) *Proc. 4th Int. Symp. Rockbursts and Seismicity in Mines*, Balkema, Rotterdam, pp. 69-80.

MUIRWOOD, A.M. (1972) Tunnels for roads and motorways. *Quarterly J. Eng. Geol.*, vol. 5, pp. 119-120.

NAKANO, R. (1979) Geotechnical properties of mudstone and neogene tertiary in Japan. In: *Proc. Int. Symp. Soil Mechanics*, Oaxaca, pp. 75-92.

NAPIER, J.A.L. (1990) Modelling of fracturing near deep level mine excavations using a displacement discontinuity approach. In: ROSSMANITH, H.P. (ed.) *Mechanics of jointed and faulted rock*, Balkema, Rotterdam, pp. 709-715.

NAPIER, J.A.L. and MALAN, D.F. (1997) A viscoplastic discontinuum model of time-dependent fracture and seismicity effects in brittle rock. *Int. J. Rock Mech. Min. Sci. & Geomech. Abstr.*, vol. 34, pp. 1075-1089.

NAPIER, J.A.L. and PEIRCE, A. P. (1995) Simulation of extensive fracture formation and interaction in brittle materials. In: ROSSMANITH, H.P. (ed.) *Mechanics of Jointed and Faulted Rock* : MJFR2, Balkema, Rotterdam, pp. 63-74.

NAPIER, J.A.L. and STEPHANSON, S.J. (1987) Analysis of deep-level mine design problems using the MINSIM-D boundary element program. In: APCOM87, *Proc. 20th Int. Symp. on the Application of computers and mathematics in the mineral industries*, vol. 1, SAIMM, pp. 3-19.

NAWROCKI, P.A. (1995) One-dimensional semi-analytical solution for time-dependent behaviour of a seam. *Int. J. Num. Anal. Meth. Geomech.*, vol. 19, pp. 59-74.

PAN, Y.W. and DONG, J.J. (1991a) Time-dependent tunnel convergence - I. Formulation of the model. *Int. J. Rock Mech. Min. Sci.*, vol. 28, pp. 469-475.

PAN, Y.W. and DONG, J.J. (1991b) Time-dependent tunnel convergence - II. Advance rate and tunnel-support interaction. *Int. J. Rock Mech. Min. Sci.*, vol. 28, pp. 477-488.

PANET, M. (1996) Two case histories of tunnels through squeezing rocks. *Rock Mech. Rock Engng.*, vol. 29, pp. 155-164.

PATERSON, M.S. and LUAN, F.C. (1990) Quartzite rheology under geological conditions. In: KNIPE, R.J. and RUTTER, E.H. (eds), *Deformation mechanisms, rheology and tectonics, Geol. Soc. Spec. Publ.*, no. 54, pp. 299-307.

PERZYNA, P. (1966) Fundamental problems in viscoplasticity. *Adv. Appl. Mech.*, vol. 9, pp. 243-377.

PIPER, P.S. and WAGNER, H. (1982) A brief evaluation of the longterm stability of the refrigiration complex on 71 level no. 6 shaft Hartebeestfontein mine. *Unpublished Chamber of Mines report.*

PLEWMAN, R.P., DEIST, F.H. and ORTLEPP, W.D. (1969) The development and application of a digital computer method for the solution of strata control problems. *J. S. Afr. Inst. Min. Metall.*, vol. 70, pp. 33-44.

POMEROY, C.D. (1956) Creep in coal at room temperature. *Nature*, vol. 178, pp. 279-280.

POST, A.D., TULLIS, J. and YUND, R.A. (1996) Effects of chemical environment on dislocation creep of quartzite. *J. Geophys. Res.*, vol. 101, pp. 22143-22155.

POTTS, E.L.J. and HEDLY, D.G.F. (1964) The influence of time-dependent effects on the design of mine pillars. *Int. Bureau of Rock Mech. Proc. 6th Int. Conf.*, Leipzig.

PUSCH, R. (1993) Mechanisms and consequences of creep in crystalline rock. In: HUDSON, J.A. (ed.) *Comprehensive rock engineering*, vol. 1, Pergamon Press, pp. 227-241.

ROBERTS, M.K.C and JAGER, A.J. (1988) Hartebeestfontein refrigeration chamber: A summary of closure and extensometer results. *Unpublished Chamber of Mines report.*

ROBERTSON, E.C., (1964) Viscoelasticity of Rocks. In: JUDD, W.R. (ed.) *State of stress in the earth's crust. Proc. Int. Conf.*, Santa Monica, California, pp.181-233.

ROBERTS, W.J. and EINSTEIN, H.A. (1978) Comprehensive model of rock discontinuities. *Jl. A.S.C.E.*, vol. 104, pp. 553-569.

ROUX, A.J.A. and DENKHAUS, H.G. (1954) An investigation into the problem of rock bursts - An operational research project. *J. Chem. Metall. Min. Soc. S. Afr.*, vol. 55, pp. 103-124.

RYDER, J.A. (1991) Optimal iteration schemes suitable for general non-linear boundary element modelling applications. In: BEER, BOOKER and CARTER (eds), *Computer Methods and Advances in Geomechanics*, pp. 1079-1084.

RYDER, J.A. and NAPIER, J.A.L. (1985) Error analysis and design of a large-scale tabular mining stress analyser. In: *Proc. 5th. Int. Conf. Num. Meth. Geomech.*, pp. 1549-1555.

RYDER, J.A. and OFFICER, N.C. (1964) An elastic analysis of strata movement observed in the vicinity of inclined excavations. *J. S. Afr. Inst. Min. Metall.*, vol. 64, p. 219.

SAGAWA, Y., YAMATOMI, J. and MOGI, G. (1995) A rheology model for non-linear and time-dependent behaviour of rocks. In: FUJII, T. (ed.) *Proc. 8th Int. Cong. Rock Mech. ISRM*, Balkema, Rotterdam, pp. 311-314.

SALAMON, M.D.G. (1968) Two-dimensional treatment of problems arising from mining tabular deposits in isotropic or transversely isotropic ground. *Int. J. Rock Mech. Min. Sci.*, vol. 5, pp. 159-185.

SALAMON, M.D.G. (1974) Rock mechanics of underground excavations. In: *Proceedings 3rd Congress of the International Society for Rock Mechanics*, pp. 951-1099.

SALAMON, M.D.G., RYDER, J.A. and ORTLEPP, W.D. (1964) An analogue solution for determining the elastic response of strata surrounding tabular mining excavations. *J. S. Afr. Inst. Mining Metall.*, vol. 64, pp. 115-137.

SAMTANI, N.C., DESAI, C. S. and VULLIET, L. (1996) An interface model to describe viscoplastic behaviour. Int. *J. Num. Anal. Meth. Geomech.*, vol. 20, pp. 231-252.

SCHWARTZ, C.W. and KOLLURU, S. (1984) The influence of stress level on the creep of unfilled rock joints. In: *Proc. 25th Symp. Rock Mech.*, pp. 333-340.

SCHWEITZER, J.K. and JOHNSON, R.A. (1997) Geotechnical classification of deep and ultra-deep Witwatersrand mining areas, South Africa. *Mineralium Deposita*, vol. 32, pp. 335-348.

SCHUBERT, W. (1996) Dealing with squeezing conditions in Alpine tunnels. *Rock Mech. Rock Engng.*, vol. 29, pp. 145-153.

SEPEHR, K. and STIMPSON, B. (1988) Potash mining and seismicity: A time-dependent finite element model. *Int. J. Rock Mech. Min. Sci & Geomech. Abstr.*, vol. 25, pp. 383-392.

SOLBERG, P.H., LOCKNER, D.A., SUMMERS, R.S., WEEKS, J.D. and BYERLEE, J.D. (1978) Experimental fault creep under constant differential stress and high confining pressure. In: KIM, Y.S. (ed.) *19th US Symp. Rock Mech.*, Stateline, Nevada, pp. 118-121.

SONG, D. (1993) Non-linear viscoplastic creep of rock surrounding an underground excavation. *Int. J. Rock Mech. Min. Sci. & Geomech. Abstr.*, vol. 30, pp. 653-658.

STEINER, W. (1996) Tunneling in squeezing rocks: case histories. *Rock Mech. Rock Engng.*, vol. 29, pp. 211-246.

STEWART, R.D. and SPOTTISWOODE, S.M. (1993) A technique for determining the seismic risk in deep-level mining. In: YOUNG, R.P. (ed.) *Rockbursts and Seismicity in Mines*, pp. 123-128.

SWOBODA, G., MERTZ, W. and BEER, G. (1987) Rheological analysis of tunnel excavations by means of coupled finite element (FEM)-boundary element (BEM) analysis. *Int. J. Num. Anal. Methods. Geomech.*, vol. 11, pp. 115-129.

TAN, T. (1993) The importance of creep and time-dependent dilatancy, as revealed from case records in China. In: HUDSON, J.A. (ed.) *Comprehensive Rock Engineering*, vol. 3, Rock Testing and site characterisation, pp. 709-744.

TAN, T. and KANG, W. (1980) Locked in stresses, creep and dilatancy of rocks, and constitutive equations. *Rock Mech.*, vol. 13, pp. 5-22.

TAN, T. K. and WU, H.Q. (1989) Creep and time dependent dilatancy of rocks at large depths. In: MAURY, V. and FOURMAINTRAUX, D. (eds) *Rock at great depth. Proc. ISRM-SPE*, Elf Aquitaine, Pau, Balkema, Rotterdam, pp. 67-76.

TOPER, Z. (1997) Personal communication.

TURNER, P.A. (1984) Report on an investigation of several hard patches in the mechanical mining site at Doornfontein between January and June 1984. *COMRO (Now CSIR Miningtek) Internal report.*

VERMEER, P.A. and DE BORST, R. (1984) Non-associated plasticity for soils, concrete and rock. *Heron,* vol. 29, pp. 5-62.

VOGLER, U.W. (1990) Creep tests on argillaceous footwall quartzite. *CSIR Report,* EMA-C 9052.

VOGLER, U.W. and DRESCHER, K. (1997) Creep tests on Ventersdorp Lava. *CSIR Internal Report.*

VOGLER, U.W., MALAN, D.F. and DRESCHER, K. (1998) Development of shear testing equipment to investigate the creep behaviour of discontinuities in hard rock. Accepted for publication in: ROSSMANITH, H.P. (ed.) *Proc. Mechanics of Jointed and Faulted Rock, MJFR-3*, Balkema, Rotterdam.

WALSCH, J.B., LEYDE, E.E., WHITE, A.J.A. and CARRAGHER, B.L. (1977) Stope closure studies at West Driefontein gold mine. *Int. J. Rock Mech. Min. Sci & Geomech. Abstr.*, vol. 14, pp. 277-281.

WAWERSIK, W.R. (1974) Time-dependent behaviour of rock in compression. In: Advances in Rock Mechanics. *Proc. 3rd Congr. Int. Soc. Rock Mech.*, Denver, Colorado, pp. 357-363.

WESSON, R.L. (1988) Dynamics of fault creep. *J. Geophys. Res.*, vol. 93, pp. 8929-8951.

WIID, B.L. (1966) The time-dependent behaviour of rock: Considerations with regard to a research programme. *CSIR Report,* MEG 514.

WIGGILL, R.B. (1965) The effects of different support methods on strata behaviour around stoping excavations. *Symposium on Rock Mechanics and Strata Control in Mines: J. S. Afr. Inst. Min. Metall.*, pp. 1-35.

Appendix A

A1: Calculating the time-dependent strain of a cylindrical specimen of Burgers material under uniaxial compression

Lama and Vutukuri (1978) derived the time-dependent strain of a tensile rod composed of a Burgers material subjected to a constant normal tensile stress. Unfortunately this calculation was made for a Poisson's ratio $\nu = 0.5$. As this value is in general not applicable to rocks, this equation is also derived in this appendix, but for a generalised value ν.

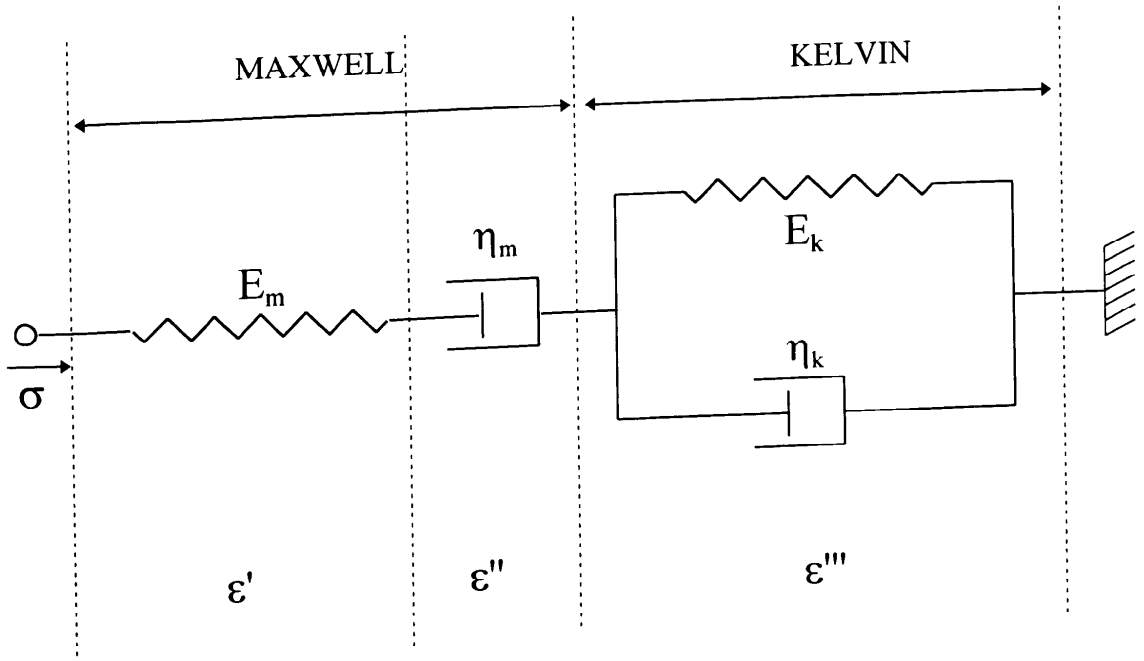

Figure A1. Burgers model.

If a cylindrical specimen of rock (assumed to behave as a Burgers material) is suddenly loaded at time $t = 0$ under uniaxial conditions, the following time-dependent strain function can be derived. The total time-dependent strain ε_t in the axial direction is given as

$$\varepsilon_t = \varepsilon' + \varepsilon'' + \varepsilon''' \qquad [A1]$$

The elastic components behave instantaneously and therefore

$$\varepsilon' = \frac{\sigma}{E_m} \qquad [A2]$$

where σ is the applied stress and E_m is the Young's modulus of the Maxwell component. A perfectly viscous material develops shear stresses proportional to the rate of change of shear strain

$$\tau = \eta\dot{\gamma} \qquad [A3]$$

where τ is the shear stress, $\dot{\gamma}$ is the rate of shear strain and η is the viscosity coefficient. For the uniaxial loading of the rock sample, the maximum shear stress can be given by

$$\tau = \frac{\sigma}{2} \qquad [A4]$$

The lateral strains $\varepsilon_{\ell 1}$, $\varepsilon_{\ell 2}$ are related to the axial strain ε

$$-\varepsilon_{\ell 1} = -\varepsilon_{\ell 2} = \nu\varepsilon \qquad [A5]$$

The maximum shear strain

$$\gamma = \varepsilon - \varepsilon_{\ell 1} = \varepsilon(1+\nu) \qquad [A6]$$

From equations [A3], [A4] and [A6] the normal stress is related to the normal strain by

$$\sigma = 2\eta\dot{\varepsilon}(1+\nu) \qquad [A7]$$

For the Maxwell dashpot therefore

$$\dot{\varepsilon}'' = \frac{\sigma}{2\eta_m(1+\nu)} \qquad [A8]$$

When integrating equation [A8] with respect to time and noting that at $t = 0$, $\varepsilon'' = 0$

$$\varepsilon'' = \frac{\sigma t}{2\eta_m(1+\nu)} \qquad [A9]$$

For the Kelvin component the total stress will be the sum of the stress in the two elements

$$\sigma = \sigma_{elas} + \sigma_{vis} \qquad [A10]$$

From equations [A2] and [A7]

$$\sigma = \varepsilon'''E_k + 2\eta_k\dot{\varepsilon}'''(1+\nu) \qquad [A11]$$

When solving equation [A11] by separation of variables

$$-\frac{1}{E_k}\ln\left[\sigma - \varepsilon'''E_k\right] = \frac{t}{2\eta_k(1+\nu)} + C \qquad [A12]$$

At $t = 0$, $\varepsilon''' = 0$ and therefore

$$C = \frac{-\ln\sigma}{E_k} \qquad [A13]$$

and from equation [A12]

$$\varepsilon''' = \frac{\sigma}{E_k}\left(1 - e^{\frac{-E_k t}{2\eta_k(1+\nu)}}\right) \qquad [A14]$$

Inserting equations [A2], [A9] and [A14] in equation [A1] gives

$$\varepsilon_t = \frac{\sigma}{E_m} + \frac{\sigma t}{2\eta_m(1+\nu)} + \frac{\sigma}{E_k}\left(1 - e^{\frac{-E_k t}{2\eta_k(1+\nu)}}\right) \qquad [A15]$$

Appendix B

B1: Viscoelastic convergence solution for a parallel-sided tabular excavation in a Kelvin material

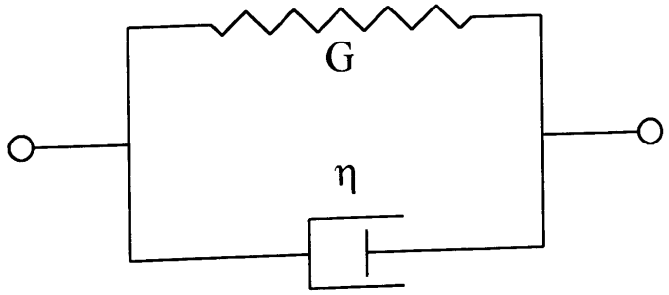

Figure B1. The Kelvin model representing the rock behaviour in distortion.

If it is assumed that the rock behaves like an elastic solid in dilatation and as a two-element Kelvin model in distortion, the following convergence model can be derived (Malan, 1995). For the Kelvin distortional component, equation [3.4] can be written as

$$\sigma_d = q_0\varepsilon_d + q_1\dot{\varepsilon}_d \qquad [B1]$$

where q_1 is the viscosity coefficient η. If the viscosity coefficient is reduced to zero, the behaviour of the model will be purely elastic and therefore from equation [3.12] it follows that $q_0 = 2G$. Subjecting equation [B1] to the Laplace transformation gives

$$\tilde{\sigma}_d = (q_0 + q_1 s)\tilde{\varepsilon}_d \qquad [B2]$$

It therefore follows from equations [3.14] and [3.17] that

$$\tilde{P}' = 1 \qquad \tilde{P}'' = 1 \qquad \tilde{Q}' = 3K \qquad \tilde{Q}'' = q_0 + sq_1 \qquad [B3]$$

When inserting this in equation [3.25]

$$F(t) = L^{-1}\left[\frac{3K + 2q_0 + 2q_1 s}{s(q_0 + sq_1)(6K + q_0 + sq_1)}\right] \qquad [B4]$$

$$= \frac{2}{q_1} L^{-1}\left[\frac{\frac{3K + 2q_0}{2q_1} + s}{s\left(\frac{q_0}{q_1} + s\right)\left(\frac{6K + q_0}{q_1} + s\right)}\right]$$

Finding the inverse Laplace transformation by partial fraction expansion gives

$$F(t) = \frac{3K + 2q_0}{q_0(6K + q_0)} - \frac{1}{2q_0} e^{-\frac{q_0}{q_1}t} - \frac{3}{12K + 2q_0} e^{-\frac{6K+q_0}{q_1}t} \qquad [B5]$$

Substituting equation [B5] into equation [3.24] gives

$$S_z(x,t) = -4W_z\sqrt{\ell^2 - x^2}\ (1 + \frac{dx}{2})g_2\left[1 + c_1 e^{-\alpha_1 t} + c_2 e^{-\alpha_2 t}\right] \qquad [B6]$$

where

$$g_2 = \frac{3K + 2q_0}{q_0(6K + q_0)} \qquad [B7]$$

$$\alpha_1 = \frac{q_0}{q_1} \qquad [B8]$$

$$\alpha_2 = \frac{6K + q_0}{q_1} \qquad [B9]$$

$$c_1 = -\frac{6K + q_0}{6K + 4q_0} \qquad [B10]$$

$$c_2 = -\frac{3q_0}{6K + 4q_0} \qquad [B11]$$

At time t = 0, F(t) reduces to $g_2\left[1+c_1+c_2\right]$. This shows correctly that for the Kelvin stope convergence model at t = 0, $S_Z(x,t) = 0$ because $\left[1+c_1+c_2\right]=0$ from equations [B10] and [B11]. As $c_2 = -\left[c_1+1\right]$, equation [B6] can be written as:

$$S_z(x,t) = -4W_z\sqrt{\ell^2 - x^2}\,(1+\frac{dx}{2})g_2\left[1+c_1e^{-\alpha_1 t}-(c_1+1)e^{-\alpha_2 t}\right] \qquad [B12]$$

When $t \rightarrow \infty$, the viscoelastic convergence approaches an asymptotic value given by

$$S_z(x) = -4W_z g_2\sqrt{\ell^2 - x^2}\left(1+\frac{dx}{2}\right) \qquad [B13]$$

The only viscoelastic parameter present in equation [B13] is g_2. It follows from the definition of g in equation [B7] that it is only a function of the bulk and shear modulus. The magnitude of the viscoelastic convergence at $t \rightarrow \infty$ is therefore not dependent on the viscosity coefficient. It can easily be shown that at $t \rightarrow \infty$, the viscoelastic solution is identical to the elastic solution by substituting equation [B7] in equation [B13] and rewriting the bulk and shear modulus in terms of Young's modulus and Poisson's ratio. (The elastic solution is given in equation [3.1].)

The length of span L_c at which there is contact between the hangingwall and footwall at the centre of the stope (x = 0) at time $t \rightarrow \infty$ is

$$L_c = 2\ell = \frac{S_z}{-2W_z g_2\left(1+\frac{dx}{2}\right)} \qquad [B14]$$

with S_z set equal to the stoping width.

To examine the behaviour of the model, a horizontal stope of span 100 m was simulated at a depth of 2000 m. Figure B2 illustrates the effect of the viscosity parameter η. The convergence approaches an asymptotic value given by equation [B13]. The viscosity parameter controls the rate at which this asymptotic value is approached. As expected at time t = 0, the convergence is 0. The elastic parameter controls the magnitude of the asymptotic convergence value as illustrated in Figure B3.

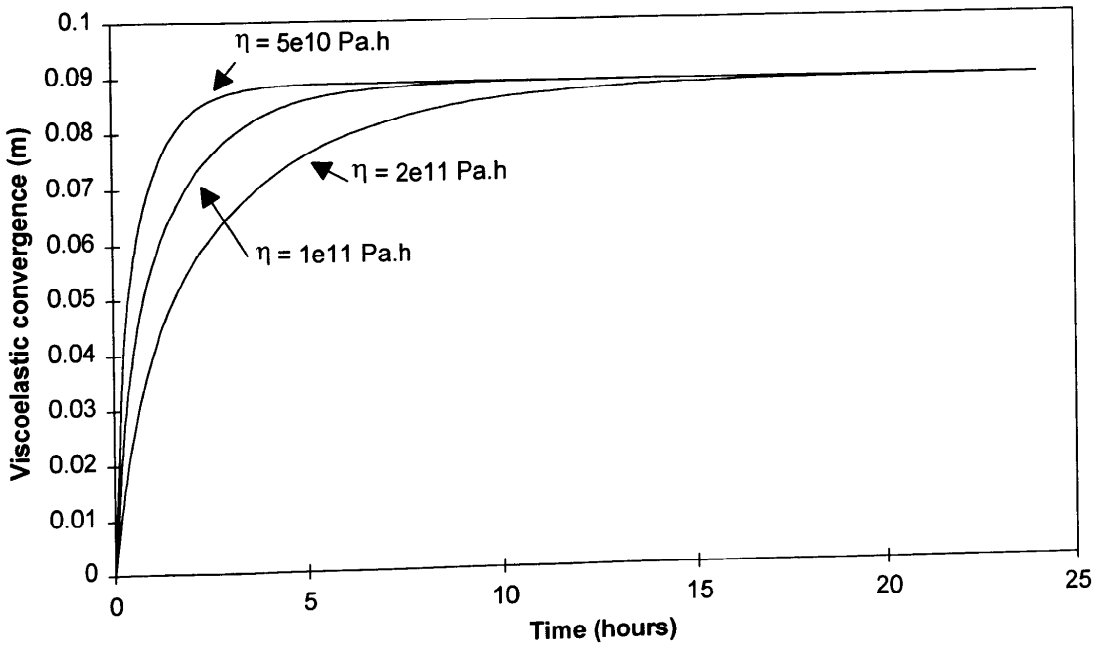

Figure B2. The effect of the viscosity parameter (η) on the behaviour of the Kelvin convergence model. Other values used in this simulation are E = 70×10^9 Pa, ν = 0.2, L = 50 m, x = 40 m, H = 2000 m, $\alpha = 0°$, k = 0.5, g = 9.81 m/s^2 and ρ = 2700 kg/m^3.

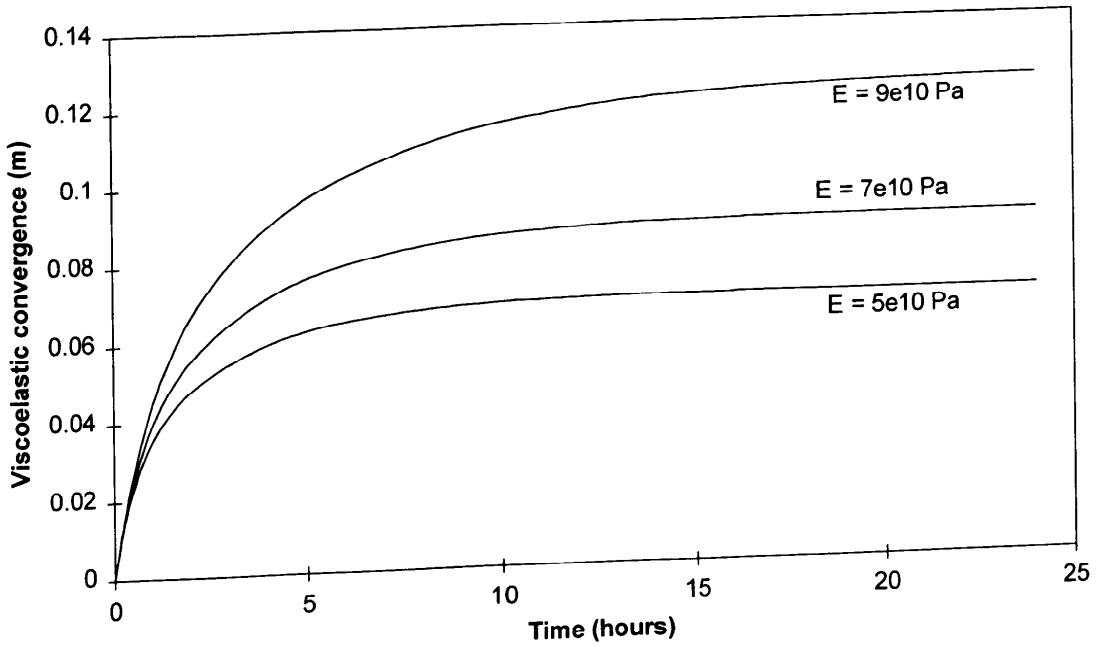

Figure B3. The effect of Young's modulus (E) on the behaviour of the Kelvin convergence model. Other values used in this simulation are $\eta = 2\times10^{11}$ Pa.h, ν = 0.2, L = 50 m, x = 40 m, H = 2000 m, $\alpha = 0°$, k = 0.5, g = 9.81 m/s^2 and ρ = 2700 kg/m^3.

B2: Viscoelastic convergence solution for a parallel-sided tabular excavation in a 3-parameter solid material

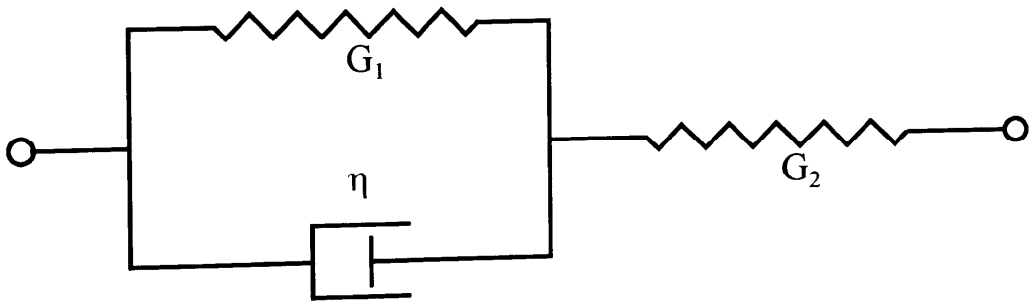

Figure B4. The 3-parameter solid representing the rock behaviour in distortion.

If it is assumed that the rock behaves like an elastic solid in dilatation and as a 3-parameter solid in distortion, the following convergence model can be derived. For the distortional component, equation [3.4] can be written as

$$\sigma_d + p_1\dot{\sigma}_d = q_0\varepsilon_d + q_1\dot{\varepsilon}_d \qquad [B15]$$

where

$$p_1 = \frac{\eta}{2(G_1+G_2)} \qquad q_0 = \frac{2G_1G_2}{G_1+G_2} \qquad q_1 = \frac{G_2\eta}{G_1+G_2} \qquad [B16]$$

G_1 is the shear modulus of the elastic element in parallel to the dashpot with viscosity coefficient η. The third elastic element (in series with the other components) has a shear modulus of G_2. Subjecting equation [B15] to the Laplace transformation gives

$$(1+p_1s)\tilde{\sigma}_d = (q_0+q_1s)\tilde{\varepsilon}_d \qquad [B17]$$

It therefore follows from equations [3.14] and [3.17] that

$$\tilde{P}' = 1 \qquad \tilde{P}'' = 1+p_1s \qquad \tilde{Q}' = 3K \qquad \tilde{Q}'' = q_0+sq_1 \qquad [B18]$$

Substituting this into equation [3.25] gives

$$F(t) = L^{-1}\left[\frac{3K(1+p_1s)^2 + 2(1+p_1s)(q_0+q_1s)}{s(q_0+sq_1)\{6K(1+p_1s)+(q_0+q_1s)\}}\right] \qquad [B19]$$

$$= \frac{p_1(3Kp_1+2q_1)}{q_1(6Kp_1+q_1)} L^{-1}\left[\frac{\left(\frac{1}{p_1}+s\right)\left(\frac{3K+2q_0}{3Kp_1+2q_1}+s\right)}{s\left(\frac{q_0}{q_1}+s\right)\left(\frac{6K+q_0}{6Kp_1+q_1}+s\right)}\right]$$

Finding the inverse Laplace transformation by partial fraction expansion gives

$$F(t) = \frac{3K+2q_0}{q_0(6K+q_0)} + \frac{p_1q_0-q_1}{2q_0q_1} e^{-\frac{q_0}{q_1}t} + \frac{3(p_1q_0-q_1)}{2(6Kp_1+q_1)(6K+q_0)} e^{-\frac{6K+q_0}{6Kp_1+q_1}t} \qquad [B20]$$

Substituting equation [B20] into equation [3.24] gives

$$S_z(x,t) = -4W_z\sqrt{\ell^2-x^2}\ (1+\frac{dx}{2})g_2\left[1+c_3e^{-\alpha_1 t}+c_4e^{-\alpha_3 t}\right] \qquad [B21]$$

where

$$\alpha_3 = \frac{6K+q_0}{6Kp_1+q_1} \qquad [B22]$$

$$c_3 = \frac{q_0(p_1q_0-q_1)(6K+q_0)}{2q_0q_1(3K+2q_0)} \qquad [B23]$$

$$c_4 = \frac{3q_0(p_1q_0-q_1)}{2(6Kp_1+q_1)(3K+2q_0)} \qquad [B24]$$

Parameters g_2 and α_1 are already defined in equations [B7] and [B8]. The format of equation [B21] is therefore similar to equation [B6] with parameters α_2, c_1 and c_2 replaced by α_3, c_3 and c_4. At time t = 0 equation [B21] becomes

$$S_z(x,t=0) = -4W_z\sqrt{\ell^2-x^2}\ (1+\frac{dx}{2})g\left[1+c_3+c_4\right] \qquad [B25]$$

As $\left[1+c_3+c_4\right] \neq 0$, $S_z(x,t=0) \neq 0$ and the 3-parameter stope convergence model gives an instantaneous deformation at time t = 0. The magnitude of this instantaneous deformation is given by equation [B25].

Appendix C

C1: Calculating the inverse Laplace transformation for the Burgers convergence model

To obtain the solution for the Burgers convergence model in Chapter 3, the inverse Laplace transform of equation [3.41] had to be found. The method used is described in this appendix. Equation [3.41] is given as

$$F(t) = L^{-1}\left[\frac{3K\left(1+p_1s+p_2s^2\right)^2 + 2\left(1+p_1s+p_2s^2\right)\left(q_1s+q_2s^2\right)}{s\left(q_1s+q_2s^2\right)\left[6K\left(1+p_1s+p_2s^2\right)+\left(q_1s+q_2s^2\right)\right]}\right] \qquad [C1]$$

This can be written as

$$F(t) = L^{-1}\left[\frac{\left(1+p_1s+p_2s^2\right)\left\{3K+\left(3Kp_1+2q_1\right)s+\left(3Kp_2+2q_2\right)s^2\right\}}{s\left(q_1s+q_2s^2\right)\left\{6K+\left(6Kp_1+q_1\right)s+\left(6Kp_2+q_2\right)s^2\right\}}\right] \qquad [C2]$$

and after further manipulation

$$F(t) = L^{-1}\left[\frac{a\left(b+cs+s^2\right)\left(d+es+s^2\right)}{s^2(f+s)\left(g+hs+s^2\right)}\right] \qquad [C3]$$

where

$$a = \frac{p_2\left(3Kp_2+2q_2\right)}{q_2\left(6Kp_2+q_2\right)} \qquad b = \frac{1}{p_2} \qquad c = \frac{p_1}{p_2} \qquad d = \frac{3K}{3Kp_2+2q_2}$$

$$e = \frac{3Kp_1+2q_1}{3Kp_2+2q_2} \qquad f = \frac{q_1}{q_2} \qquad g = \frac{6K}{6Kp_2+q_2} \qquad h = \frac{6Kp_1+q_1}{6Kp_2+q_2} \qquad [C4]$$

Expanding equation [C3]

$$F(t) = a \cdot L^{-1}\left[\frac{bd + (be+cd)s + (b+ce+d)s^2 + (c+e)s^3 + s^4}{s^2(f+s)\left(g+hs+s^2\right)}\right] \qquad [C5]$$

After partial fraction expansion of equation [C5]

$$F(t) = a \cdot L^{-1}\left[\frac{A}{s} + \frac{B}{s^2} + \frac{D}{f+s} + \frac{G}{g+hs+s^2} + \frac{Hs}{g+hs+s^2}\right] \qquad [C6]$$

where A, B, D, G and H can be calculated from the set of simultaneous equations in equation [C7]. (The computer program, MATHEMATICA version 2.2 from Wolfram Research was used to solve these parameters.)

$$\begin{bmatrix} A \\ B \\ D \\ G \\ H \end{bmatrix} \begin{bmatrix} 0 & fg & 0 & 0 & 0 \\ fg & fh+g & 0 & 0 & 0 \\ fh+g & f+h & g & f & 0 \\ f+h & 1 & h & 1 & f \\ 1 & 0 & 1 & 0 & 1 \end{bmatrix} = \begin{bmatrix} bd \\ be+cd \\ b+ce+d \\ c+e \\ 1 \end{bmatrix} \qquad [C7]$$

As $\left(s^2 + hs + g\right)$ can be written as $\left(s+\frac{h}{2}\right)^2 - \left(\frac{h^2}{4} - g\right)$, equation [C6] become

$$F(t) = a \cdot L^{-1}\left[\frac{A}{s} + \frac{B}{s^2} + \frac{D}{f+s} + \frac{\left(G - H\left(\frac{h}{2}\right)\right)}{\sqrt{\frac{h^2}{4} - g}} \frac{\sqrt{\frac{h^2}{4} - g}}{\left(s+\frac{h}{2}\right)^2 - \left(\frac{h^2}{4} - g\right)} + \frac{H\left(s+\frac{h}{2}\right)}{\left(s+\frac{h}{2}\right)^2 - \left(\frac{h^2}{4} - g\right)}\right] \qquad [C8]$$

Taking the inverse Laplace transform gives

$$F(t) = a\left[A + Bt + De^{-ft} + \frac{G - \frac{Hh}{2}}{\sqrt{\frac{h^2}{4} - g}} \sinh\left(\sqrt{\frac{h^2}{4} - g}\right) te^{\frac{-ht}{2}} + H\cosh\left(\sqrt{\frac{h^2}{4} - g}\right) te^{\frac{-ht}{2}}\right] \qquad [C9]$$

By replacing A, B, D, G and H in terms of b, c, d, e, f, g and h from equation [C7] and inserting equation [C4], equation [C9] can be written as

$$F(t) = g_1\left[1 + c_5 t + c_6 e^{-ft} + \left(c_7 \sinh bt + c_8 \cosh bt\right)e^{\frac{-ht}{2}}\right] \qquad [C10]$$

where

$$b = \sqrt{\frac{\left(6Kp_1 + q_1\right)^2 - 24K\left(6Kp_2 + q_2\right)}{4\left(6Kp_2 + q_2\right)^2}} \qquad [C11]$$

$$g_1 = \frac{2Kp_1q_1 + {q_1}^2 - 2Kq_2}{4K{q_1}^2} \qquad [C12]$$

$$c_5 = \frac{2Kq_1}{2Kp_1q_1 + {q_1}^2 - 2Kq_2} \qquad [C13]$$

$$c_6 = \frac{2K\left(p_2{q_1}^2 - p_1q_1q_2 + {q_2}^2\right)}{q_2\left(2Kp_1q_1 + {q_1}^2 - 2Kq_2\right)} \qquad [C14]$$

$$c_7 = \frac{{q_1}^2\left(-12Kp_2q_1 + 6Kp_1q_2 - q_1q_2\right)}{2w\left(6Kp_2 + q_2\right)^2\left(2Kp_1q_1 + {q_1}^2 - 2Kq_2\right)} \qquad [C15]$$

$$c_8 = \frac{{q_1}^2q_2}{\left(6Kp_2 + q_2\right)\left(-2Kp_1q_1 - {q_1}^2 + 2Kq_2\right)} \qquad [C16]$$

Appendix D

D1: Listing of the displacement discontinuity program developed to solve incremental problems in viscoelasticity

This program was written to implement the methodology developed in Section 3.6 of Chapter 3. As basis of this program, the listing of a boundary element program (TWODD) to solve elastic problems given by Crouch and Starfield (1983) was used. This was extensively modified to calculate the viscoelastic solutions and to deal with incremental problems as dictated by the structure of Figure 3.13. Some of the conventions and input parameters used by the original TWODD program is still valid. Below is an explanation of these together with the new input parameters.

Input parameters

NINC = Number of increments. Every change in geometry such as enlargements of slit type openings (used to represent the tabular stopes) should be counted as additional increments. There is no limit to the number of increments that can be specified. The user should however take care not to exceed the maximum number of elements.

KSYM = Specification of symmetry.
KSYM = 1 : No symmetry.
KSYM = 2 : A line of symmetry parallel to y-axis at x = XSYM.
KSYM = 3 : A line of symmetry parallel to x-axis at y = YSYM.
KSYM = 4 : Both x = XSYM and y = YSYM are lines of symmetry .

PR = Poisson's ratio.

E = Young's modulus.

VIS = Viscosity coefficient of the Kelvin model.

TIME = The problem time for which the solution needs to be calculated.

PXX = Horizontal stress. Note that compressive stresses are negative.

PYY = Vertical Stress. Note that compressive stresses are negative.

PXY = Shear stress.

NSTEP = Step number.

NUMBS = Number of straight line segments.

NUMOS = Number of straight line segments to define positions where benchmark points are calculated in the field.

TSTART = Time when the particular increment is made

TEND = Time when the next increment is made or if it is the last increment, the maximum time for which the problem needs to be solved.

NUM = Number of equally spaced elements for each segment. The program below limits the user to 200 elements in total.

XBEG = x co-ordinate of beginning of line segement
YBEG = y co-ordinate of beginning of line segement
XEND = x co-ordinate of end of line segement
YEND = y co-ordinate of end of line segement

KODE = Type of stresses or displacements prescribed for each segement
KODE = 1: σ_s and σ_n prescribed
KODE = 2: u_s and u_n prescribed
KODE = 3: u_s and σ_n prescribed
KODE = 4: σ_s and u_n prescribed

BVS = resultant shear stress σ_s or shear displacement u_s

BVN = resultant normal stress σ_n or normal displacement u_n

NUMPB = number of equally spaced points between the specified first and last points

The listing of the program is given on the next page while an example of an input file is given in Appendix D2.

```
      PROGRAM VISCODD
C
C     ***************************************************************
C     *                                                             *
C     *  Displacement discontinuity program to solve incremental problems in
C     *   viscoelasticity                                           *
C     *                                                             *
C     *  VERSION 1.0                                                *
C     *                                                             *
C     *  Kelvin model                                               *
C     *  Multiple mining increments                                 *
C     *  200 elements                                               *
C     *                                                             *
C     ***************************************************************
C
      COMMON/S1/PI,PR,VIS,TIME,T,E,G1,G2,G3,A1,A2,C1
      COMMON/S2/SXXS,SXXN,SYYS,SYYN,SXYS,SXYN,UXS,UXN,UYS,UYN
C
C...C(400,400) KERNEL TABLE
C...B(400) BOUNDARY CONDITIONS
C...D(400) DISCONTINUITIES
C...DTEMP(400) ARRAY FOR DOING SUPERPOSITION OF DIFFERENT
SOLUTIONS
C...BTEMP(400) ARRAY FOR STORING B(400) WHILE SOLVING - SOLVE
MODIFIES B(400)
C
      COMMON/S3/C(400,400),B(400),D(400),DTEMP(400),BTEMP(400),DSTORE(400)
C
      DIMENSION XM(200),YM(200),A(200),COSBET(200),SINBET(200),KOD(200)
      DIMENSION UX1(8,50),UY1(8,50),UXN1(200),UYN1(200)
C
      CHARACTER*20 FIN,FUS
C...OUTPUT FILE
      LUS=4
C...INPUT FILE
      LIN=3
C
      WRITE(*,21)
C
      READ(*,22)FIN
      OPEN(LIN,FILE=FIN)
C
C...ENTER OUTPUT REPORT FILE NAME
      WRITE(*,23)
C
      READ(*,22)FUS
C
      OPEN(LUS,FILE=FUS)
      CLOSE(LUS,STATUS='DELETE')
      OPEN(LUS,FILE=FUS)
C
```

```
C...NINC = Number of increments
C...KSYM = Type of Symmetry
C...XSYM = X position of symmetry
C...YSYM = Y position of symmetry
C
      READ (LIN,3) NINC,KSYM,XSYM,YSYM
C
C...PR = Poisson's Ratio
C...E = Young's Modulus
C...VIS = Viscosity coefficient
C...TIME = Time
C
      READ (LIN,4) PR,E,VIS,TIME
C
C...PXX,PYY,PXY = Stress components
C
      READ (LIN,5) PXX,PYY,PXY
C
      GO TO (80,85,90,95),KSYM
   80 WRITE (LUS,7)
      GO TO 100
   85 WRITE (LUS,8) XSYM
      GO TO 100
   90 WRITE (LUS,9) YSYM
      GO TO 100
   95 WRITE (LUS,10) XSYM,YSYM
C
  100 CONTINUE
      WRITE (LUS,11) PR,E,VIS
      WRITE (LUS,12) PXX,PYY,PXY
C
      PI=4.*ATAN(1.)
      G1=(1.-(PR*PR))/E
      G2=(1.+PR)/E
      G3=((1.-(2*PR))*(1.+PR))/E
      A1=E/(VIS*(1.+PR))
      A2=(3.*E)/(VIS*(1.-2.*PR)*(1.+PR))
      C1=-1./(2.*(1.-PR))
C
C...INITIALIZE DTEMP
C
      DO 102 L=1,400
      DTEMP(L) = 0
  102 CONTINUE
C
C....INITIALIZE UXN1 AND UYN1
C
      DO 103 L=1,200
      UXN1(L)=0
      UYN1(L)=0
  103 CONTINUE
C
```

```
C....INITIALIZE UX1 AND UY1
C
      DO 104 L=1,8
      DO 104 LL=1,50
      UX1(L,LL)=0
      UY1(L,LL)=0
  104 CONTINUE
C
C     REPEAT FOR NUMBER OF INCREMENTS
C
      DO 900 K=1,NINC
C
C     DEFINE LOCATIONS, SIZES ORIENTATIONS AND BOUNDARY CONDITIONS
OF
C       BOUNDARY ELEMENTS
C
C...NUMBS = Number of Segments
C...NUMOS = Number of Benchmarks
C...TSTART = Time when excavation is made
C...TEND = Time when next increment is mined
C...NSTEP = Step number
C
      READ (LIN,24) NSTEP,NUMBS,NUMOS,TSTART,TEND
C
C     DEFINE TIME
      T = TIME
C
      IF (K .GT. 1) GO TO 105
      NUMBE=0

  105 CONTINUE
      NUMBEINC=0
      DO 110 N=1,NUMBS
      READ (LIN,14) NUM,XBEG,YBEG,XEND,YEND,KODE,BVS,BVN
      XD=(XEND-XBEG)/NUM
      YD=(YEND-YBEG)/NUM
      SW=SQRT(XD*XD+YD*YD)
C
      DO 110 NE=1,NUM
      NUMBE=NUMBE+1
      NUMBEINC=NUMBEINC+1
      M=NUMBE
      XM(M)=XBEG+0.5*(2.*NE-1.)*XD
      YM(M)=YBEG+0.5*(2.*NE-1.)*YD
      A(M)=0.5*SW
      SINBET(M)=YD/SW
      COSBET(M)=XD/SW
      KOD(M)=KODE
      MN=2*M
      MS=MN-1
      B(MS)=BVS
  110 B(MN)=BVN
```

```
C
      WRITE (LUS,13) NSTEP,TSTART,TEND

      DO 115 M=1,NUMBE
      SIZE=2.*A(M)
      ANGLE=180.*ATAN2(SINBET(M),COSBET(M))/PI
      WRITE (LUS,15) M,KOD(M),XM(M),YM(M),SIZE,ANGLE,B(2*M-1),B(2*M)
  115 CONTINUE
C
C     ADJUST STRESS BOUNDARY VALUES TO ACCOUNT FOR INITIAL
STRESSES.
C
      NSTART=(NUMBE-NUMBEINC)+1
      DO 150 N=NSTART,NUMBE
      NN=2*N
      NS=NN-1
      COSB=COSBET(N)
      SINB=SINBET(N)
      SIGS=(PYY-PXX)*SINB*COSB+PXY*(COSB*COSB-SINB*SINB)
      SIGN=PXX*SINB*SINB-2.*PXY*SINB*COSB+PYY*COSB*COSB
      GO TO (120,150,130,140),KOD(N)
  120 B(NS)=B(NS)-SIGS
      B(NN)=B(NN)-SIGN
      GO TO 150
  130 B(NN)=B(NN)-SIGN
      GO TO 150
  140 B(NS)=B(NS)-SIGS
  150 CONTINUE
C
C     COMPUTE INFLUENCE COEFFICIENTS AND SET UP SYSTEM OF
ALGEBRAIC
C       EQUATIONS
C
      DO 300 I=1,NUMBE
      IN=2*I
      IS=IN-1
      XI=XM(I)
      YI=YM(I)
      COSBI=COSBET(I)
      SINBI=SINBET(I)
      KODE=KOD(I)
C
      DO 300 J=1,NUMBE
      JN=2*J
      JS=JN-1
      CALL INITL
      XJ=XM(J)
      YJ=YM(J)
      COSBJ=COSBET(J)
      SINBJ=SINBET(J)
      AJ=A(J)
      CALL COEFF(XI,YI,XJ,YJ,AJ,COSBJ,SINBJ,+1)
```

```
      GO TO (240,210,220,230),KSYM
C
 210 XJ=2.*XSYM-XM(J)
      CALL COEFF(XI,YI,XJ,YJ,AJ,COSBJ,-SINBJ,-1)
      GOTO 240
C
 220 YJ=2.*YSYM-YM(J)
      CALL COEFF(XI,YI,XJ,YJ,AJ,-COSBJ,SINBJ,-1)
      GOTO 240
C
 230 XJ=2.*XSYM-XM(J)
      CALL COEFF(XI,YI,XJ,YJ,AJ,COSBJ,-SINBJ,-1)
      XJ=XM(J)
      YJ=2.*YSYM-YM(J)
      CALL COEFF(XI,YI,XJ,YJ,AJ,-COSBJ,SINBJ,-1)
      XJ=2.*XSYM-XM(J)
      CALL COEFF(XI,YI,XJ,YJ,AJ,-COSBJ,-SINBJ,+1)
C
 240 CONTINUE
      GO TO (250,260,270,280),KODE
C
 250 C(IS,JS)=(SYYS-SXXS)*SINBI*COSBI+SXYS*(COSBI*COSBI-SINBI*SINBI)
      C(IS,JN)=(SYYN-SXXN)*SINBI*COSBI+SXYN*(COSBI*COSBI-SINBI*SINBI)
      C(IN,JS)=SXXS*SINBI*SINBI-2.*SXYS*SINBI*COSBI+SYYS*COSBI*COSBI
      C(IN,JN)=SXXN*SINBI*SINBI-2.*SXYN*SINBI*COSBI+SYYN*COSBI*COSBI
      GO TO 300
C
 260 C(IS,JS)=UXS*COSBI+UYS*SINBI
      C(IS,JN)=UXN*COSBI+UYN*SINBI
      C(IN,JS)=-UXS*SINBI+UYS*COSBI
      C(IN,JN)=-UXN*SINBI+UYN*COSBI
      GO TO 300
C
 270 C(IS,JS)=UXS*COSBI+UYS*SINBI
      C(IS,JN)=UXN*COSBI+UYN*SINBI
      C(IN,JS)=SXXS*SINBI*SINBI-2.*SXYS*SINBI*COSBI+SYYS*COSBI*COSBI
      C(IN,JN)=SXXN*SINBI*SINBI-2.*SXYN*SINBI*COSBI+SYYN*COSBI*COSBI
      GO TO 300
C
 280 C(IS,JS)=(SYYS-SXXS)*SINBI*COSBI+SXYS*(COSBI*COSBI-SINBI*SINBI)
      C(IS,JN)=(SYYN-SXXN)*SINBI*COSBI+SXYN*(COSBI*COSBI-SINBI*SINBI)
      C(IN,JS)=-UXS*SINBI+UYS*COSBI
      C(IN,JN)=-UXN*SINBI+UYN*COSBI
C
 300 CONTINUE
C
C    SOLVE SYSTEM OF ALGEBRAIC EQUATIONS
C
C...STORE B IN BTEMP BECAUSE SOLVE MODIFY B
C
      DO 310 L=1,(2*NUMBE)
      BTEMP(L)=B(L)
```

```
 310 CONTINUE
C
    N=2*NUMBE
    CALL SOLVE(N)
C
C...STORE D IN DSTORE FOR MULTIPLICATION
    DO 315 L=1,(2*NUMBE)
    DSTORE(L)=D(L)
 315 CONTINUE
C
C...RESTORE CONTENTS OF B TO ADD NEXT STEP
C
    DO 320 L=1,(2*NUMBE)
    B(L)=BTEMP(L)
 320 CONTINUE
C
C
    T=TIME-TSTART
    COMPL1=1./(4.*PI*G1*(1.+(C1*EXP(-A1*T))-((C1+1.)*EXP(-A2*T))))
 322 DO 325 L=1,(2*NUMBE)
    D(L)=DSTORE(L)/COMPL1
 325 CONTINUE
C
C...APPLY SUPERPOSITION RULE IN DTEMP
C
 330 DO 340 L=1,(2*NUMBE)
    DTEMP(L) = DTEMP(L) + D(L)
 340 CONTINUE
C
    IF (TIME .LT. TEND) GOTO 400
    T=TIME-TEND
    COMPL1=1./(4.*PI*G1*(1.+(C1*EXP(-A1*T))-((C1+1.)*EXP(-A2*T))))
 342 DO 345 L=1,(2*NUMBE)
    D(L)=DSTORE(L)/COMPL1
 345 CONTINUE
C
 350 DO 360 L=1,(2*NUMBE)
    DTEMP(L) = DTEMP(L) - D(L)
 360 CONTINUE
C
 400 CONTINUE
C
C...COPY CONTENTS OF DTEMP TO D FOR STRESS AND DISPLACEMENT
CALCULATIONS

 410 DO 420 L=1,(2*NUMBE)
    D(L) = DTEMP(L)
 420 CONTINUE
C
C   COMPUTE BOUNDARY DISPLACEMENTS AND STRESSES
C
    T = TIME
```

```
C
      IF (K .NE. NINC) GOTO 450
      WRITE (LUS,16) TIME
  450 CONTINUE

      DO 600 I=1,NUMBE
      IN=2*I
      IS=IN-1
      XI=XM(I)
      YI=YM(I)
      COSBI=COSBET(I)
      SINBI=SINBET(I)
C
      UXNEG=0
      UYNEG=0
      SIGXX=PXX
      SIGYY=PYY
      SIGXY=PXY
C
      T=TIME-TSTART
C
      DO 570 J=1,NUMBE
      JN=2*J
      JS=JN-1
      CALL INITL
      XJ=XM(J)
      YJ=YM(J)
      AJ=A(J)
      COSBJ=COSBET(J)
      SINBJ=SINBET(J)
      CALL COEFF(XI,YI,XJ,YJ,AJ,COSBJ,SINBJ,+1)
      GO TO (540,510,520,530),KSYM
C
  510 XJ=2.*XSYM-XM(J)
      CALL COEFF(XI,YI,XJ,YJ,AJ,COSBJ,-SINBJ,-1)
      GO TO 540
C
  520 YJ=2.*YSYM-YM(J)
      CALL COEFF(XI,YI,XJ,YJ,AJ,-COSBJ,SINBJ,-1)
      GO TO 540
C
  530 XJ=2.*XSYM-XM(J)
      CALL COEFF(XI,YI,XJ,YJ,AJ,+COSBJ,-SINBJ,-1)
      XJ=XM(J)
      YJ=2.*YSYM-YM(J)
      CALL COEFF(XI,YI,XJ,YJ,AJ,-COSBJ,SINBJ,-1)
      XJ=2.*XSYM-XM(J)
      CALL COEFF(XI,YI,XJ,YJ,AJ,-COSBJ,-SINBJ,+1)
C
  540 CONTINUE
C
      UXNEG=UXNEG+UXS*DSTORE(JS)+UXN*DSTORE(JN)
```

```
      UYNEG=UYNEG+UYS*DSTORE(JS)+UYN*DSTORE(JN)
      SIGXX=SIGXX+SXXS*DSTORE(JS)+SXXN*DSTORE(JN)
      SIGYY=SIGYY+SYYS*DSTORE(JS)+SYYN*DSTORE(JN)
      SIGXY=SIGXY+SXYS*DSTORE(JS)+SXYN*DSTORE(JN)
C
  570 CONTINUE
      UXN1(I)=UXN1(I)+UXNEG
      UYN1(I)=UYN1(I)+UYNEG
C
      IF (TIME .LT. TEND) GOTO 596
C
      UXNEG=0
      UYNEG=0
      SIGXX=PXX
      SIGYY=PYY
      SIGXY=PXY
C
      T=TIME-TEND
C
      DO 595 J=1,NUMBE
      JN=2*J
      JS=JN-1
      CALL INITL
      XJ=XM(J)
      YJ=YM(J)
      AJ=A(J)
      COSBJ=COSBET(J)
      SINBJ=SINBET(J)
      CALL COEFF(XI,YI,XJ,YJ,AJ,COSBJ,SINBJ,+1)
      GO TO (590,575,580,585),KSYM
C
  575 XJ=2.*XSYM-XM(J)
      CALL COEFF(XI,YI,XJ,YJ,AJ,COSBJ,-SINBJ,-1)
      GO TO 590
C
  580 YJ=2.*YSYM-YM(J)
      CALL COEFF(XI,YI,XJ,YJ,AJ,-COSBJ,SINBJ,-1)
      GO TO 590
C
  585 XJ=2.*XSYM-XM(J)
      CALL COEFF(XI,YI,XJ,YJ,AJ,+COSBJ,-SINBJ,-1)
      XJ=XM(J)
      YJ=2.*YSYM-YM(J)
      CALL COEFF(XI,YI,XJ,YJ,AJ,-COSBJ,SINBJ,-1)
      XJ=2.*XSYM-XM(J)
      CALL COEFF(XI,YI,XJ,YJ,AJ,-COSBJ,-SINBJ,+1)
C
  590 CONTINUE
C
      UXNEG=UXNEG+UXS*DSTORE(JS)+UXN*DSTORE(JN)
      UYNEG=UYNEG+UYS*DSTORE(JS)+UYN*DSTORE(JN)
      SIGXX=SIGXX+SXXS*DSTORE(JS)+SXXN*DSTORE(JN)
```

```
      SIGYY=SIGYY+SYYS*DSTORE(JS)+SYYN*DSTORE(JN)
      SIGXY=SIGXY+SXYS*DSTORE(JS)+SXYN*DSTORE(JN)
C
 595 CONTINUE
      UXN1(I)=UXN1(I)-UXNEG
      UYN1(I)=UYN1(I)-UYNEG
C
 596 CONTINUE
C
      IF (K .NE. NINC) GOTO 597
C
      USNEG=UXN1(I)*COSBI+UYN1(I)*SINBI
      UNNEG=-UXN1(I)*SINBI+UYN1(I)*COSBI
      USPOS=USNEG-D(IS)
      UNPOS=UNNEG-D(IN)
      UXPOS=USPOS*COSBI-UNPOS*SINBI
      UYPOS=USPOS*SINBI+UNPOS*COSBI
      SIGS=(SIGYY-SIGXX)*SINBI*COSBI+SIGXY*(COSBI*COSBI-SINBI*SINBI)
      SIGN=SIGXX*SINBI*SINBI-2.*SIGXY*SINBI*COSBI+SIGYY*COSBI*COSBI
C
      WRITE (LUS,17)
I,D(IS),USNEG,USPOS,D(IN),UNNEG,UNPOS,UXN1(I),UYN1(I),
     1          UXPOS,UYPOS,SIGS,SIGN
C
 597 CONTINUE
 600 CONTINUE
C
C    COMPUTE DISPLACEMENTS AND STRESSES AT SPECIFIED POINTS IN
BODY
C
      IF (NUMOS.LE.0) GO TO 900
C
      IF (K .NE. NINC) GOTO 602
      WRITE (LUS,18) TIME
 602 CONTINUE
C
      NPOINT=0
      DO 898 N=1,NUMOS
      READ (LIN,19) XBEG,YBEG,XEND,YEND,NUMPB
 610 CONTINUE
      NUMP=NUMPB+1
      DELX=(XEND-XBEG)/NUMP
      DELY=(YEND-YBEG)/NUMP
      IF (NUMPB.GT.0) NUMP=NUMP+1
      IF (DELX**2+DELY**2.EQ.0.) NUMP=1
C
      T=TIME-TSTART
C
      DO 890 NI=1,NUMP
      XP=XBEG+(NI-1)*DELX
      YP=YBEG+(NI-1)*DELY
C
```

```
      UX=0.
      UY=0.
      SIGXX=PXX
      SIGYY=PYY
      SIGXY=PXY
C
      DO 880 J=1,NUMBE
      JN=2*J
      JS=JN-1
      CALL INITL
      XJ=XM(J)
      YJ=YM(J)
      AJ=A(J)
C
      IF (SQRT((XP-XJ)**2+(YP-YJ)**2).LT.2.*AJ) GO TO 890
C
      COSBJ=COSBET(J)
      SINBJ=SINBET(J)
      CALL COEFF(XP,YP,XJ,YJ,AJ,COSBJ,SINBJ,+1)
      GO TO (840,810,820,830),KSYM
C
  810 XJ=2.*XSYM-XM(J)
      CALL COEFF(XP,YP,XJ,YJ,AJ,COSBJ,-SINBJ,-1)
      GO TO 840
C
  820 YJ=2.*YSYM-YM(J)
      CALL COEFF(XP,YP,XJ,YJ,AJ,-COSBJ,SINBJ,-1)
      GO TO 840
C
  830 XJ=2.*XSYM-XM(J)
      CALL COEFF(XP,YP,XJ,YJ,AJ,COSBJ,-SINBJ,-1)
      XJ=XM(J)
      YJ=2.*YSYM-YM(J)
      CALL COEFF(XP,YP,XJ,YJ,AJ,-COSBJ,SINBJ,-1)
      XJ=2.*XSYM-XM(J)
      CALL COEFF(XP,YP,XJ,YJ,AJ,-COSBJ,-SINBJ,+1)
C
  840 CONTINUE
C
      UX=UX+UXS*DSTORE(JS)+UXN*DSTORE(JN)
      UY=UY+UYS*DSTORE(JS)+UYN*DSTORE(JN)
      SIGXX=SIGXX+SXXS*DSTORE(JS)+SXXN*DSTORE(JN)
      SIGYY=SIGYY+SYYS*DSTORE(JS)+SYYN*DSTORE(JN)
      SIGXY=SIGXY+SXYS*DSTORE(JS)+SXYN*DSTORE(JN)
C
  880 CONTINUE
C
      UX1(N,NI)=UX1(N,NI)+UX
      UY1(N,NI)=UY1(N,NI)+UY
C
      NPOINT=NPOINT+1
      IF (K .NE. NINC) GOTO 890
```

```
      WRITE (LUS,20) NPOINT,XP,YP,UX1(N,NI),UY1(N,NI),SIGXX,SIGYY,SIGXY
C
  890 CONTINUE
C
      IF (K .EQ. NINC) GOTO 898
C
      T=TIME-TEND
C
      DO 896 NI=1,NUMP
      XP=XBEG+(NI-1)*DELX
      YP=YBEG+(NI-1)*DELY
C
      UX=0.
      UY=0.
      SIGXX=PXX
      SIGYY=PYY
      SIGXY=PXY
C
      DO 895 J=1,NUMBE
      JN=2*J
      JS=JN-1
      CALL INITL
      XJ=XM(J)
      YJ=YM(J)
      AJ=A(J)
C
      IF (SQRT((XP-XJ)**2+(YP-YJ)**2).LT.2.*AJ) GO TO 896
C
      COSBJ=COSBET(J)
      SINBJ=SINBET(J)
      CALL COEFF(XP,YP,XJ,YJ,AJ,COSBJ,SINBJ,+1)
      GO TO (894,891,892,893),KSYM
C
  891 XJ=2.*XSYM-XM(J)
      CALL COEFF(XP,YP,XJ,YJ,AJ,COSBJ,-SINBJ,-1)
      GO TO 894
C
  892 YJ=2.*YSYM-YM(J)
      CALL COEFF(XP,YP,XJ,YJ,AJ,-COSBJ,SINBJ,-1)
      GO TO 894
C
  893 XJ=2.*XSYM-XM(J)
      CALL COEFF(XP,YP,XJ,YJ,AJ,COSBJ,-SINBJ,-1)
      XJ=XM(J)
      YJ=2.*YSYM-YM(J)
      CALL COEFF(XP,YP,XJ,YJ,AJ,-COSBJ,SINBJ,-1)
      XJ=2.*XSYM-XM(J)
      CALL COEFF(XP,YP,XJ,YJ,AJ,-COSBJ,-SINBJ,+1)
C
  894 CONTINUE
C
      UX=UX+UXS*DSTORE(JS)+UXN*DSTORE(JN)
```

```
      UY=UY+UYS*DSTORE(JS)+UYN*DSTORE(JN)
      SIGXX=SIGXX+SXXS*DSTORE(JS)+SXXN*DSTORE(JN)
      SIGYY=SIGYY+SYYS*DSTORE(JS)+SYYN*DSTORE(JN)
      SIGXY=SIGXY+SXYS*DSTORE(JS)+SXYN*DSTORE(JN)
C
  895 CONTINUE
C
      UX1(N,NI)=UX1(N,NI)-UX
      UY1(N,NI)=UY1(N,NI)-UY
C
  896 CONTINUE
C
  898 CONTINUE
C
  900 CONTINUE
C
C     FORMAT STATEMENTS
C
C...NINC,KSYM,XSYM,YSYM
    3 FORMAT (2I4,2F14.4)
C...PR,E,VIS,T
    4 FORMAT (F6.2,E11.4,E11.3,F11.3)
C...PXX,PYY,PXY
    5 FORMAT (3E11.4)
    6 FORMAT (/,109H NUMBER OF STRAIGHT-LINE SEGMENTS (EACH
 CONTAINING A
     1T LEAST ONE BOUNDARY ELEMENT) USED TO DEFINE BOUNDARIES
 =,I3,//,12
     23H NUMBER OF STRAIGHT-LINE SEGMENTS USED TO SPECIFY OTHER
 LOCATION
     3S (I.E., NOT ON A BOUNDARY) WHERE RESULTS ARE TO BE FOUND =,I3)
    7 FORMAT (/,32H NO SYMMETRY CONDITIONS IMPOSED.)
    8 FORMAT (/,18H THE LINE X = XS =,F12.4,23H IS A LINE OF SYMMETRY.)
    9 FORMAT (/,18H THE LINE Y = YS =,F12.4,23H IS A LINE OF SYMMETRY.)
   10 FORMAT (/,19H THE LINES X = XS =,F12.4,13H AND Y = YS =,F12.4,
     1 23H ARE LINES OF SYMMETRY.)
   11 FORMAT (/,18H POISSON'S RATIO =,F6.2,//,18H YOUNG'S MODULUS =,E11.
     14,//,24H VISCOSITY COEFFICIENT =,E11.3)
   12 FORMAT (/,31H XX-COMPONENT OF FIELD STRESS =,E11.4,//,31H YY-
 COMPO
     1NENT OF FIELD STRESS =,E11.4,//,31H XY-COMPONENT OF FIELD STRESS =
     2,E11.4)
   13 FORMAT (1H ,/,25H    ELEMENT DATA - STEP ,I4,/
     1,20H    STARTING TIME =,F11.3,/,18H    ENDING TIME =,F11.3,//,96H
     2ELEMENT    KODE  X (CENTRE)  Y (CENTRE)    LENGTH      ANGLE  U
     3S OR SIGMA-S  UN OR SIGMA-N,/)
   14 FORMAT (I4,4F12.4,I4,2E11.4)
   15 FORMAT (2I9,3F12.4,F12.2,2E15.4)
   16 FORMAT (1H ,/,66H    DISPLACEMENTS AND STRESSES AT MIDPOINTS OF
 B
     1OUNDARY ELEMENTS.,/,22H    SOLVED AT TIME = ,F11.3,//
     2,40H  ELEMENT      DS    US(-)    US(+),
```

```
   3 60H      DN    UN(-)   UN(+)   UX(-)   UY(-)   UX(+),
   4 30H    UY(+)  SIGMA-S  SIGMA-N,/)
  17 FORMAT (I10,10F10.6,2F10.1)
  18 FORMAT (1H ,/,64H    DISPLACEMENTS AND STRESSES AT SPECIFIED
POIN
    1TS IN THE BODY.,/,22H    SOLVED AT TIME = ,F11.3,//
    2,93H   POINT   X CO-ORD   Y CO-ORD        U
    3X        UY      SIGXX      SIGYY      SIGXY,/)
  19 FORMAT (4F12.4,I4)
  20 FORMAT (I9,2F12.4,2F12.6,3F12.1)
  21 FORMAT (/2X,'ENTER INPUT FILE NAME:-')
  22 FORMAT (A20)
  23 FORMAT (//2X,'ENTER REPORT FILE NAME (/ TO EXIT):-' )
  24 FORMAT (3I4,2F11.3)
C
     END


     SUBROUTINE INITL
C
     COMMON/S2/SXXS,SXXN,SYYS,SYYN,SXYS,SXYN,UXS,UXN,UYS,UYN
C
     SXXS=0.
     SXXN=0.
     SYYS=0.
     SYYN=0.
     SXYS=0.
     SXYN=0.
C
     UXS=0.
     UXN=0.
     UYS=0.
     UYN=0.
C
     RETURN
     END


     SUBROUTINE COEFF(X,Y,CX,CY,A,COSB,SINB,MSYM)
C
     COMMON/S1/PI,PR,VIS,TIME,T,E,G1,G2,G3,A1,A2,C1
     COMMON/S2/SXXS,SXXN,SYYS,SYYN,SXYS,SXYN,UXS,UXN,UYS,UYN
C
     COS2B=COSB*COSB-SINB*SINB
     SIN2B=2.*SINB*COSB
     COSB2=COSB*COSB
     SINB2=SINB*SINB
C
     XB=(X-CX)*COSB+(Y-CY)*SINB
     YB=-(X-CX)*SINB+(Y-CY)*COSB
C
     R1S=(XB-A)*(XB-A)+YB*YB
```

```
      R2S=(XB+A)*(XB+A)+YB*YB
      FL1=0.5*ALOG(R1S)
      FL2=0.5*ALOG(R2S)
      FB2=(FL1-FL2)
      IF (YB.NE.0.) GO TO 10
      FB3=0.
      IF (ABS(XB).LT.A) FB3=PI
      GO TO 20
   10 FB3=-(ATAN((XB+A)/YB)-ATAN((XB-A)/YB))
   20 FB4=(YB/R1S-YB/R2S)
      FB5=((XB-A)/R1S-(XB+A)/R2S)
      FB6=(((XB-A)**2-YB*YB)/R1S**2-((XB+A)**2-YB*YB)/R2S**2)
      FB7=2.*YB*((XB-A)/R1S**2-(XB+A)/R2S**2)
C
      COMPL1=1./(4.*PI*G1*(1.+(C1*EXP(-A1*T))-((C1+1.)*EXP(-A2*T))))
      COMPL2=G2*(1.-EXP(-A1*T))
      COMPL3=G3*(1.-EXP(-A2*T))
C
      UXDS=-
(COMPL3)*SINB*FB2+(1/(2*PI*COMPL1))*COSB*FB3+(YB*COMPL2*(SINB*FB4-
COSB*FB5))
      UXDN=-(COMPL3)*COSB*FB2-(1/(2*PI*COMPL1))*SINB*FB3-
(YB*COMPL2*(COSB*FB4+SINB*FB5))
      UYDS=(COMPL3)*COSB*FB2+(1/(2*PI*COMPL1))*SINB*FB3-
(YB*COMPL2*(COSB*FB4+SINB*FB5))
      UYDN=-(COMPL3)*SINB*FB2+(1/(2*PI*COMPL1))*COSB*FB3-
(YB*COMPL2*(SINB*FB4-COSB*FB5))
C
      SXXDS=(2.*COSB2*FB4+SIN2B*FB5+YB*(COS2B*FB6-SIN2B*FB7))
      SXXDN=(-FB5+YB*(SIN2B*FB6+COS2B*FB7))
      SYYDS=(2.*SINB2*FB4-SIN2B*FB5-YB*(COS2B*FB6-SIN2B*FB7))
      SYYDN=(-FB5-YB*(SIN2B*FB6+COS2B*FB7))
      SXYDS=(SIN2B*FB4-COS2B*FB5+YB*(SIN2B*FB6+COS2B*FB7))
      SXYDN=(-YB*(COS2B*FB6-SIN2B*FB7))
C
      UXS=UXS+MSYM*UXDS
      UXN=UXN+UXDN
      UYS=UYS+MSYM*UYDS
      UYN=UYN+UYDN
C
      SXXS=SXXS+MSYM*SXXDS
      SXXN=SXXN+SXXDN
      SYYS=SYYS+MSYM*SYYDS
      SYYN=SYYN+SYYDN
      SXYS=SXYS+MSYM*SXYDS
      SXYN=SXYN+SXYDN
C
      RETURN
      END

      SUBROUTINE SOLVE(N)
```

```
C
      COMMON/S3/A(400,400),B(400),X(400),DTEMP(400),BTEMP(400),DSTORE(400)
C
      NB=N-1
      DO 20 J=1,NB
      L=J+1
      DO 20 JJ=L,N
      XM=A(JJ,J)/A(J,J)
      DO 10 I=J,N
   10 A(JJ,I)=A(JJ,I)-A(J,I)*XM
   20 B(JJ)=B(JJ)-B(J)*XM
C
      X(N)=B(N)/A(N,N)
      DO 40 J=1,NB
      JJ=N-J
      L=JJ+1
      SUM=0.
      DO 30 I=L,N
   30 SUM=SUM+A(JJ,I)*X(I)
   40 X(JJ)=(B(JJ)-SUM)/A(JJ,JJ)
C
      RETURN
      END
```

D2: Input file for solving the incremental enlargement of a tabular stope

The input file is of fixed format type with each parameter assigned a specific column width. This must be strictly adhered to. The appropriate column width for each is given in Figure D1. Each data file needs to include the first three lines of parameters. This is followed by the different increment definitions in sequence. Each increment definition consists of a) the header line followed by b) the segment definitions and c) the benchmark specifications. No blank lines should be inserted.

The input file for the incremental mining of the stope in Chapter 3 is given below (see Chapter 3 for a specification of the problem). This problem is consisting of three increments with mining of these increments at t = 0 hours, t = 24 hours and t = 48 hours. Four benchmark definitions calculate stresses and displacement in the field at specified points for each step. Note that if these benchmark values are only required for the last step, it is still important to include the benchmark calculations for each increment as these intermediate values are needed for the final calculation.

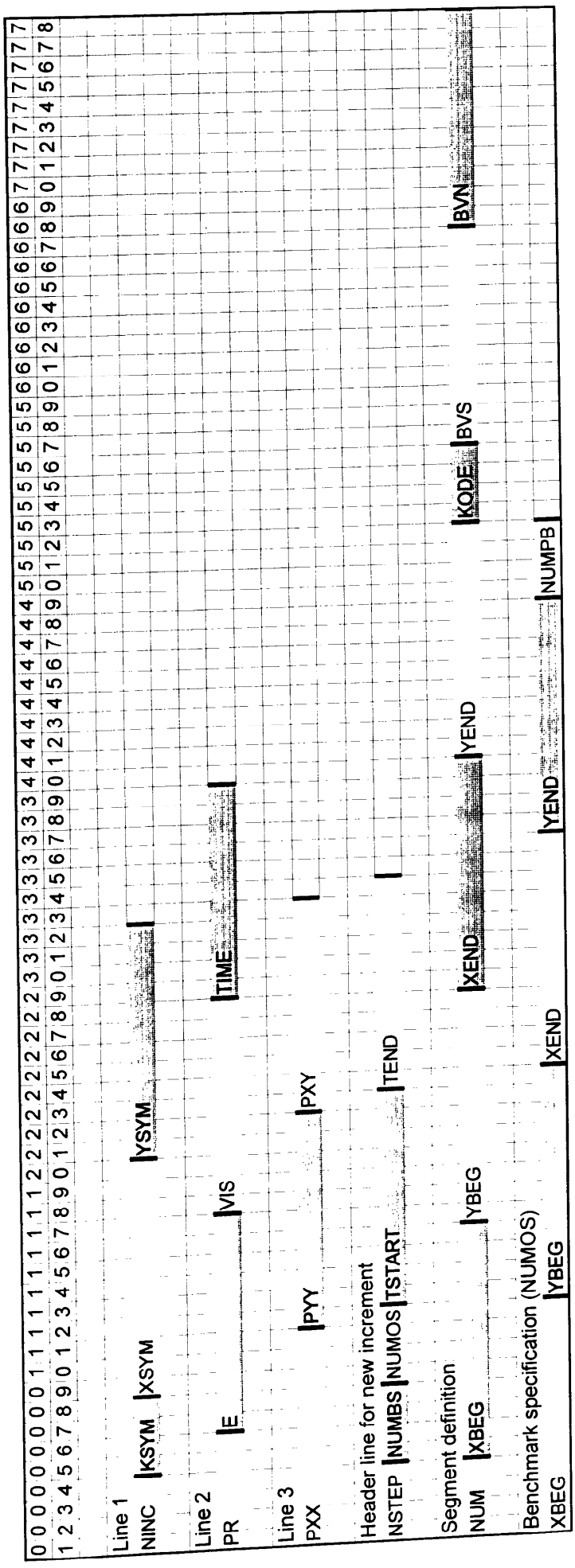

Figure D1. Fixed format used for the input files of VISCODD.

Input file for the incremental mining problem

(Note that the fixed format is violated by the word processor)

```
3  1     0.0000     0.0000
  0.20 0.7000e 11 0.5000e 12    70.000
-0.3000e 08-0.6000e 08 0.0000e 00
  1  40  4     0.000    24.000
  1    0.0000    0.0000    0.2500    0.0000  1 0.0000e 00 0.0000e 00
  1    0.2500    0.0000    0.5000    0.0000  1 0.0000e 00 0.0000e 00
  1    0.5000    0.0000    0.7500    0.0000  1 0.0000e 00 0.0000e 00
  1    0.7500    0.0000    1.0000    0.0000  1 0.0000e 00 0.0000e 00
  1    1.0000    0.0000    1.2500    0.0000  1 0.0000e 00 0.0000e 00
  1    1.2500    0.0000    1.5000    0.0000  1 0.0000e 00 0.0000e 00
  1    1.5000    0.0000    1.7500    0.0000  1 0.0000e 00 0.0000e 00
  1    1.7500    0.0000    2.0000    0.0000  1 0.0000e 00 0.0000e 00
  1    2.0000    0.0000    2.2500    0.0000  1 0.0000e 00 0.0000e 00
  1    2.2500    0.0000    2.5000    0.0000  1 0.0000e 00 0.0000e 00
  1    2.5000    0.0000    2.7500    0.0000  1 0.0000e 00 0.0000e 00
  1    2.7500    0.0000    3.0000    0.0000  1 0.0000e 00 0.0000e 00
  1    3.0000    0.0000    3.2500    0.0000  1 0.0000e 00 0.0000e 00
  1    3.2500    0.0000    3.5000    0.0000  1 0.0000e 00 0.0000e 00
  1    3.5000    0.0000    3.7500    0.0000  1 0.0000e 00 0.0000e 00
  1    3.7500    0.0000    4.0000    0.0000  1 0.0000e 00 0.0000e 00
  1    4.0000    0.0000    4.2500    0.0000  1 0.0000e 00 0.0000e 00
  1    4.2500    0.0000    4.5000    0.0000  1 0.0000e 00 0.0000e 00
  1    4.5000    0.0000    4.7500    0.0000  1 0.0000e 00 0.0000e 00
  1    4.7500    0.0000    5.0000    0.0000  1 0.0000e 00 0.0000e 00
  1    5.0000    0.0000    5.2500    0.0000  1 0.0000e 00 0.0000e 00
  1    5.2500    0.0000    5.5000    0.0000  1 0.0000e 00 0.0000e 00
  1    5.5000    0.0000    5.7500    0.0000  1 0.0000e 00 0.0000e 00
  1    5.7500    0.0000    6.0000    0.0000  1 0.0000e 00 0.0000e 00
  1    6.0000    0.0000    6.2500    0.0000  1 0.0000e 00 0.0000e 00
  1    6.2500    0.0000    6.5000    0.0000  1 0.0000e 00 0.0000e 00
  1    6.5000    0.0000    6.7500    0.0000  1 0.0000e 00 0.0000e 00
  1    6.7500    0.0000    7.0000    0.0000  1 0.0000e 00 0.0000e 00
```

```
1   7.0000   0.0000   7.2500   0.0000  1 0.0000e 00 0.0000e 00
1   7.2500   0.0000   7.5000   0.0000  1 0.0000e 00 0.0000e 00
1   7.5000   0.0000   7.7500   0.0000  1 0.0000e 00 0.0000e 00
1   7.7500   0.0000   8.0000   0.0000  1 0.0000e 00 0.0000e 00
1   8.0000   0.0000   8.2500   0.0000  1 0.0000e 00 0.0000e 00
1   8.2500   0.0000   8.5000   0.0000  1 0.0000e 00 0.0000e 00
1   8.5000   0.0000   8.7500   0.0000  1 0.0000e 00 0.0000e 00
1   8.7500   0.0000   9.0000   0.0000  1 0.0000e 00 0.0000e 00
1   9.0000   0.0000   9.2500   0.0000  1 0.0000e 00 0.0000e 00
1   9.2500   0.0000   9.5000   0.0000  1 0.0000e 00 0.0000e 00
1   9.5000   0.0000   9.7500   0.0000  1 0.0000e 00 0.0000e 00
1   9.7500   0.0000   10.0000   0.0000  1 0.0000e 00 0.0000e 00
  5.0000   2.0000   5.0000   2.0000  1
  5.0000   6.0000   5.0000   6.0000  1
  5.0000   10.0000   5.0000   10.0000  1
  16.0000   0.0000   16.0000   0.0000  1
 2  8  4   24.000   48.000
 1   10.0000   0.0000   10.2500   0.0000  1 0.0000e 00 0.0000e 00
 1   10.2500   0.0000   10.5000   0.0000  1 0.0000e 00 0.0000e 00
 1   10.5000   0.0000   10.7500   0.0000  1 0.0000e 00 0.0000e 00
 1   10.7500   0.0000   11.0000   0.0000  1 0.0000e 00 0.0000e 00
 1   -1.0000   0.0000   -0.7500   0.0000  1 0.0000e 00 0.0000e 00
 1   -0.7500   0.0000   -0.5000   0.0000  1 0.0000e 00 0.0000e 00
 1   -0.5000   0.0000   -0.2500   0.0000  1 0.0000e 00 0.0000e 00
 1   -0.2500   0.0000   0.0000   0.0000  1 0.0000e 00 0.0000e 00
  5.0000   2.0000   5.0000   2.0000  1
  5.0000   6.0000   5.0000   6.0000  1
  5.0000   10.0000   5.0000   10.0000  1
  16.0000   0.0000   16.0000   0.0000  1
 3  8  4   48.000   72.000
 1   11.0000   0.0000   11.2500   0.0000  1 0.0000e 00 0.0000e 00
 1   11.2500   0.0000   11.5000   0.0000  1 0.0000e 00 0.0000e 00
 1   11.5000   0.0000   11.7500   0.0000  1 0.0000e 00 0.0000e 00
 1   11.7500   0.0000   12.0000   0.0000  1 0.0000e 00 0.0000e 00
 1   -2.0000   0.0000   -1.7500   0.0000  1 0.0000e 00 0.0000e 00
```

1 -1.7500 0.0000 -1.5000 0.0000 1 0.0000e 00 0.0000e 00

1 -1.5000 0.0000 -1.2500 0.0000 1 0.0000e 00 0.0000e 00

1 -1.2500 0.0000 -1.0000 0.0000 1 0.0000e 00 0.0000e 00

5.0000 2.0000 5.0000 2.0000 1

5.0000 6.0000 5.0000 6.0000 1

5.0000 10.0000 5.0000 10.0000 1

16.0000 0.0000 16.0000 0.0000 1

Appendix E

E1: Correction procedure for the clockwork closure meter data

As the design of the instrument (see Chapter 4) is such that instantaneous closure is recorded as an arc (Figure E1), the time scale is distorted and the data needs to be corrected.

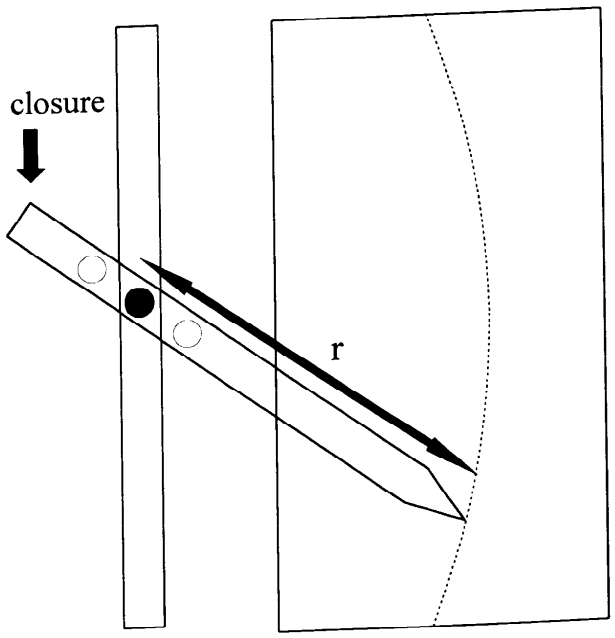

Figure E1. Recording mechanism of the clockwork closure meter. Also see Figure 4.3 in Chapter 4. The particular setting of the needle arm for the meters used in this study (r = 102 mm) resulted in the closure being amplified by a factor of 1.86 on the drum.

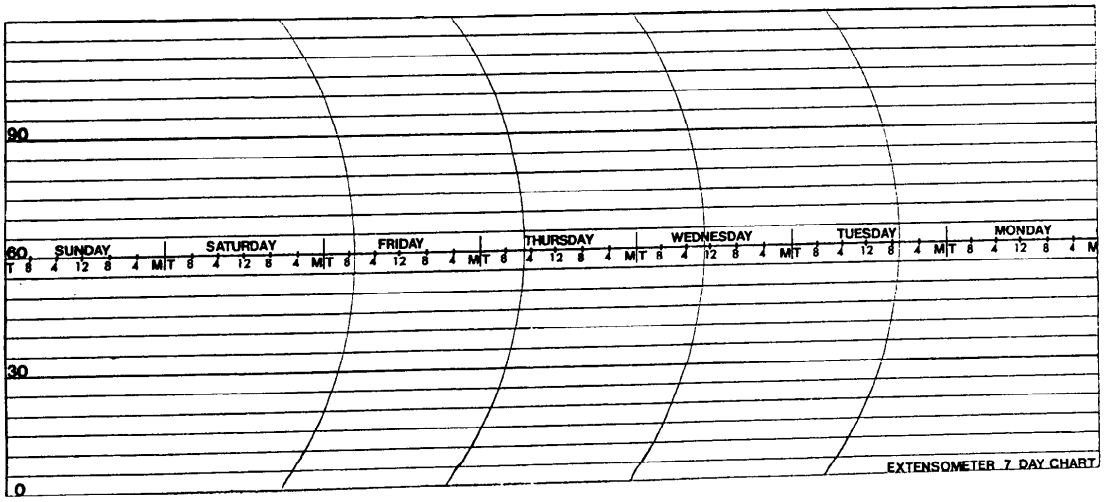

Figure E2. Sample of the calibration curves of the clockwork closure meters (not to scale).

For the correction procedure, the radius r needs to be determined. Although this can be directly measured at the instrument, it can also be calculated from the calibration curves in Figure E2.

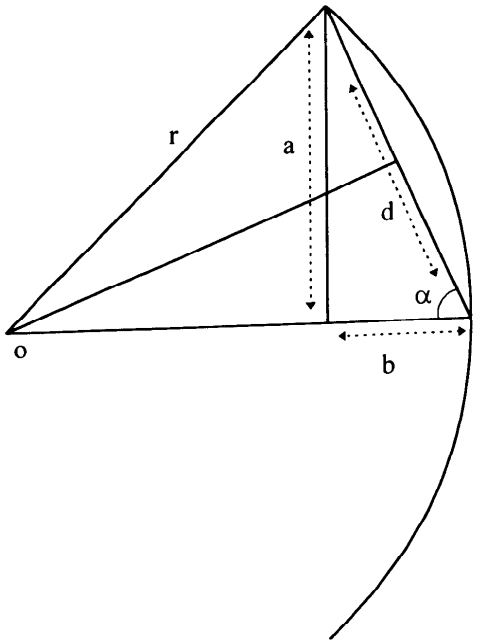

Figure E3. Calculation of the radius r from the calibration curves.

From Figure E3

$$d = \sqrt{a^2 + b^2} \qquad [E1]$$

$$\alpha = \sin^{-1}\left(\frac{a}{d}\right) \qquad [E2]$$

$$r = \frac{d}{2\cos\alpha} \qquad [E3]$$

Inserting equations [E1] and [E2] in equation [E3]

$$r = \frac{\sqrt{a^2 + b^2}}{2\cos\left[\sin^{-1}\left(\frac{a}{\sqrt{a^2 + b^2}}\right)\right]} \qquad [E4]$$

For the instruments used in this study a = 60 mm and b was measured from the calibration curves in Figure E2 as 19.5 mm. Inserting these values in equation [E4] gives r = 102 mm.

For correction of the data, it was assumed that the x-values along the horizontal line in the centre of the graph paper (marked 60, Figure E2) were correct. Any deviation from this line gives an error in x-value, $C_X(y)$, which becomes progressively worse as the distance from this line increases (Figure E4).

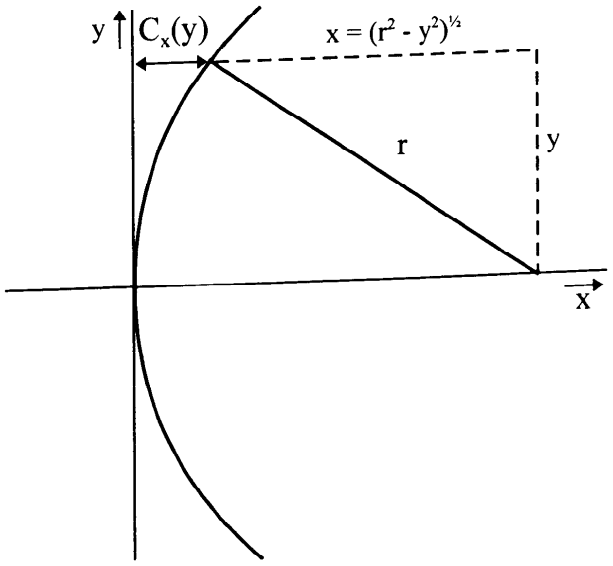

Figure E4. Illustration of the error in x-value as the curve deviates from the central horizontal line. The construction of the meter and the rotation of the drum is such that time (x-axis) is increasing away from the concave part of the arc.

The equation of the circle is given by $x^2 + y^2 = r^2$ or $x = \sqrt{r^2 - y^2}$ and therefore the error in x-value as a function of y is given as

$$C_x(y) = r - \sqrt{r^2 - y^2} \qquad [E5]$$

For a list of faulty data points (x_{old}, y_{old}) each data point should be corrected according to

$$x_{new} = x_{old} - C_x(y) = x_{old} - \left(r - \sqrt{r^2 - y_{old}^2}\right) \qquad [E6]$$

$$y_{new} = \frac{y_{old}}{m} \qquad [E7]$$

where m is the closure amplification factor (see Figure E1). In this study the meters were set to have a closure amplification factor of 1.86.

As a first step in the correction procedure, the data must be digitised and any commercial package can be used. UNGRAPH Version 2.0 from BIOSOFT was used in this study. A computer program was written to read the faulty digitised data and correct it according to equations [E6] and [E7]. This program is given in the next section.

E2: Pascal program to implement the correction procedure

```
Program Closure_correction;
uses crt;
{This program corrects the data recorded by the mechanical clockwork
closure meters. The design of these meters is such that instantaneous
closure is not recorded as a straight line on the graph paper but as
a curve. For these particular meters the curve can be described as part
of a circle with radius 102 mm. The program reads an input file containing
the faulty digitised values and outputs a corrected set in another file.}

Var
fin  : text;
fout : text;
xdataprev,
xdata,
ydata : real;
inputfile,
outputfile : String[50];

Begin
Clrscr;
inputfile:= '';
outputfile:= '';
Writeln('This program corrects the data recorded by the mechanical');
Writeln('clockwork closure meters. The design of these meters is such');
Writeln('that instantaneous closure is not recorded as a straight line');
Writeln('on the graph paper but as a curve. For these particular meters');
Writeln('the curve can be described as part of a circle with radius 102');
Writeln('mm. The program reads an input file containing the faulty');
Writeln('digitised values and outputs a corrected set in another file.');
Writeln(' ');
Writeln(' ');
Writeln('Enter the filename containing the faulty data.');
Readln(inputfile);
Writeln('Enter the filename to store the output data.');
Readln(outputfile);
Assign(fin,inputfile);
Reset(fin);
Assign(fout,outputfile);
Rewrite(fout);
xdataprev:= -100000;
While not Eof(fin) do
 Begin
  Readln(fin,xdata,ydata);
  xdata:= xdata/100;    {Divide by 100 because of digitiser scaling}
  ydata:= (ydata/100)-60; {-60 because digitiser reads from bottom and
  centre of page must be zero line for correction}
  xdata:= xdata-(102-sqrt(10404-(ydata*ydata)));
  If xdata < xdataprev then
```

```
    Begin
      xdata:= xdataprev;      {To correct for slight mistakes in the}
    End;                      {digitizing}
   xdataprev:= xdata;
   ydata:= (ydata + 60)/1.86;  {Divide by the closure amplification factor of 1.86}
   Writeln(fout,xdata:10:6,'  ',ydata:10:6);
 End;
close(fin);
close(fout);
End.
```

Appendix F

F1: Implementation of the elasto-viscoplastic model as a constitutive model in FLAC

The model developed in Chapter 5 was implemented in FLAC using the FISH language. The reader is referred to the FLAC manual (Itasca, 1993) for details on writing new constitutive models using FISH. The implementation of the visocplastic model is given below. It is based on the FISH function of the standard Mohr-Coulomb plasticity (not time-dependent) given with the code. This was modified into the appropriate time-dependent viscoplastic function.

```
;-----------------------------------------------------------
;FISH version of viscoplastic model
;Flow rule based on classical viscoplasticity (Perzyna, 1966)
;Yield function identical to standard Mohr-Coulomb
;Stress-dependent cohesion decay with time
;-----------------------------------------------------------
set echo on
def m_viscoplc
 constitutive_model
 f_prop  m_g m_k m_coh m_fric m_dil m_ind m_ten m_csnp m_fluid
 f_prop m_cohres m_cohdecay m_flag m_csnpres
 f_prop  m_nphi m_npsi m_tenmn m_e1 m_e2 m_x1 m_sh2
 float $sphi $spsi $s11i $s22i $s12i $s33i $sdif $s0 $rad $s1 $s2 $s3
 float $si $sii $psdif $fs $alams $cs2 $si2 $dc2 $ds2 $ttol $dss $fres
 float $apex $apsav
 int   $icase $apex_flag $m_err

 Case_of  mode
; ---------------------
; Initialisation section
; ---------------------
   Case 1
    $ttol = 1.00001
    $m_err = 0
    if m_fric > 89.0 then
     $m_err = 1
```

```
    end_if
    if abs(m_dil) > 89.0 then
     $m_err = 2
    end_if
    if m_coh < 0.0 then
     $m_err = 3
    end_if
    $sphi   = sin (m_fric * degrad)
    $spsi   = sin (m_dil * degrad)
    m_nphi  = (1.0 + $sphi) / (1.0 - $sphi)
    m_npsi  = (1.0 + $spsi) / (1.0 - $spsi)
    m_csnpres  = 2.0 * m_cohres * sqrt(m_nphi)
    m_e1    = m_k + 4.0 * m_g / 3.0
    m_e2    = m_k - 2.0 * m_g / 3.0
    m_x1    = m_e1 - m_e2*m_npsi + m_e1*m_npsi*m_nphi - m_e2*m_nphi
    m_sh2   = 2.0 * m_g
    if tenflg # 0 then
      if m_fric = 0.0 then
       m_tenmn = min(1.0e20,m_ten*$ttol)
      else
       m_tenmn = min(m_ten*$ttol,m_coh/tan(m_fric*degrad))
      end_if
    else
      m_tenmn = 1.0e20
    end_if
    if abs(m_x1) < 1e-6 * (abs(m_e1) + abs(m_e2)) then
     $m_err = 4
    end_if
    if $m_err # 0 then
     nerr  = 126
     error = 1
    end_if
  Case 2
; ---------------
; Running section
; ---------------
    zvisc = 1.0
    $apex_flag = 0
    if m_ind # 0.0 then
     m_ind = 1.0
    end_if
;--- get new trial stresses from old, assuming elastic increments ---
    $s11i = zs11 + (zde22 + zde33) * m_e2 + zde11 * m_e1
    $s22i = zs22 + (zde11 + zde33) * m_e2 + zde22 * m_e1
    $s12i = zs12 + zde12 * m_sh2
    $s33i = zs33 + (zde11 + zde22) * m_e2 + zde33 * m_e1
    $sdif = $s11i - $s22i
    $s0   = 0.5 * ($s11i + $s22i)
    $rad  = 0.5 * sqrt ($sdif*$sdif + 4.0 * $s12i*$s12i)
;--- principal stresses ---
    $si   = $s0 - $rad
    $sii  = $s0 + $rad
```

```
    $psdif =  $si - $sii
;--- determine case ---
    section
     if $s33i > $sii then
;--- s33 is minor p.s. ---
      $icase = 3
      $s1   = $si
      $s2   = $sii
      $s3   = $s33i
      exit section
     end_if
     if $s33i < $si then
;--- s33 is major p.s. ---
      $icase = 2
      $s1   = $s33i
      $s2   = $si
      $s3   = $sii
      exit section
     end_if
;--- s33 is intermediate ---
     $icase = 1
     $s1   = $si
     $s2   = $s33i
     $s3   = $sii
    end_section
;--------------------------
    section
     if m_ind = 1.0 then
      if crtime > m_flag then
       $fres = $s1 - $s3 * m_nphi + m_csnpres
        if $fres < 0.0 then
          m_coh = m_coh + (m_cohdecay * $fres * crtdel)
          m_flag = crtime
           if m_coh < m_cohres then
            m_coh = m_cohres
           end_if
         end_if
       end_if
     end_if
     m_csnp = 2.0 * m_coh * sqrt(m_nphi)
;--- general tension failure?
     if $s1 >= m_tenmn then
      if m_tenmn > m_ten then
        $apex_flag = 1
      end_if
;------ set stresses to plastic apex ---
      zs11      = m_tenmn
      zs22      = m_tenmn
      zs12      = 0.0
      zs33      = m_tenmn
      if m_tenmn  = 0.0 then
        m_ind   = 5.0
```

```
        else
          m_ind  = 1.0
        end_if
        zvisc = 0.0
        exit section
      end_if
;--- check for shear yield ---
      $fs   = $s1 - $s3 * m_nphi + m_csnp
      $alams = 0.0
      if $fs < 0.0 then
;--- yielding in shear ---
        $alams = $fs / m_x1
        $s1 = $s1 - m_fluid * crtdel * $fs * (m_e1 - m_e2 * m_npsi)
        $s2 = $s2 - m_fluid * crtdel * $fs * m_e2 * (1.0 - m_npsi)
        $s3 = $s3 - m_fluid * crtdel * $fs * (m_e2 - m_e1 * m_npsi)
        m_ind = 1.0
      else
        if $s3 < m_tenmn then
;--- no failure at all ---
          zs11 = $s11i
          zs22 = $s22i
          zs33 = $s33i
          zs12 = $s12i
          exit section
        end_if
      end_if
;--- general tension failure?
      if $s1 >= m_tenmn then
        if m_tenmn > m_ten then
          $apex_flag = 1
        end_if
;------ set stresses to plastic apex ---
        zs11      = m_tenmn
        zs22      = m_tenmn
        zs12      = 0.0
        zs33      = m_tenmn
        if m_tenmn  = 0.0 then
          m_ind  = 5.0
        else
          m_ind  = 1.0
        end_if
        zvisc     = 0.0
        exit section
      end_if
;--- uniaxial tension ... intermediate p.s. ---
      if $s2 >= m_tenmn then
        if $fs < 0.0 then
          m_ind = 4.0
        else
          m_ind = 3.0
        end_if
        if m_tenmn > m_ten then
```

```
        $apex_flag = 1
      end_if
      $s2 = m_tenmn
      $s3 = m_tenmn
    else
;--- uniaxial tension ... minor p.s. ---
      if $s3 >= m_tenmn then
       if $fs < 0.0 then
        m_ind = 4.0
       else
        m_ind = 3.0
       end_if
       if m_tenmn > m_ten then
         $apex_flag = 1
       end_if
       $s3 = m_tenmn
       $s2 = min($s2,$s3)
      end_if
    end_if
;--- direction cosines ---
    if $psdif = 0.0 then
     $cs2  = 1.0
     $si2  = 0.0
    else
     $cs2  = $sdif     / $psdif
     $si2  = 2.0 * $s12i / $psdif
    end_if
;--- resolve back to global axes ---
    case_of  $icase
     case 1
      $dc2  = ($s1 - $s3) * $cs2
      $dss  =  $s1 + $s3
      zs11  = 0.5 * ($dss + $dc2)
      zs22  = 0.5 * ($dss - $dc2)
      zs12  = 0.5 * ($s1  - $s3) * $si2
      zs33  = $s2
     case 2
      $dc2  = ($s2 - $s3) * $cs2
      $dss  =  $s2 + $s3
      zs11  = 0.5 * ($dss + $dc2)
      zs22  = 0.5 * ($dss - $dc2)
      zs12  = 0.5 * ($s2  - $s3) * $si2
      zs33  = $s1
     case 3
      $dc2  = ($s1 - $s2) *$cs2
      $dss  =  $s1 + $s2
      zs11  = 0.5 * ($dss + $dc2)
      zs22  = 0.5 * ($dss - $dc2)
      zs12  = 0.5 * ($s1  - $s2) * $si2
      zs33  = $s3
    end_case
    zvisc = 0.0
```

```
    end_section

; -------- reset tensile strength ----------
    if $apex_flag = 1 then
      $apex = $apex + 1.0
    end_if
    $apsav = 0.0
    if zsub > 0.0 then
      $apsav = $apex / zsub
      if $apsav > 0.0 then
        if tenflg # 0 then
          m_ten = 0.0
          m_tenmn = 0.0
        end_if
      end_if
; --- reset for next zone ------
      $apex = 0.0
    end_if

  Case 3
; ----------------------
; Return maximum modulus
; ----------------------
    cm_max = m_k + 4.0 * m_g / 3.0
    sm_max = m_g
  Case 4
; ---------------------
; Add thermal stresses
; ---------------------
    ztsa = ztea * m_k
    ztsb = zteb * m_k
    ztsc = ztec * m_k
    ztsd = zted * m_k
 End_case
end
opt m_viscoplc
set echo on
```